ETH No. 16489

Neutron Scattering Study of Complex Magnetic Properties of Strongly Correlated Electron Systems

Dissertation

Petra S. Häfliger

Laboratorium für Neutronenstreuung

Eidg. Technische Hochschule Zürich

CH-5232 Villigen PSI

2006

ETH No. 16489

Neutron Scattering Study of Complex Magnetic Properties of Strongly Correlated Electron Systems

A dissertation submitted to the

SWISS FEDERAL INSTITUTE OF TECHNOLOGY ZURICH

for the degree of

Doctor of Sciences

presented by
Petra S. Häfliger
Dipl. Phys. ETH Zürich
born 14.05.1976
citizen of Luzern

accepted on the recommendation of

Prof. Dr. M. Sigrist, examiner
Prof. Dr. A. Furrer, co-examiner
Prof. Dr. H.-U. Güdel, co-examiner

2006

Abstract

In the present Ph.D. thesis we investigated two materials belonging to the class of strongly correlated electron systems. We applied the neutron scattering technique to **(A)** a dilute magnetic system $La_{1.96-x}Sr_xHo_{0.04}CuO_4$ (high-temperature superconductor) and to **(B)** a tetramer-based magnetic cluster system α-$MnMoO_4$ (insulator).

(A) We studied the relaxation behavior of the ground state crystal-field transition associated with the Ho^{3+} ion in dependence of temperature by means of neutron spectroscopic experiments. Neutron crystal-field spectroscopy has been chosen to investigate the pseudogap issue because it monitors the low-energy spectral weight.
According to the well-known Korringa law, in the normal metallic state the line width of the crystal-field transition is a linear function of temperature. However, in the pseudogap state, the density of states at the Fermi level is suppressed and therefore the line broadening is reduced giving rise to deviations from the Korringa law. The temperature where the linewidth starts to deviate from the Korringa law, is attributed to the pseudogap temperature T^*, i.e. the temperature where the pseudogap opens.
Hereby we investigated the doping, oxygen isotope and pressure dependence of the pseudogap. We found clear evidence for the opening of a pseudogap in the whole doping regime $0.11 \leq x \leq 0.25$, even in the heavily overdoped compound (x=0.25). Furthermore we found that oxygen isotope substitution enhances T^*, whereas the application of hydrostatic pressure on the optimally doped compound (x=0.15) results in a downward shift of T^*. The opposite effects of oxygen isotope substitution and pressure emphasize the phonon contribution to the pseudogap formation.
Our relaxation data are generally compatible with a d-wave symmetry of the superconducting gap. However, with decreasing doping more relaxation channels are opened, which can be explained by phase separation and/or a modification of the gap function in the underdoped regime.

(B) α-$MnMoO_4$ is a tetrameric cluster system which undergoes a transition into a three-dimensional antiferromagnetic order. In the ordered state the Mn^{2+} spins (with $S_i = 5/2$) are ferromagnetically aligned within the tetrameric cluster, resulting in a total cluster spin S=10. Inelastic neutron scattering experiments on polycrystalline α-$MnMoO_4$ were previously performed. These measurements revealed four well defined inelastic lines, which could be assigned to transitions from the ground state to excited tetramer states. The intracluster coupling constants were deduced from the observed level scheme, and a

mean-field approach yielded the energy scale for the intercluster coupling.
We focused our attention to inelastic neutron scattering experiments taken on a single crystal. The single-crystal data clearly show the dispersive behavior of these magnetic excitations in reciprocal space proving a coupling between the tetramers. In addition, a spin-wave gap for the lowest mode has been detected, which implies the existence of an anisotropy term.
The analysis of the single-crystal data goes far beyond the powder experiments. They provide access to the individual intertetramer exchange parameters, in which the powder measurements can only reveal an average value for these intercluster couplings. We applied a cluster model based on random phase approximation in order to determine the various coupling constants. It turned out that the clusters are strongly interacting and that the dispersions of the different branches are interrelated by the corresponding transition matrix elements.
However, it seemed that the RPA cluster model encounters its limits, because it could not account for all the measured dispersions. Thus we have considered a toy model of a 1D dimer chain and computed the dispersions based on linear spin-wave theory drawing qualitative conclusions for α-$MnMoO_4$.

Inelastic neutron scattering is a powerful tool to investigate the dilute magnetic system (**A**) as well as the magnetic cluster system (**B**), because the eigenenergies associated with the magnetic interactions are directly revealed by spectroscopic experiments in zero field. Line broadening yields information about relaxation effects, whereas direct access to exchange coupling parameters is provided through the wave-vector dependence of excitations due to magnetic interactions.

Zusammenfassung

In der vorliegenden Dissertation haben wir zwei Materialien untersucht, die zur Klasse der stark korrelierten Elekron Systeme gehören. Wir haben Neutronenstreuung angewendet auf **(A)** ein verdünntes magnetisches System $La_{1.96-x}Sr_xHo_{0.04}CuO_4$ (Hochtemperatur-Supraleiter) und **(B)** ein tetranukleares magnetisches System α-$MnMoO_4$ (Isolator).

(A) Wir haben das Relaxationsverhalten vom tiefsten Kristallfeld-Übergang in Abhängigkeit der Temperatur mit Hilfe von Neutronen-Spektroskopie untersucht. Neutronen-Kristallfeld Spektroskopie wurde gewählt, um das Pseudogap zu untersuchen, da sie auf Änderungen der Zustandsdichte sensitiv ist.
Im normalen metallischen Zustand ist die Linienbreite des Kristallfeld-Übergangs eine lineare Funktion der Temperatur - gemäss dem wohlbekannten Korringa-Gesetz. In der Pseudogap-Phase hingegen ist die Zustandsdichte an der Fermikante reduziert, was zu einer Abweichung vom Korringa Verhalten führt. Deshalb wird die Temperatur, bei welcher die Linienbreite anfängt unter die Korringa Linie zu fallen, als die Pseudogap Temperatur T^* definiert.
Mit dieser Methode haben wir die Dotierungs-, Isotopen- und Druck-Abhängigkeit untersucht. Unsere Messungen zeigen klar, dass es im ganzen Dotierungsbereich ($0.11 \leq x \leq 0.25$), sogar im hoch überdotierten Bereich ein Pseudogap gibt. Ausserdem haben wir gefunden, dass der Sauerstoff-Isotopen-Effekt T^* erhöht, während die Anwendung von hydrostatischem Druck auf die optimal dotierte Probe (x=0.15) in einer Reduktion von T^* resultiert. Der gegenteilige Effekt von Isotopen-Substitution und Druck unterstreicht die Theorie, dass Phononen zur Bildung des Pseudogaps beitragen.
Unsere Relaxationsdaten sind generell kompatibel mit einer d-Wellen-Symmetrie des supraleitenden Gaps. Wir haben aber auch beobachtet, dass sich mit abnehmender Dotierung mehr Relaxations-Kanäle öffnen. Dies kann man mit einer generischen Inhomogenität dieser Hochtemperatur-Materialien und/oder mit einer Änderung der Gap Funktion im unterdotierten Bereich erklären.

(B) α-$MnMoO_4$ ist ein tetranukleares Clustersystem, welches eine drei- dimensionale antiferromagnetische Ordnung aufzeigt. Im geordneten Zustand sind die Mn^{2+} Spins (mit $S_i = 5/2$) ferromagnetisch gekoppelt innerhalb des Clusters, was zu einem Cluster-Spin $S = 10$ führt. Vorhergehend wurde ein Pulver dieses Materials mit Hilfe inelastischer Neutronenstreuung untersucht. Die Messungen zeigten vier deutlich definierte inelastische Peaks, die als Übergänge vom Grundzustand in angeregte Zustände identifiziert

werden konnten. Davon wurden die Intracluster-Wechselwirkungskonstanten abgeleitet, die Energieskala für den Intercluster-Austausch wurde im Rahmen einer Molekularfeld-Rechnung berücksichtigt.
Wir haben uns auf inelastischen Neutronenstreu-Experimente an einem Einkristall konzentriert. Die Einkristall-Daten zeigen klar ein dispersives Verhalten der magnetischen Anregungen im reziproken Raum, was die Existenz einer Austausch- Wechselwirkung zwischen den Clustern beweist. Ausserdem haben wir für den tiefsten Mode ein Spingap beobachtet. Dies weist auf eine anisotrope Wechselwirkung hin.
Die Analyse der Einkristall-Daten geht weit über die Pulver-Experimente hinaus, da die Einkristall-Daten erlauben, die individuellen Intercluster-Kopplungskonstanten zu bestimmen, während die Pulver-Daten nur einen Durchschnittswert dafür liefern konnten. Wir haben ein Cluster-Modell im Rahmen von Random-Phase- Approximation (RPA) angewendet, um die verschiedenen Kopplungskonstanten zu bestimmen. Es stellte sich heraus, dass die Cluster sehr stark wechselwirken und dass die Dispersionen der verschiedenen Moden über die Übergangsmatrix-Elemente korreliert sind.
Es scheint jedoch, dass das RPA Cluster Modell seine Grenzen hat, denn wir konnten damit nicht alle Dispersionen erklären. Deshalb haben wir ein einfaches Modell einer ein-dimensionalen Dimer-Kette betrachtet und deren Dispersionen mit Hilfe linearer Spinwellen Theorie berechnet wurden. Von den erhaltenen Resultaten haben wir dann qualitative Schlussfolgerungen für α-$MnMoO_4$ gezogen.

Inelastische Neutronenstreuung eignet sich hervorragend, um sowohl das verdünnte magnetische System (**A**) als auch das magnetische Cluster-System (**B**) zu untersuchen, denn die entsprechenden Eigenenergien können mit Hilfe spektroskopischer Methoden direkt im Nullfeld aufgezeigt werden. Linienverbreiterungen geben Aufschluss über Relaxationseffekte, während die Abhängigkeit der Anregungsenergie vom Wellenvektor eine Bestiummung von magnetische Kopplungen erlaubt.

Contents

List of Abbrevation

List of frequently used abbreviations.

Abbrevation	Meaning
LSCO, La124	$La_{2-x}Sr_xCuO_4$
BSCCO, Bi2212	$Bi_2Sr_2CaCu_2O_{8+\delta}$
YBCO	$YBa_2Cu_3O_7$
CEF	crystal-field
OIE	oxygen isotope effect
IE	isotope effect
FWHM	full width at half maximum
RPA	random phase approximation
INS	inelastic neutron scattering
ARPES	angle resolved photoemission spectroscopy
μSR	muon spin rotation
NMR	nuclear magnetic resonance
EPR	electron paramaagnetic resonance
PPMS	physical properties measurement system

Chapter 1

Introduction

1.1 Strongly correlated electron systems

The essence of strongly correlated electron systems is the subtle coupling and competition between spin, charge, lattice and orbital degrees of freedom which demands a new picture for quasiparticles to be defined, see Fig. 1.1. Examples of systems where this situation occurs are:

- high-T_C superconductors
- colossal magnetoresistance manganites
- organic superconductors
- Kondo systems
- dilute magnetic semiconductors
- and many more.

The absence of a proper description for complex materials is asking for a careful and direct investigation of elementary excitations, as they reflect the interplay between the low-energy degrees of freedom and determine fundamental macroscopic physical properties. Some open issues in corrleated electron systems are discussed for instance in Ref. [1].

1.2 High-temperature superconductivity

The phenomenon of superconductivity was first discovered in 1911 by Kamerlingh-Onnes, they observed a sudden drop of the resistance in mercury below a critical temperature T_c of 4.2 K [2].
In 1933 Meissner and Ochsenfeld found out that a superconductor behaves like a perfect diamagnet, because an external magnetic field is expelled and cannot penetrate the superconducting sample: this is the so-called Meissner effect.
A microscopic and quantitative theory explaining the experimental facts was only developed in 1957 by Bardeen, Cooper and Schrieffer (BCS theory [3]). Superconductivity is

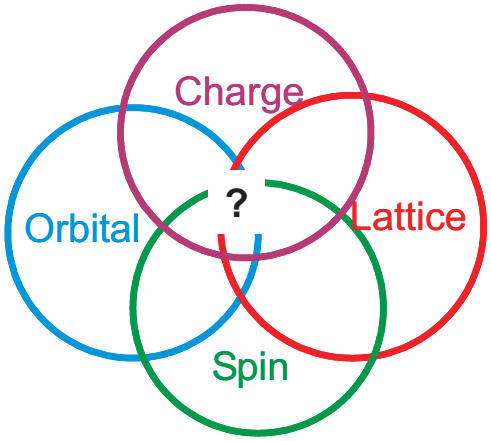

Figure 1.1: In strongly correlated electron systems there is a complicated interplay between spin, charge, lattice and orbital degrees of freedom.

induced by the formation of Cooper pairs due to an electron-phonon interaction, where two electrons condense into a spin singlet state. As a result, a superconducting gap Δ opens in the electronic density-of-states. (Note that $\Delta(T)$ is the order parameter, it vanishes at the transition temperature T_c.) A simple relation between the zero-temperature superconducting gap and T_c has been established:

$$2\Delta(T=0) \sim 3.5 k_B T_c \qquad \text{BCS.} \tag{1.1}$$

For a long time T_c has been limited to low temperatures $\sim$ 30 K. But in 1986 K.A. Müller and G. Bednorz [4] from IBM Rüschlikon, Switzerland, made a revolutionary discovery: they demonstrated the existence of superconductivity in the pervoskites $La_{2-x}(Ba,Sr)_xCuO_4$ (La214), $x < 1$. The chemical unit cell is shown in Fig. 1.2.
An important feature is the anisotropic layered pervoskite-type structure of these compounds, the cuprates are composed of CuO_2 layers alternating with so-called reservoir layers as schematically drawn in Fig. 1.2. In the case of LSCO doping is realized by substituting La^{3+} by Sr^{2+} which introduces holes into the CuO_2 planes, these charge carriers reside primarily on the oxygen site [5, 6]. A modification of the reservoir layers allows to control the doping level of the CuO_2 planes, which in turn sets T_c.
These fascinating findings motivated physicists, material scientists to search for compounds with even a higher T_c and indeed soon after superconductivity was discovered, results about Y123 and Bi2212 with T_c above the temperature of liquefaction of nitrogen were reported. So far the highest T_c achieved is 133 K, found by the Ott group in 1993 [7] in a mercury based compound, namely in $HgBa_2CaCu_2O_{6+x}$.
Some common characteristics of the high-temperature superconductors are that they are - surprisingly - poor metals at room temperature. The cuprates contain few charge carriers compared to normal metals, and they display highly anisotropic electrical and magnetic properties. Table 1.1 points out that the high-T_c materials dramatically differ in the normal state behavior from their low-T_c counterparts.
Moreover, also the properties of the superconducting state are different from the ones of a conventional superconductors: BCS pairing takes place in a singlet s-wave state, which means that the quasiparticle energy gap at low temperatures is finite and isotropic as

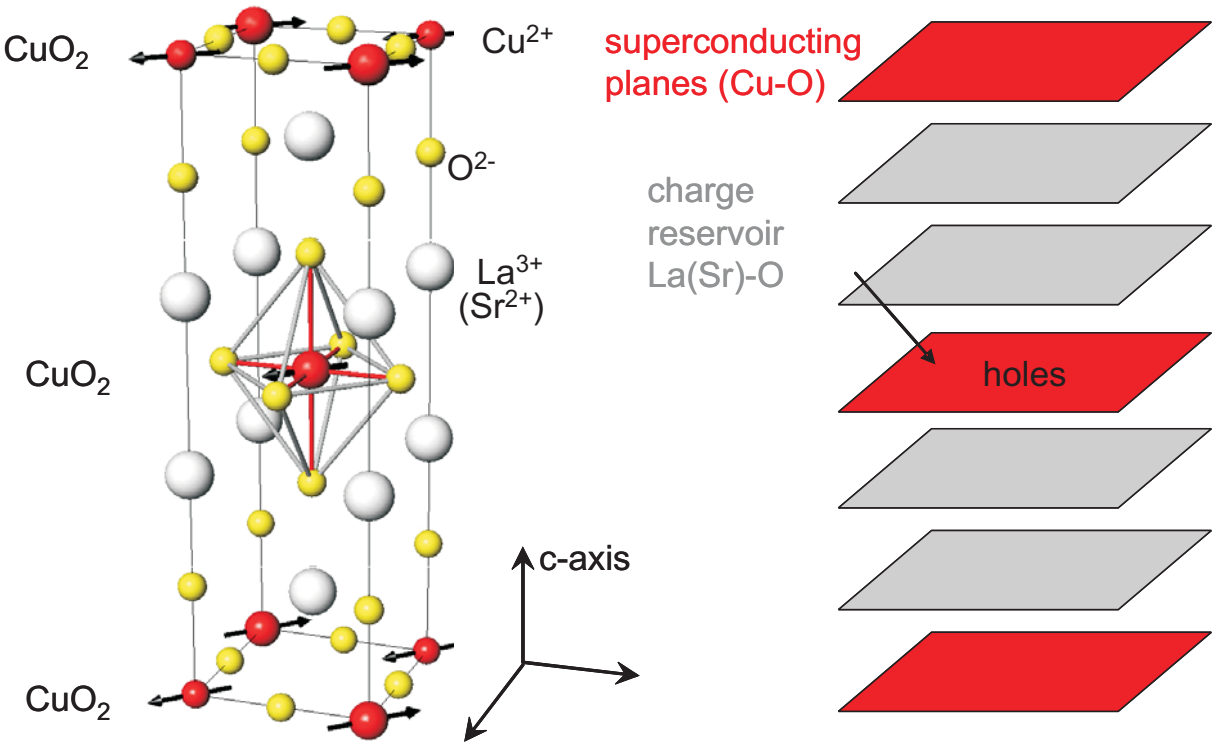

Figure 1.2: Structure of La_2CuO_4. On the left side the chemical unit cell is shown, whereas the right side illustrates schematically the layered structure common to all cuprates. In $La_{2-x}Sr_xCuO_4$ holes are introduced into the CuO_2 planes due to the doping with Sr.

Table 1.1: Anomalous normal state behavior of the cuprates as compared to conventional BCS superconductors. a denotes the lattice constant, ξ_{AF} is the antiferromagnetic correlation length.

	Conventional	High-T_c
Resistivity	$\rho \sim T^2$	$\rho \sim T$
Spin excitation spectrum	flat	peaked at $\mathbf{Q} \sim (\pi/a, \pi, a)$
Characteristic spin excitation energy	$\sim E_f$	$\omega \sim T \ll E_f$
Antiferromagnetic correlations	none	strong with $\xi_{AF} \geq 2a$

one moves around the Fermi surface. On the other hand an anisotropic gap function has been clearly identified in high-T_cs by means of angle-resolved photoemission spectroscopy (ARPES) [8, 9, 10] and phase sensitive experiments [11].

The most prominent difference to classical BCS superconductors is the fact that the cuprates are doped insulators with the parent compound being an antiferromagnet as well as a Mott insulator. (The phase diagram as a function of doping and temperature will be addressed in Section 1.2.2.)

1.2.1 Why are the high-T_c superconductors still a hot topic? - Potential applications

The discovery of high-temperature superconducting materials produced a tremendous excitement. Since the mechanism leading to superconductivity has not been understood yet, it seemed that a T_c in the range of room temperature was realistic. Scientists were dreaming about a whole new age opening up for practical applications and aluminum and copper were expected to be completely replaced by high-T_c materials in electromagnets, generators, motors, magnetic energy storage and many more.
But the initial enthusiasm was damped because these grandiose expectations turned out to be unrealistic. (Of course T_cs above the boiling point of liquid nitrogen, made already enormous savings possible.) The high-T_cs have several deficiencies: first of all critical current densities tend to be naturally too low for technological application. Secondly the ceramic and anisotropic nature of these materials makes it very difficult to produce long and flexible superconducting wires, which would be necessary for large-scale applications. Nowadays - after vast research to overcome the above mentioned deficiencies - low- and high-temperature superconductor small scale-devices are commercially available. An example is a SQUID device containing a chip with a superconducting ring: it has the advantage of smaller size because the necessary refrigeration system is smaller and its power consumption is much smaller. In general YBCO is used for small-scale devices, the reason is simply that it has a high critical temperature and it can accommodate high current densities.
On the other hand the development of high-T_c large-scale applications is still in its infancy. The much larger currents and lengths required for the corresponding devices present a major challenge to materials scientists. At the present time, research focuses on applications related to magnet technology which is probably among the most significant ones. These include magnetic energy storage, magnets for MRI (magnetic resonance imaging) and other medical imaging applications.
Compounds of the BSCCO family are the most promising candidates, because it is easier to grow BSCCO in bulk than YBCO. The technical performance of long, state-of-the-art BSCCO wires have allowed prototypes to be constructed. It is expected that there will be further progress in bringing down the costs of these materials, leading to significant advantages in efficiency and energy savings. For details, see Ref. [12, 13]

The understanding of the mechanism leading to superconductivity in the cuprates would facilitate the research for potential applications. Once these materials are understood, it might be possible to obtain higher T_cs and to improve the design of applications for commercial use. In the present work we elucidate the pseudogap which is supposed to be crucial for the understanding of the occurrence of superconductivity.

1.2.2 Phase diagram

The generic phase diagram of a high-temperature superconductor is sketched in Fig. 1.3. As mentioned above, the parent compound is antiferromagnetic (AF) and insulating, the copper spins in the planes are staggered. With small doping the Néel temperature then

drops rapidly and vanishes. This part of the phase diagram is very well understood. Upon further doping the system enters a spin glass phase, where a crossover to the pseudogap state occurs while increasing the temperature.
With a strontium content of 5% in LSCO, superconductivity (SC) appears with a raising T_c in the underdoped region (UD) up to optimal doping, then T_c decreases again in the overdoped regime (OD) and finally vanishes. Underdoped (overdoped) means that the doping level is less (higher) than the level where T_c reaches its maximum (optimal doping).
Finally when superconductivity vanishes, the compound becomes a Fermi-liquid.

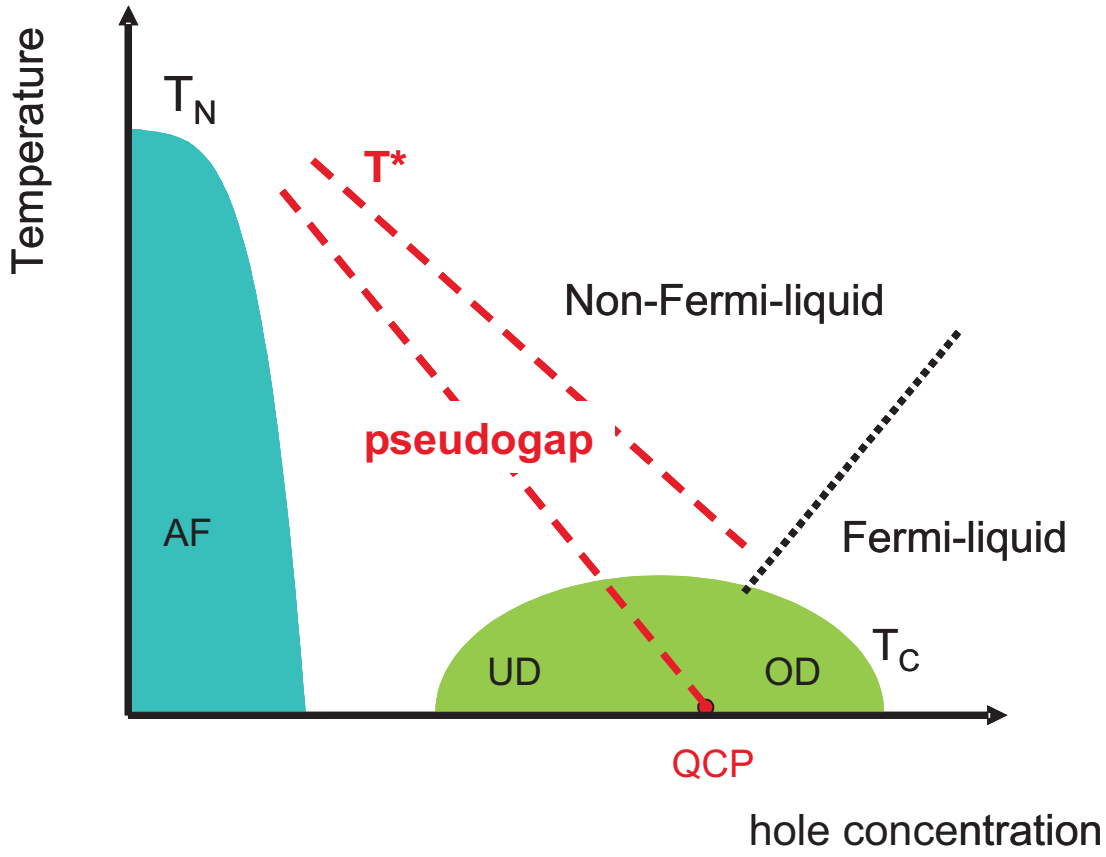

Figure 1.3: The generic phase diagram of a high-temperature superconductor with varying temperature and doping (AF=antiferromagnetic region, SC=superconducting dome). The crossover into the pseudogap state is indicated by the dashed lines which correspond to two fundamentally different models: the model based on antiferromagnetic fluctuation claims a quantum critical point, whereas the precursor pairing model predicts the existence of the pseudogap in the overdoped regime. For further elucidations we refer to the text.

We now describe the different phases in more detail.

Antiferromagnetic region

In the undoped parent compound a spin 1/2 is situated at the Cu-site interacting antiferromagnetically with its neighboring spins, which results in a 3D ordered state. Above T_N ∼250 K the spin system La_2CuO_4 can be treated as a 2D $S = 1/2$ Heisenberg antiferromagnet [14, 15]. Neutron scattering experiments have shown that a 2D antiferromangetic correlation develops among the Cu spins well above T_N, its correlation length is in the range of 200 Å at 300 K [15].
An important factor is the dimensionality: the CuO_2 planes are only weakly coupled, so that the dimensionality of the system is reduced to 2D. Due to a small interlayer coupling, antiferromagnetic ordering occurs. (Note that the Mermin-Wagner theorem states that an isotropic 2D system does not order.) However, the magnetization is reduced due to quantum effects. Anderson even argued that fluctuations could destroy the long-range antiferromagnetic order, which leads to a new ground state, the Resonanting Valence Bond (RVB) state: the system resonates between states in which different pairs of spins form singlet states [16].
The long-range order is drastically suppressed by doping holes into the copper oxide planes, because the spins of the doped holes are strongly coupled to the Cu spins and therefore limit the antiferromagnetic correlation length [17, 18], which is shortest around $x = 0.06$ ($\xi_{af} \sim 20$ Å). The Néel state persists to higher hole concentration in Ca-doped YBCO ($p \leq 0.035$) as compared to LSCO ($p \leq 0.02$). Upon further doping, the system enters a spin-glass-like state [19] characterized by a slowing down of the spin dynamics. The glass phase of LSCO has been studied in detail by the Wakimoto group [20], they investigated the behavior of incommensurate peaks as well as the ratio of statically ordered and dynamically fluctuating components as a function of doping. Niedermayer et al. applied the μSR (muon spin rotation) technique in order to investigate this phase and they discovered that the glass regime extends far into the superconducting state up to $p \leq 0.10$ [21]. Moreover, they found that the spin glass ordering temperature T_g varies continuously across the insulator-superconductor boundary. Since the glassy phase as well as the superconductivity are bulk phases, without any hint of macroscopic phase separation, the coexistence has to occur on a small length scale. This phenomenon has been observed in both YBCO and LSCO, thus it seems that the coexistence of the superconducting and antiferromangetic order is an intrinsic property of the CuO_2 planes [21, 22].

Superconducting phase

At first sight, the superconducting phase is not so different from that of classical superconductors. It is also characterized by zero resistance and the Meissner effect occurs, too. Moreover the superconducting objects carry a charge $2e$, which implies that pairs are formed. The phase boundary of superconductivity as a function of doping encloses a dome-shaped part of the phase diagram between x=0.06 and $x = 0.28$ in the case of LSCO. In this doping range, the $x = 1/8$ sample behaves in a peculiar way: T_c is slightly suppressed [23], while the antiferromagnetic correlation length is enhanced to its maximum value of $\xi_{af} \sim 200$ Å [22].
What is unusual, though, are the short coherence lengths in the cuprates (in-plane coherence length $\xi_{ab} \sim 20$ Å), whereas in conventional superconductors the coherence length is

normally several hundred Å or even more. Moreover the cuprates are essentially composed of Josephson coupled planes as has been demonstrated experimentally [24].
As opposed to BCS-type superconductors, the superconducting gap function is anisotropic as already mentioned, nodes have been clearly clarified by means of ARPES [8, 9] and phase sensitive experiments [11].
In contrast to conventional superconductors, there is evidence for phase separation by a number of experiments, a review is given in Ref. [25]. In slightly doped La_2CuO_4 for instance, field dependent magnetization measurements showed the formation of conducting phases by the existence of a percolative phase separation. Hizhnyakov experimental findings show that superconductivity can almost completely be suppressed by rapid temperature quenching of the sample [26], whereas under slow cooling conditions a percolative phase separation can occur [27].
While in the normal state some broad excitations exist centered around (π, π) (in LSCO doped with Sr, these excitations are at some incommensurate wave vector $(\pi + \delta, \pi)$[28, 29]), a strong renormalization of the spectral weight distribution is observed as one enters the superconducting state: a spin gap opens in LSCO [30] and YBCO [31] , which means that the spectral weight at low energies in the vicinity of (π, π) is depleted. In YBCO [32] and BSCCO [33] a so-called resonance emerges i.e. there is a lot of intensity at energies larger than the spin gap energy.

Pseudogap

One of the most unusual phenomena observed in high-temperature superconductors is the existence of the so-called pseudogap region in the temperature range $T_c < T < T^*$. The pseudogap phenomenon manifests itself as a suppression of the electronic density of states at the Fermi level as well as the magnetic low-energy excitation spectrum.
Such a depletion of the density-of-states is reflected in e.g.

- specific heat:
  reduction of the Sommerfeld coefficient $\gamma(T)$ well above T_c, whereas it is constant in the normal state (e.g. Ref. [34, 35, 36]).

- uniform magnetic susceptibility:
  it follows the Curie-Weiss law at high temperatures, but it starts to decrease gradually after exhibiting a broad peak at around T^* (e.g. Ref. [37]).

- in-plane resistivity and Hall coefficient R_H:
  R_H is constant above T^*, but it increases rapidly below T^* (e.g. Ref. [38, 37, 39]).

- nuclear magnetic resonance (NMR):
  decrease of the Knight shift and rapid reductin of the nuclear relaxation rate (e.g. Refs. [40, 41, 42, 43] and overview [44]).

- angle-resolved photoemission spectroscopy (ARPES):
  momentum-resolved information about the opening of the pseudogap (e.g. Ref. [45, 46, 47] and overview [48]).

- electronic Raman scattering:
  persistence of peak associated with superconductivity above T_c (e.g. [49] and overview [50])

- scanning tunneling spectroscopy:
  dip and hump in the $I - V$ characteristics as a signature of the opening of a gap (for instance in Ref. [51, 52] different behavior of the superconducting gap and the pseudogap could be traced for the first time. For a review, see Ref. [53].)

and

- neutron crystal-field spectroscopy: it monitors the low-energy spectral weight. The results on the pseudogap temperature of the present work are obtained by this technique. See also [54].

Note that neutron scattering experiments elucidating directly the pseudogap state have been rather scarce in the past. Actually Fauque et al. [55] observed for the first time a novel magnetic order in the pseudogap phase of $YBa_2Cu_3O_{6+x}$, which can be explained in terms of the circulating current theory of the pseudogap state [56, 57, 58]. This unusual magnetic order implies the existence of a hidden order parameter for the pseudgap phase in high-T_cs and therefore supports the occurrence of a quantum critical point, see Section 1.2.3.
What has been clarified using inelastic neutron scattering is the existence of well-defined (commensurate and incommensurate) magnetic excitations, both in the superconduducting and normal states [59, 60]. Depending on the doping level a spin gap may appear below T_c.
There is ample and undisputed evidence that the pseudogap opens in the underdoped region at a temperature T^* which is significantly larger than the superconducting transition temperature T_c [50]. And it is also commonly agreed that T^* decreases with increasing doping. However, as one approaches the overdoped regime, the opinions about the existence of the pseudogap differ [50, 53].

Non-Fermi liquid

At higher temperatures (above the crossover into the pseudogap region) the system is in the normal state, but in the underdoped region the normal state cannot be described by a conventional Fermi liquid. All the transport properties are governed by exceptionally simple but unusual power laws as a function of temperature. Many of these properties are understood assuming a marginal Fermi-liquid phenomenology [61]. The underlying idea is that the electrons are interacting with a spectrum of bosonic excitations, which has no other energy scale present besides the temperature, thus it exhibits quantum critical scaling. Within this theory there is no clear definition of quasiparticles.
A deficiency of the model is that there is no explicit momentum dependence, thus it cannot explain the d-wave symmetry of the superconducting gap.

Fermi-liquid region

The heavily overdoped non-superconducting region is characterized by a Landau-Fermi-liquid, which is one of the central concepts in solid state physics. The electrons are

renormalized by interactions and form quasiparticles so that there is a clear definition of the Fermi surface.

Magnetic phase diagram

The magnetic properties of the cuprates are very fascinating in themselves, they have been studied in great detail by means of muon-spin rotation (μSR) [62] as well as neutron scattering [63] experiments by many groups.
The high-temperature superconductors belong to the class of type-II superconductors, which means that there are two critical magnetic fields: at temperatures below T_c, an external magnetic field higher than the upper critical field induces the transition to the normal state, where the magnetic field penetrates the sample. Below the lower critical field the system is in the Meissner phase, where the magnetic field is completely expelled from the superconductor (perfect diamagnet).
In between is a mixed phase, the magnetic field can penetrate the sample in form of flux-lines (vortices) each carrying a flux quantum $\Phi_0 = \frac{hc}{2e}$. These vortices consist of a normal conducting core region surrounded by superconducting currents. Due to repulsive interactions, the vortices were predicted to arrange themselves in a lattice.
Such vortex lattices have also been observed in high-temperature superconductors: YBCO was the first high-T_c material where vortex lattices were detected [64]. In overdoped LSCO, Gilardi et al. [63, 65, 66] discovered a field-induced transition from a hexagonal to a square vortex lattice by means of small-angle neutron scattering. Also BSCCO has a vortex lattice at low fields [67] indicating that these properties are generic to all high-T_cs. However, the physical reason for the field-induced change in symmetry is still an open question, it is certainly related to thermal fluctuations and anisotropy effects which are important in the high-T_cs.

1.2.3 Theoretical models

Soon after the discovery of the high-T_c materials, it was realized that the phonon interaction alone cannot satisfactorily explain the high critical temperatures observed in the cuprates.
In the past two decades various and sometimes competing theoretical models have been developed in order to explain the underlying pairing mechanism. But despite the vast experimental information, there is still no model which is able to explain all the various experimentally observed features. Especially the discovery of the pseudogap phase has presented a major challenge for theoreticians.
From the theoretical perspective one of the most interesting aspects of the cuprates is that they belong to a class of materials which show strong electronic correlations.
The occurrence of the pseudogap is believed to hold the key to the understanding of high-T_c superconductivity itself. Two principal concepts which are still vigorously debated, have been worked out, they both explain the opening of a gap well above T_c.

- In the first one, the pseudogap is related to a precursor superconducting state that is lacking macroscopic phase coherence [68]. Within this scenario, the pseudogap evolves smoothly and persists in the overdoped regime.

- In the second model the pseudogap corresponds to a different kind of electronic or magnetic correlation that competes with superconductivity. T^* is then expected to fall rapidly around optimal doping and to reach zero at a critical doping point (quantum critical point) shortly past optimum doping.

Here we briefly mention the most important concepts:

Antiferromagnetic fluctuations

In the undoped materials the afore-mentioned correlations lead to the antiferromagnetic ordering of the Cu^{2+} spins. The proximity of the antiferromagnetic and the superconducting region naturally raises the question if the occurrence of superconductivity is related to magnetic correlations. Scenarios based on spin fluctuations [69], which is essentially a weak coupling approach, and RVB theory [70, 71, 72](strong coupling) predict the existence of a superconducting order parameter which changes sign upon 90° rotation (so-called *d*-wave gap). Indeed, ARPES clearly revealed the existence of nodes in the gap function [45]. The fact that Cooper pairing occurs with (predominantly) *d*-wave symmetry - unlike conventional superconductors - suggest that the pairing may be mediated by non-phononic excitations.
A concept exclusively based on antiferromagnetic correlations cannot explain the various observed isotope effects.

Preformed pairs and superconducting fluctuations

In this approach the pseudogap temperature T^* is thought as the temperature where the Cooper pairs start to form and overall phase coherence occurs then as the temperature crosses T_c. A consequence is then that the pseudogap evolves smoothly from the superconducting gap [68] and it represents a precursor to superconductivity.
Considering the short coherence lengths in the cuprates as well as the low carrier densities and quasi-two dimensionality, the concept of preformed pairs is well suited. The afore-mentioned conditions favor a suppression of the transition temperature relative to its mean-field value, because phase fluctuations become important [68, 73].
But specific heat data - particularly for underdoped samples - are opposed to the mean-field character of the superconducting phase [74], but rather support theoretical descriptions of the strong coupling limit.

Stripes

At low doping, materials can be subject to electronic phase separation. Stripes have been observed in LSCO by means of neutron scattering experiments [6]. LSCO is special in the sense that near 1/8 doping it tends to distort from the normal low-temperature orthorhombic (LTO) phase to the low temperature tetragonal (LTT) phase [75]. Doping with neodymium stabilizes the LTT phase and both charge and spin ordering occurs.
The existence of magnetic stripes [76, 77, 78] explains the antiferromagnetic domains of the cluster spin-glass, but it does not allow one to deduce whether all of the spatial inhomogeneity is due to the stripe pattern or whether additional phenomena, such as phase separation between striped and non-striped regions, take place. Moreover, if the stripe

picture is able to account alone for the coexistence of superconductivity and magnetism, is still an open question. What remains controversial, though, is whether stripes exist only for this anomalous doping and whether the formation of stripes is related to the opening of the pseudogap.

Spin-charge separation

Models have been developed where the spin and charge degrees of freedom of the holes are separated [79]. The spins form a d-wave singlet and the so-called spin gap refers to the energy needed to split them apart, whereas the charge degrees of freedom underlie no constraints. Spin-charge separation is one of the key issues in the physics of strongly correlated electronic systems.
Obviously such a theoretical concept cannot be verified directly by experiments. But one of its consequences namely that the characteristic spin gap energy is the exchange energy, which is approximately 100 meV in the undoped compound, is accessible in the experiment. This statement is reasonable because the derived value corresponds to the pseudogap energy extrapolated to zero doping.
P.W. Anderson perused these ideas and developed the so-called RVB (resonating valence bond) theory [16], where the Néel order is destroyed due to strong quantum fluctuations. The RVB theory is the strong coupling version of the spin fluctuation approach.
However, it has been observed that the specific heat and the magnetic susceptibility behave in a similar way in the pseudogap regime, even though the specific heat captures all excitations, whereas the susceptibility is related to spin excitations only, which puts the spin-charge separation approach in question.

Quantum critical points

A quantum phase transition is a phase transition which occurs at zero temperature, where thermal fluctuations do not come into play.
It has been suggested that the pseudogap temperature T^* crosses the superconducting phase boundary and ends in a quantum critical point (goes to zero) at a doping level which is slightly above optimum doping [53]. In this scenario the pseudogap is associated with an ordered phase competing with superconductivity. The quantum critical point partitions the phase diagram into a (nearly) ordered, a quantum critical, and a quantum disordered region corresponding to the underdoped, optimally doped, and overdoped region. The ordered phase occurs below a second-order transition line which is connected to the crossover into the pseudogap state [80]. Such a novel magnetic order has been observed in the pseudogap state of YBCO [55].
In the proximity of quantum criticality, critical fluctuations mediate a singular interaction among the quasiparticles. The violation of the Fermi-liquid behavior in the normal phase and the strong pairing mechanism leading to high-T_c superconductivity can be explained by this interaction associated with different quantum criticalities: antiferromagnetic [81, 82], excitonic [57], change in the symmetry of the superconducting order parameter [83], or incommensurate charge-density wave [84].

The understanding of the normal state properties in the pseudogap, non-Fermi liquid and Fermi liquid region may hold the key for the understanding of the physics of the cuprates and in turn high-temperature superconductivity.
On the other hand, recent ARPES experiments in the colossal magnetoresistive bilayer manganite $La_{1.2}Sr_{1.8}Mn_2O_7$ revealed properties which are characteristic for the pseudogap [85]! Manella et al. found that the electronic structure of $La_{1.2}Sr_{1.8}Mn_2O_7$ is strikingly similar to that found in the pseudogap phase of the copper oxide high-T_cs. Since metallic ferromagnetism and superconductivity are entirely different phenomena, one may draw the conclusion that the pseudogap state is not necessarily connected with the corresponding ground state.

1.2.4 Isotope effects and application of pressure

An isotope effect on a certain parameter is defined as the change of the parameter upon substitution of $^{\alpha}$X by its isotope $^{\beta}$X, where X is a chemical element and α, β the mass number.
The observation of an isotope effect on T_c in conventional superconductors was a crucial experimental fact, which guided the development of the BCS theory.
Concerning the cuprate superconductors the study of isotope effects also contributes to the theoretical understanding and the results may be incorporated in a microscopic theory as has been done for conventional superconductors.
During 20 years of research in the field of high-T_c cuprates isotope effects have been observed for various parameters:

- superconducting transition temperature T_c [86]
- in-plane penetration depth λ [86]
- charge-stripe ordering temperature T_{CO} [87]
- electron paramagnetic resonance (EPR) linewidth [88]

and also for the

- pseudogap temperature T^* [87, 89, 90, 91, 92].

In LSCO a huge oxygen isotope shift of T^* was found in the underdoped [87] regime, whose characteristic temperature T^* increases from 110 to 170 K upon replacing ^{16}O by ^{18}O. At optimal doping [90] neutron crystal-field spectroscopy revealed ΔT^*=(+9.0±2.5) K. The same technique applied to slightly underdoped $HoBa_2Cu_4O_8$ yielded also a large oxygen isotope effect on the pseudogap of $\Delta T^* \approx$+50 K [89].
Also the isotope dependence of the magnetic resonance has been investigated in optimally doped YBCO [93]: the inelastic neutron scattering experiments revealed no significant shift of the magnetic resonance peak energy, which was then interpreted as a negligible spin-phonon coupling.

Another type of experiment probing phonon contributions is the application of hydrostatic pressure which affects the lattice degrees of freedom in a manner different from oxygen

isotope substitution. However, there are only few pressure-dependent experiments on the pseudogap temperature T^* in the literature, and unfortunately the results are contradicting [94, 95, 96].

1.2.5 Why Ho@LSCO?

The purpose of introducing holmium into the high-T_c superconductor LSCO ($La_{1.96-x}Sr_xHo_{0.04}CuO_4$) is that we have used the rare-earth ion Ho^{3+} as a local probe: The presence of holmium lifts the degeneracy of the J-multiplets due to crystal-field effects. These splittings can be measured quite accurately with today's neutron high-resolution time-of-flight spectrometers. The linewidth of the peak associated with the lowest-lying crystal-field ground state transition monitors relaxation effects. Since the interaction of the crystal-field levels with the charge carriers is the most important relaxation channel, a suppression of the density of states at the Fermi level is directly unraveled, which in turn reveals the opening of the pseudogap. Thus there is no need for a complicated mathematical machinery to deduce the pseudogap T^* and the asessment of T^* is not dependent on any specific model developed for the high-T_cs.

1.3 Magnetic spin systems

Single atoms embedded in a non-magnetic environment can be handled relatively easily, the quantum mechanical state of an atom is governed by the Hund's rule.
But if the considered atom is a rare-earth ion in a solid, the crystal-field interaction comes into play, which originates from the electric field of the neighboring ions. This interaction modifies the eigenenergies derived from the Hund's rule, it lifts the $(2J+1)$-fold degeneracy of the J multiplets. In that case, it is even difficult to predict the states of a single-rare-earth ion and appropriate approximations have to be made. *Ab initio* calculations cannot determine the new eigenenergies, experimental investigations are necessary to determine the various crystal-field parameters.

The discovery of the magnetic exchange mechanism by Heisenberg [97], Dirac [98] in 1926 and Van Vleck [99] in 1932 signified the breakthrough in the understanding of magnetism. It is based on a fundamental component of quantum mechanics, namely the Pauli exclusion principle, which governs the spatial and momentum distribution of spins depending on their relative orientations. The basic idea is that the interaction strength between the spins $\mathbf{S}_i$ and $\mathbf{S}_j$ at site i and j, respectively, is given by the parameter J_{ij} in a way that the corresponding Hamiltonian reads

$$\mathcal{H}_{ij} = J_{ij}\mathbf{S}_i \cdot \mathbf{S}_j. \tag{1.2}$$

In principle J_{ij} is calculable within band structure theory [100] , but in practice an experimental investigation is indispensable because theoretical predictions alone are usually only of qualitative nature. Combining experiments with theoretical concepts such as spin wave calculations, allow one to deduce concrete values of the interaction parameters. Among experimental methods, inelastic neutron scattering has the advantage that it yields direct

information about the exchange interaction, because the energies of transitions between the exchange-split ground-state levels can be directly determined.
Note that in Eq. 1.2 effects such as crystal fields, spin-orbit coupling and anisotropic exchange are neglected, even though they might be important in three-dimensional crystals. But the degree of complexity enhances drastically if these effects are included.
However, there is an alternative to obviate difficulties which arise in a cooperative system: if one studies a group of a few magnetic exchange-coupled ions embedded in a non-magnetic environment, it is possible to get rid of the complexity of the macroscopic world. The reason is that these so-called isolated clusters hold the advantage that their theoretical handling is relatively simple due to the small number of interactions.

In the past decade, several scientific developments have emphasized the importance and relevance of studies of isolated clusters. First of all the knowledge in magnetism gathered from classical cluster systems can be incorporated into quantum spin system which belong to one of the favorite research fields in modern solid state physics. Quantum spin systems have been found to exhibit quantum-critical phenomena resulting from the interplay of intra- and intercluster interactions [101]. Moreover it is crucial to understand how the quantum properties of spins are affected by their environment [102], if the potential of quantum spin devices or applications in spintronics is to be realized.
Another reason for the continued interest in quantum magnetism relies on the deep connection between layered Cu^{2+} antiferromagnets and high-T_c materials, as well as on quantum fluctuations in low-dimensional $S = 1/2$ systems. Therefore doped spin liquids have been studied intensively and in fact, two-leg ladders systems have been representing the prominent model systems for discussing superconductivity. A theoretical investigation of stability of the superconducting state in such two-leg ladders revealed that inhomogeneous doping is harmful for the formation of the superconducting state[103].

A new emerging field in which chemists and physicists are engaged in a transdisciplinary effort, is the area of molecular magnetism: single-molecule magnets (SMM), which are spin clusters with large spin ground states, present an alternative way to the understanding of the behavior of a quantum spin system.
SMMs have some outstanding and novel properties such as molecular hysteresis and slow relaxation of the magnetization at low temperatures. The observation of quantum tunneling is another reason why SMMs have attracted great interest in recent years. Since SMMs can be arranged so as to minimize the magnetic interaction between them [104], their behavior can be compared to small cluster systems,see e.g. Ref. [105]. If such SMMs are weakly coupled, fancy effects like spin-spin cross relaxation effects were detected [106, 107].

Molecular (bottum-up) vs. classical (top-down) approach

The understanding of magnetic phenomena can be tackled from two direction as illustrated in Fig. 1.4, namely

- molecular (bottom-up) approach starting in the quantum regime

- classical (top-down) approach starting in the classical regime.

In the *bottum-up* approach, one starts with an ensemble of simple, identical objects, let us assume for example an isolated dimer system. Then one enhances the complexity of the system by increasing the number of spins constituting a cluster step by step (e.g. Mn_4, Mn_{12}, Mn_{30}, Mn_{84}). Or alternatively, the introduction of cluster-cluster interaction, brings cooperative phenomena along, e.g. dimer systems with weak intercluster interaction [108] or a tetranuclear cluster such as α-$MnMoO_4$ [109]. Additionally quantum effects can be or have to be incorporated in low-spin systems where the constituents of the cluster carry a quantum mechanical spin $S = 1/2$. This way the observed or calculated effects become more sophisticated and maybe even new phenomena arise - observed in experiments or predicted by theory - and answers to the question how a quantum spin behaves embedded in a solid might be found.
The *top-down* approach starts from the classical world, for example from a cobalt nanoparticle [110] shown in Fig. 1.4. The idea is that while decreasing the number of spins, the importance of quantum effects successively grows. It has been reported that the giant Mn_{84} single-molecule magnet (SMM) exhibits both magnetization hysteresis and quantum tunnelling effetcs, where the latter is a point of relevance to the general question of how large magnetic nanoparticles can become and still display quantum effects [111]. The Mn_{84} SMM essentially presents a long-sought after meeting of the bottum-up and top-down approach to nanoscale magnetic materials.

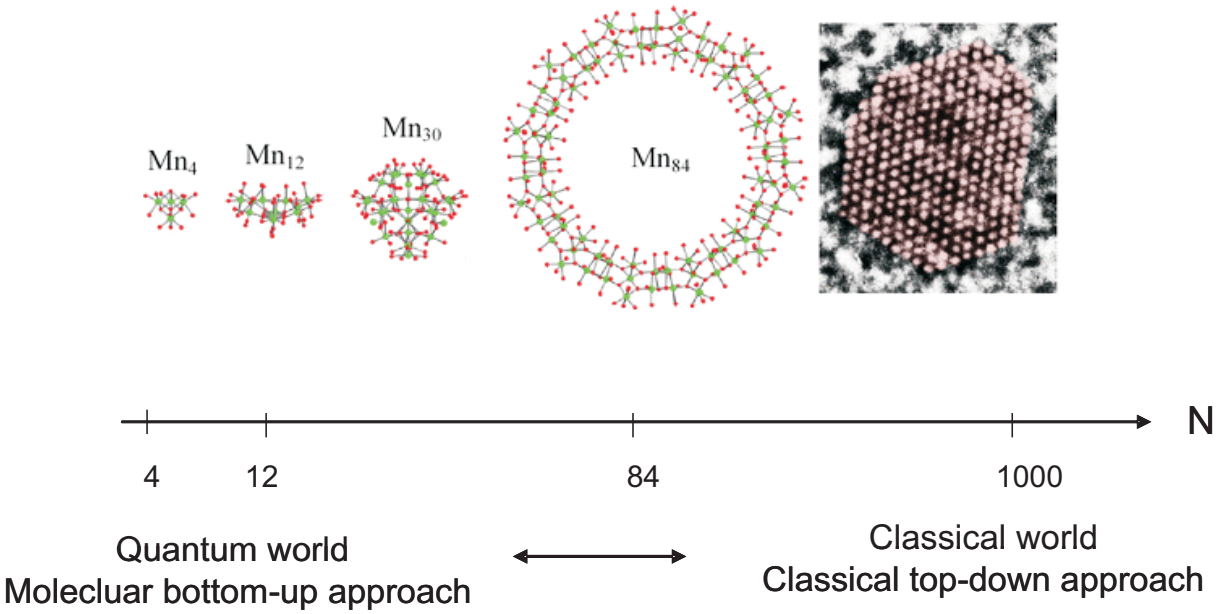

Figure 1.4: Illstruation of the molecular bottom-up approach as compared to the classical top-down approach. Both serve to improve the understanding of magnetism, where in the first case a spin system with increasing number of magnetic ions up to a molecule containing 84 manganese ions is considered. In the second case one starts with a macroscopic classical system, on the far right a high-resolution transmission electron microscopy view of a cobalt nanoparticle with 1000 Co atoms [110] exhibiting a fcc structure with magnetic anisotropy.

Nano-sized magnetic particles - finite-size spin wave theories

The synthesis and the subsequent experimental investigation has lead to the development of finite-size spin wave theories. The discovery of high-temperature superconductivity in materials containing 2D antiferromagnetic CuO_2 planes initiated a huge interest in the properties of 2D Heisenberg antiferromagnets [112]. Obviously it is of large interest to know when long-range order at zero temperature sets in in such lattices.
However, this question could not be answered successfully so far. Therefore numerical calculations would be extremely helpful in order to investigate that issue. But so far only small clusters can be handled numerically, where finite-size effects are pronounced. The goal of finite-size theories is to provide reliable methods for the finite-size scaling [113]. It is therefore obvious that the synthesis of larger magnetic grids is highly desirable in order to verify finite-size theories.

1.3.1 Classical cluster systems

Classical cluster systems are characterized by an assembly of classical spins, which means that the constituents of the cluster carry a spin $S > 1/2$, so that quantum effects can be neglected.
Magnetic cluster systems are not only interesting in itself, but they have also some important applications. Biological systems have been found with similar magnetic properties as the molecular transition metal complexes [114]. Moreover, the characterization of a spin glass is essentially based on the detailed energy level structure of magnetic clusters.

Isolated clusters

Isolated clusters of magnetic atoms may be divided into two classes [115]:

- the clusters occur naturally in pure compounds
- the clusters are produced artificially by forming solid solutions of magnetic and non-magnetic compounds.

As for the first ones, their crystal structures are usually complex and sometimes not even known, while in simpler crystal structures cooperative phenomena tend to be dominant.
A. Furrer and H.U. Güdel rendered considerable efforts to the understanding of magnetic clusters [105, 116, 117, 118]. Furrer pioneered in calculating the eigenvalues for very general cluster configurations of binuclear, trinuclear and tetranuclear clusters based on irreducible tensor methods. He also worked out the expressions for the corresponding neutron scattering cross section [119].
In these studies [105, 116, 117, 118] neutron scattering has proven to be a potent tool in order to derive the coupling parameters and also the geometrical configuration of the cluster. As for the latter one, the magnetic form factor of the scattering cross section shows interference effects which in turn yield direct information about the internal structure of the cluster. As already mentioned above the transition energies reveal the eigenvalues of the system, which depend on the internal coupling parameters.

Interacting clusters

If the cluster themselves are interacting, the description of the system gets significantly more complicated: the states of the single ions belonging to one cluster not only couple to new states of the cluster, but these cluster states are also perturbed by the interaction with spins from neighboring clusters. Hence the simple molecular picture is no longer valid , which results in a distinctly new situation of alternating strong (intracluster) and weak (intercluster) coupling.
As long as the intercluster interactions are small, the system might be treated within a mean-field approach where the interaction between the clusters are taken into account by an internal magnetic field. Alternatively one may use a random phase approximation (RPA), where the clusters are considered as a unit. The analysis of neutron spectroscopic experiments on a single crystal within RPA yields the direction dependent interaction parameters between the clusters.
An example is the dimer compound $Cs_3Cr_2Br_9$, which enters an antiferromagnetically ordered state below 1.6 K. The intradimer interaction is antiferromagnetic giving rise to a singlet ground state. Also rare-earth and transition metal ions are characterized by this type of ground state, which is attributed to spin-orbit and anisotropic crystal-field interactions though. Anyway, the magnetic interaction in metallic rare-earth systems is mediated by the long-range RKKY (Rude-Kittel-Kasya-Yosida) exchange [120], whereas interdimer coupling in a insulating compound such as $Cs_3Cr_2Br_9$ is restricted to nearest-neighbors. A detailed neutron scattering study revealed an pronounced energy dispersion resulting from a weak interdimer interaction [121].

1.3.2 Quantum spin systems

Quantum magnetism captures the complexity of many-body quantum mechanics with simple interaction models. Even though the spin-spin dynamics is well determined by the Heisenberg Hamiltonian in Eq. 1.2, classical approaches based on a mean-field-like behavior usually fail to account for the collective nature of the ground state and the magnetic excitations in quantum spin systems. In particular low-dimensional antiferromagnets differ substantially from the classical behavior due to quantum fluctuations: classically the ground state is expected to be a staggered Néel state, but it is not realized, because quantum fluctuations restore the $O(3)$ spin symmetry which results in a collective singlet ground state [122]. For instance $CaCuGe_2O_6$ contains zigzag chains of Cu^{2+} ions which are well described by an ensemble of weakly interacting antiferromagnetic dimers [123], the ground state is not an antiferromagnetic chain as expected in the classical limit. The non-magnetic singlet ground state can be so robust, that a gap arises in the excitation spectrum, for instance in the $S = 1$ Haldane chains [124] and the $S = 1/2$ even-leg ladders [112].
Another important point is the frustration which is a signature of unconventional magnetism. Prominent examples are 1D frustrated spin-Peierls compounds, see e.g. Ref. [125], or a 2D orthogonal spin-dimer system with frustrating interdimer couplings [126]. Currently frustrating systems involving triangular or tetrahedral units are á la mode. Note that the classical ground state of these systems is macroscopically degenerate [127, 128], while in the quantum regime the ground state can be characterized by the absence of

long-range order [128, 129] or a valence bond-crystal [130], for example.

Quantum dimer systems

$S = 1/2$ quantum magnets $TlCuCl_3$ and $KCuCl_3$ represent model three-dimensional Heisenberg systems with a singlet ground state. The observed singlet-triplet excitation modes exhibit a dispersive behavior above a finite gap [131], which has been analyzed within perturbational considerations around the dimer limit.
The possibility to observe Bose Einstein condensation of magnetic quasiparticles in magnetic insulators has attracted considerable theoretical and experimental interest [132, 101, 133, 134]. Indeed Rüegg et al. [101] found that in the afore mentioned quantum spin liquids a field-induced ordering occurs by Bose Einstein condensation of dilute magnons. This quantum phase transition is realized by the closing of the spin gap when the energy of the lowest Zeeman split triplet component overcomes the gap energy [101, 135, 136] upon application of a magnetic field. Not only a magnetic field, but also the application of pressure can induce a quantum phase transition because pressure offers the possiblity to tune the exchange coupling constants, a phase diagram has been predicted in Ref. [137, 138].

Quantum tetramer systems

The copper tellurates $Cu_2Te_2O_5X_2$ (X=Cl,Br) belong to a new family of quantum spin systems where frustration effects become relevant. They contain tetrahedral clusters of $S = 1/2$ Cu^{2+} spins aligned in tubes along one crystallographic direction [139]. An incommensurate antiferromagnetic long-range order below $T_N = 18$ K due to geometrical frustration has been observed in both system by neutron diffraction studies [140]. It turned out that the magnetic moments are low, where the value of the compound containing Br is lower indicating that this system is closer to the quantum critical point than the Cl analogue [141, 142, 143]. However, the relavant magnetic interactions as well as the effective dimensionality remain an open question. Also the observed dispersive behavior of magnetic excitations [144] could not clarifiy this issue.
However, the persistence of a q-dependent behavior of the dispersions above T_N suggests that the inter- and intratetrahedral couplings are of similar strength. A 3D cluster-spin model, which is highly frustrated has been investigated by Brenig [145] who performed quadrumer series-expansion using the flow-equation method. Certainly further studies on the theoretical side are needed to accomplish the quantum phase diagram and additional experiments, preferentially inelastic neutron scattering are of crucial importance in order to clarify the relation of the cluster spin model to theses tellurate compounds.

The above mentioned systems present an ideal testing ground for quantum phase transitions. Moreover, possible new concepts in this field may be discovered in experimental studies.

1.3.3 Single-molecule magnets

SMMs are individual molecules which can function as magnets, each molecule is a single-domain magnetic particle. They occur as assemblies embedded in a crystalline

environment, there exist intermolecular interactions which, in most cases, can be assumed to be negligibly small.
Below their blocking temperature, magnetization hysteresis is observed, which is the macroscale property of a magnet. At the same time SMMs exhibit some spectacular and novel features, for instance quantum tunneling processes can reverse a spin at low temperatures [146, 147]. Usually SMMs have axial anisotropy.

In the following we will give some examples of SMMs and we will underline their outstanding properties.

Mn_{12} - a SMM in the quantum regime:

The ground state of the Mn_{12} SMM is characterized by $S = 10$, its molecules crystallize in a tetragonal lattice and intercluster interactions are negligible. Experimental investigations indicate a large magnetocrystalline anisotropy [148]. Just like an ordinary magnet, SMMs also exhibit hysteresis effects, but in the case of Mn_{12} the magnetization as a function of the applied field behaves slightly more complicated: it displays step-like features separated by plateaus. This novel behavior is associated with field-tuned resonant tunnelling between quantum spin states [146, 149]. At zero field the ground state is degenerate with two states $M = -S$ and $M = +S$ separated by an anisotropy barrier. The application of a magnetic field breaks the symmetry and in turn identifies one of the states as the real ground state. Tunnelling across the barrier is induced when such a state is resonant with an excited level due to the magnetic field, a rapid decay down to the ground state follows. Since SMM are identical objects in a given compound, the sample can be characterized precisely.

Mn_{84} - a SMM at the interface of classical and quantum regime:

The giant Mn_{84} SMM comprises 84 Mn^{3+} ions, it is established as the largest SMM yet discovered. Fig. 1.4 shows this molecule as compared to the smaller clusters on the left. The constituent of the molecule form a torus-like shape with a diameter of ~ 4.2 nm and a thickness of ~ 1.2 nm. Magnetization measurements on a single crystal clearly showed a smooth hysteresis [150], the diagnostic property of a magnet. In contrast to several smaller SMMs such as Mn_{12} [151, 152, 146], Mn_4 [153, 154] and Fe_8 [149, 155] as well as the exchange-biased $[Mn_4]_2$ [108] dimer described below, the hysteresis loop of Mn_{12} shows no sign of steps diagnostic related to quantum tunnelling. However, by investigating the magnetization relaxation, it turned out that quantum tunnelling still occurs. In that particular case quantum digging is a potent tool to find out if the compound is in the quantum regime [156], because it is able to establish quantum tunnelling of magnetization even when no step-like features are apparent in hysteresis loops. Hence Mn_{84} still exhibits the quantum behavior, which means that Mn_{84} straddles the classical/quantum interface.

Intramolecular coupling in SMMs:

An example of a SMM with intermolecular interaction is $Mn_4O_3(OSiMe_3)(OAc)_3(dbm)_3$ or simply called $[Mn_4]_2$ dimer. The dimer coupling is of antiferromagnetic nature. In this

system a spin-spin cross relaxation phenomenon, the so-called exchange-bias tunneling, has been observed [106]. This is a simultaneous transition of two spins, where only one spin tunnels and the other one makes a transition in the same well. Just like a system of isolated SMMs, the magnetization curve also displays step-like features separated by plateaus due to quantum tunnelling processes. However, due to the weak antiferromagnetic interaction within the dimers, each half of the $[Mn_4]_2$ dimer acts as a field bias on its neigbhor, which results in a shift of the tunnelling resonances to new positions as compared to isolated Mn4 molecules.

Magnetic molecular wheels and grids:

Grid and ring molecules have a lot in common: they both exhibit very high molecular symmetry, which reduces the number of free parameters in the microscopic Hamiltonian. Moreover, the periodic boundary conditions makes them easier to handle from a theoretical point of view.
Hence these systems are generally described to a very high degree of accuracy by the simplest model Hamiltonian consistent with their structure and the maximal symmetry.
Many complexes with a planar, square matrix-like arrangement of four paramagnetic centers, such as Cu(II), Ni(II), Co(II), Fe(II), and Mn(II) have ben synthesized so far [157, 158, 159], where the classification as $[2 \times 2]$ grids, tetranuclear rings, or squares is not always obvious. The exchange coupling is generally observed to be antiferromagnetic [157, 159]. The study of various compounds [160, 161, 162] has unravelled a novel situation: it seems that the exchange couplings are predominantly determined by magneto-electronic correlations, structural properties play a less important role.
Also in grid compounds magnetization steps have been observed upon application of a magnetic field perpendicular to the grid [163]. This remarkable magnetic behavior has been associated with a ground-state level-crossing.
In magnetic grids usually non-trivial spin terms such as next-nearest neighbor exchange, anisotropic, antisymmetric and biquadratic exchange become relevant. For example $[2 \times 2]$ Ni-grid represents a rare example of a system, where biquadratic exchange could be convincingly demonstrated by magentization studies [164].

Another type of systems attracting a lot of interest currently are molecular wheels, where the decanuclear Fe-wheel, shortly called Fe10 has become the prototype for this class of compounds [165, 166]. In the last decade, many wheels with different metal ions and number of centers in the ring have been successfully realized [162, 167, 168, 169].

Initially antiferromagnetic wheels were widely regarded as models for one-dimensional antiferromagnetic chains because they have periodic boundary conditions, whereas chains are treated to be infinitesimally long. However, it was clarified that finite-size effects are strong in those wheels, which leads to a behavior much different from 1D AF chains. The energy spectra showed that spin wave-like excitations are not the lowest excitations observed in AF wheels. But the low-lying excitations were identifed as rotational modes [170] corresponding to an additional term in the Hamiltonian $\mathcal{H}_{rot} = \frac{S^2}{2I}$, where I denotes the momentum of inertia. Such rotation modes are responsible for the magnetization steps found in Refs. [166, 171, 172, 173]. The physical interpretation of these

excitations was actually already given more than 50 years ago by Anderson in his AF spin-wave theory [122, 174]. These bands of states were called 'tower of states' and they arise from a coherent rotation of all the spins in the AF ring, because the orientation of the classical ground state spin configuration in space is not fixed. But in extended antiferromagnets such modes cannot be observed, the lowest-lying modes are spin wave excitations.
Another important difference between extended antiferromagnets and AFHRs is prominent as it comes to quantum fluctuations: in 1D antiferromagnetic chains quantum fluctuations are most prominent and they lead to a behavior distinct from the classical one. On the other hand, quantum fluctuations in AFHRs decline with increasing ring size N and increasing spin length S [175].

1.3.4 Potential applications

Digital information storage

The fundamental unit of information is a bit, each classical bit is realized through the magnetization on a hard disk, DVD or the charge on a capacitor. In 2001, IBM reported the 'Pixie Dust' breakthrough to quadruple disk drive density presenting a huge success in data storage using ruthenium, which is expected to permit hard disk drives to store 100 gigabits.
There is great interest by high-tech companies in increasing the density of information storage, which means increasing the number of bits of information in a given area. To do so, the size of each magnetic particle has to be decreased and the size has to be equal for all particles in order to assure that the particles will behave the same.

SMMs are potential candidates for applications in information storage, because they have many important advantages over conventional nanoscale magnetic particles, such as uniform size, solubility in organic solvents among others. Moreover SMMs containing manganese are much smaller than the particles currently used in information storage, but nevertheless they are magnets at low temperatures. Thus each molecule can be considered as an ultra-small magnetic particle which promises access to the ultimate high-density information storage. It is expected that the information density could be enhanced by a factor of 3×10^3.
However, SMMs have a chance to be used for information storage if and only if there is no tunnelling process at zero field, which applies to $[Mn_4]_2$ dimer presented above.

Spintronics and quantum computing

Conventional electronic devices manipulate the flow of electronic charge, but it would be highly desirable to exploit also the spins into such devices. In order to realize such devices, it is necessary to trap electrons and to protect their spins form outside influences in order to preserve spin-coherence over time and distance as long as possible. The field which deals with the issue of coherence of spins is called spintronics and considerable efforts in basic research has been rendered by the Santa Barbara group [176].
A possible realization of spintronics-based devices is to store the electrons on quantum

dots, which are linked so that the transfer of spins i.e. information becomes possible. The Awschalom group developed a device where organic molecules build a bridge between the quantum dots [177, 178] where the coherence times and distances are much longer than in conventional metals and semiconductors.

While a classical computer obeys the well understood laws of classical physics, a quantum computer is a device that harnesses physical phenomenon unique to quantum mechanics to realize a fundamentally new mode of information processing. The basic priniciple is as follows: the information is stored in the quantum mechanical state of a physical system. For example a SMM could serve as such a physical system where the qubits are characterized by the different cluster states. A huge advantage arises then, namely that the eigenenergies of any Hamiltonian would be available, which means that any physical process could in prinicple be modeled perfectly by a quantum computer. A classical computer can theoretically simulate a quantum computer, but it is incredibly inefficient: For example a system of 500 qubits represents a quantum superposition of as many as 2^{500} states, which are impossible to deal with using a conventional computer. Thus a quantum computer would have capabilities far beyond those of any traditional classical computer.
A few potentially large obstacles still remain which prevent the concrete realization of a quantum computer. The decoherence of states due to the interaction with the environment is certainly an important difficulty because it induces the breakdown of information stored. But reseach concerning the development of the suitable hardware is still in its infancy. In principle single-molecule magnets are very promising candidates, but they function at temperatures too low for commercial applications.
To summarize quantum computing remains in its pioneering stage because on the one hand quantum hardware technology is only an emerging field. Another reason why quantum computing is still in its infancy is that certain basic points are not yet fully understood, for instance the properties of a quantum spin, how it is affected by its environment and what phenomena occur due to the complicated interplay of intra- and intercluster interaction and which finite-size effects may arise. A review about quantum computation is given e.g. in Ref. [179].

1.3.5 Why α-$MnMoO_4$?

In the present study we focus on the tetramer-based Mn^{2+} compound α-$MnMoO_4$. On the one hand it is closely related to the $[Mn_4]_2$ dimer system mentioned above.
Concerning SMMs, α-$MnMoO_4$ is a simpler model in the sense that a cluster is built of 'only' four spins giving rise to much less cluster states than SMMs containing twelve or more spins. Thus the study of intracluster interaction is certainly facitlitated here and basic concepts might be verified or discovered.

On the other hand α-$MnMoO_4$ is some sort of a classical analogue to tellurate compounds $Cu_2Te_2O_5X_2$ (X=Cl,Br) because both systems contain tetrameric clusters, but α-$MnMoO_4$ exhibits classical behavior due to the large spins of the Mn^{2+} ions. Thus the complicated interplay of intra- and intertetramer coupling can be studied in the classical

limit where no quantum effects have to be taken into account. It represents therefore an appropriate playing ground for such complicated quantum systems which are not yet fully understood. The analysis of the magnetic excitations of α-$MnMoO_4$ presented in this work may therefore serve as a starting point from where on quantum effects can be included.

1.4 Program

This thesis is organized as follows:

We will introduce the theoretical background in Chapter 2, which gives examples how to deal with strongly correlated systems. It will also be clarified how isolated spins as well as equally interacting spins are treated and the complicated case in-between, namely interacting cluster systems, is also described. The next chapter is then devoted to the experimental techniques, in particular neutron scattering but also macroscopic measurements are discussed. We present the results of the LSCO-project where the pseudogap is studied in $La_{1.96-x}Sr_xHo_{0.04}CuO_4$ in Chapter 4. And α-$MnMoO_4$ is discussed in the sequent Chapter 5. In the last chapter a summary and outlook is given.

The pseudogap in $La_{1.96-x}Sr_xHo_{0.04}CuO_4$

In spite of the vast experimental information on the pseudogap seen in all high-T_c compounds, a common consensus on the origin of the pseudogap is lacking [50]. Consequently, experiments which produce changes of the pseudogap temperature T^* are of crucial importance to discriminate between the different pairing scenarios developed for the cuprate superconductors.
Neutron crystal-field spectroscopy has been proven to be a highly potent tool to investigate the pseudogap issue [89, 90, 91, 92]. Thus we decided to continue this track, which has been initiated by A. Furrer and K.A. Müller, in the case of $La_{1.96-x}Sr_xHo_{0.04}CuO_4$. We have been exploring systematically how the pseudogap temperature T^* depends on

- doping: x=0.11, 0.2 and 0.25.
  Moreover we also measured non-superconducting samples near the antiferromagnetic phase (x=0.02) as well as in the heavily overdoped regime (x=0.28, 0.375).
- oxygen isotope substitution (^{18}O vs. ^{16}O) at different doping levels (x=0.11, 0.2, 0.25).
- hydrostatic pressure in the optimally doped compound (x=0.15) : p=0.8 GPa and 1.2 GPa.

The corresponding superconducting transition temperature T_c by macroscopic measurements.

The samples were synthesized by conventional solid-state reaction based on the knowledge worked out by Breuer et al. [180]. Oxygen isotope susbstitution has been studied in detail by Conder et al. [181].

Magnetic excitations in α-$MnMoO_4$

The tetramer-based compound α-$MnMoO_4$ undergoes a three-dimensional order below 10.7 K. The purpose of our experiments and analysis is to deduce the relevant intra- and intercluster coupling parameters, which is a challenging task because of the large number of interaction parameters.

In summary

- We have performed single-crystal neutron diffraction experiments in order to investigate the magnetic structure.
- The powder experiments revealed the states of the cluster and in turn the intracluster interaction.
- The single-crystal experiments rendered detailed information at given points in reciprocal space about the dispersive behavior of magnetic excitations from where the intercluster coupling parameters can be found.

Chapter 2

Strongly correlated electron systems

We specify strongly correlated electron systems and characterize their features. In general this class of materials can be described by the Hubbard model, where electron-phonon coupling might be included. High-T_c superconductors are the prime example of strongly correlated systems.
In a second part we will present magnetic systems with different strength of interaction. On the one hand we consider a dilute magnetic system with crystal-field excitations such as $La_{1.96-x}Sr_xHo_{0.04}CuO_4$. On the other hand the case of interacting spins is discussed within random phase approximation and linear spin-wave theory. The theoretical concepts introduced at this point will be applied in Chapter 4 and 5.

2.1 The Hubbard model

Strongly correlated systems are characterized by a competition between *localization* (on-site Coulomb repulsion) and *delocalization* effects (hopping to lower the kinetic energy). The Coulomb repulsion can be so strong that the electrons prefer localized wave functions to the extended Bloch states in order to minimize their overlap [182]. As a result the system is an insulator (a so-called Mott-insulator) even though there is a half-filled band which is characteristic for metallic behavior in terms of band theory.
The basic dynamics of a strongly correlated system can be described by the Hubbard model:

$$\mathcal{H} = \mathcal{H}_{kin} + \mathcal{H}_C = -t \sum_{i,j} \sum_{s=+,-} (c_{is}^\dagger c_{js} + c_{js}^\dagger c_{is}) + U \sum_i n_{i+} n_{i-} \tag{2.1}$$

where c_{js} ($c_{js}^\dagger$) annihilates (creates) an electron with spin s on site j corresponding to a state with a Wannier function $\psi_j(\vec{r})$ and $n_{js} = c_{js}^\dagger c_{js}$ denotes the number operator. The first term of Eq. 2.1 stands for the kinetic energy which arises from hopping of electrons to nearest neighbor sites $\langle i, j \rangle$ with matrix element $-t$. The second term describes the Coulomb repulsion acting for electrons on the same site only.
The electrical properties (metal or insulator) of the system will depend on the ratio $|t|/U$:

- $|t|/U \gg 1$: metallic state.

- $|t|/U \ll 1$: insulator $\rightarrow$ La_2CuO_4, α-$MnMoO_4$.

Note that $La_{1.96-x}Sr_xHo_{0.04}CuO_4$ is in fact metallic, but only due to a change in the number of charge carriers induced by doping.
For strongly correlated systems the assumption $|t| \sim U$ is appropriate, which means that it is expensive to doubly occupy a site, so that the electrons remain localized.
From an experimental point of view the transition from the insulating to the metallic state can be induced by e.g. chemical doping or pressure. For instance, in LSCO-type high-T_cs the strontium concentration allows to tune the free carrier density.

2.1.1 Jahn-Teller coupling

The Hubbard model represented by Eq. 2.1 is valid if only one band is relevant. But if the crystal contains ions with an orbitally degenerate ground state (Jahn-Teller ions), electron phonon coupling may become important. According to the Jahn-Teller theorem [183], the interactions of the degenerate orbital states with the vibrational modes of the crystal have a destabilizing effect on its lattice surrounding. The lattice deformation results in a splitting of the orbitals and makes one energy level more stable than the other ones. This so-called Jahn-Teller effect can therefore support a certain orbital order.

2.1.2 Spin systems

The Hubbard model introduced in the previous section accounts for the strong Coulomb interaction between the electrons. If additionally the electrons of the half-filled lower Hubbard band are arranged in a way that the total spin is non-zero, the system results in a spin lattice. The effective interaction between the spins can then be described e.g. in a Heisenberg model under the assumption that $t/U \ll 1$

$$\mathcal{H}_{eff} = J \sum_{i,j} \vec{S}_i \vec{S}_j \tag{2.2}$$

where J is the exchange coupling between neighboring spins. Second order perturbation theory for $|t|/U \ll 1$ leads to

$$J = \frac{4t^2}{U} \tag{2.3}$$

Note that the effect of U becomes virutal, leading to a superexchange interaction between the Cu spins of strenght J. This is easily understood by noting that two parallel spins are not allowed to occupy the same Cu site due to the Pauli exclusion principle. But for antiparrallel spins, which are not prohibited to remain at the same site, an energy saving of t^2/U arises.

2.2 High-temperature superconductors

The class of high-T_c superconductors is a prime example of a strongly correlated system [184].

As mentionned in the introduction, superconductivity is induced by chemical doping. In LSCO stoichiometrically, trivalent La^{3+} donates three electrons per atom, while each O^{2-} atom absorbs two electrons in order to fill its p-shell. Therefore we have the following ionization configuration:

$$La^{3+} \qquad Cu^{2+}(3d^9) \qquad O^{2-}.$$

In the solid, the Cu^{2+} ion is in a d^9 configuration and the O^{2-} ion in a p^6 configuration, with the Cu 3d energy level above and relatively close to the O $2p$ energy level. In the layered perovskites, the single $3d$ band has $d_{x^2-y^2}$ symmetry due to the tetragonal environment of the Cu^{2+} ion. Thus the dominant energy is the bonding-antibonding splitting, which involves the hybridization of the Cu $3d$ $x^2 - y^2$ orbital and the planar O $2p_x$ and $2p_y$ orbitals. This results in one half filled band in the parent compound, which means that the band structure is metallic. But due to the strong on-site Coulomb interaction the localization effects dominate and the antibonding band is split into an empty upper Hubbard band and a filled lower Hubbard band. The nonbonding band is largely of oxygen nature, but since it is located between the lower Hubbard and the upper Hubbard band, the lowest excitation is of charge transfer type.
Upon doping the remaining spins become mobile because some Cu-sites are empty. A combination of Eq. 2.1 and Eq. 2.2 then yields the so-called t-J model which is an extended Heisenberg model, it is the simplest model which accounts for that specific situation, see e.g. Ref. [16, 185]:

$$\mathcal{H}_{tJ} = -t \sum_{i,j} \sum_{s} \left[c^{\dagger}_{is}(1 - n_{i,-s})(1 - n_{j,-s}) c_{js} + \text{h.c.} \right] + J \sum_{i,j} \vec{S}_i \vec{S}_j \tag{2.4}$$

The model has been extended to include next-nearest neighbor coupling using a Landau-Fermi liquid approach[186].

In the case of high-T_c cuprates the following values are used:

$$U \sim 5 \text{ eV} \quad t \sim 0.4 \text{ eV} \rightarrow J \sim 0.12 \text{ eV}.$$

The kinetic term which describes the moving spins, does not have the simple form of the tight-binding model, because double occupancy of a copper site is not allowed. (Equivalently P.W. Anderson [16] introduced the Gutzwiler projection operator.)
Another approach has been proposed by Zhang and Rice [187] where the hybridization is supposed to strongly bind a hole on each square of O atoms to the central Cu^{2+} ion to form a local singlet. This Zhang-Rice singlet moves then through the lattice of the Cu^{2+} ions in a similar way as a hole. Moreover, two holes feel a strong repulsion against residing on the same square, so that the single-band model is recovered.
Within the t-J model the pairing of charge carriers can be explained by two sequent holes moving in the lattice so that they do not disturb the antiferromagnetic order. However, this simple picture is only partially valid because the antiferromagnetic ground state is subjected to strong quantum fluctuations. It has been shown on the basis of analytical and numerical studies, that a low concentration of holes in an antiferromagnet is unstable

to phase separation into a hole-rich and a hole-deficient phase, see e.g. Ref. [188]. Phase separation can be thought of as a strong interaction between holes. The characteristic energy of this interaction is set by magnetic energies, so this phenomena is supposed to occur only below temperatures of the order of the exchange interaction J. Phase separation is expected to be important at low doping levels from a theoretical point of view.
A natural consequence within this scenario is the formation of stripes:
Indeed at low doping, materials can be subject to electronic phase separation. This tendency is not only due to the argument pointed out above, but also due to the fact that each doped hole breaks four magnetic bonds and hence favors a clumping of holes, because this way the magnetic energy loss can be minimized. The first evidence of stripes was given by Tranquada et al. [189] by neutron scattering experiments. In LSCO the occurrence of stripes is supposed to be most stable near 1/8 doping, where LSCO tends to distort from its normal orthorhombic phase to the low-temperature tetragonal structure. The most dramatic example for electronic inhomogeneity has been provided by STM studies on underdoped Bi2212 by Davis' group [190]. A nice overview about experimental evidence and theoretical models predicting phase separation is given in Ref. [25].
An inhomogeneous character of the sample implies that the superconducting properties arise from a percolation mechanism: by doping, holes are continuously transferred into the CuO_2 planes forming local regions of metallic character. For some critical concentration a percolative network is built up, and the system undergoes a transition to the superconducting state. Such a scenario has been proposed by Gor'kov [191] in terms of a 2-component model of itinerant and localized charge carriers.

2.2.1 Electron-phonon coupling

The t-J model in Eq. 2.4 is certainly a good starting point because it captures many of the electronic properties of the CuO_2 planes. But in its simplest form, it does not incorporate potentially important effects such as lattice vibrations and disorder. Hence *a priori* it cannot explain isotope effects observed for various parameters.

Hence the next step is to include the lattice into the Hamiltonian of Eq. 2.4:

$$\begin{aligned}\mathcal{H}_{tJ} &= -t\sum_{i,j}\sum_{s}\left[c_{is}^{\dagger}(1-n_{i,-s})(1-n_{j,-s})c_{js}+\text{h.c.}\right]+J\sum_{i,j}\vec{S}_i\vec{S}_j \\ &\quad +\sum_{k,q}\left[\lambda(q)b_q c_{k+q}^{\dagger}c_k+h.c.\right] \qquad (2.5)\end{aligned}$$

where b_q ($b_q^{\dagger}$) is the annihilation (creation) operator for phonon modes and λ determines the electron-phonon coupling. The last term denotes the electron-lattice interaction, where we assume that an electron with momentum $\mathbf{k}$ interacts with a phonon with momentum $\mathbf{q}$ which is then absorbed and the final particle is an electron with momentum $\mathbf{k}+\mathbf{q}$. Since the last term consists of three operators, there will be no longer an exact solution.

2.3 Dilute magnetic systems: the single-ion case

If the coupling between the spins of magnetic ions is vanishing, we end up with a single-ion problem where the energy levels are discrete and the states are localized. Such a situation occurs, when a magnetic ion is embedded into a solid. Its incomplete shell experiences the electrostatic potential generated by neighboring ions, which is the so-called crystalline electric field or shortly crystal field.

2.3.1 Description of the crystal field

The free ion energies of a magnetic ion situated in a crystalline lattice are perturbed by the electrostatic potential arising from the neighboring charges. The total Hamiltonian of the crystal including the crystal-field potential can be written as

$$\begin{aligned} \mathcal{H} &= \mathcal{H}_0 + \mathcal{H}_{CEF} \\ \mathcal{H}_{CEF} &= V_{CEF}(r) = \sum V(\mathbf{r}_i) \end{aligned} \tag{2.6}$$

where $\mathcal{H}_0$ is the unperturbed Hamiltonian and $\mathbf{r}_i$ denotes the position of the neighboring ligand ions. In the case of rare-earth ions, the $4f$ shell is unfilled because of the electronic configuration $4d^{10}4f^N5s^25p^6$ giving rise to a magnetic moment $\mathbf{J}$, which is the total angular momentum. Assuming that the single rare-earth ion has the total angular momentum quantum number J with the $2J+1$ eigenstates $|m>$, $m = -J, -J+1, ..J-1, J$ and the eigenergies E_m, the crystal-field Hamiltoninan can then be written as

$$\mathcal{H}_{CEF} = \sum_{m=-J}^{J} E_m |m\rangle\langle m|. \tag{2.7}$$

For the rare-earth ions the mean radii are smaller than the overall size of the ion and the perturbation by the crystal-field is smaller than both, the intra-atomic repulsion between the electrons (of order of a few eV) and the spin-orbit coupling (in the range of 0.1 eV). This potential partly or totally lifts the $(2J+1)$ degeneracy of the J-multiplets of the free-ion levels.
Since the potential V fulfills the Laplace equation $\Delta V = 0$ at the rare-earth site, it may be written as a multipole series

$$V(\mathbf{r}) = \sum_{n,m} c_n^m r^n Y_n^m(\theta, \phi) \tag{2.8}$$

in the spherical harmonics Y_n^m.

Stevens operator equivalent method

As outlined by Stevens, simple relations exist between the polynomial terms in the Cartesian coordinates $\mathbf{r}_i$ and the polynomial terms O_n^m in the angular momentum operators J^z, J^+, J^-. The Hamiltonian in Eq. 2.6 reads then

$$\mathcal{H}_{CEF} = \sum_{n=0}^{6} \sum_{m=0}^{n} B_n^m O_n^m. \tag{2.9}$$

Here the B_n^m are the crystal-field parameters, the O_n^m are the Stevens operators. In order to compare directly the crystal-field parameters for different rare-earth ions in isostructural series, it is more convenient to express these parameters in terms of the parameters A_n^m

$$B_n^m = A_n^m \langle r^n \rangle \chi_n \tag{2.10}$$

with the proportionality factors χ_n the reduced matrix elements, $\langle r^n \rangle$ the 2nd moment of the $4f$ electron radial distribution tabulated by Hutchings [192].
The Stevens operator method represents a convenient simplification for computations of the crystal-field levels and their matrix elements: it eliminates the necessity to go back to single-electron wave functions.

Point-charge model

In principle the crystal-field parameters can be calculated on the basis of the charge distribution $\rho(\mathbf{r})$. This is the starting point of the so-called point-charge model: effective charges q_i are ascribed to the neighboring sites of the rare-earth ion under consideration:

$$\rho(\mathbf{r}) = \sum_i q_i \delta(\mathbf{R}_i - \mathbf{r}) \tag{2.11}$$

where $\mathbf{r}$ is the site of the rare-earth ion and $\mathbf{R}_i$ denotes the position of the neighboring ligand ions carrying an effective charge q_i.
Then the crystal-field parameters A_n^m in Eq. 2.10 can be expressed as follows:

$$A_n^m = e|e| \langle r^n \rangle \sum_i Z_i \gamma_n^m(i) \tag{2.12}$$

with

$$\gamma_n^m(i) = f_n^m(\theta_i . \phi_i) \frac{1}{|\mathbf{r} - \mathbf{R}_i|^{n+1}}. \tag{2.13}$$

The sum i runs over all neighbouring ions at position $\mathbf{R}_i = (R_i, \theta_i, \phi_i)$, $f_{nm}(\theta_i, \phi_i)$ are tesseral harmonics, $\langle r^n \rangle$ is the n-th moment of the radial distribution of the 4f electrons, Z_i is the charge of the i-th ligand ion in units of the electron charge $|e|$, and $\gamma_{n,m}^i$ are the geometrical coordination factors as defined for instance in Ref. [192].
In general this model is not able to reproduce the observed energies and intensities. Some corrections have been induced to improve the point-charge model:

- Shielding of the $4f$ electrons by the outer electron shell, see Sternheimer [193, 194]
- $\langle r^n \rangle$ for the free ion is modified when placed into a crystal, see Ref. [195].
- Screening effects of the conduction electrons should be taken into account by a Yukawa potential.

Parameter modeling

The determination of crystal-field parameters from experimental data is a challenging task. For low-symmetry sites such as orthorhombic symmetry there are nine independent crystal-field parameters, which have to be determined by a least-squares fitting procedure. The simplest way is to start from a compound whose crystal-field parameters $A_n^m(1)$ has been established and then extrapolates the parameters of the new compound $A_n^m(2)$ by taking into account the geometrical coordination of the nearest-neighboring ligands.

$$A_n^m(2) = A_n^m(1) \cdot \frac{\gamma_n^m(2)}{\gamma_n^m(1)} \tag{2.14}$$

This modeling has demonstrated success in the analysis of neutron scattering data: the crystal-field level scheme of $ErBa_2Cu_3O_7$ [196] and $HoBa_2Cu_3O_{7-\delta}$ [197] have successfully been established by the Furrer group. The procedure above has also been applied to optical data across the rare-earth garnet series with satisfactory results [198].

2.3.2 Relaxation Mechanisms

In a real crystal the crystal-field levels are subject to an interaction with charge carriers, spin fluctuations and phonons. Hence the system is characterized by

$$\mathcal{H} = \mathcal{H}_0 + \mathcal{H}' \tag{2.15}$$

where $\mathcal{H}_0$ describes the unperturbed system and $\mathcal{H}'$ is the interacting part. $\mathcal{H}'$ leads to a shift of the energy levels E_m in Eq. 2.9 and to a finite lifetime τ, which can be computed in principle from 2^{nd} order perturbation theory.
The starting point is the resolvent (Green function)

$$G(z) := (z - \mathcal{H})^{-1}, \quad z \in C \tag{2.16}$$

The Dyson equation for the resolvent projected to the eigenspace of the unperturbed Hamiltonian then yields the self-energy decomposed into its Hermitian (energy shift) and anti-Hermitian (lifetime) components.

Interaction with the charge carriers

The interaction with the charge carriers is by far the dominating relaxation mechanism in the metallic rare-earth compounds. The corresponding theoretical work has been done by Becker, Fulde and Keller [199, 200]: They started with the following Hamiltonian

$$\begin{aligned} \mathcal{H} &= \mathcal{H}_{CEF} + \mathcal{H}_{el} + \mathcal{H}' \\ &= \mathcal{H}_0 + \mathcal{H}'. \end{aligned} \tag{2.17}$$

The first part, $\mathcal{H}_0$, describes two non-interacting subsystems, namely a single rare-earth ion and the kinetic energy of charge carriers. $\mathcal{H}_{CEF}$ encodes the energy levels in an

incomplete 4-f shell subjected to a crystal-field, whereas $\mathcal{H}_{el}$ accounts for the energy of non-interacting conduction electrons. The conduction electrons are described by the non-interacting Hamiltonian

$$\mathcal{H}_{el} = \sum_{\mathbf{k}} \sum_{s=+,-} \left(\epsilon_{\mathbf{k}} c^{\dagger}_{\mathbf{k},s} c_{\mathbf{k},s} + h.c. \right) \tag{2.18}$$

where $\epsilon_{\mathbf{k}}$ is the single-particle energy of a Bloch wave with momentum $\mathbf{k}$ and spin s, $c^{\dagger}_{\mathbf{k},s}$ ($c_{\mathbf{k},s}$) denotes the usual creation (annihilation) operator.
The second part $\mathcal{H}^{'}$, describes the interaction between the conduction electrons with spin $\mathbf{s}$ and the single rare-earth ion with angular momentum $\mathbf{J}$:

$$\mathcal{H}^{'} = -J_{ex} \mathbf{s} \cdot \mathbf{J}. \tag{2.19}$$

The coupling constant J_{ex} sets the scale of the interaction.

Other relaxation mechansims are discussed in Chapter 4.

2.4 Correlated Spins

We start with the effective Hamiltonian given in Eq. 2.2 in Section 2.1.2. The interaction between spins localized at each lattice sites may lead to an ordered ground state. The simplest approximation is the mean-field approach, which neglects any fluctuations of the spins. It is therefore a static and macroscopic approximation. In order to capture the dynamics, it is necessary to go beyond the mean-field approach and to apply a more sophisticated formalism: spin-wavetheory or random phase approximation both belonging to a microscopic approach. We start with the dimensionality of the system.

2.4.1 Models and dimensionality

We consider the following model

$$\mathcal{H} = -\sum_{i \neq j} J_{ij} \left(a \cdot (S^x_i S^x_j + S^y_i S^y_j) + (1-a) \cdot S^z_i S^z_j \right) \quad |a| \leq 1 \tag{2.20}$$

where the summation is taken over neighboring spins and J_{ij} denotes the exchange interaction between spins located at site i and site j. The sign of J_{ij} determines the type of interaction:

$$\begin{aligned} J_{ij} &> 0 \quad \text{ferromagnetic} \\ J_{ij} &< 0 \quad \text{antiferromagnetic} \end{aligned} \tag{2.21}$$

Corresponding to the dimensionality, there are three systems, see Table 2.1:
The case of $a = b = \frac{1}{2}$ stands for the Heisenberg model, where the exchange interaction is isotropic. In the XY-model the interaction is restricted to the xy-components of the spin operator which means that $a = 1$. The Ising model ($a = 0$) assumes an anisotropic interaction, where only the z-component of the spins can interact.

Table 2.1: Depending on the spin model with parameter a, see Eq. 2.20 there is no long-range order in certain dimensions.

a	$1-a$	model	no ordering in
$\frac{1}{2}$	$\frac{1}{2}$	Heisenberg	1D, 2D
1	0	XY	1D
0	1	Ising	1D

Within the frame of the Ising model, an ordered state is energetically not favorable at finite temperatures. In the XY model fluctuations allow an ordered state neither in 1D nor in 2D. But the 2D case is marginal in the sense that the correlation decays to zero, but only slowly. The system behaves like a critical system at the phase transition, it is then common standard to talk about quasi-long range order. The Mermin-Wagner theorem states that a pure isotropic exchange like in the Heisenberg model can induce magnetic ordering neither in 1D nor in 2D. A strictly Heisenberg ferromagnet does only occur in 3D. This means that the small interlayer coupling between the CuO_2 layer in the high-T_cs is sufficient to stabilize the system and to induce long-range order. A pure Heisenberg system is rather scarce, usually there are additional terms D and E describing an anisotropy:

$$\mathcal{H} = -\sum_{i \neq j} \left(J_{ij} \mathbf{S}_i \mathbf{S}_j + D(S_i^z)^2 + E[(S_i^x)^2 - (S_i^y)^2] \right). \tag{2.22}$$

2.4.2 Mean-field treatment

We consider a three-dimensional Heisenberg ferromagnet, with the Hamiltonian

$$\mathcal{H} = -\frac{1}{2} \sum_{i \neq j} J_{ij} \mathbf{S}_i \mathbf{S}_j, \tag{2.23}$$

where $\mathbf{S}_i$ is the spin at the position $\mathbf{R}_i$ in a Bravais lattice and J_{ij} is the interaction parameter. Note that for convenience we introduced a factor $1/2$ as compared to Eq. 2.2. Furthermore the '-'sign means that J_{ij} being positive yields a ferromagnetic ground state. We may choose the z-axis as the direction of the magnetic field:

$$\langle \mathbf{S}_i \rangle = \langle S \rangle \hat{\mathbf{z}} \qquad \text{at } T = 0. \tag{2.24}$$

Above zero temperature, this result is no longer exact, and appropriate approximations have to be made. The first step is to introduce the thermal expectation value $\langle \mathbf{S}_i \rangle = \langle \mathbf{S} \rangle = \langle S \rangle \hat{\mathbf{z}}$ which is independent on site i. Hence writing

$$\mathbf{S}_i = (\mathbf{S}_i - \langle \mathbf{S} \rangle) + \langle \mathbf{S} \rangle \tag{2.25}$$

leads to the expression for the Hamiltonian in Eq 2.23

$$\begin{aligned}\mathcal{H} &= \sum_i \mathcal{H}_i - \frac{1}{2}\sum_{i\neq j} J_{ij}(\mathbf{S}_i - \langle\mathbf{S}\rangle)\cdot(\mathbf{S}_j - \langle\mathbf{S}\rangle) \\ \mathcal{H}_i &= -J(\mathbf{0})S_i^z\langle S\rangle + \frac{1}{2}J(\mathbf{0})\langle S\rangle^2 \end{aligned} \tag{2.26}$$

where we made use of the Fourier transform of J_{ij}:

$$J(\mathbf{q}) = \frac{1}{N}\sum_{i\neq j} J_{ij}e^{-i\mathbf{q}\cdot(\mathbf{R}_i-\mathbf{R}_j)}. \tag{2.27}$$

In the mean-field approximation, the dynamic correlation between spins on different sites is neglected. This means that the second term of the Hamiltonian in Eq. 2.26 is disregarded, reducing the original many-spin Hamiltonian to a sum of N independent single-spin Hamiltonians. Thus the presence of the neighboring spins is only considered to generate a static exchange field:

$$\begin{aligned}\mathcal{H}_{mf} &= \sum_i \mathcal{H}_i = \sum_i \left(S_i^z h_i^{mf} + \frac{1}{2}\langle S\rangle h_i^{mf}\right) \\ h_i^{mf} &= \sum_j J_{ij}\langle S\rangle \end{aligned} \tag{2.28}$$

Assuming a homogeneous system with z nearest neighbors, the effective field becomes $h = zJ\langle S\rangle$ and $\langle S\rangle$ is determined by the self-consistent equation

$$\begin{aligned}\langle S\rangle &= \frac{1}{Z}\sum_{M=-S}^{+S} M e^{MJ\langle S\rangle/k_BT} \\ Z &= \sum_{M=-S}^{+S} e^{MJ\langle S\rangle/k_BT} \quad \text{partition function} \end{aligned} \tag{2.29}$$

Below the critical temperature T_c there is a solution $\langle S\rangle \neq 0$ besides the trivial solution.

2.4.3 Random phase approximation (RPA)

Although limited in its prediction, mean-field theory can be used as a starting point for a spin many-body problem. The next step is then to include fluctuations in order to capture the time-dependence of the Hamiltonian. The dynamics can be treated on the basis of linear response theory, which is done in RPA.

Linear response theory

Linear response theory provides a general framework for analyzing the dynamical properties of a condensed-matter system close to equilibrium. The dynamical processes may either be spontaneous fluctuations, or due to external perturbations. These two phenomena are interrelated.
A response function for a macroscopic system relates the change of an ensemble-averaged physical observable $\langle B(t)\rangle$ to an external force $f(t)$, e.g. $f(t) = g\mu_B H(t)$, Zeeman term. The total Hamiltonian $\mathcal{H}$ of the system is

$$\begin{aligned} \mathcal{H} &= \mathcal{H}_0 + \mathcal{H}_1 \\ \mathcal{H}_1 &= -Af(t) \end{aligned} \tag{2.30}$$

where A is a time-independent operator. Since we are only interested in the linear part of the response, we assume $\mathcal{H}_1$ to be a small perturbation.
We define the linear response function Φ_{BA} as

$$\begin{aligned} \langle \delta B(t)\rangle &= \langle B(t)\rangle - \langle B\rangle \\ &= \int_{-\infty}^{t} dt' \Phi_{BA}(t-t') f(t') \\ \Phi_{BA}(t) &= 0 \qquad \text{for } t < 0. \end{aligned} \tag{2.31}$$

The last requirement ensures causal behavior, where we assumed $t' = 0$ due to time invariance. The expectation value in the presence of a perturbation $f(t)$ can be expressed by

$$\begin{aligned} \langle B\rangle &= \langle B(t=-\infty)\rangle = tr[\rho_0 B] \\ \langle B(t)\rangle &= tr[\rho(t) B] \\ \rho_0 &= \frac{1}{Z_0} e^{-\mathcal{H}_0/k_B T} \quad ; \quad Z_0 = tr e^{-\mathcal{H}_0/k_B T} \\ \rho(t) &= \frac{1}{Z(t)} e^{-\mathcal{H}/k_B T} \quad ; \quad Z(t) = tr e^{-\mathcal{H}/k_B T}, \end{aligned} \tag{2.32}$$

with ρ_0 and Z_0 ($\rho(t)$ and $Z(t)$) being the density operator and the partition function of unperturbed (total) Hamiltonian. The generalized susceptibility $\chi_{BA}(z)$ as a function of the complex variable z is then defined as the Laplace transformation of Φ_{BA}:

$$\chi_{BA}(z) = \int_0^\infty dt \Phi_{BA}(t) e^{izt}. \tag{2.33}$$

With the generalized Fourier transform

$$\langle B(\omega)\rangle = \lim_{\epsilon\to 0} \int_{-\infty}^{\infty} dt \left(\langle B(t)\rangle - \langle B\rangle\right) e^{i\omega t} e^{-\epsilon t} \tag{2.34}$$

we obtain a particularly simple expression for Eq. 2.31

$$\begin{aligned} \langle B(\omega)\rangle &= \chi_{BA}(\omega) f(\omega) \\ \chi_{BA}(\omega) &= \lim_{\epsilon\to 0} \chi_{BA}(z = \omega + i\epsilon) \end{aligned} \tag{2.35}$$

The susceptibility is decomposed into two terms:

$$\begin{aligned}
\chi_{BA}(z) &= \chi'_{BA}(z) + i\chi''_{BA}(z) \\
\chi'_{BA}(z) &= \chi'_{AB}(-z) \equiv \frac{1}{2}\left[\chi_{BA}(z) + \chi_{AB}(z^*)\right] \quad \text{reactive part} \\
\chi''_{BA}(z) &= -\chi''_{AB}(-z) \equiv \frac{1}{2i}\left[\chi_{BA}(z) - \chi_{AB}(z^*)\right] \quad \text{absorptive part}
\end{aligned} \tag{2.36}$$

It can be shown that the real and imaginary part of $\chi_{BA}(\omega)$ are related through the Kramers Kronig relations.

Response function

Since the goal is to treat the dynamics, it is useful to put the time dependence into the operator B i.e. we go over to the Heisenberg picture

$$B(t) = e^{i\mathcal{H}t/\hbar} B e^{-i\mathcal{H}t/\hbar} \tag{2.37}$$

corresponding to the equation of motion

$$\frac{d}{dt}B(t) = \frac{i}{\hbar}[\mathcal{H}, B(t)], \tag{2.38}$$

where we assumed that B does not depend explicitly on time. We wish to find an expression for $\langle \delta B(t) \rangle$. From Eq. 2.31 and Eq. 2.32 it is obvious that the density operator $\rho(t)$ is an important ingredient of the linear response theory, because it enters the expectation value. It can be written in a similar form like $B(t)$:

$$\rho(t) = e^{i\mathcal{H}t/\hbar}\rho e^{-i\mathcal{H}t/\hbar} \Leftrightarrow \frac{d}{dt}\rho(t) = -\frac{i}{\hbar}[\mathcal{H}, \rho(t)] \tag{2.39}$$

We then find for the linear response of B to a small perturbation $Af(t)$

$$\begin{aligned}
\langle \delta B(t) \rangle &= \langle B(t) \rangle - \langle B \rangle = tr[(\rho(t) - \rho_0)B] \\
&= \frac{i}{\hbar}\int_{-\infty}^{t} dt' \langle [B_0(0), A_0(t')] \rangle_0 f(t'),
\end{aligned} \tag{2.40}$$

where we defined $A_0(t) = e^{i\mathcal{H}_0 t/\hbar} A e^{-i\mathcal{H}_0 t/\hbar}$. The density operator has been decomposed into a thermal-equilibrium ρ_0 and a perturbation part $\rho(t)$. The intermediate steps are given in Appendix A.2.
A comparison of this result with the definition of the response function Φ_{BA} in Eq. 2.31 yields the following expression

$$\Phi_{BA}(t) = \frac{i}{\hbar}\Theta(t)\langle [B(0), A(t)] \rangle, \tag{2.41}$$

where Θ is the Heavyside function, i.e. the step function taking the value 0 when $t < 0$ and 1 otherwise. The expression for Φ_{BA} points out that the response function is a retarded Green's function. Here and below we omit the index 0, but we emphasize that

the expectation values are determined by the unperturbed Hamiltonian $\mathcal{H}_0$. It is useful to introduce the following function:

$$\begin{aligned} K_{BA}(t) &= \frac{i}{\hbar}\langle[B(t), A(0)]\rangle = \frac{i}{\hbar}\langle[B(0), A(-t)]\rangle \\ &= -K_{AB}(t) = \frac{i}{\hbar}\langle[A(t), B(0)]\rangle \end{aligned} \tag{2.42}$$

Hence

$$\begin{aligned} K_{BA}(t) &= \Phi_{BA}(t) \qquad \text{for } t > 0 \\ K_{BA}(t) &= -\Phi_{AB}(t) \qquad \text{for } t < 0 \end{aligned} \tag{2.43}$$

It can be shown that the real and imaginary part of $\chi_{BA}(\omega)$ are related through the Kramers Kronig relations.
Assuming that the eigenstates and eigenvalues of the Hamiltonian can be written as

$$\mathcal{H}_0|\alpha\rangle = E_\alpha|\alpha\rangle \tag{2.44}$$

we may derive an explicit expression for $\chi_{BA}(\omega)$: Introducing the population factors

$$n_\alpha = \frac{1}{Z}e^{-E_\alpha/k_BT} \qquad ; \qquad Z = \sum_{\alpha'} e^{-E_{\alpha'}/k_BT}, \tag{2.45}$$

and performing the time Fourier transform leads to

$$\begin{aligned} \chi_{BA}(\omega) &= \lim_{\epsilon\to 0}\int_0^\infty dt K_{BA}(t)e^{i(\omega+i\epsilon)t} \\ &= \lim_{\epsilon\to 0}\sum_{\alpha,\alpha'}\frac{\langle\alpha|B|\alpha'\rangle\langle\alpha'|A|\alpha\rangle}{E_{\alpha'} - E_\alpha - \hbar\omega - i\hbar\epsilon}(n_\alpha - n_{\alpha'}) \end{aligned} \tag{2.46}$$

Generalized susceptibility within the RPA

In this section we will exemplify the principles of the formalism of the RPA applied to a Heisenberg ferromagnet.
The starting point is the following Hamiltonian

$$\begin{aligned} \mathcal{H} &= \sum_i \mathcal{H}_i^{mf} - \frac{1}{2}\sum_{i\neq j} J_{ij}(\mathbf{S}_i - \langle\mathbf{S}\rangle)\cdot(\mathbf{S}_j - \langle\mathbf{S}\rangle) \\ \mathcal{H}_{mf} &= \sum_i \mathcal{H}_i. \end{aligned} \tag{2.47}$$

Our goal is to compute the linear response of $\langle S(t)\rangle$ of the system to a small perturbative field $\mathbf{h}_j(t) = g\mu_B\mathbf{H}_j(t)$ (the Zeeman term arising from a static field is taken as included in $\mathcal{H}_{mf}$). We then transform the above Hamiltonian to the Heisenberg picture

$$\begin{aligned} \mathcal{H} &= \sum_i \mathcal{H}_i \\ \mathcal{H}_i(t) &= \mathcal{H}_i^{mf}(t) - (\mathbf{S}_i(t) - \langle\mathbf{S}_i\rangle)\cdot\left(\sum_j J_{ij}(\mathbf{S}_j(t) - \langle\mathbf{S}_j\rangle) + \mathbf{h}_i(t)\right). \end{aligned} \tag{2.48}$$

In RPA the fluctuations $\mathbf{S}_i(t) - \langle \mathbf{S} \rangle$ in Eq. 2.26 are considered, but are assumed to fluctuate in a virtually uncorrelated manner from ion to ion; their contribution to the whole sum in Eq. 2.26 is therefore expected to be small (justifying the name *random phase approximation*) and we can replace operators $\mathbf{S}_i(t)$ by their expectation value $\langle \mathbf{S}_j(t) \rangle$:

$$\mathbf{S}_i(t) \rightarrow \langle \mathbf{S}_j(t) \rangle \qquad \text{RPA.} \tag{2.49}$$

It is clearly best justified when the fluctuations are small, i.e. at low temperatures, and RPA can be applied to a three-dimensional spin system with long-range interaction, which means that many sites contribute to the sum in Eq. 2.26. Thus we define an effective field by

$$\begin{aligned} \mathcal{H}_i(t) &= \mathcal{H}_i^{mf}(t) - (\mathbf{S}_i(t) - \langle \mathbf{S}_i \rangle) \cdot \mathbf{h}_i^{eff} \\ \mathbf{h}_i^{eff} &= \mathbf{h}_i(t) + \sum_j J_{ij}(\mathbf{S}_i(t) - \langle \mathbf{S}_i \rangle). \end{aligned} \tag{2.50}$$

Recalling the generalized Fourier transform in Eq. 2.34 and Eq. 2.35 we then find

$$\langle \mathbf{S}_i(\omega) \rangle = \chi_i^0(\omega) \mathbf{h}_i^{eff} \tag{2.51}$$

because the dynamical response of spin i is given by the non-interacting one-spin susceptibility χ_i^0 under the effect of $\mathbf{h}_i^{eff}(\omega)$. This may be compared to the general response determined by the two-spin susceptibilities, after

$$\langle \mathbf{S}_i(\omega) \rangle = \sum_j \chi_{ij}(\omega) \mathbf{h}_j(\omega) \tag{2.52}$$

where χ_{ij} is a 3N matrix. It then follows

$$\chi_{ij}(\omega) = \chi_i^0(\omega) \left(\delta_{ij} + \sum_{j'} J_{ij'} \chi_{j'j}(\omega) \right). \tag{2.53}$$

This is a self-consistent equation. In the case of a ferromanget which is uniform, i.e.$\langle \mathbf{S}_i \rangle = \langle \mathbf{S} \rangle$ and $\chi_i^0(\omega) = \chi_i^0(\omega)$ we get the final result

$$\chi(\mathbf{q}, \omega) = \frac{\chi^0(\omega)}{\mathbb{1} - \chi^0(\omega) J(\mathbf{q})} \tag{2.54}$$

with $\mathbb{1}$ the unit matrix.
The energy dispersion is determined by the poles of the dynamic susceptibility in Eq. 2.54. The example of a ferromagnetic Heisenberg chain can be found in Appendix A.2.

In the RPA, the effects of the surrounding ions are accounted for by a time-dependent molecular field, which self-consistently enhances the response of the isolated ions. The RPA has its limit at high temperatures, because thermal fluctuations introduce damping effects which are not included in the RPA. Hence the obtained description of the dynamical behavior is incomplete. Nevertheless the simplicity of the RPA result 2.35 makes it suitable for application to complex systems.

2.5 Spin-wave theory

Another approach to treat the dynamics of a spin system is provided by spin-wave theory which is based on a fully aligned Néel state. The low-lying energy states of spins coupled by exchange interactions are wavelike. These waves are called spin waves, and they represent the propagation of a disturbance with respect to a static magnetization. The energy of a spin wave is quantized, and the unit of a spin wave is called a magnon.
Spin waves have been studied for all types of ordered spin arrays, including ferromagnetic, ferrimagnetic, antiferromagnetic, canted and spiral arrays.

2.5.1 Linear spin-wave theory

In the following we will consider a one-dimensional spin system with either ferromagnetic or antiferromagnetic interactions and we will derive the corresponding dispersion relations. Details can be found in Ref. [201].

Ferromagnetic magnons

We start with the Hamiltonian of a ferromagnetic Heisenberg chain where the spins are separated by a distance δ. Assuming nearest neighbor interaction between the spins at site R_i and R_j leads to

$$\begin{aligned} \mathcal{H} &= -\frac{1}{2}J\sum_{i\neq j}\mathbf{S}_i\mathbf{S}_j \\ &= -J\sum_i\left(\mathbf{S}_i\mathbf{S}_{i+1}+\mathbf{S}_i\mathbf{S}_{i-1}\right) \end{aligned} \tag{2.55}$$

The constants of the motion of the Hamiltonian include

$$\begin{aligned} \mathcal{S}^2 &= \left(\sum_j \mathbf{S}_j\right)^2 \qquad \text{total spin} \\ \mathcal{S}^z &= \sum_j S_j^z \qquad \text{z-component of the total spin} \end{aligned} \tag{2.56}$$

the product $\mathbf{S}_i\mathbf{S}_j$ can be written in terms of spin operators S^+ and S^-. It is then useful to perform the so-called *Holstein-Primakoff Transformation*, which allows us to express the Hamiltonian in Eq. 2.55 in terms of spin-wave variables:

$$\begin{aligned} \mathcal{H} &= -JNzS^2+\mathcal{H}_0 \\ \mathcal{H}_0 &= \sum_k a_k^\dagger a_k\omega_k; \qquad \omega_k = 2JSz(1-\gamma_k) \end{aligned} \tag{2.57}$$

where

$$\gamma_k = \frac{1}{z}\sum_\delta e^{ik\cdot\delta} = \frac{1}{2}\left(e^{ik\cdot\delta}+e^{-ik\cdot\delta}\right) = cos(k\cdot\delta) \tag{2.58}$$

assuming $z = 2$ nearest neighbor in the case of a ferromagnetic Heisenberg chain. The spin operators $a_k^\dagger$ and a_k denote the creation and annihilation of a magnon, respectively. The name *linear* spin-wavetheory refers to the linearization of the Holstein-Primakoff transformation as explained in the Appendix A.3.
ω_k gives the dispersion relation for magnons in a ferromagnetic spin chain, it corresponds to Eq. A.14. In the long wavelength limit i.e. $|k \cdot \delta| \ll 1$ we expand γ_k up to 1^{st} order

$$\gamma_k =\approx \quad [1 + (k \cdot \delta)^2] \tag{2.59}$$

and the dispersion relation reads then

$$\omega_k \approx 2JS(k \cdot \delta)^2 \tag{2.60}$$

we obtained the same results as derived within RPA, see Eq. A.15 of Appendix A.3.

Antiferromagnetic magnons

In principle we start with the same Hamiltonian as above in Eq. 2.55, but assume J to be negative and therefore accounting for antiferromagnetic interaction. In addition, we have to distinguish between the two sublattices A and B with a net magnetization S and $-S$, respectively.

$$\mathcal{H} \;=\; -\frac{1}{2}J\sum_{ij}\mathbf{S}_{Ai}\mathbf{S}_{Bj} \tag{2.61}$$

where the spins $\mathbf{S}_{Aj}$ and $\mathbf{S}_{Bj}$ belong to the sublattice A and B. Again the Holstein-Primakoff transformation is applied with respect to the two sublattices and after some technical tricks, which are demonstrated in Appendix A.3, we find the Hamiltonian of Eq. 2.61 in a diagonalized form

$$\begin{aligned} \mathcal{H} &= -2NJzS(S+1) + \sum_k \omega_k(\alpha_k^\dagger\alpha_k + \beta_k^\dagger\beta_k + 1) \\ \omega_k^2 &= (2JzS)^2(1-\gamma_k^2). \end{aligned} \tag{2.62}$$

In the long-wavelength limit we then find

$$\omega(k) = 4JS \cdot k\delta. \tag{2.63}$$

Again we have taken $z = 2$ for a chain.
The formulas given above are easily extended to the case of spin systems forming a Bravais lattice by replacing

$$\begin{aligned} k &\rightarrow \mathbf{k} \\ \delta &\rightarrow \boldsymbol{\delta} \\ z = 2 &\rightarrow z \text{ nearest neighbors} \end{aligned} \tag{2.64}$$

2.5.2 Beyond linear spin-wave theory

So far we assumed that the ground state is a perfectly ordered state (Ferromagnet or Néel state) where all spins are aligned. This was the starting point for both the non-interacting susceptibility $\chi_0(\omega)$ (in RPA) and introduction of the spin-waveoperators $a_j^\dagger$, a_j and $a_k^\dagger$, a_k, respectively (in linear spin-wave theory). We dropped any site dependence and considered all spins to be equivalent. However, if we include quantum effects, the remanent magnetization is reduced and eventually magnetic ordering is destroyed.
Interaction between magnons is discarded in the linearized Hamiltonian. We refer to the literature, e.g. Kittel [201].

2.6 Magnetic cluster systems

A magnetic cluster system is characterized by an assembly of N spins which interact so strongly that they form a unit, a so-called cluster. The interaction of a spin of one cluster with a spin of another cluster is weaker (interacting clusters) and sometimes even vanishing (isolated cluster). In a cluster system the states of the individual spins $|\lambda_{old}\rangle$ couple to new states of the cluster $|\lambda_{new}\rangle$:

$$|\lambda_{new}\rangle = \sum_i a_i |\lambda_{old}\rangle \tag{2.65}$$

which is a basis transformation from $|\lambda_{old}\rangle$ to $|\lambda_{new}\rangle$. The task consists in computing the possible eigenstates of the cluster and in determining the intra- and intercluster coupling strength based on the experimental information.
Here we give a short general description and we will focus on the tetramer system in Chapter 5.

2.6.1 Isolated cluster

In the case of isolated clusters the summation in Eq. 2.55 is not taken over the whole crystal, but restricted to some specific couplings. In order to keep it simple, we will treat the case of binuclear clusters where the spins at site $\mathbf{R}_1$ and $\mathbf{R}_2$ in the unit cell interact. The exchange Hamiltonian of the cluster is then given by

$$\mathcal{H}_c = -J \cdot \mathbf{S}_1 \mathbf{S}_2 \tag{2.66}$$

Since $\mathcal{H}_c$ commutes with the total spin $\mathbf{S} = \mathbf{S}_1 + \mathbf{S}_2$, $\mathbf{S}$ is a good quantum number, thus Eq. 2.66 can also be expressed as

$$\mathcal{H}_c = -J \cdot \frac{1}{2}\left(\mathbf{S}^2 - \mathbf{S}_1^2 - \mathbf{S}_2^2\right). \tag{2.67}$$

The wave function of the system may be expressed as $|S_1, S_2, S, M\rangle$. Recalling that $\mathbf{S}^2|S_1, S_2, S, M\rangle = S(S+1)$ we can directly write down the eigenvalues

$$\begin{aligned} E &= \frac{1}{2}J \cdot [S(S+1) - S_1(S_1+1) - S_2(S_2+1)] \\ \text{with} \quad \mathbf{S}^2|S_1, S_2, S, M\rangle &= S(S+1)|S_1, S_2, S, M\rangle \\ \mathbf{S}_1^2|S_1, S_2, S, M\rangle &= S_i(S_i+1)|S_1, S_2, S, M\rangle \quad i = 1, 2. \end{aligned} \tag{2.68}$$

Assuming $S_1 = S_2 = 1/2$ we obtain for the singlet ($S = 0$) and triplet ($S = 1$) state, respectively

$$\begin{aligned} E_S &= -J \cdot \frac{3}{4} \\ E_T &= J \cdot \frac{1}{4} \end{aligned} \tag{2.69}$$

Irreducible tensor methods

In general it is not possible to derive the eigenvalues of a cluster system in a straight forward manner. For cluster systems of lower symmetry as well as for higher order exchange interactions, the irreducible tensor method developed by Fano and Racah [202] and by Wigner [203] has to be applied. In this formalism the exchange Hamiltonian may be written in terms of tensor operators u_i^k of rank k as has been done by Furrer [105, 119].

$$\begin{aligned} \mathcal{H}_c &= \sum_k \sum_{i>j} a_k(i,j) u_i^k \cdot u_j^k \\ \langle S_i || u_i^k || S_i' \rangle &= \delta(S_i, S_i') \end{aligned} \tag{2.70}$$

The spin operator $\mathbf{S}_i$ and the tensor operator u_i^1 are related through

$$\langle S_i | \mathbf{S}_i | S_i' \rangle \delta(S_i, S_i') \tag{2.71}$$

Hence we find

$$\mathbf{S}_i = \sqrt{S_i(S_i+1)(2S_i+1)}\, u_i^1 \tag{2.72}$$

In order to derive the eigenvalues of $\mathcal{H}_c$ it is necessary to compute the matrix elements $\langle S_1, S_2, S, M | \mathcal{H}_c | S_1', S_2', S', M' \rangle$.
The difficulty consists in finding the Clebsch-Gordon coefficients of the basis transformation from the states of the individual spins to the states of the cluster

$$\begin{aligned} |S_1, M_1, S_2, M_2, S_3, M_3, S_4, M_4\rangle &= |S_1, M_1\rangle + |S_2, M_2\rangle + |S_3, M_3\rangle + |S_4, M_4\rangle \\ &\rightarrow |S_{12}, S_{34}, S, M\rangle \\ \text{with} \quad & \mathbf{S}_{12} = \mathbf{S}_1 + \mathbf{S}_2, \quad \mathbf{S}_{34} = \mathbf{S}_3 + \mathbf{S}_4 \\ & \mathbf{S} = \sum_{i=1}^{4} \mathbf{S}_i. \end{aligned} \tag{2.73}$$

We will work out the details in Chapter 5 and in Appendix B, directly applied to the tetramer system α-$MnMoO_4$.

2.6.2 Interacting cluster

As soon as the clusters are interacting, the eigenvalues of the cluster are no longer constant, but the magnetic excitations exhibit a dispersive behavior i.e. the excitations become q-dependent.
Ther intercluster interaction can be described by

- a mean-field approach
- RPA
- linear spin-wave theory

The latter two yield the direction dependent interaction strength for the intercluster coupling, whereas the mean field approach gives an average field due to the intercluster interaction.
An interacting cluster system is characterized by a strong intracluster interaction J_{kl} and a weaker intercluster interaction J_{ij}.

$$\begin{aligned} \mathcal{H}_{ic} &= \mathcal{H}_{intra} + \mathcal{H}_{inter} \\ \mathcal{H}_{intra} &= -\sum_{k,l=1}^{4} J_{kl}\mathbf{S}_k\mathbf{S}_l \\ \mathcal{H}_{inter} &= -\sum_{i,j} J_{ij}\mathbf{S}_i\mathbf{S}_j \\ & \quad |J_{kl}| > |J_{ij}| \end{aligned} \tag{2.74}$$

If

$$|J_{kl}| \gg |J_{ij}|, \tag{2.75}$$

the clusters are only weakly coupled.

Chapter 3

Neutron Scattering

In the present work we are mainly occupied with inelastic magnetic neutron scattering with the purpose to study dynamical effects in both materials $La_{1.96-x}Sr_xHo_{0.04}CuO_4$ as well as α-$MnMoO_4$. We have also performed neutron diffraction experiments and susceptibility experiments in order to characterize the samples.

3.1 Neutron Scattering in general

In modern condensed matter research thermal neutrons have become a valuable experimental tool for investigating many features of solids. The unique properties of neutrons allow a detailed understanding of the structure and dynamics of materials:

- The neutron is uncharged, which means that it interacts with the nucleus and not with the electrons. Thus neutrons can easily penetrate the sample and therefore reveal the bulk properties of the material. Furthermore they can distinguish isotopes as opposed to x-ray scattering.
- The mass of the neutron leads to the de Broglie wavelength of thermal neutrons being of the order of interatomic distances in solids. Hence neutron scattering is well suited to study the structure of solids.
- The energy of thermal neutrons is comparable to the energy of elementary excitations in matter. Measuring the neutron energy therefore reveals dynamic processes.
- Due to the magnetic moment of the neutron the said experimental technique provides accurate information about magnetic structures and magnetic excitations.

The principle of scattering of particles by a sample is common to most kinds of radiation. The partial differential cross section is the key quantity: it represents the number of neutrons scattered into a small solid angle $d\Omega$ with final energy between $\hbar\omega$ and $\hbar\omega+d(\hbar\omega)$. The total cross section results from integration in angle and energy:

$$\sigma = \int d\Omega \left(\frac{d\sigma}{d\Omega}\right) = \int d\Omega \int d\hbar\omega \left(\frac{d^2\sigma}{d\Omega d\hbar\omega}\right) \tag{3.1}$$

Because of the conservation of momentum and energy, the momentum

$$\begin{aligned} \hbar\mathbf{Q} &= \hbar(\mathbf{k}_i - \mathbf{k}_f) \\ \mathbf{Q} &= \boldsymbol{\tau} + \mathbf{q} \end{aligned} \tag{3.2}$$

and the energy

$$\pm\hbar\omega = \frac{\hbar^2}{2m}(\mathbf{k}_i^2 - \mathbf{k}_f^2) \tag{3.3}$$

are transferred to the sample, see Fig. 3.1. $\mathbf{k}_i$ and $\mathbf{k}_f$ denote the momentum of the initial and final state, respectively. $\mathbf{Q}$ is known as the scattering vector, it is usually decomposed into a reciprocal lattice vector $\boldsymbol{\tau}$ which reflects the periodicity of the lattice and $\mathbf{q}$, the wave vector of the excitation. Elastic scattering i.e. $\hbar\omega$=0 equivalent to $|\mathbf{k}_i| = |\mathbf{k}_f|$ provides information about static effects such as the position of atoms, size and distribution of inhomogeneities in a sample. In that case $\mathbf{Q} = \boldsymbol{\tau}$ holds which is known as Bragg's law. Inelastic scattering $|\mathbf{k}_i| \neq |\mathbf{k}_f|$ reveals dynamical effects: If $\hbar\omega > 0\,(< 0)$, the neutrons transfer energy to the sample (gain energy from the sample), which is a so-called Stokes (Antistokes) process, thus an excitation is created (annihilated). These principles are sketched in Fig. 3.1

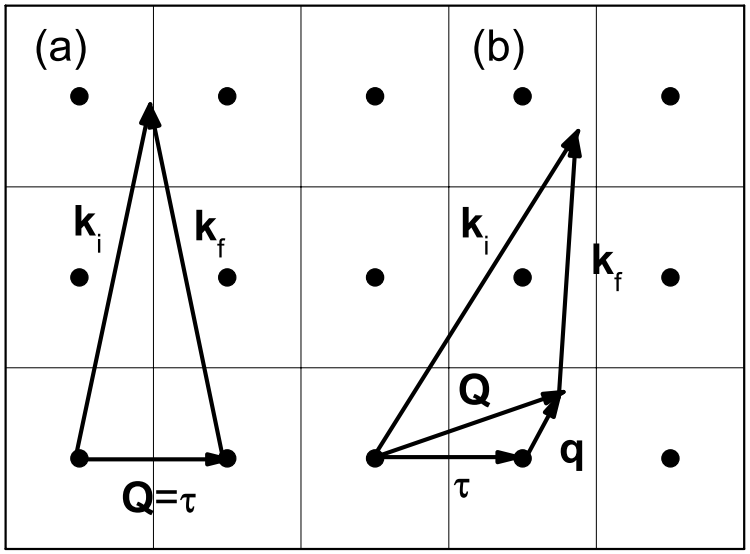

Figure 3.1: Principle of neutron scattering in reciprocal space: (a) reperesents elastic scattering with energy transfer $\hbar\omega$=0 and momentum transfer ($\mathbf{k}_i = \mathbf{k}_f + \boldsymbol{\tau}$). (b) illustrates the inelastic scattering process with ($\hbar\omega \neq 0$, $\mathbf{k}_i = \mathbf{k}_f + \boldsymbol{\tau} + \mathbf{Q}$).

The basic expression for the partial differential cross section can be obtained by the use of Fermi's golden rule and it is equivalent to the Born approximation, where it is assumed

that the scattered wave function $|\mathbf{k}_f, \lambda_f\rangle$ does not substantially differ from the incident wave function $|\mathbf{k}_i, \lambda_i\rangle$

$$\frac{d^2\sigma}{d\Omega d\omega} = \left(\frac{m}{2\pi\hbar^2}\right)^2 \sum_i p_i \sum_f |\langle \mathbf{k}_f, \lambda_f | \hat{U} | \mathbf{k}_i, \lambda_i \rangle|^2 \delta(\hbar\omega + E_i - E_f) \tag{3.4}$$

where m is the mass of the neutron. The averaging over the initial and final states is done on the basis of $|\lambda_i\rangle$ being occupied with the probability p_i, and the summing over the final states is done by summing over the index f. The operator $\hat{U}$ represents the interaction of the neutrons with the sample, which can be of nuclear or magnetic origin.

General properties of neutron scattering cross section

The partial differential scattering cross section is of the general form:

$$\begin{aligned} \frac{d^2\sigma}{d\Omega d\omega} &\propto \int_{-\infty}^{\infty} dt e^{i\omega t} \langle \hat{A}(t)\hat{B}(0)\rangle \\ S_{BA}(t) &= \langle \hat{A}(t)\hat{B}(0)\rangle \end{aligned} \tag{3.5}$$

The choice of the operators $\hat{A}(t)$ and $\hat{B}(0)$ depends on wether the neutron is scattered by the nucleon-nucleon interaction or by magnetic moments. The brackets denote a statistical average in the canonical ensemble whose dynamics is captured by some Hamiltonian. $S_{BA}(t)$ is called the pair correlation function, it is related to the retareded Green's function introduced in Chapter 2 in Eq. 2.41 in the following sense:

$$\begin{aligned} \Phi_{BA}(t) &= \frac{i}{\hbar}\Theta(t)\langle B(0)A(t) - A(t)B(0)\rangle \\ &= \frac{i}{\hbar}\Theta(t)[S_{AB}(-t) - S_{AB}(t)] \end{aligned} \tag{3.6}$$

It is thus assumed that the neutron acts as an infinitesimal small perturbation, and we can neglect deviations from thermodynamic equilibrium in the target induced by the incoming neutron flux in spite of the fact that energy has been exchanged between the target and the neutrons. It is standard practice to call

$$S_{AB}(\omega) := \int_{-\infty}^{\infty} dt e^{i\omega t} S_{AB}(t) \tag{3.7}$$

the scattering function. A detailed investigation of the analytic properties of S_{AB} shows that there is an assymmetry between the Stokes and anti-Stokes intensities:

$$S_{AB}(\omega) = e^{\hbar\omega/k_BT} S_{AB}(-\omega), \tag{3.8}$$

which is known as the principle of detailed balance. It basically results from the Bose-Einstein population factors for excitations:

$$\begin{aligned} \langle n\rangle &= \frac{1}{e^{\hbar\omega/k_BT} - 1} \qquad \langle n+1\rangle = \frac{e^{\hbar\omega/k_BT}}{e^{\hbar\omega/k_BT} - 1} \\ \Rightarrow e^{\hbar\omega/k_BT} &= \frac{\langle n+1\rangle}{\langle n\rangle}. \end{aligned} \tag{3.9}$$

With the combination of Eqs. 3.6 and 3.8 we get the following important relation between the correlation function and the susceptibility, which is basically the retarded Green's function, within linear response theory:

$$S_{AB}(\omega) \propto \frac{1}{1-e^{\hbar\omega/k_BT}} \cdot \Im G^R_{AB}(\omega) \tag{3.10}$$

which is called the fluctuation-dissipation theorem. This relation points out that there is an explicit relationship between molecular dynamics at thermal equilibrium, and the macroscopic response that is observed in a dynamic measurement. This means concretely applied to the case of magnetic interaction that the magnetic moment of the neutron acts on the sample as a frequency and wavevector dependent magnetic field $\mathbf{B}(\mathbf{Q},\omega)$. The response of the sample $\mathbf{M}(\mathbf{Q},\omega)$ is then

$$\mathbf{M}_\alpha(\mathbf{Q},\omega) = \sum_\beta \chi^{\alpha\beta}(\mathbf{Q},\omega)\mathbf{B}_\beta(\mathbf{Q},\omega) \qquad \alpha,\beta = x,y,z. \tag{3.11}$$

$\chi^{\alpha\beta}(\mathbf{Q},\omega)$ is the generalized susceptibility tensor, defined in Chapter 2.

3.2 Magnetic scattering

Since the neutron has a spin, there is an interaction between the magnetic moment of the neutron and the magnetic field which is created by the unpaired electrons in the sample. The interaction operator $\hat{U}$ in Eq. 3.4 assumes then the following expression:

$$\hat{U} = \frac{2\pi\hbar^2}{m}\sum_j b_j F_j(\mathbf{Q})\delta(\mathbf{r}-\mathbf{r}_j) \tag{3.12}$$

where b_j is the magnetic scattering length of atom j at position $\mathbf{r}_j$. $F_j(\mathbf{Q})$ is the so-called magnetic form factor, it is obtained from the Fourier transform of the normalised spin density $s_j(\mathbf{r})$ of the unpaired electrons.

$$F_j(\mathbf{Q}) = \int d\mathbf{r} s_j(\mathbf{r}) e^{i\mathbf{Q}\cdot\mathbf{r}} \tag{3.13}$$

It falls off with increasing modulus of $\mathbf{Q}$. Assuming unpolarised neutrons and identical magnetic moments gives the expression for Eq. 3.4 in the case of magnetic scattering:

$$\begin{aligned} \frac{d^2\sigma}{d\Omega d\omega} &= \frac{k_f}{k_i} exp(-2W)(\gamma r_0)^2 F(\mathbf{Q})^2 \sum_{\alpha,\beta}\left(\delta_{\alpha,\beta} - \frac{Q_\alpha Q_\beta}{Q^2}\right) S^{\alpha\beta}(\mathbf{Q},\omega) \\ S^{\alpha\beta}(\mathbf{Q},\omega) &= \sum_{j,j'} e^{i\mathbf{Q}\cdot(\mathbf{r}_j-\mathbf{r}_{j'})} \sum_{\lambda_i,\lambda_f} p_{\lambda_i}\langle\lambda_i|\hat{S}^\alpha_{j'}|\lambda_f\rangle\langle\lambda_f|\hat{S}^\beta_j|\lambda_i\rangle\delta(E_{\lambda_i}-E_{\lambda_f}+\hbar\omega) \end{aligned} \tag{3.14}$$

α, β are Cartesian coordinates x, y, $\hat{S}^\alpha_j$ denotes the operator of the spin component of atom j. The magnetic scattering function $S^{\alpha\beta}(\mathbf{Q},\omega)$ corresponds to the Fourier transform of the magnetic pair correlation function written here in the Schrödinger picture. Since the pair correlation function describes to find a magnetic moment at position 1 at a time

t and a magnetic moment at position 2 at $t = 0$, the magnetic cross section dependes on both magnetic as well as on vibrational degrees of freedom. Note that the polarization factor allows only the coupling of neutrons to magnetic moments perpendicular to $\mathbf{Q}$.

In the present work we study

- a dilute magnetic systems ($La_{1.96-x}Sr_xHo_{0.04}CuO_4$), where the single spins do not interact → crystal-field transitions
- a magnetic cluster system (α-$MnMoO_4$) with a strong interaction between the clusters → cluster and spinwave excitations

Next we give the concrete expressions of the corresponding differential partial cross section: The details about the physical properties can be found in Chapter 2 and Chapters 4 and 5.

3.2.1 Spin waves

If the spins on a lattice in an ordered system are strongly interacting through an exchange coupling, the basic excitations are spin waves. Spin waves are propagating states, thus the scattering cross section given in Eq. 3.14 shows a $\mathbf{q}$ dependence:

$$\begin{aligned}\left(\frac{d^2\sigma}{d\Omega d\omega}\right)_{sw} \sim & \left(\frac{g}{2}F(\mathbf{Q})\right)^2 \frac{k_f}{k_i} S \left(1+\left(\frac{Q_z}{Q}\right)^2\right) e^{-2W} \\ & \times \sum_{\boldsymbol{\tau},\mathbf{q}} (\langle n+1\rangle \delta(\mathbf{Q}-\mathbf{q}-\boldsymbol{\tau})\delta(\omega_{\mathbf{q}}-\omega) \\ & + \langle n\rangle \delta(\mathbf{Q}+\mathbf{q}-\boldsymbol{\tau})\delta(\omega_{\mathbf{q}}+\omega)) \end{aligned} \tag{3.15}$$

where g is the Landé factor, S is the magnitude of the spin and $Q = |\mathbf{Q}|$. The δ-functions reflect the conservation of energy and momentum, the last two terms correspond to spin wave creation and annihilation, respectively. Measuring the energy spectrum of scattered neutrons at different $\mathbf{Q}$ points yields the dispersion relation of the spin waves. In addition the values of the magnetic interaction parameters between the magnetic moments can be exctracted from this dispersion relation.

3.2.2 Crystal-field excitations

If the coupling between the spins of the magnetic ions is vanishing, we are left with a single-ion problem. Since the states are localized, the energy of the magnetic excitations will be independent of the scattering vector $\mathbf{Q}$. In this case the dominant mechanism is the crystal-field interaction which (partially) removes the degeneracy of the ground-state J-multiplet.
The resonance peaks in the observed energy spectra are then identified with the transitions between the crystal-field states Γ_n. Hence the neutron scattering experiments directly reveal the sequence of crystal-field levels with the cross section for the transition $|\Gamma_n\rangle \rightarrow |\Gamma_m\rangle$ with energies E_n and E_m:

$$\left(\frac{d^2\sigma}{d\Omega d\omega}\right)_{cef} \sim \left(\frac{g}{2}F(\mathbf{Q})\right)^2 \frac{k_f}{k_i} \times p_n \sum_\alpha \left(1-\left(\frac{Q_\alpha}{Q}\right)^2\right) |\langle\Gamma_m|\hat{J}^\alpha|\Gamma_n\rangle|^2 \delta(\hbar\omega + E_n - E_m). \quad (3.16)$$

where p_n is the Boltzmann population factor for the initial state. For experiments on polycrystalline powder the transition matrix element becomes $|\langle\Gamma_m|\hat{\mathbf{J}}_\perp|\Gamma_n\rangle|^2$ with $\hat{\mathbf{J}}_\perp$ being the component of the angular momentum perpendicular to the scattering vector.

Neutron Crystal-Field Spectroscopy applied to high-temperature superconductors

The underlying idea is to replace e.g. in $YBa_2Cu_3O_x$ or $La_{2-x}Sr_xCuO_4$ a small amount of the Y^{3+} or La^{3+} ions, respectively, by paramagnetic rare-earth (R^{3+}) ions, which are situated close to the copper-oxide planes where the superconducting carriers are located, thus the crystal-field potential at the R^{3+} sites constitutes an ideal probe of the local symmetry as well as the local charge distribution. It therefore monitors directly changes of the carrier concentration induced by ion substitutions, external fields, opening of an electronic gap which will be explained below. This property results from the short-range nature of the leading terms in the crystal-field potential.
Neutron crystal-field spectroscpopy has the advantage to probe the static susceptibility in zero magnetic field as opposed to other relaxation methods such as NMR and NQR.
In order to make sure that the observed peaks in the energy spectra really arise from crystal-field transition, and not from, say, phonon scattering, one has to check the intensity as a function of temperature and momentum transfer: While crystal-field intensity decreases with increasing Q according to $F^2(Q)$, the phonon peak intensity grows with Q^2. Furthermore, phonons obey Bose statistics, whereas the population of crystal-field levels is governed by Boltzmann statistics.

The crystal-field states Γ_n are subjected to interactions with phonons, spin fluctuations, and charge carriers, which limit the lifetime of the excitations, thus the observed resonance peaks exhibit line broadening: The δ-function in Eq. 3.16 becomes a Lorentzian.

$$\begin{aligned} E_{nm}(t) = |E_n - E_m|(t) &= E_{nm}\cdot e^{\Gamma_{nm}t/\hbar} \\ \delta(\hbar\omega + E_n - E_m) &\rightarrow \frac{\Gamma_{nm}^2}{E_{nm}^2+\Gamma_{nm}^2} \\ 2\Gamma_{nm} &= \text{FWHM (full width at half maximum)} \end{aligned} \quad (3.17)$$

3.2.3 Magnetic cluster

For magnetic cluster systems the expression in Eq. 3.14 undergoes two principle modifications:

- the spin operators $\hat{S}_j^\alpha$ have to be replaced by irreducible tensor operators $\hat{T}_j^q$ of rank 1

- the geometrical structure factor $S(\mathbf{Q})$ of the cluster has to be included in the formula for the cross section. $S(\mathbf{Q})$ incorporates the internal geometry of one cluster.

If the clusters do not interact, the scattering cross section was derived by Furrer [105, 119] to be:

$$\frac{d^2\sigma}{d\Omega d\omega} \propto \sum_j \frac{k_f}{k_i} |\langle \hat{T}_j^q \rangle|^2 S_j(\mathbf{Q}) \delta(\hbar\omega + E_i - E_f) \tag{3.18}$$

where we used $\langle \hat{T}_j^q \rangle \equiv \langle S'_{12} S'_{34} S' M' | \hat{T}_j^q | S_{12} S_{34} S M \rangle$. The meaning of these matrix elements will become clear when we discuss α-$MnMoO_4$ in Chapter 5.
In the case of tetranuclear cluster with spins at site $\mathbf{R}_i$ and $\mathbf{R}_j$ of the rhombic cluster, the structure factor $S(\mathbf{Q})$ becomes

$$\begin{aligned} S(\mathbf{Q}) &= \sum_{i,j=1}^{4} e^{i\mathbf{Q}\cdot(\mathbf{R}_i - \mathbf{R}_j)} \\ &= 4 + cos(\mathbf{Q}\cdot\mathbf{R}_{12}) + cos(\mathbf{Q}\cdot\mathbf{R}_{34}) \\ &+ cos(\mathbf{Q}\cdot\mathbf{R}_{13}) + cos(\mathbf{Q}\cdot\mathbf{R}_{14}) + cos(\mathbf{Q}\cdot\mathbf{R}_{23}) + cos(\mathbf{Q}\cdot\mathbf{R}_{24}) \end{aligned} \tag{3.19}$$

$\mathbf{R}_{ij} = \mathbf{R}_i - \mathbf{R}_j$ is the vector connecting the Mn^{2+} ions of the cluster at site $\mathbf{R}_i$ and $\mathbf{R}_j$. The scattering cross section is therefore proportional to

$$\begin{aligned} \frac{d^2\sigma}{d\Omega d\omega} \propto\ & \delta(S_{34}S_{34'}) \left[1 + (-1)^{S_{12}-S_{12'}} cos(\mathbf{Q}\cdot\mathbf{R}_{12})\right] |\langle \hat{T}_j^1 \rangle|^2 \\ & + \delta(S_{12}S_{12'}) \left[1 + (-1)^{S_{34}-S_{34'}} cos(\mathbf{Q}\cdot\mathbf{R}_{34})\right] |\langle \hat{T}_3^1 \rangle|^2 \\ & + \delta(S_{12}S_{12'})\delta(S_{34}S_{34'}) \left[cos(\mathbf{Q}\cdot\mathbf{R}_{13}) + cos(\mathbf{Q}\cdot\mathbf{R}_{14})\right. \\ & \left. + cos(\mathbf{Q}\cdot\mathbf{R}_{23}) + cos(\mathbf{Q}\cdot\mathbf{R}_{24})\right] \\ & \langle \hat{T}_1^1 \rangle \langle \hat{T}_3^1 \rangle \end{aligned} \tag{3.20}$$

For experiments on polycrystalline material Eq. 3.20 has to be averaged in $\mathbf{Q}$-space:

$$\begin{aligned} \frac{d^2\sigma}{d\Omega d\omega} \propto\ & \delta(S_{34}, S'_{34}) \left[1 + (-1)^{S_{12}-S'_{12}} \frac{sin(QR_{12})}{R_{12}}\right] |\langle \hat{T}_1 \rangle|^2 \\ & + \delta(S_{12}, S'_{12}) \left[1 + (-1)^{S_{34}-S'_{34}} \frac{sin(QR_{34})}{R_{34}}\right] |\langle \hat{T}_3 \rangle|^2 \\ & + 4 \cdot \delta(S_{12}, S'_{12})\delta(S_{34}, S'_{34}) \frac{sin(Q/2\sqrt{R_{12}^2 + R_{34}^2})}{Q/2\sqrt{R_{12}^2 + R_{34}^2}} \langle \hat{T}_1 \rangle \langle \hat{T}_3 \rangle \end{aligned} \tag{3.21}$$

where R_{12} and R_{34} corresponds to the length of the diagonals and $Q = |\mathbf{Q}|$.
It is interesting to note that Eq. 3.20 contains three different interference terms each of which has its own characteristic Q-dependence. This will serve as a powerful tool to identify the observed transitions between the various cluster states. We will make use of this in Chapter 5.

Table 3.1: Summary of the neutron scattering experiments.

sample	Instrument	type of experiment	goals & results
α-$MnMoO_4$	TriCS	elastic, single-crystal	magnetic structure: 3D antiferromagnetic order below 10.7 K
	FOCUS	inelastic, powder	cluster states: intracluster coupling parameters
	RITA II TASP	inelastic, single-crystal	dispersive behavior of magnetic excitiations: intercluster coupling parameter
$La_{1.96-x}Sr_xHo_{0.04}CuO_4$	HRPT	elastic, powder	chemical structure: no structural phase transition up to 100 K
	FOCUS	inelastic, powder	relaxation rate: pseudogap temperature
	MARI	inelastic, powder	crystal-field level scheme: only one transition up to 12 meV

3.3 Neutron scattering experiments

We investigated structural and dynamical properties of $La_{1.96-x}Sr_xHo_{0.04}CuO_4$ and α-$MnMoO_4$ by means of elastic and inelastic neutron scattering experiments, respectively. Table 3.1 presents a summary of the performed neutron scattering experiments and states which kind of sample has been measured on which instrument.

3.3.1 Diffraction

The chemical and magnetic structure may be investigated by neutron diffraction. Its basic idea is that the signals from the elastic scattering are collected over a broad angle range. As most novel materials are only available as powder, usually powder diffraction measurements are performed first. They are simpler and faster to be carried out. Moreover they are necesseary as a perliminary investigation, for instance a powder diffraction pattern

gives accurate information on the lattice parameters and the point symmetry group, while single-crystal diffraction is well suited to study details such as the direction of magnetic moments.
Powder diffraction may be limited if reflections are overlapping, then there is need for single-crystal experiments, which allow to scan the reciprocal space unambiguously.

Powder diffraction: experimental setup

The powder diffraction experiments were performed on the multidetector diffractometer HRPT [204] using thermal neutrons. HRPT is designed as a flexible instrument for efficient neutron powder diffraction studies. We collected diffraction patterns for $La_{1.81}Sr_{0.15}Ho_{0.04}CuO_4$ at different temperatures (T = 15 K, 80 K, 100 K and at 250 K) in order to check if there is any structural phase transition occuring. The powder with m=15 g has been mounted into a cryostat. At all the temperatures the wavelength was chosen to be $\lambda = 1.9$ Å.

Single-crystal diffraction: experimental setup

A single crystal ($m \approx$1 g) of α-$MnMoO_4$ was measured on the thermal neutron diffractometer TriCS [205] at SINQ in a temperature range from 1.5 to 15 K at an incident wavelength λ=1.179 Å. An Euler cradle, which rotates the sample in real space combined with two-dimensional detectors allows data collection in the whole reciprocal space. The purpose of this experiment has been to determine the magnetic structure of α-$MnMoO_4$.

3.3.2 Inelastic neutron scattering experiments

For experiments on polycrystalline samples time-of-flight spectrometers are preeminently appropriate to study any sort of excitations, e.g. crystal-field transitions. The concept of the instrument consists in measuring the time-of-flight of the scattered neutrons, which arrive in temporary pulses. The pulses of neutrons are produced by two in phase rotating choppers (disc chopper and Fermi chopper). The energy transfer $\hbar\omega$ and the modulus of the scattering vector $\mathbf{Q}$ are then determined by the flight time of the neutrons from the Fermi chopper to the detector and the scattering angle which the detector is positioned at, respectively. The time delay yields then information on the energy gain (loss) of the neutron due to de-excitations (excitations) of the quantum mechanical state of the sample. A time-of-flight experiments on a powder sample collects the data in a large Q range, which depends on the chosen energy window.
If a single-crystal is available, a triple-axis spectrometer (TAS) is able to reveal much more detailed information at a specific $\mathbf{Q}$-point. The intensity of the scattered neutrons is measured as a function of momentum transfer $\hbar\mathbf{Q}$ and energy transfer $\hbar\omega$. A schematic view of a TAS instrument is shown in Fig. 3.2.
The white spectrum of the neutron source is scattered by the monochromator crystal (first axis) and therewith determines the wavevector $\mathbf{k}_i$ of the incident beam. The monochromatic beam is scattered from the sample along a direction defined by the scattering angle 2θ (second axis). The scattered neutrons with wavevector $\mathbf{k}_f$ are then reflected by the

analyser crystal (third axis) and finally hit the detector thereby defining the energy transfer $\hbar\omega$. Thus a TAS instrument provides controlled access to the variables θ, $\mathbf{k}_i$ and $\mathbf{k}_f$, $\mathbf{Q}$ as well as ω determining the scattering function $S(\mathbf{Q},\omega)$, which is needed in order to describe the system under investigation.
The outstanding advantage of such a spectrometer is that the data can be taken either for a fixed energy transfer along a particular line in reciprocal space (constant-E scan) or at a pre-determined point in reciprocal space (constant-$\mathbf{Q}$ scan). This way dispersion relations in single crystals can be measured in a controlled manner.

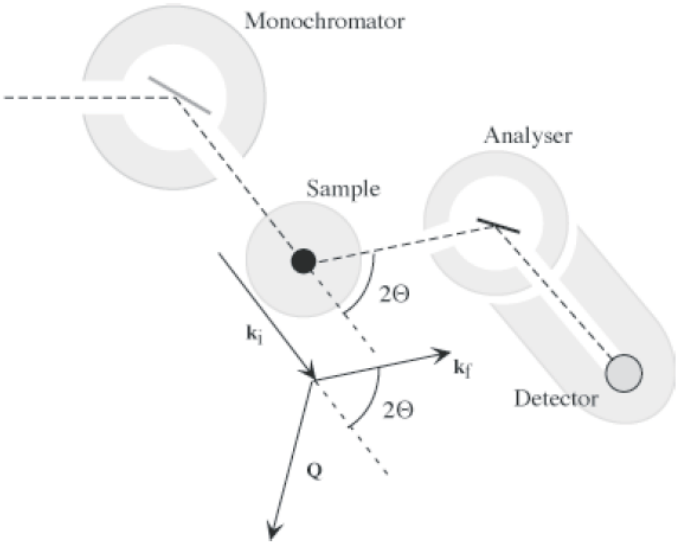

Figure 3.2: The principle of a TAS instrument.

Inelastic powder measurements on $La_{1.96-x}Sr_xHo_{0.04}CuO_4$: experimental setup

FOCUS: All our experiments elucidating the pseudogap phenomenon have been carried out on the high-resolution time-of-flight spectrometer FOCUS [206, 207].
FOCUS was always operated at a fixed incident wavelength of $\lambda = 5.75$ Å, which corresponds to an energy $E_i = 2.47$ meV of the incoming beam. For such long wavelengths additionally a cooled Be-filter had to be placed within the monochromator shielding in order to prevent contamination from higher orders. This experimental setup gives an energy resolution at the elastic line of 51 μeV.
The samples were enclosed in Al cylinders and mounted in a He cryostat in order to collect data in the temperature range $1.5 \leq T \leq 140$ K. The data were corrected for absorption, detector efficiency, background and detailed balance effects according to standard procedures.

MARI & IN4: We tried to establish the crystal-field level scheme by neutron spectroscopic experiments on the time-of-flight spectrometer IN4 [208] located at the Institute Laue Langevin in Grenoble, France. The experiments were carried out using an incoming beam with $\lambda = 2.6$ Å, which corresponds to $E_i = 12.1$ meV at various temperatures between 1.5 K and 60 K.

Since the background effects were too intense to state unambiguously that there is only one excited level up to an energy transfer of 10 meV, we performed measurements on MARI [209, 210] at the spallation neutron source ISIS, Rutherford Appleton Laboratory, England. MARI is a direct geometry chopper spectrometer and it is able to map large regions of the $Q - E$ space in a single measurement. MARI was operated at an incident beam energy of 100 meV at temperatures of 14 and 100 K.

Application of hydrostatic pressure:

In order to apply hydrostatic pressure, the sample was enclosed in an axially symmetric pressure cell made of hardened aluminium and mounted in a He cryostat. The total accessible sample volume in the pressure cell amounted to about 1.6 cm^3, whereas the size of the pressure cell exceeds the sample volume by far as illustrated in Fig. 3.3.
Fluorinert F-77 was used as pressure medium. The applied pressure was determined by a callibration measurements on NaCl in the same pressure cell carried out on the powder diffractometer DMC in order to determine the shift of the lattice constants.

Figure 3.3: The pressure cell used for the time-of-flight experiments on FOCUS. The maximum applied pressure amounts to 1.2 GPa.

Inelastic powder measurements on α-$MnMoO_4$: experimental setup

α-$MnMoO_4$ was preliminary investigated in powder from. The corresponding inelastic neutron scattering experiments were performed on the high-resolution time-of-flight spectrometer FOCUS, located at SINQ. The instrument was operated at a wavelength of 4.75 Å, the temperature was kept at 1.5 K.

Table 3.2: Adjustment of the triple-axes instruments RITA II and TASP (fixed final energy E_f,wave vector k_f)and corresponding resolution $\Gamma_g(0)$ during the data collection.

Instrument	E_f [meV]	k_f [Å^{-1}]	$\Gamma_g(0)$ [μeV]
RITA 2	4.9	1.54	235
TASP	4.9	1.54	238
	3.8	1.35	141
	2.5	1.1	66

Single-crystal measurements: experimental setup

A large single-crystal ($m \approx 11$ g) has been grown by the Güdel group and we took the chance to study it on RITA II [211, 212] and TASP [213], both located at SINQ. Scans were performed at constant final energy E_f under standard focussing conditions. Both instruments were operated at a fixed final energy E_f i.e. final wavevector k_f listed in Table 3.2. In all the experiments a beryllium filter was placed in front of the analyzer in order to prevent higher order reflections.
The single-crystals could be oriented in the a^*b^*- as well as in the b^*c^*-plane. The orientation was determined by elastic Bragg scattering.

3.4 Macroscopic measurements: AC susceptibility

Macroscopic measurements such as DC magnetization, AC susceptibilty, specific heat etc. have been extensively applied to high-T_c materials. These techniques are very useful to investigate basic properties, namely zero-resistance and diamagnetism below T_c. It is also possible to extract some basic key parameters, such as the penetration depth λ, the anisotropy $\gamma = \sqrt{m_c^*/m_{ab}^*}$ and the correlation length ξ [63]. Moreover, macroscopic measurements are an excellent tool to study the magnetic phase diagram which has been done in detail by R. Gilardi et al. on LSCO [63].

DC magnetization measurements determine the equilibirum value of the magnetization in the sample. The sample is magnetized by a constant external magnetic field and its magnetic moment is measured by induction. When the sample is moved through the detection coils, a voltage is induced and the amplitude of the signal is proportional to the magnetic moment of the sample.
The temperature scans were performed zero-field-cooled as well as field-cooled.
In the case of AC magnetic measurements, a time dependent magnetic moment is induced in the sample by a small AC magnetic field superimposed on the DC field

$$H = H_{DC} + H_{AC} \cdot cos(\omega_{AC} t). \tag{3.22}$$

Thus there is no need for a movement of the sample.
As long as the frequency ω_{AC} is small, the resulting moment M in the sample is in phase with the oscillating magnetic field H:

$$M_{AC} \;=\; \chi \cdot cos(\omega_{AC} t)$$

$$\chi = \frac{dM}{dH} H_{AC} \quad \text{susceptiblity.} \tag{3.23}$$

At higher frequencies, M_{AC} may lag behind the drive field due to dynamic effects in the sample. Hence two quantities are measured:

- the magnitude of the susceptibility
- the phase shift between the measured and the drive signal.

Equivalently the susceptibilty is considered to be a complex quantity

$$\begin{aligned} \chi &= \chi' + i\chi'' \\ \chi' &= \frac{1}{\pi H_{AC}} \int_0^{2\pi} M(\tau) cos(\tau) d\tau \\ \chi'' &= \frac{1}{\pi H_{AC}} \int_0^{2\pi} M(\tau) sin(\tau) d\tau, \end{aligned} \tag{3.24}$$

where we set $\tau = \omega t$. The in-phase part χ' is the reactive part, whereas the out-of-phase part χ'' incorporates the dissipation of energy, see also the Section 2.4.2 about RPA.

3.4.1 Experimental setup

AC susceptibility and DC magnetization measurements were performed using a commercial Quantum Design Physical Properties Mesurements System (PPMS). In order to determine T_c, we mainly used AC-susceptibility measurements with an amplitude $H_{AC} = 10$ Oe and freuqency $\omega = 100$ Hz. We also performed measurements with $\omega = 1000$ Hz, but it yielded the same results like the other susceptibility data.

3.4.2 Application of pressure

The basic ideas for the design of the pressure cell are borrowed from the experience with hydrostatic clamp pressure cell as used for neutron scattering experiments under pressure. The sample is enclosed in a container made of lead and then mounted into the pressure cell together with the pressure medium fluorinert FC-77. Lead becomes superconducting below 7.2 K [214], thus the susceptibility data are then dominated by the diamagnetic signal originating from lead. Since it is well known (see Ref. [215]) that the pressure effect on $T_c(Pb)$ of lead is

$$\frac{dT_c}{dp} = -0.36 \text{ K/GPa}, \tag{3.25}$$

the applied pressure can be determined from the low-temperature data as illustrated in Fig. 3.4. From the comparison of these two data sets, a value of 1 GPa has been derived for the hydrostatic pressure in the present experiment.

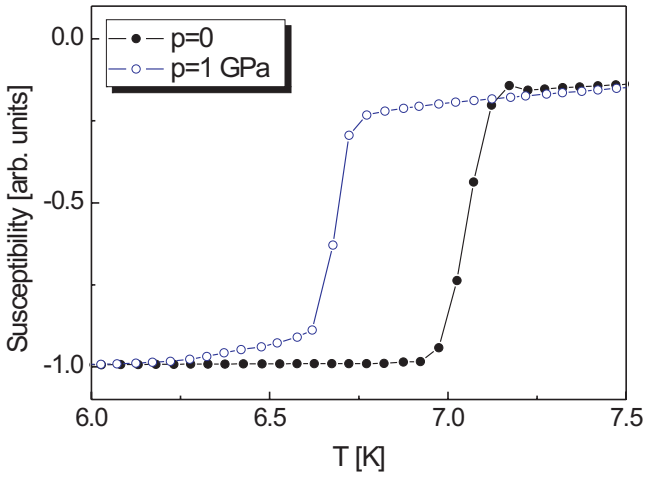

Figure 3.4: Dynamic susceptibility measurements taken for $La_{1.81}Sr_{0.15}Cu^{16}O_4$. Only the low-temperature part is shown, which illustrates the pressure-induced shift of lead which the pressure cell is made of. From the value of dT_c/dp of lead the applied pressure is determined as explained in the text.

Chapter 4

The pseudogap in $Ho@La_{2-x}Sr_xCuO_4$ as seen by neutron crystal-field spectroscopy

In spite of the vast experimental and theoretical work a common consensus on the origin of the pseudogap is lacking. Consequently, experiments which produce changes of the pseudogap temperature T^* are of crucial importance to discriminate between pairing scenarios developed for the cuprate superconductors. We therefore decided to investigate systematically the dependence of T^* on doping, oxygen isotope substitution and pressure by means of neutron crystal-field spectroscopy.

4.1 Introduction

4.1.1 Oxygen isotope effect

In conventional superconductors a dependence of T_c on the atomic mass was first observed in mercury [216]. The isotope shift may be quantified by

$$T_c \sim M^{-\alpha}, \quad \alpha = -\frac{d\,lnT_c}{d\,lnM}, \tag{4.1}$$

where M is the isotope mass, and α is the so-called isotope-effect exponent.
Within BCS theory the superconducting transition temperature T_c can be expressed as follows [217]

$$T_c \approx \Theta_D exp\left(-\frac{1}{N(E_F)V_{ee}}\right), \tag{4.2}$$

where Θ_D denotes the Debye temperature, $N(E_F)$ is the electronic density of states at the Fermi energy, and V_{ee} is the attractive pairing interaction. It turned out that $\alpha_{BCS} \approx 1/2$. This is in agreement with a number of experiments (ordinary metal superconductors), whereas transition metals usually differ substantially from this value (e.g. Zr and Ru

with $\alpha \approx 0$). The reason for such a deviation is that the conventional phonon-mediated theory ($\alpha = 1/2$) is based on the Migdal adiabatic approximation, where the density of states $N(E_F)$, the electron-phonon coupling constant λ_{ep} and the effective supercarrier mass m^* are all independent of the mass M of the lattice atoms. However, if the interaction between the carriers and the lattice ions is strong enough, the Migdal approximation breaks down [218] so that the interaction parameter V_{ee} needs some more detailed consideration: V_{ee} is basically the result of the difference between the attractive electron-phonon interaction and the Coulomb repulsion. Mc Millan introduced these interactions explicitly into a non-adiabatic theory and found an expression for T_c [219]:

$$T_c \propto \omega_D \cdot exp\left(-\frac{\lambda^* + 1}{\lambda^* - \mu^*(1 + \lambda^* \cdot \langle\omega\rangle/\omega_D)}\right) \tag{4.3}$$

where λ^* and μ^* are the renormalized electron-phonon and Coulomb interaction, respectively, which can be revealed by experiments. $\langle\omega\rangle$ is the mean value of the lattice frequencies.
The isotope effect - on any quantity - reflects the influence of lattice fluctuations. Also in novel superconductors such as MgB_2 a remarkable isotope shift of T_c was observed upon B isotope (^{10}B vs. ^{11}B) substitution [220].

Unconventional isotope effects in the cuprates

According to the introduction above, unconventional isotope effects on various quantities are expected for the cuprate superconductors, which belong to the class of non-adiabatic superconductors.

OIE on the superconducting transition temperature T_c: The oxygen isotope effect on T_c was investigated in great detail, a review is given in Ref. [86]. It is now well established that the doping dependence of the OIE exponent α_O is a generic feature of the cuprates [221, 222, 223]: In the underdoped region it was found that $\alpha_O \geq \alpha_{BCS}$, whereas it is small in the optimally doped and overdoped regime.
LSCO is a special case: the isotope effect ΔT_c is strictly negative at all doping levels. At the famous doping $x = 1/8$ there is a lattice instability [224] as well as an electronic instability which favors the occurence of stripes [6]. 1/8 is also the doping level where α_O is unusually large [221].

OIE on the magnetic in-plane penetration depth λ_{ab}: The magnetic in-plane penetration depth λ_{ab} is related to the in-plane effective mass m^*_{ab} and the superconducting carrier density n_s by the following expression:

$$\frac{1}{\lambda^2_{ab}} \propto \frac{n_s}{m^*_{ab}}. \tag{4.4}$$

Note that m^*_{ab} is not equal to the band mass. Within standard BCS theory which is based on the Migdal adiabatic approximation, the effective mass of the supercarriers is not affected by a change in the mass of the lattice atoms.
But in the high-T_cs an isotope effect on λ_{ab} has been found which in turn reveals a mass

dependence of m^*_{ab} provided that the change in n_s is known. Such an effect has been discovered both in LSCO and YBCO by magnetization measurements [221, 222] and by muon-spin rotation (μSR) experiments [225], which provide a detailed information about the magnetic field distribution.

An empirical relation between the OIE on T_c and λ_{ab} has been reported by Khasanov et al. [225], which is a crucial parameter to understand the role of phonons in the high-T_cs. For both quantities, T_c and λ_{ab}, the planar oxygen sites (CuO_2 planes) mainly contribute to the total OIE on T_c and λ_{ab}, which has been demonstrated by site-selective oxygen-isotope effect experiments reported in Ref. [226] and Ref. [225]

OIE on the pseudogap temperature T^*: ^{89}Y NMR experiments in YBCO showed no isotope effect on the pseudogap [43]. On the other hand X-ray absorption near-edge spectroscopy (XANES) experiments [87] revealed a huge isotope effect associated with the onset of local lattice fluctuations in underdoped $La_{1.94}Sr_{0.06}CuO_4$, whose characteristic temperature T^* increases from 110 to 170 K upon replacing ^{16}O by ^{18}O. A large oxygen isotope effect on the pseudogap was also observed by neutron crystal-field spectroscopy for slightly underdoped $HoBa_2Cu_4O_8$ with $\Delta T^* \approx$50 K [89]. The same technique applied to optimally doped $La_{1.81}Sr_{0.15}Ho_{0.04}CuO_4$ yielded T^*=(61.0±1.3) K - which coincides with the onset of charge order [227] - and ΔT^*=(+8.0±2.5) K [90]. The large oxygen isotope shifts ΔT^* observed by XANES and neutron spectroscopy experiments were quantitatively accounted for by models based on dynamical charge ordering [228], phonon-induced stripe formation [229], and bipolaron formation associated with Jahn-Teller-like oxygen vibrations [230].

The reason why the NMR experiments show the absence of an isotope effect on T^* might be attributed to the different time scale of the experimental techniques: The time-scale of NMR and NQR is rather slow ($\sim 10^{-6}$) whereas e.g. neutron crystal-field spectroscopy with a time-scale of 10^{-12} s is able to detect dynamical effects. Its time scale is in the range of atomic/molecular vibrations and spin fluctuations.

OIE on the electron paramagnetic resonance (EPR) linewidth: In order to observe an EPR signal in the cuprates, it is necessary to dope them with a small amount of some paramagnetic ions such as Mn^{2+}. Similary to neutron crystal-field spectroscopy where a small amount of a rare-earth ion (Ho^{3+}) is introduced, Mn^{2+} serves to probe the intrinsic behavior. The Keller group observed a large isotope effect on the EPR linewidth in underdoped samples, which decreases with Sr doping and almost vanishes in the overdoped regime [88].

OIE on the glass temperature T_g: μSR- experiments in Mn-doped LSCO samples in the non-superconducting regime [231] revealed a huge isotope effect on the spin glass temperature T_g, whereas the isotope effect on Mn-free samples is rather small. This unusual effect shows that the coupling of the electrons to the lattice influences magnetism in the cuprates, because conventional theories of magnetism neglect the atomic motion and therefore no isotope effect is expected [231]. Note that Shengelaya et al. further observed

an enhancement of T_g as compared to pure LSCO. Such an effect can be explained by a reduced carrier mobility.

Isotope substitution will hardly affect disorder and Coulomb repulsion, thus any non-vanishing IE implies the influence of the mass of the corresponding atoms, which can be understood as a contribution of electron-phonon coupling to Cooper pairing. However, it has to be clarified whether the phonons are directly or indirectly involved in the pairing mechanism.

4.1.2 Pressure studies

Pressure effect on the superconducting transition temperature T_c

The application of high pressure creates 22 new elemental superconductors due to a pressure induced insulator-metal transition, but for most conventional superconductors T_c decreases under pressure. The ubiquitous suppression of T_c in all simple metal superconductors (e.g. Pb: $dT_c/dp = -0.36$ K/GPa, see Ref. [215]) is not an electronic effect, but arises predominately from a stiffening of the lattice with increasing pressure. We can make this argument more specific by considering the BCS expression for the transition temperature in Eq. 4.2: The principal reason for the observed decrease in T_c with pressure is that the pairing interaction V_{ee} itself decreases by a sizeable amount due to lattice stiffening, which makes it increasingly difficult for the anions in the crystal lattice to couple with the electrons.
From the McMillan equation [219] for strongly correlated electrons, the relative change in T_c is deduced:

$$\begin{aligned}
\frac{\partial ln(T_c)}{\partial p} &= \frac{\partial ln(\Theta_D)}{\partial p} + \left(\frac{1}{N(E_F)V_{ee}}\right)^2 \cdot \frac{\partial N(E_F)V_{ee}}{\partial p} \\
&= \frac{\gamma}{\kappa} - \frac{\Delta}{\kappa}\left(\frac{\partial ln(\eta)}{dln(V)} + 2\gamma\right), \\
\gamma &:= \frac{\partial ln(\langle\omega\rangle)}{dln(V)} \quad \text{Grüneisen parameter} \\
\eta &:= N(E_F)\langle I^2\rangle \\
\Delta &:= 1.04 \cdot \lambda \frac{1 + 0.38\mu^*}{(\lambda - \mu^*(1 + 0.62 \cdot \lambda))^2}
\end{aligned} \tag{4.5}$$

where κ is the bulk modulus, $\langle I^2\rangle$ is the matrix element for electron-phonon interaction, λ its coupling parameter and $\mu^* = 0.1$ a renormalized Coulomb potential [232]. The Coulomb repulsion is weakened through the retardation of the phonon-induced interaction. For superconductors whose electrons possess s or p character, the expression above leads to a negative pressure effect.

Pressure studies in high-temperature superconductors

Pressure has been recognized as one of the key parameters that strongly affect the transition temperatures of cuprate superconductors. Although there is still no consensus on the underlying mechanism responsible for the superconducting pairing, it has been established that the carrier density in the CuO_2 planes is a principal parameter determining T_c.
On a global scale - just as in BCS superconductors - the change in the lattice constant is reflected to the electronic band structure and the phonon spectrum, which results in changes of the density of states at the Fermi level and of the electron-phonon coupling strength. On a more local scale, the modified bond lengths may change the Madelung potential at individual sites, which in turn may give rise to a charge redistribution. Moreover pressure will also affect the values of the hopping integral t and the exchange coupling J, which are the main ingredients of the t-J model. These aspects can be expressed by the following formula:

$$\begin{aligned} \frac{\partial T_c}{\partial p} = \left(\frac{\partial T_c}{\partial p}\right)^{intrinsic} &+ \frac{\partial T_c}{\partial n} \cdot \frac{\partial n}{\partial p} \\ \left(\frac{\partial T_c}{\partial p}\right)^{intrinsic} &> 0 \quad \text{at optimal doping} \end{aligned} \tag{4.6}$$

A fundamental result from high-pressure experiments is the fact that the intrinsic pressure effect is positive at optimal doping [232]. It has been found that the anisotropic properties of the cuprates are also reflected in the pressure effect on T_c: studies on Ca-substituted Y-123 revealed that the compression along the c axis has no effect on T_c, whereas compression in the CuO_2 planes causes the ubiquitous increase in T_c. An experimental rule has been established [232]

$$T_c \sim a^{-4.5}, \tag{4.7}$$

which states that T_c is approximately proportional to the inverse square of the area of the CuO_2 planes.
Murayama et al. [233] investigated the correlation between the pressure-induced changes of the Hall coefficient and T_c in several superconducting cuprates such as LSCO, YBCO, BSCCO and $Tl_2Ba_2CuO_{6+y}$. They found that the behavior of the LSCO system is different from others in that R_H does not change with pressure and that T_c increases with pressure both in the underdoped and overdoped regions. So according to Eq. 4.7 the intrinsic pressure effect on T_c is always positive in the whole doping range, which emphasizes that the pressure-induced charge redistribution has a profound effect on T_c.

Pressure effect on the pseudogap: Unfortunately, there are only few pressure-dependent experiments on the pseudogap temperature T^* in literature, and the results are contradicting. Nuclear quadrupole resonance (NQR) experiments for $YBa_2Cu_4O_8$ [94] as well as resisitivity measurements for quenched and Ca-doped $YBa_2Cu_3O_7$ compounds [95] show a (continuous) decrease of T^* with increasing pressure, whereas from the analysis of resisitivity measurements for optimally doped $Hg_{0.82}Re_{0.12}Ba_2Ca_2Cu_3O_{8+\delta}$ [96] a linear increase of T^* with pressure is reported.

To the best of our knowledge, there are no model calculations which could predict the behavior of T^* as a function of pressure. The analysis of the pressure effect on the pseudogap is a particularly difficult problem on a theoretical ground, because pressure affects not only lattice fluctuations, but through subtle structural changes it also modifies the coupling parameter of the copper spins and the hopping integral for the charge carriers. Hence one should start with a Hamiltonian based on the t-J model, and include simultaneously the electron-phonon interaction. Such a model has been proposed by Bussmann-Holder [234] where the attractive pairing potential based on electron-phonon coupling is mediated by Jahn-Teller Q_2-type mode. However, it is not clear so far how t and the Hubbard potential U and this way J through Eq. 2.3 will be affected by pressure. Therefore there are still too many unknown parameters, it is not even possible to give only a qualitative trend for dT^*/dp.

4.1.3 The role of phonons in high-T_c compounds

In BCS theory the attractive electron-phonon interaction gives rise to a new state, the state of superconductivity. In high-T_c materials it has become clear that phonons alone cannot produce such high transition temperatures, moreover a lot of experimental observations, such as the anisotropy of the gap function, are not consistent with s-wave pairing.
There are models based on antiferromagnetic fluctuations alone, e.g. the t-J model which can explain some experimental observations and parts of the phase diagram, but *a priori* it is not able to predict oxygen isotope effects because the octahedra around the Cu ion is assumed to be stiff. Other models which include the effect of phonons, such as the mechanism originally developed by Höck [235] have difficulties to explain for instance the anisotropy of the superconducting order parameter. But oxygen effects naturally arise from such models - at least qualitatively. So far the role of phonons is subject of a highly controversial debate among the high-T_c community. Here we outline some experimental facts - besides the isotope effects described in a previous section - and theoretical concepts which suggest a considerable electron-phonon interaction in the cuprate superconductors.

ARPES measurements of various high-T_c compounds exhibit a kink in the electronic dispersion [236] at an energy of ~ 70 meV. This energy corresponds to the energy of longitudinal optical phonon modes measured by inelastic neutron scattering [237]. In these experiments an anomalous doping dependent change of weight of two phonon branches of equal symmetry in the middle of the Brioullin zone have been observed, which implies a distortion of the copper-oxide plane. Also other experimental techniques have unraveled distorted copper-oxide planes, namely EXAFS [238] and ESR measurements [237]. There are two types of octahedra: the first type of octahedra is nearly regular, whereas the second one is strongly deformed according to the Jahn-Teller effect, so that the Cu-O squares are Q_2 distorted. Hence these data suggest the presence of two types of quasiparticles as envisaged first by Gor'kov and Sokol [239]. Following this idea and incorporating the concept of Jahn-Teller polarons [235] leads to a displacement of the oxygen atoms, which in turn gives rise to a large effective mass. Thus the phonon and electronic energies are of comparable size, which means that the Born-Oppenheimer approach breaks down,

because the electronic and lattice degrees of freedom can no longer be decoupled.

Another experiment emphasizing the polaron and/or bipolaron type of carriers is the observation of a large OIE on the charge ordering temperature in LSCO [87]. Since the carrier concentration difference upon oxygen isotope substitution is negligible [240, 241], these findings suggest that the stripe formation is not caused by purely electronic interaction.
The afore mentioned OIE on the EPR linewidth can be explained within a model including a linear coupling of the Q_4 and Q_5 phonon modes to Dzyaloshinsky-type spin terms [88]. Moreover, another EPR study [242] suggested the existence of an $S = 1/2$ three spin polaron which consists of two Cu^{2+} ions and one oxygen hole. Such a three spin polaron leads to a dynamical Q_2 mode distortion of the oxygen square around a Cu^{2+} ion in the CuO_2 plane. Analyzing these results [88, 242] and incorporating the two local octahedral distortions [238] mentioned above, simultaneously reveals the relation of the Q_4/Q_5 with the Q_2 dynamics: the CuO_4 platelet of CuO_6 octahedra gets tilted out of the plane by Q_4/Q_5 rotation due to the elongation along one direction. Thus it has been suggested that the linear relationship between the planar Jahn-Teller Q_2 distortion and the Q_4/Q_5 tilting of the octahedra is responsible for the observed EPR data.
We have already mentioned that Shengelaya et al. [231] found an OIE on the spin glass transition T_g in Mn-doped LSCO samples, which can be explained by a reduced carrier mobility. This shows that there might be a complicated interplay of magnetic order and phonons. It remains to be clarified if lattice effects influence magnetic features through a slight distortion which modifies the exchange integral of the Cu spins or whether phonons affect only the superconducting properties.

Andergassen et al. [228] evaluated the crossover line marking the opening of the pseudogap within the Hubbard-Holstein model. They attributed the observed isotope shifts to a lattice mechanism which underlies the instability marked by a quantum critical point. This way they are able to reproduce IEs over a large doping range, only in the far underdoped region, where other effects (magnetic, polaronic, and lattice pinning) become important, the predictions are only of qualitative nature.

4.2 Structure and Crystal-field interaction in Ho@LSCO

The crystal-field is sensitive to the surrounding of the rare-earth ion according to Chapter 2, Section 2.3. It is therefore in turn strongly dependent on the symmetry of the structure. We focus first on the symmetry before we consider the crystal-field itself.

4.2.1 Crystal symmetry

Some aspects concerning the structure of the high-temperature superconductors have already been introduced in Chapter 1, the chemical structure is shown in Fig. 1.2.
We would like to emphasize that the high-T_c cuprates are characterized by a layered-

perovskite crystal structure containing a planar CuO_2 network, where each Cu ion is fourfold coordinated with O ions. The low energy electronic carriers reside on these planes.
The structural properties of LSCO have been investigated in detail by means of neutron powder diffraction [23] for various doping levels and at different temperatures. The lattice parameters for the optimally doped compound turned out to be

$$a = 5.3247 \text{ Å}, \quad b = 5.3486 \text{ Å}, \quad c = 13.1973 \text{ Å}.$$

The structural phase diagram of $La_{2-x}Sr_xCuO_4$ contains only two crystallographic phases up to $x = 0.375$: the high-temperature tetragonal (HTT) one with space group symmetry $I4/mmm$ and the low-temperature orthorhombic (LTO) one characterized by $Cmca$. (The corresponding nonstandard space notations are $F4/mmm$ and $Bmba$ for the HTT and the LTO phase, respectively.) These two phases are shown in Fig. 4.1.
The reduction of the symmetry from tetragonal to orthorhombic in the low-temperature, low-doping region is associated with the CuO_2 layers being under compression, while the LaO layers are under tension - in the case of $LaCuO_2$. This mismatch between the layers decreases as a function of x. In the tetragonal phase the length of the axes a and b are equal.

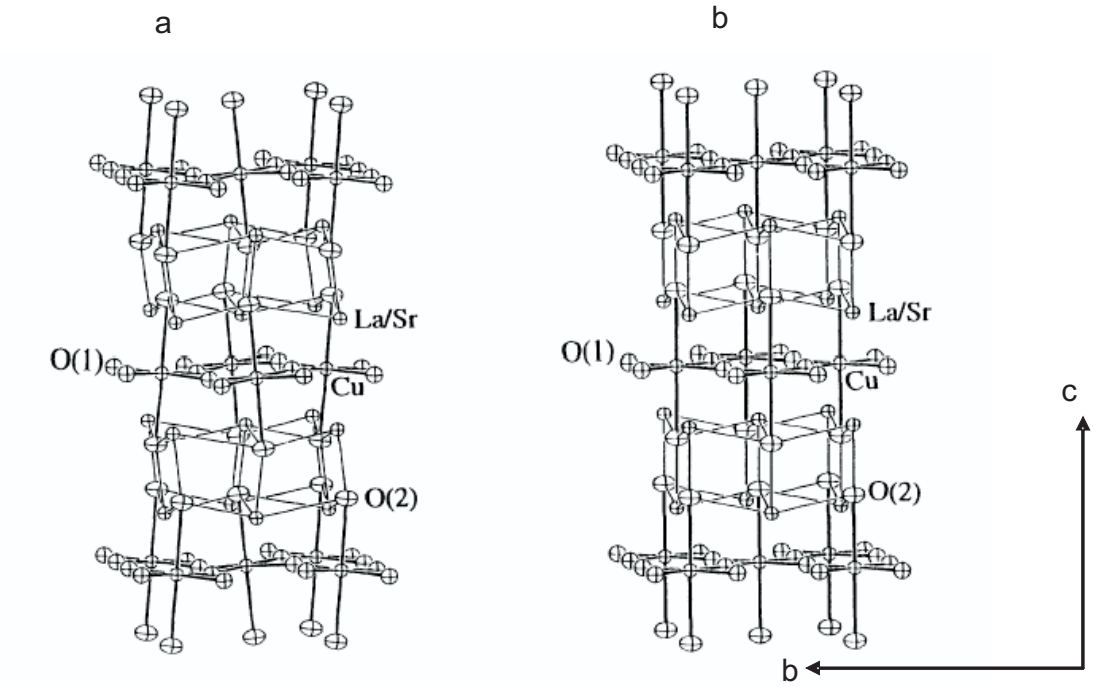

Figure 4.1: Structure of the LTO (a) and HTT (b) phases as taken from Ref. [23]. The LTO phase is characterized by a cooperative tilt of the CuO_6 octahedra.

4.2.2 Crystal-field parameters of Ho@LSCO

$La_{1.96-x}Sr_xHo_{0.04}CuO_4$ is subject to a crystal-field interaction due to the rare-earth ion holmium. The Ho^{3+} ion is a non-Kramers ion because it has ten electrons in the $4f$

Table 4.1: Crystal-field paramters B_n^m for Ho@$La_{2-x}Sr_xCuO_4$,which result from the extrapolation procedure based on structural effects alone as explained in the text.

B_2^0	-9.52·10^{-2}
B_2^0	0.911·10^{-2}
B_4^0	-0.141·10^{-2}
B_4^2	6.29·10^{-6}
B_4^4	0.161·10^{-2}
B_6^0	-2.36·10^{-6}
B_6^2	1.68·10^{-}
B_6^4	4.37·10^{-5}
B_6^6	-2.06·10^{-6}

shell ($L = 6$ and $J = 8$) which is equivalent to the $^5I_8$ configuration of the ground-state J-multiplet. Therefore the $2J + 1$=17-fold degeneracy of the J-ground-state multiplet is completely lifted.

So far the crystal-field level scheme of Ho^{3+} in $La_{2-x}Sr_xCuO_4$ has not been established experimentally. Therefore we derived the crystal-field parameters by extrapolation from those of $HoBa_2Cu_3O_7$ [197] based on the procedure described in Chapter 2, Section 2.3 (see also Ref. [243]) and using the structural parameters for $HoBa_2Cu_3O_7$ [244] and $La_{2-x}Sr_xCuO_4$ [23]. The results are given in Table 4.1.

This extrapolation procedure predicts the first-excited crystal-field level to lie at 0.25 meV, separated from the next excited levels by about 10 meV. The transition matrix elements of the latter are at least an order of magnitude smaller than for the lowest crystal-field transition observed in the present work, which was recently confirmed by neutron spectroscopic experiments [245]. For the experimental confirmation of the extrapolation we refer to Section 5.5.2.

Once the crystal-field parameters were obtained, we defined them to correspond to the strongly underdoped compound $La_{1.94}Sr_{0.02}Ho_{0.04}CuO_4$. We used this set of parameter $B_n^m(x = 0.02)$ as a reference from where we deduced the crystal-field parameters $B_n^m(x)$ for the other doping levels of $La_{1.96-x}Sr_xCuO_4$ using the procedure described in Chapter 2.

We assumed that the crystal-field potential is mainly determined by the nearest-neighbor oxygen shell, which is generally true in the high-T_c compounds, see e.g. Ref. [243]. Thus we include in the calculation of the geometrical coordination factors $\gamma_n^m(i)$ the four O(1) ions in the Cu plane and the five O(2) ions in the (La,Sr,Ho) plane.

Neglecting changes in the effective charges, the relation between $B_n^m(x, p)$ and $B_n^m(x = 0.02, p = 0)$ based on the point-charge model (see Eq. 2.10, 2.12, 2.14) reads

$$B_n^m(x, p) = B_n^m(x = 0.02, p = 0) \cdot \frac{\gamma_n^m(x, p)}{\gamma_n^m(x = 0.02, p = 0)}. \tag{4.8}$$

γ_n^m is given in Eq. 2.13:

$$\begin{aligned} \gamma_n^m(i) &= f_n^m(\theta_i.\phi_i)\frac{1}{|\mathbf{r}-\mathbf{R}_i|^{n+1}} \\ \mathbf{r} &: \mathrm{Ho}^{3+}\ \text{site} \\ \mathbf{R}_i &: \begin{cases} \mathrm{O}(1) & 1 \le i \le 4 \\ \mathrm{O}(2) & 5 \le i \le 8. \end{cases} \end{aligned} \tag{4.9}$$

The corresponding structural parameters can be found in Ref. [23] and in Ref. [246] for the case of doping and pressure dependence, respectively.

It might be reasonable to go one step back, because the approximation that the effective charges do not change with doping might be too daring. In fact the crystal-field parameters are a function of both the structure and the charge distribution as explained in Chapter 2 (see Eq. 2.12). We will address this particular issue when we discuss the results of the crystal-field transitions.

4.3 Relaxation of crystal-field levels in the normal state and in the pseudogap state

4.3.1 Relaxation rate of crystal-field transitions

In metallic systems the interaction with the charge carriers is by far the dominating relaxation mechanism [91]. The intrinsic linewidth of a transition between the states $|i\rangle$ and $|j\rangle$ with energy $\hbar\omega_{ij} = \hbar\omega_i - \hbar\omega_j$ is given by [247]

$$\begin{aligned} \Gamma_n^{ij}(T) &= 2J_{ex}^2\left[M_{ij}^2 coth\left(\frac{\hbar\omega_{ij}}{2k_BT}\right)\chi^{''}(\hbar\omega_{ij})\right. \\ &\quad + \sum_{k\neq i} M_{ik}^2 \cdot \frac{\chi^{''}(\hbar\omega_{ik})}{exp(\hbar\omega_{ik}/k_BT)-1} \\ &\quad \left. + \sum_{l\neq j} M_{lj}^2 \cdot \frac{\chi^{''}(\hbar\omega_{lj})}{exp(\hbar\omega_{lj}/k_BT)-1}\right] \end{aligned} \tag{4.10}$$

where J_{ex} is the exchange integral between the charge carriers and the 4f electrons of the R^{3+} ions, M_{ij} is the transition matrix element of the crystal-field transition $|i\rangle \rightarrow |j\rangle$ and $\chi^{``}$ is the imaginary part of the susceptibility summed over the Brillouin zone. According to the previous section, we can restrict Eq. 4.10 to the ground-state and the first excited level, which reduces Eq. 4.10 to

$$\begin{aligned} \Gamma_n(T) &\equiv \Gamma_n^{01}(T) = 2J_{ex}^2\left[M_{01}^2 coth\left(\frac{\hbar\omega_{01}}{2k_BT}\right)\chi^{''}(\hbar\omega_{01})\right] \\ &\approx 4J_{ex}^2\left[M_{01}^2\frac{k_BT}{\hbar\omega_{01}}\chi^{''}(\hbar\omega_{01})\right] \end{aligned} \tag{4.11}$$

where $\Gamma_n(T)$ has been expanded up to first order under the assumption $\hbar\omega \ll k_B T$. We then use a Fermi-liquid approach for the imaginary part of the susceptibility

$$\chi^{``}(\hbar\omega) = \pi N^2(E_F)\hbar\omega, \tag{4.12}$$

with $N(E_F)$ being the density-of-states of the charge carriers at the Fermi energy E_F. This leads to the following expression for the relaxation rate:

$$\Gamma_n(T) = 4\pi M^2 j_{ex}^2 N^2(E_F) k_B T. \tag{4.13}$$

It predicts the linewidth to increase linearly with temperature according to the well-known Korringa law [248].
In the superconducting state, on the other hand, the pairing of the charge carriers creates an energy gap Δ below the superconducting transition temperature T_c (or a pseudogap below a characteristic temperature T^*), thus crystal-field transitions with energy $\hbar\omega < 2\Delta$ do not have enough energy to span the gap, and consequently there is no interaction with the charge carriers. For an isotropic gap, the intrinsic linewidth in the superconducting state is then given by

$$\begin{aligned} \Gamma_s(T) &= \Gamma_n(T) \cdot exp\left(-\frac{\Delta}{k_B T}\right) \\ &\Rightarrow \Gamma_s(T) \approx 0 \quad \text{for} T \ll T_c \end{aligned} \tag{4.14}$$

Hence line broadening is exponentially reduced just as soon as the pseudogap opens. Therefore, the corresponding pseudogap temperature T^* can be directly derived from the temperature where the linewidth starts to deviate from the Korringa behavior.

Other relaxation channels

The previously described model is based on the interaction with the charge carriers being the most important one, but there are also other relaxation channels, namely:

- magnetic interactions
- interaction with phonons.

Their contribution to the relaxation rate in the normal state is schematically illustrated in Fig. 4.2.
Magnetic interactions would be dominant at low temperatures and become negligible in the high-temperature region. In Ref. [249] a model for the relaxation based on magnetic interactions is discussed and exemplified by $Tm_{0.1}Y_{0.9}Ba_2Cu_3O_x$ [250]. Aksenov et al. [249] include an exchange interaction between the spin of the Cu ion and the $4f$ electrons, also the spin dynamics in the CuO_2 planes is considered. It turned out that the main contribution to the relaxation arises then from one-magnon absorption processes in the antiferromagnetic insulating state [249]. In the superconducting state, antiferromagnetic fluctuations lead only to a small broadening of the linewidth. Another approach has

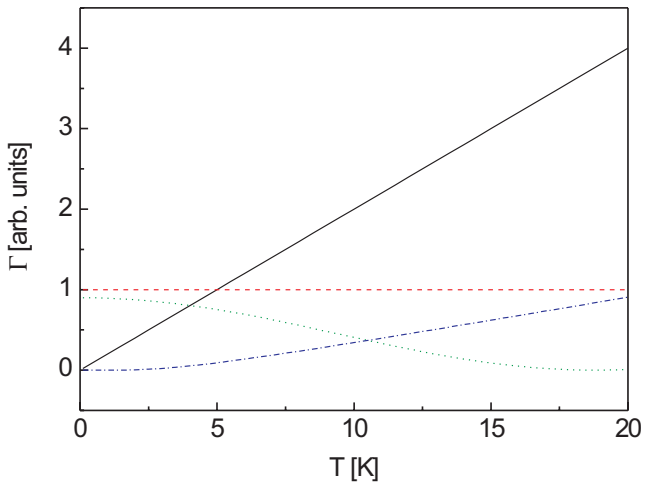

Figure 4.2: The temperature dependence of the relaxation rate based on different models is schematically drawn: the black solid line corresponds to the interaction with the charge carriers, the red dashed line corresponds to local structural distortions, the green dotted line arises from magnetic interactions and the blue dashed-dotted line results from the interaction with phonons.

been suggested by Kovacevic and Plakida [251] in order to explain the linewidth data for $Tm_{0.1}Y_{0.9}Ba_2CCu_3O_{6.9}$ [250]: they included the experimental data for the susceptibility of $YBa_2Cu_3O_{6.92}$ near the antiferromagnetic wave vector $\mathbf{Q} = (1/2, 1/2, 1.6)$ [252], which lead them to the conclusion that antiferromagnetic fluctuations in the CuO_2 planes have to be considered in a model explaining the temperature dependence of the linewidth of crystal-field transitions.
In both Refs. [249] and [251] the crystal-field of $Tm_{0.1}Y_{0.9}Ba_2Cu_3O_{6.9}$ was approximated by two levels. However, the sharp decrease of the experimentally observed linewidth [250] as one enters the pseudogap state could not be explained.

Lovesey and Staub [253, 254] assumed that lattice vibrations influence the crystal-field levels based on a so-called Orbach process [255]. They performed perturbational model calculations for a magnetoelastic interaction being proportional to the normal modes of vibration of the ions in the nearest-neighbor coordination shell. This results in a modulated crystal-field potential due to lattice vibrations and in turn modifies the relaxation rate. They found a reasonable agreement with experimental data [247, 250, 256]. But their approximation involves the neglect of all but three of the crystal-field levels. It has been shown by Boothroyd [257] that the inclusion of other thermally populated levels leads to results which do not differ significantly from those calculated with exchange-coupling model used previously [247]. Moreover, he found that the coupling constant of the magnetoelastic model depends strongly on the number of crystal-field levels considered. Thus Boothroyd concluded that the accidental agreement between data and magnetoelastic model calculations cannot be taken as an evidence that phonons rather than charge carriers are the most important sources of relaxation.

Anyway, a model based on phonon interaction has difficulties to explain the sudden decrease of the relaxation rate induced by the opening of an *electronic* gap, the pseudogap. Based on these considerations, we conclude that the interaction with the charge carriers is the dominant relaxation channel.

Local structural distortions also lead to a broadening of the experimentally observed linewidth, but this effect is of static nature and does not contribute to the relaxation. Thus the intrinsic linewidth is obtained by a subtraction of the constant broadening due to local structural distortions.

Neutron crystal-field spectroscopy has several advantages over other experimental techniques: it is

- truly bulk-sensitive
- fast in order to be able to detect dynamical effects with a time scale of 10^{-12}-10^{-13} s (typical of spin and lattice fluctuations)
- direct in order to reveal a distinct crossover temperature (without involving a complicated mathematical machinery to derive T^* from the raw data).

This technique has already been successfully applied to other high-T_c compounds [89, 90, 258].

4.3.2 Influence of the nature of the gap function on the relaxation rate

It is widely believed that the symmetry of the superconducting order parameter has predominantly d-wave character, and this holds also for the pseudogap [46]. Therefore the isotropic gap in Eq. 4.14 has to be replaced by a d-wave gap function of the form

$$\begin{aligned} \Delta_{x^2-y^2}(\mathbf{k}) \equiv \Delta(\mathbf{k}) &= \Delta_0 \cdot [cos(k_x) - cos(k_y)] \\ \Leftrightarrow \Delta(\phi) &= \Delta_0 \cdot cos(2\phi) \\ \phi &:= arctan\left(\frac{\pi - k_y}{\pi - k_x}\right) \qquad 0 \le \phi \le \pi/2 \\ \Delta_0 &:= max\Delta(\mathbf{k}), \quad \mathbf{k} \in \text{ Fermi surface.} \end{aligned} \tag{4.15}$$

Thus the calculation of $\Gamma_s(T)$ requires an integration in the (k_x, k_y) plane:

$$\begin{aligned} \Gamma_s(T) &= \Gamma_n(T) \oint_{\mathbf{k}_F} dk G_k \\ G_k &= \begin{cases} 1 & : \text{ if } \hbar\omega > 2|\Delta(\mathbf{k})| \\ exp\left(-\frac{\Delta(\mathbf{k})}{k_B T}\right) & : \text{ if } \hbar\omega < 2|\Delta(\mathbf{k})| \end{cases} \end{aligned} \tag{4.16}$$

where $\mathbf{k}_F$ is the Fermi vector. This procedure has been developed by Mesot et al. [259]. However, slight modifications of this general behavior have been observed. Their influences on the relaxation data are presented below and depicted in Fig 4.4.

Magnitude of the superconducting gap Δ_0

Ido et al. [36] found that Δ_0 is closely related to T^* in both BSCCO ($Bi_2Sr_2CaCu_2O_{8+\delta}$) and LSCO ($La_{2-x}Sr_xCuO_4$) systems, namely

$$T^* \sim 2\Delta_0/4.3k_B \tag{4.17}$$

over a large doping range. However, the size of Δ_0 has only a small influence on the relaxation rate as visualized in panel (a) of Fig 4.4.

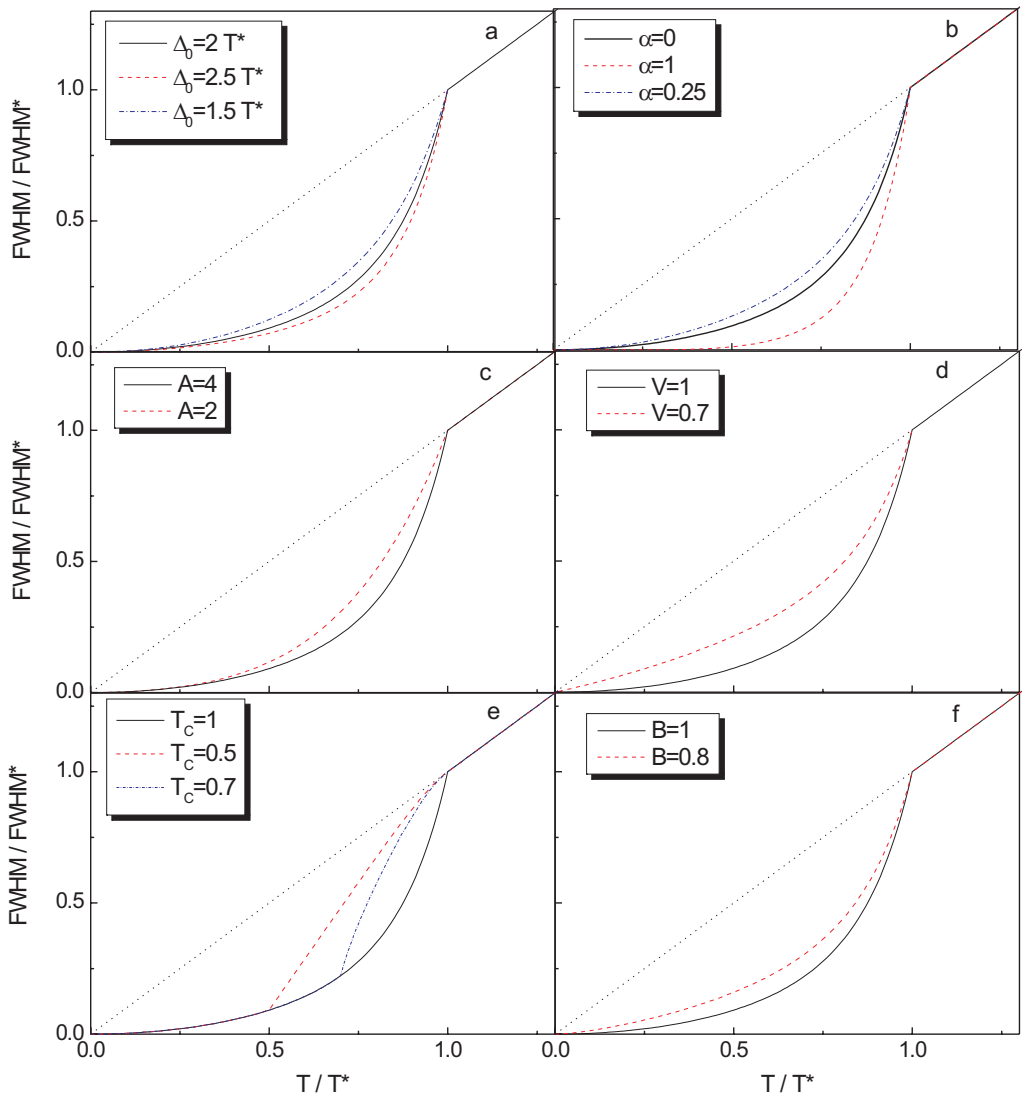

Figure 4.3: Illustration of the influence of various features of the gap function on the relaxation rate as discussed in the text. (a) Magnitude of the maximum amplitude Δ_0, (b) s-wave contribution α to the superconducting gap, (c) temperature exponent A of the gap function, (d) superconducting volume fraction V, (e) gapless Fermi-arcs and (f) contribution of higher harmonics B to the d-wave gap.

s-wave contribution α to the superconducting gap

A *d*-wave gap offers relaxation channels even at the lowest temperatures due to the nodes in the gap function. But an *s*-wave contribution α to the gap shifts these nodes, which can readily be seen from the expression:

$$\Delta_0(\mathbf{k}, T) = \Delta_0 \left[(1-\alpha) \cdot (cos(k_x) - cos(k_y)) + \alpha\right], \tag{4.18}$$

where $\alpha = 1$ stands therefore for an isotropic gap as in Eq. 4.14. Hence in comparison with the linewidth data calculated for a pure *d*-wave gap, a pure *s*-wave gap reduces the linewidth substantially at low temperatures, see panel (b) of Fig. 4.4.
As long as the amplitude of the *d*-wave gap is larger than the *s*-wave gap, there is still a node in the gap function. However, this node is shifted to a larger angle ϕ and moreover the shape of the gap is no longer symmetric around $\phi = 45°$. Such a behavior has recently been observed in untwined YBCO [260] by angle-resolved electron tunneling.
In order to quantify the effect of an *s*-wave contribution on the relaxation rate we recall that the relaxation rate is sensitive to the gap integrated in the reciprocal space. It is therefore helpful to consider

$$D(\alpha) = \int_0^{\pi/2} (|(1-\alpha) \cdot cos(2\phi) + \alpha|) d\phi \tag{4.19}$$

Let us define $\alpha_{min} \in [0, 1]$ as the value where $D(\alpha_{min})$ has a minimum. Consequently the relaxation rate $\Gamma(\alpha_{min})$will then be largest. A numerical calculation yields $\alpha_{min} = 0.4$ as displayed in Fig 4.4. This means that up to a 40% percentage of *s*-wave character of the gap, the linewidth lies therefore above the one obtained for a pure *d*-wave as well as for a pure *s*-wave gap.

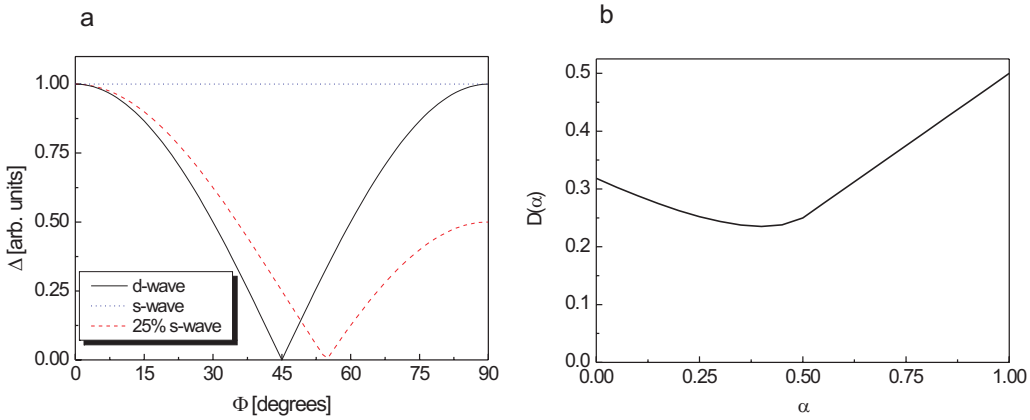

Figure 4.4: Mixture of *d*- and *s*-wave gap: (a) displays the shape of the gap when 25% *s*-wave character (dashed line) is introduced as compared to a pure *d*-wave gap (solid line) and a pure *s*-wave gap (dotted line). (b) illustrates the behavior of the integral of the gap function dependent on temperature. $D(\alpha)$ acquires a minimum for $\alpha_{min} = 0.4$.

An example of how the *s*-wave contribution affects the linewidth is given in Fig. 4.4(b), where the total gap has been kept constant. It is obvious that a *s*-wave contribution of 25% ($\alpha = 0.75$) has only a small effect.

Temperature exponent A of the gap function

The temperature dependence of the gap function can be described by

$$\Delta(\mathbf{k},T) \;=\; \Delta(\mathbf{k})\left(1-\frac{T}{T^*}\right)^A \tag{4.20}$$

From ARPES measurements on optimally doped and underdoped BSCCO [46] we deduce A=4 and A=2, respectively. As shown in Fig 1(c) the size of A has an appreciable effect on the relaxation rate at higher temperatures.

Superconducting volume fraction V

Underdoped high-T_c compounds are inhomogeneous, i.e., there are superconducting and non-superconducting regions with a superconducting volume fraction:

$$V=\frac{v_s}{v_{tot}}<1 \tag{4.21}$$

where v_s denotes the volume of the superconducting regions and v_{tot} stands for the total volume. $\Gamma(T)$ is then the resulting linewidth as a function of temperature:

$$\Rightarrow \Gamma(T) \;=\; \Gamma_s(T)\cdot V+\Gamma_n(T)\cdot(1-V) \tag{4.22}$$

Such a phase separation which was clearly observed e.g. by neutron crystal-field spectroscopy in $ErBa_2Cu_3O_x$ ($6<x<7$) by Mesot et al. [258, 261], has important consequences for the relaxation rate: the relaxation rate is enhanced predominantly at low temperatures due to the Korringa behavior of the non-superconducting regions as visualized in Fig. 1(d).

Gapless Fermi arcs

Norman et al. detected the existence of gapless Fermi-arcs in underdoped BSCCO [262]. Their ARPES experiments revealed that on cooling the sample, the pseudogap opens up at different temperatures for different points in momentum space. More specifically, the point nodes of the d-wave gap function break up into disconnected arcs which grow in size gradually from T_c to T^*. Since this effect was only observed at a few selected temperatures, we assumed in our model calculation a linear evolution of the size of the gapless arcs with temperature. Gapless Fermi arcs open additional relaxation channels in the pseudogap region, hence the interaction is suddenly increased for $T>T_c$. This results in a kink of the linewidth at T_c.

Higher harmonics of the gap function

ARPES experiments performed by Mesot et al. [10] revealed the existence of higher d-wave harmonics of the gap function in the underdoped region of BSCCO. The gap function has then the form

$$\Delta(\mathbf{k})\equiv\Delta(\phi)=\Delta_0[Bcos(2\phi)+(1-B)cos(6\phi)],\qquad 0\le B\le 1 \tag{4.23}$$

For underdoped BSCCO (T_c = 68 K) Mesot et al. found B=0.84, which is significantly below the value B=1 for the optimally doped and overdoped BSCCO [10]. Schnyder et al. confirmed these experimental results in their theoretical work using a fermiology approach [263].
The $cos(6\phi)$ term in the Fermi surface harmonics can be shown to be closely related to the tight-binding function $cos(2k_x) - cos(2k_y)$, which represents next nearest neighbor interaction. In the same way $cos(2\phi)$ is closely related to the nearest-neighbor interaction. The parameter $B < 1$ enhances the relaxation rate in the whole temperature range as visualized in Fig. 1(f).

Comparison of various models

As illustrated in Fig. 4.4 the variation of different parameters of the gap function influences the linewidth in a different manner.
The above presented models can be classified in three categories:

- models based on different features of the gap function at zero temperature: models (a), (b), and (f) in Fig. 4.4.
- models concerning the temperature behavior of the gap: models (c) and (e) in Fig. 4.4.
- model referring to special features in real space, such as phase separation, see Fig. 4.4 (d).

It is worth mentioning that both models (d) and (f) lead to a significant increase of the linewidth at low temperatures. Note that in model (d) this effect is produced by an inhomogeneity of the sample, i.e. a real space effect, whereas in model (f) the relaxation is enhanced due to a change in the gap function, i.e. a reciprocal space effect.
Furthermore, the model (c) concerning temperature effects of the gap function changes the relaxation rate predominantly at temperatures near the closing of the pseudogap, while the low-temperature behavior remains almost unaffected.

We will discuss in section 5.6.3. which models are appropriate and consistent with our relaxation data.

4.4 Experimental data acquisition

In this section we illustrate the steps how we obtained the relaxation data from the raw time-of-flight data.

4.4.1 Data evaluation: energy spectra

As explained in Chapter 3, all the experiments investigating the relaxation rate of Ho@LSCO were carried out on the high-resolution time-of-flight spectrometer FOCUS. The first step of the analysis is to convert the raw data from the time channels to the

energy transfer using the software "Nathan". This program offers the possibility to correct the data for absorption, detector efficiency, background, and detailed balance effects according to standard procedures.

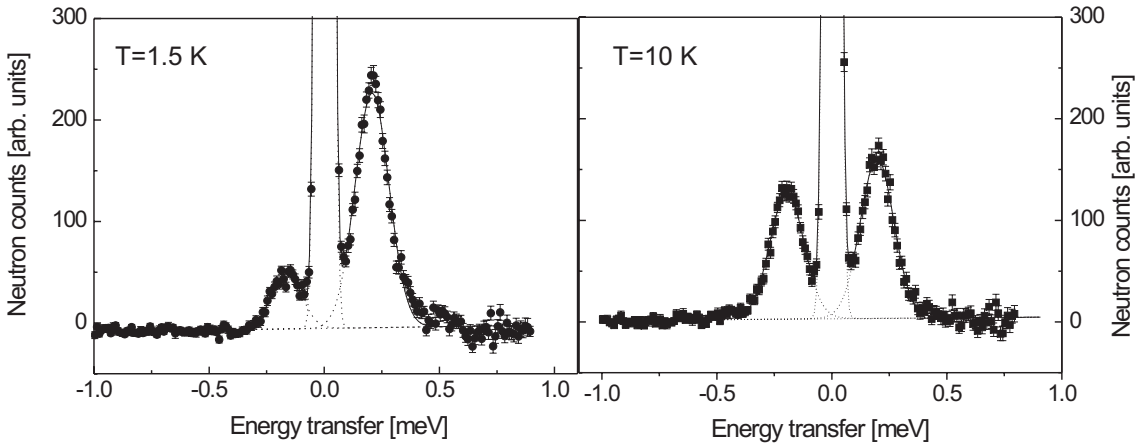

Figure 4.5: Energy spectrum of neutrons scattered from $La_{1.71}Sr_{0.25}Ho_{0.04}Cu^{18}O_4$ at T=1.5 K (left panel) and T=10 K (right panel) as taken on the time-of-flight spectrometer FOCUS at SINQ. The solid line is a fit to the data which accounts for the relaxation as described in the text. The dotted lines illustrate the subdivision of the energy spectrum into the Stokes and anti-Stokes crystal-field transitions as well as the elastic line.

A typical example of an energy spectrum of neutrons is shown in Fig. 4.5 for the case of $La_{1.71}Sr_{0.25}Ho_{0.04}Cu^{18}O_4$ at two different temperatures T=1.5 K and T=10 K. The inelastic signals at energy transfers $\hbar\omega \approx \pm 0.2$ meV correspond to the lowest-lying ground-state crystal-field transitions. The spectrum nicely illustrates the principle of detailed balance:

$$S(\mathbf{Q}, -\omega) = exp\left(\frac{\hbar\omega}{k_B T}\right) S(\mathbf{Q}, \omega) \tag{4.24}$$

where $S(\mathbf{Q}, \omega)$ denotes the scattering function. The integrated intensity of the peak on the energy gain side, the so-called anti-Stokes process, is smaller than the one on the energy loss side by the exponential factor. The thermal energy $k_B T$ at 10 K is sufficient to populate the first excited level of the crystal-field scheme.
The application of pressure leads to a considerable intensity loss due to the pressure cell which is large as compared to the amount of sample and therefore strongly influences the scattering cross section: the ratio of the integrated intensity of the elastic line to the one of the inelastic signal originating from the sample is enhanced by at least a factor of 2. Furthermore the elastic line is significantly broader because multi-scattering processes become important due to the large volume of the pressure cell.
Thus it is of crucial importance to subtract the spectrum of the empty pressure cell which is responsible for the background and to determine the position of the elastic line by vanadium. Fig. 4.6 illustrates the effect of the background subtraction for example at 10 K, which is necessary before one can start to analyze the data.

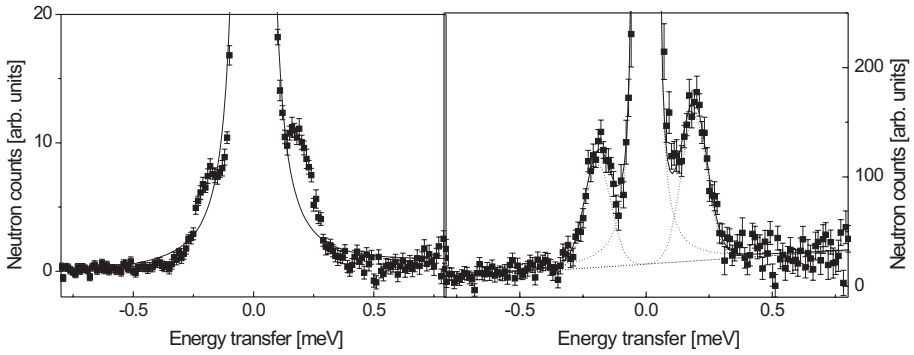

Figure 4.6: Energy spectrum of neutrons scattered from $La_{1.81}Sr_{0.15}Ho_{0.04}Cu^{16}O_4$ at T=10 K and p=1.2 GPa. In the left panel the background due to the pressure cell which is responsible for the broad elastic line has not been subtracted yet. The inelastic signal associated to the lowest crystal-field transition almost vanishes in the elastic line. The right panel displays the same data after the background subtraction, where the results for the linewidth were taken from. The solid line is a fit to the data which includes the relaxation as described in the text. The dotted lines illustrate the subdivision into the crystal-field transitions and the elastic line.

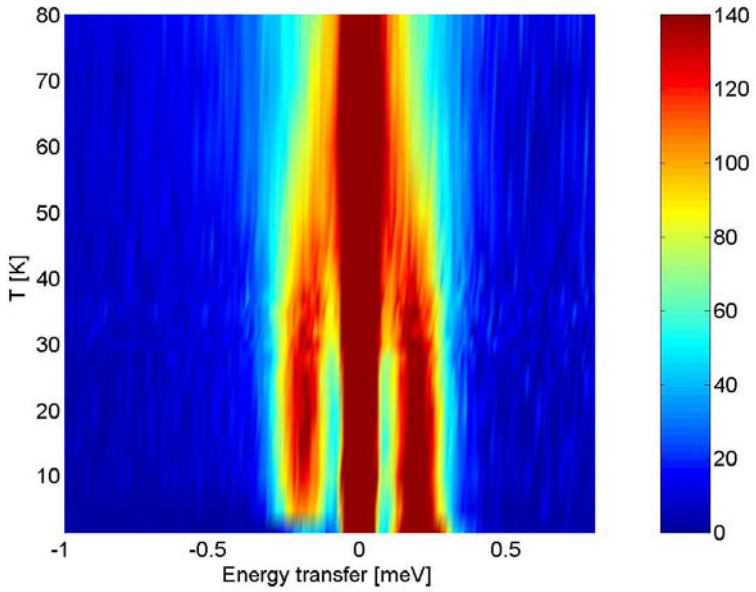

Figure 4.7: Intensity contour plot visualizing the temperature renormalization of the energy spectra taken for $La_{1.71}Sr_{0.25}Ho_{0.04}Cu^{18}O_4$.

4.4.2 Data treatment: Results for the linewidth data

Fig. 4.5 shows typical energy spectra of neutrons scattered from $La_{1.71}Sr_{0.25}Ho_{0.04}Cu^{18}O_4$ at T=1.5 K and 10 K. There are strong ground-state crystal-field transitions for both the Stokes and the anti-Stokes process at an energy transfer

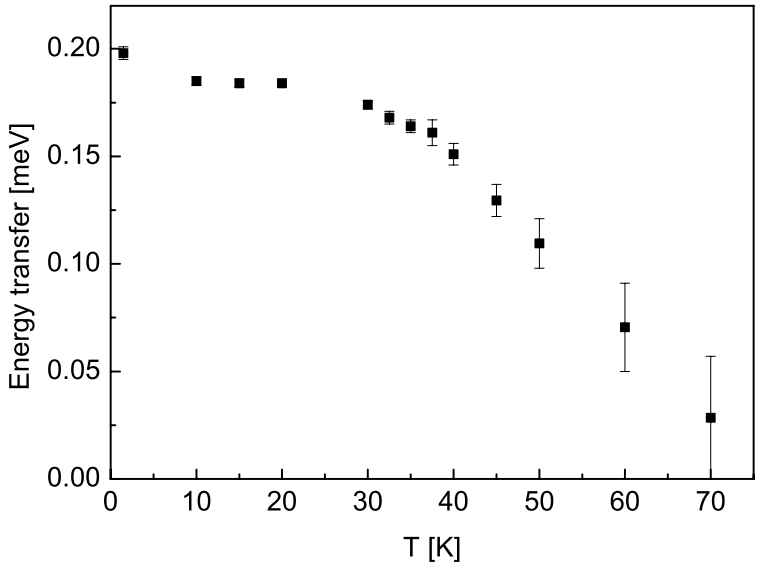

Figure 4.8: Renormalization effects of the lowest ground-state crystal-field transition in $La_{1.71}Sr_{0.25}Ho_{0.04}Cu^{18}O_4$.

$\hbar\omega \approx \pm 0.2$ meV. The width of the crystal-field transitions being typically 140 μeV is considerably broader than the instrumental resolution of 50 μeV at the given wavelength. The spectra obtained for the other $La_{1.96-x}Sr_xHo_{0.04}CuO_4$ compounds are similar.
The lines in Fig. 4.5 are the result of a least-squares fitting procedure in which the crystal-field transitions were described by a convolution of a temperature-independent Gaussian function (corresponding to the residual low-temperature width) with a temperature-dependent Lorentzian function describing the intrinsic linewidth due to the interaction with the charge carriers.
Not only the linewidth, but also the energy of the crystal-field transitions is affected by temperature: the renormalization of the crystal-field transitions due to relaxation effects is illustrated in Fig. 4.7 which visualizes the decrease of the energies as well as the increase of the linewidths of the crystal-field transitions upon raising the temperature. The energy position of the crystal-field transition as a function of temperature is displayed in Figs. 4.8 and 4.8. Similar energy spectra were observed for all the compounds under investigation.

4.5 Sample characterization: Discussion of the diffraction experiments and AC-susceptibility measurements

We present the results of the neutron diffraction experiment on HRPT, which served to reveal the symmetry of the structure of the optimally doped Ho@LSCO. AC-susceptibility measurements were used to obtain the superconducting transition temperature T_c as a function of doping, pressure and isotope substitution.

4.5.1 Symmetry investigation of the structure

We investigated $La_{1.81}Sr_{0.15}Ho_{0.04}Cu^{18}O_4$ by means of neutron diffraction experiments at 15 K and 100 K as well as at 250 K, the results are shown in Fig. 4.9. The experimental data were refined by using the Rietveld method, yielding a good agreement between the observed and the calculated intensities, see the blue line in Fig. 4.9.
It turned out that at 250 K $La_{1.81}Sr_{0.15}Ho_{0.04}Cu^{18}O_4$ is in the HTT phase like pure optimally doped LSCO [23] (panel (a) of Fig. 4.9). But for temperature $T \leq 100$ K, in both data sets clearly more Bragg peaks occur indicating a reduction of the symmetry. The diffraction pattern at these low temperatures correspond to the low-temperature orthorhombic (LTO) phase (space group *Cmca*) (panel (b) of Fig. 4.9).
At all temperatures the refined parameters are in good agreement with the results for pure $La_{1.81}Sr_{0.15}CuO_4$ reported by Radaelli et al. [23]. The fact that no structrual phase transition occurs, means that a content of 4% holmium did not induce a phase transition from LTO to a low-temperature tetragonal (LTT) structure.

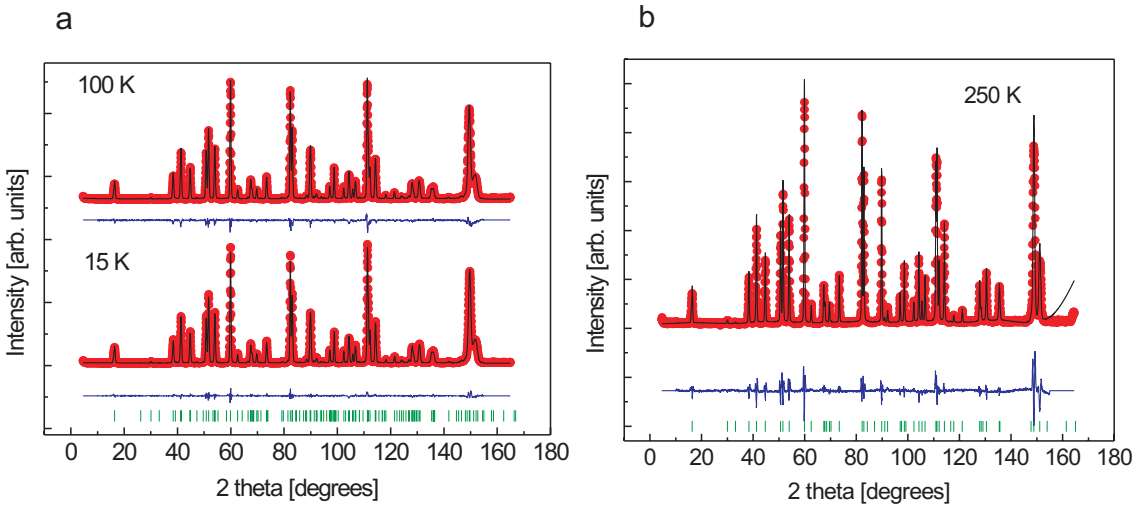

Figure 4.9: Neutron diffraction patterns for $La_{1.81}Sr_{0.15}Ho_{0.04}Cu^{18}O_4$: At T=15 K and 100 K (a) the sample is in the LTO phase, while the HTT phase was obtained for 250 K (b). The experimental data are shown by red circles, the solid line is the result of the Rietveld refinement. The difference between the calculated and observed patterns is given by the blue line. The bars denote the Bragg reflections.

4.5.2 Results for the superconducting transition temperature T_c

We performed AC-susceptibility measurements in order to investigate the doping, isotope and pressure dependence of T_c for all samples. An example is shown in Fig. 4.10 for the case of $La_{1.85}Sr_{0.11}Ho_{0.04}CuO_4$. Since a superconductor expels an external magnetic field when cooled below T_c (diamagnetic signal), the sudden decrease of the susceptibility χ' indicates the transition into the superconducting state.
In order to determine T_c consistently, we performed a linear fit in the range, where the slope $d\chi'/dT$ is nearly constant, and we defined T_c as the temperature where the line

Table 4.2: Pressure effect on T_c

x	dT_c/dp [K/GPa]	$dln(T_c)/dp$ [GPa^{-1}]
0.11	+1.2±0.6	0.094
0.15	+2.7±0.6	0.083
0.2	+2.5±0.9	0.092

associated to the fit of the diamagnetic signal intersects the straight line extrapolated from the normal state signal. These linear fits are shown as solid lines in Fig. 4.10.
As for the doping dependence, the results are given in Table 4.5. We found that $T_c(x)$ is systematically lower than the values obtained for pure LSCO [23] at all doping levels. This effect is associated with the content of 4% holmium which induces magnetic pair breaking effects [264, 265].

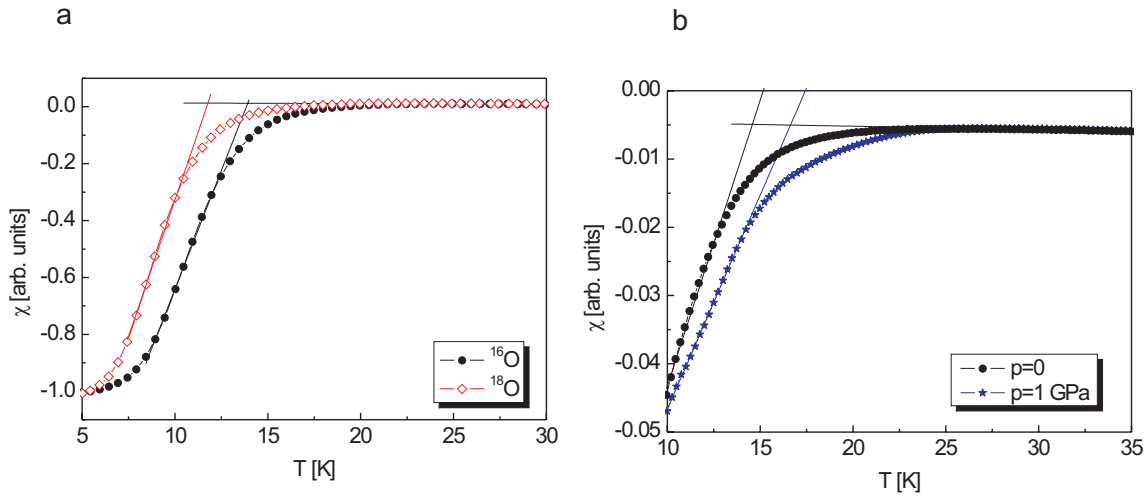

Figure 4.10: Dynamic susceptibility measurements: (a) shows the oxygen isotope effect on T_c for $La_{1.85}Sr_{0.11}Ho_{0.04}CuO_4$ (b) illustrates the pressure effect on T_c the same compound. The solid lines correspond to a linear fit as outlined in the text.

We also determined the pressure effect on T_c at various doping levels (x=0.11, 0.15 and 0.2). We observed that T_c is enhanced upon application of pressure in the doping range $0.11 \leq x \leq 0.2$. This result is in qualitative agreement with literature data [233]. However, Murayama et al. found that the pressure coefficient $d\,ln(T_c)/dp$ is largest in the underdoped region, namely 0.138 at x=0.08 and it decreases down to 0.056 at x=0.2, respectively. However, our measurements revealed that $d\,ln(T_c)/dp \approx 0.09$ and it does not change substantially with doping, see Table 4.2.

4.6 Crystal-field excitations in $La_{1.96-x}Sr_xHo_{0.04}CuO_4$

We observed that the lowest-lying crystal-field transition exhibits a doping dependence: $\hbar\omega$ slightly increases with raising doping, see Table 4.5. Also the application of pressure

leads to an enhancement of $\hbar\omega$ up to ± 0.191 meV. Table 4.5 also gives the residual low-temperature linewidth, which was found to increase with doping.
With increasing temperature the crystal-field transitions renormalize due to relaxation effects: the energy $\hbar\omega$ decreases as shown in Fig. 4.8 and simultaneously the linewidths increase. This opposite behavior of the energy $\hbar\omega$ and the linewidth is nicely displayed in Fig. 4.7. It can be qualitively explained by the theory of Becker-Fulde-Keller [199, 200], who studied the relaxation behavior of crystal-field excititations in rare-earth compounds.

4.6.1 Results for the crystal-field parameters

The experimental data taken on FOCUS revealed only the lowest-lying crystal-field transition. In order to establish the upper energy limit of the crystal-field excitations of $La_{1.96-x}Sr_xHo_{0.04}CuO_4$ experimentally and verify the extrapolated level scheme of Section 4.2.2, the measurements on the MARI spectrometer were needed. Fig. 4.11 displays a summary of the data taken at 14 K in the form of a contour plot.

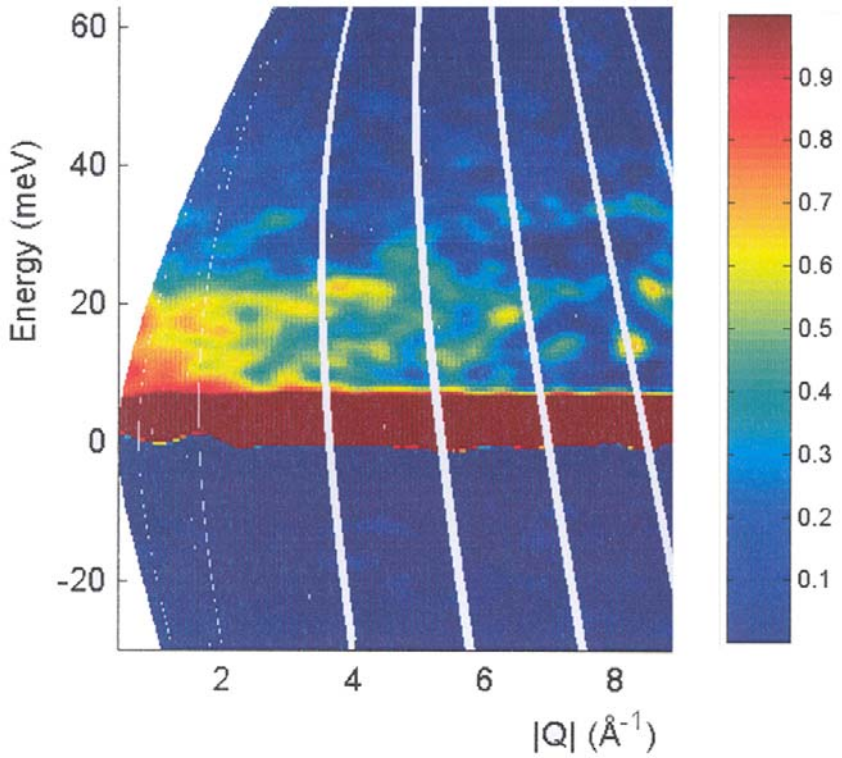

Figure 4.11: Contour plot of the magnetic excitations obtained at 14 K in $La_{1.81}Sr_{0.15}Ho_{0.04}Cu^{18}O_4$ on MARI. The nonmagnetic scattering measured for $La_{1.85}Sr_{0.15}Cu^{18}O_4$ has been subtracted.

Magnetic scattering is most prominent at small values of the scattering vector Q, thus we conclude that ground-state crystal-field excitations occur at energies lower than 25 meV. The energy spectrum in the low-energy window ($\Delta E < 10$ meV) exhibits just one inelastic peak at approximately 0.2 meV corresponding to the lowest-lying crystal-field transition.

Thus these data are in full agreement wit the extrapolation scheme mentioned in Section 4.2.2 and the assumption to analyze the linewidth of this crystal-field excitation within a two-level approximation (Eq. 4.11) is justified.

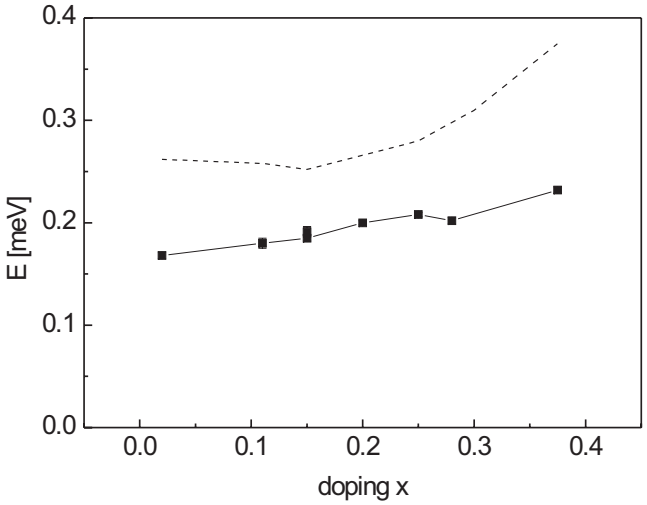

Figure 4.12: Ground-state crystal-field splittings observed for Ho@$La_{2-x}Sr_xCuO_4$ (squares and solid curves). The values extrapolated from the structural changes alone are indicated by the dashed curves.

Figure 4.12 shows the evolution of the observed ground-state crystal-field splittings $E_{obs}(x)$ whose sizes raise continuously with increasing Sr doping x. The figure also shows the modification of the crystal-field splittings $E_{cal}(x)$ calculated from the structural changes on the basis of the procedure described above. We recognize that the structural changes alone cannot reproduce the experimental data in a broad doping range ($0.1 < x < 0.3$). Clearly the charge transfer induced by Sr doping x is responsible for these deviations, i.e., according to Eq. 2.12 additional charges $\delta(x)$ are transferred to the oxygen sites. The charge transfer $\delta(x)$ can be estimated according to

$$\frac{E_{obs}(x)}{E_{obs}(x=0.02)} = [1+\delta(x)]\frac{E_{cal}(x)}{E_{cal}(x=0.02)}. \tag{4.25}$$

The resulting charge transfers $\delta(x)$ are listed in Table 4.3. We recognize that the values of $\delta(x)$ follow nicely the x-dependent changes of the slope of the Korringa line $d\Gamma/dT$ which is a measure of the density-of-states of the charge carriers. Moreover, a similar correspondence follows from a comparison of the values of $\delta(x)$ with the electronic specific heat coefficients γ [266] which are also directly related to the carrier density. Therefore we conclude that both the observed crystal-field splittings and the observed slopes of the Korringa line are qualitatively consistent with the established picture of charge transfer by doping. For Sr doping up to x=0.20 the charge transfer increases almost linearly, however, this relationship clearly does no longer hold in the heavily overdoped region ($x > 0.20$). Upon application of hydrostatic pressure, the crystal-field transition increases from $\hbar\omega = (\pm 0.185 \pm 0.003)$ at ambient pressure up to $\hbar\omega = (\pm 0.191 \pm 0.005)$ at $p = 1.2$ GPa, which

Table 4.3: Charge transfer $\delta(x)$ and changes of the slope of the Korringa line derived in the present work for Ho@$La_{2-x}Sr_xCuO_4$, in comparison with the electronic specific heat coefficients γ [266]. The values of $\delta(x)$ and $\delta(d\Gamma/dT)(x)$ are normalized to zero for x=0.02.

x	$\delta(x)$	$\delta(d\Gamma/dT)(x)$	$\gamma(x)$ [mJ/mol·K^2]
0.02	0	0	2
0.11	0.09 ±0.03	0.7±0.7	6
0.15	0.14±0.02	1.9±0.7	9
0.20	0.17±0.01	2.2±0.6	14
0.25	0.16±0.01	-0.2±0.7	12.5
0.28	0.03±0.01	-1.3±1.1	11
0.375	-0.03±0.01	-0.7±1.2	-

can be reproduced using the above mentioned extrapolation scheme based on structural parameters [23, 246] alone. Thus there is no charge transfer induced by pressure which is in agreement with the Hall coefficient being independent of pressure [233]. However, the slope of the Korringa line $d\Gamma/dT$ slightly decreases with raising pressure from $(5.8 \pm 0.1)\,\mu$eV/K at ambient pressure down to $(5.2 \pm 0.1)\,\mu$eV/K at 1.2 GPa, which means that j_{ex} is affected by pressure according to Eq. 4.13.

4.6.2 The crystal field as a local probe

Let us now discuss the temperature-independent line-broadening mechanisms. The crystal-field interaction is a local probe and thereby sensitive to local structural distortions around the Ho ions. The nearest-neighboring (La,Sr)-coordination shell around a Ho ion comprises totally eight La and Sr ions, the detailed distribution of La and Sr ions being strongly dependent upon the Sr concentration x.
The La and Sr ionic radii are different, which results in a geometrical distortion; in fact, detailed structural investigations performed by Radaelli et al. [23] show that the lattice parameter a decreases with increasing Sr content x, whereas the lattice parameter c increases at the same time. Therefore, with the crystal field being a local probe, the positions of the crystal-field transitions will be dependent on α at a given doping x.
Assuming the La and Sr ions to be statistically distributed, the following expression gives the probability for a Ho ion having at least one Sr or Ho ion in its coordination shell, which will therefore be distorted:

$$P_\alpha(x) = \sum_{\alpha=1}^{8} p_\alpha(x) \tag{4.26}$$

$$p_\alpha(x) = \binom{8}{\alpha} \cdot \left(\frac{x}{2}\right)^{8-\alpha} \left(1 - \frac{x}{2}\right)^{\alpha} \tag{4.27}$$

Thus the probability that a Ho ion has neither a Sr nor another Ho ion in its coordination shell is given by

Table 4.4: Probability $P(x)$ that a Ho ion has coordination shell which is geometrically distorted due to the presence of at least one Sr or Ho ion.

x	0.11	0.15	0.2	0.25
P_x	0.364	0.464	0.570	0.656

$$\bar{P}(x) = 1 - P(x) = p_0(x) = \left(\frac{x}{2}\right)^8 . \tag{4.28}$$

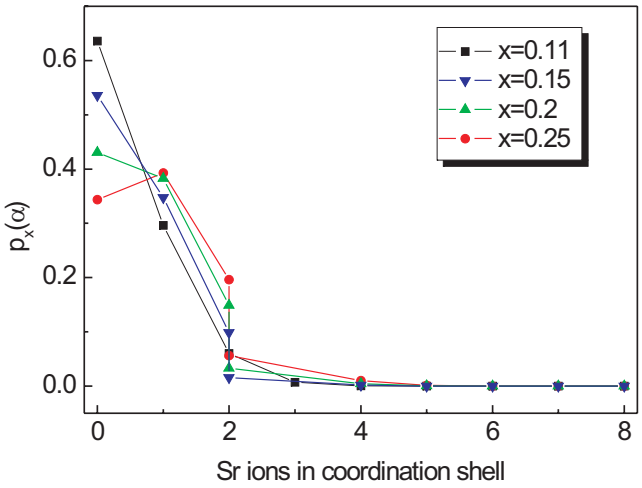

Figure 4.13: Probability $P(x)$ for Ho having a distorted shell for different doping levels.

In these equations the binomial coefficients indicate the multiplicity of possible (La,Sr) configurations. Therefore the probability that a Ho ion experiences a distorted environment is enhanced while doping increases, see Table 4.4 and also Fig. 4.13.
The probability of α Sr or Ho ions being in the coordination shell decreases rapidly with α and the decrease is faster the lower the doping. Therefore we expect the line broadening to be most pronounced at higher doping because of the weighted sum of all the different crystal-field contributions. Indeed the low-temperature residual width is growing with doping and it is 10% larger at x=0.25 than at x=0.11.

4.7 The pseudogap in $La_{1.96-x}Sr_xHo_{0.04}CuO_4$

4.7.1 Experimental results

Fig. 4.14 shows the temperature dependence of the intrinsic linewidths Γ=FWHM for $La_{1.96-x}Sr_xHo_{0.04}Cu^{16}O_4$ at different doping levels (x=0.11, 0.2 and x=0.25). They all

show a qualitatively similar behavior: the linewidth is rather small at low temperatures, then it raises with increasing slope $d\Gamma/dT$ up to about 70-80 K and 45-50 K for the underdoped and overdoped doping levels, respectively; from thereon the slope $d\Gamma/dT$ is reduced and remains constant according to the Korringa law. From these observations we can immediately conclude that the pseudogap opens at approximately 80 K and 45-50 K in the underdoped and overdoped region, respectively.
The comparison to the raw linewidth data taken for the ^{18}O compound also suggest a positive oxygen isotope effect on the pseudogap temperature T^*, since the turnover into the Korringa regime seems to occur for the ^{18}O data at a higher temperature than for the ^{16}O data. Similar data were obtained for $La_{1.81}Sr_{0.15}Ho_{0.04}CuO_4$ under pressure, see Fig 4.15. The experimental data reveal that T^* as well as ΔT^* decreases with increasing doping and that ΔT^* remains positive, whereas the application of hydrostatic pressure slightly lowers T^* as can be seen in Fig 4.15. However, due to the limited number of linewidth data, the quantitative assessment of the pseudogap temperature T^* and the oxygen isotope effect ΔT^* needs some more detailed considerations of the linewidth in the superconducting state as well as in the pseudogap state.

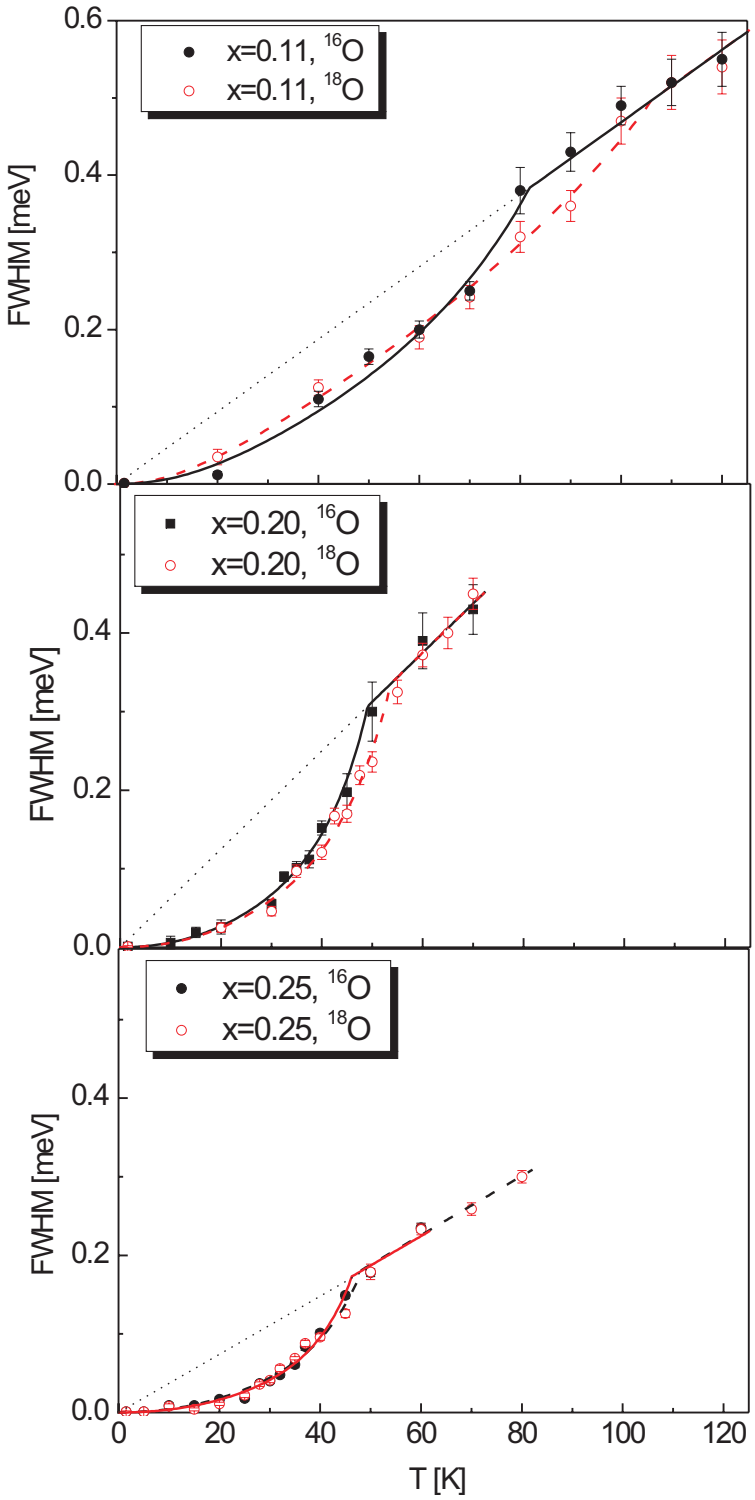

Figure 4.14: Temperature dependence of the intrinsic linewidth (FWHM) corresponding to the lowest ground-state crystal-field transition in $La_{1.96-x}Sr_xHo_{0.04}CuO_4$ at different doping levels: x=0.11 (upper panel), x=0.2 (middle panel) and x=0.25 (lower panel). The full circles correspond to the ^{16}O compound, whereas the open circles denote the ^{18}O compound. The full and dashed lines are the results of a least-squares fitting procedure as described in the text. The dotted lines indicate the Korringa behavior below T^*.

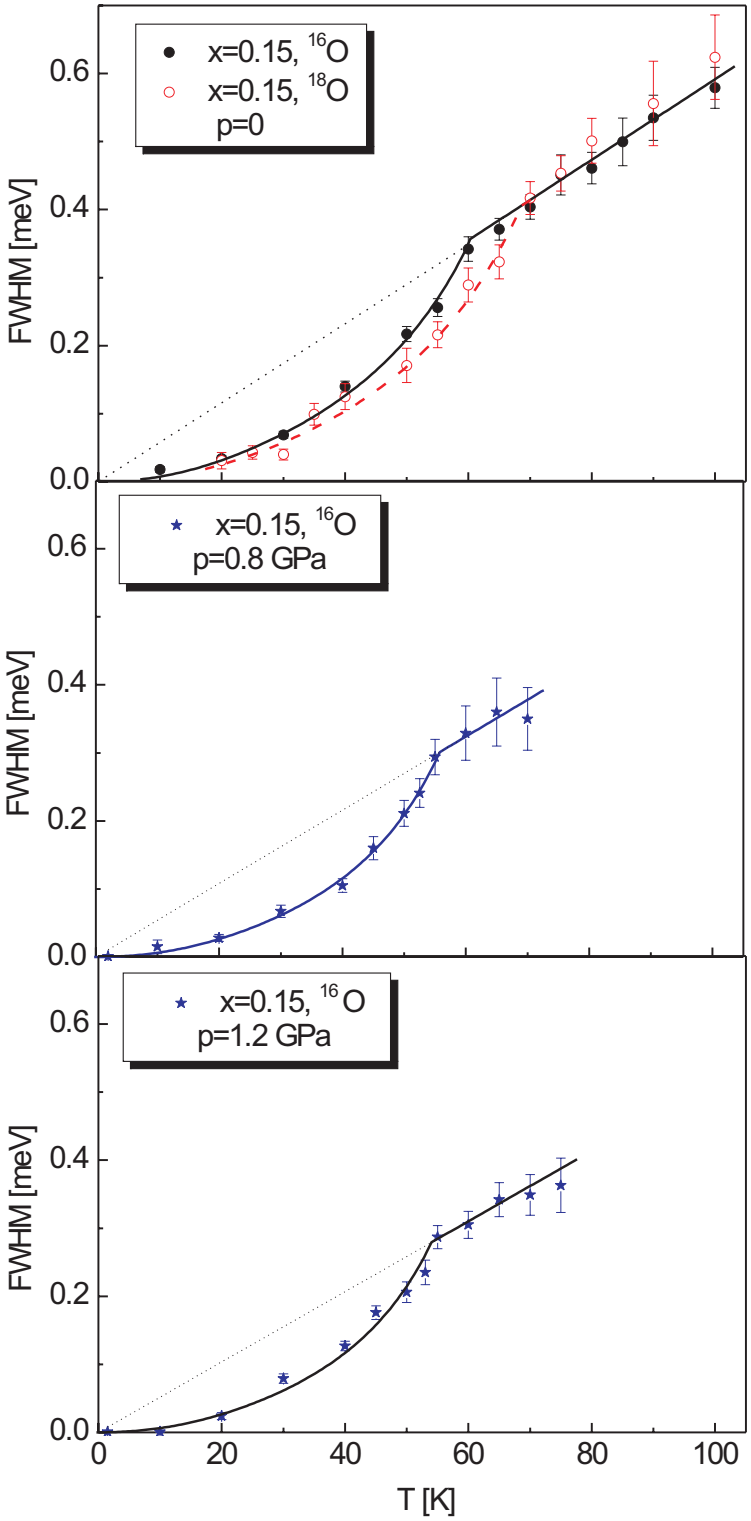

Figure 4.15: Temperature and pressure dependence of the intrinsic linewidth (FWHM) corresponding to the lowest ground-state crystal-field transition in $La_{1.81}Sr_{0.15}Ho_{0.04}Cu^{16}O_4$. The upper panel shows the relaxation rate at ambient pressure for the ^{16}O and the ^{18}O compound, whereas the middle and lower panel display the data taken for the ^{16}O compound at 0.8 and 1.2 GPa, respectively. The full lines are the results of a least-squares fitting procedure as described in the text. The dotted lines indicate the Korringa behavior below T^*.

Table 4.5: Superconducting transition temperature T_c and pseudogap temperature T^* determined for $La_{1.96-x}Sr_xHo_{0.04}CuO_4$. Also the energy of the lowest crystal-field transition $\hbar\omega$ and its residual Gaussian linewidth Γ_g at 1.5 K is given.

x	$T_c(O^{16})$ [K]	$T_c(O^{18})$ [K]	$T^*(O^{16})$[K]	$T^*(O^{18})$ [K]	$\hbar\omega_{CEF}$ [meV]	Γ_g [meV]
0.11	13.9±0.3	11.7±0.6	82.2±1.2	103.5±4	0.18±0.005	0.158±0.004
0.15	32.5±0.5	30.8±0.8	61.0±0.5	70.0±1.2	0.185±0.003	0.16±0.004
0.2	28.4±0.6	27.3.1±0.6	49.2±0.7	53.7±0.6	0.20±0.002	0.164±0.005
0.25	10.1±0.2	9.8±0.2	46.5±0.5	48.4±1.4	0.208±0.002	0.174±0.004

We applied the fitting procedure introduced in Section 4.3.2 which describes the linewidth below T^* by a d-wave gap function according to Eqs. 4.14 and 4.16. Above T^* the linewidth is governed by Eq. 4.13. The independently adjustable parameters are then T^*, Δ_0, and the slope $d\Gamma/dT$ of the Korringa line. The results of the fitting procedures are shown by solid lines in Fig. 4.14 and 4.15.
We also investigated the relaxation rate of the non-superconducting samples $La_{1.96-x}Sr_xHo_{0.04}CuO_4$ (x=0.28 and x=0.375), the results are illustrated in Fig. 4.16. Clearly these data behave in a manner different from the data of the superconducting samples, there is no exponential drop below the straight line

We now turn our attention to the discussion of the results presented above.

4.7.2 Discussion of the doping dependence of the pseudogap temperature

We find a decrease of T^* from 82.2±1.2 K to 49.2±0.7 K down to 46.5±0.5 K for x=0.11, x=0.2 and x=0.25, respectively. The optimally doped sample (x=0.15) has already been investigated earlier [90] and T^* turned out to be 61.0±0.5 K, which coincides with the charge ordering temperature [227]. The results are summarized in Table 4.5, see also Refs. [267, 268]. The doping dependence of T^* established from our experiments shows the widely accepted decrease with growing Sr content. In particular, our results up to optimal doping are in good agreement with susceptibility, resistivity and specific heat measurements [36] as well as NQR experiments [227].
For the overdoped region the situation concerning T^* is controversial. For x=0.20 our value of T^* ≈50 K is confirmed by heat capacity [36, 269] and resistivity [36] data, whereas NQR data [227] give a slightly reduced T^* ≈35 K. For $x \geq$0.22, however, the analysis of heat capacity data [36] suggests the T^* line to merge with the T_c line. Furthermore, by analyzing the resistivity data, Tallon and Loram [270] conclude that the T^* line intersects the T_c line already at $x = 1/8$ and vanishes for $x \geq$0.18. This means that our value of T^* ≈45 K for x=0.25 could not be confirmed by any other experiments so far.

The data taken for $La_{1.78}Sr_{0.28}Ho_{0.04}CuO_4$ were analyzed by a linear fit according to the

Korringa law 4.13. The linewidth deviates from the high-temperature behavior around 42 K, which indicates according to the previous considerations the opening of the pseudogap. This means that a pseudogap exists, even though the sample does not become superconducting as has been demonstrated by AC-susceptibility measurements. But it is possible that this result is a signature of superconducting fluctuations because a doping of 28% Sr is very close to the superconducting phase boundary. In the case of $La_{1.585}Sr_{0.375}Ho_{0.04}CuO_4$ we also observe the opening of a pseudogap in the same temperature range, namely around 40 K. Thus we conclude that at both doping levels preformed pairs exist, which never exhibit phase coherence, i.e. bulk superconductivity does not occur. Obviously the data sets cannot be fitted with the procedure introduced in Section 4.3.2, which is based on the properties of the superconducting gap, because long-range phase coherence does not occur and consecutively there is no superconducting gap.

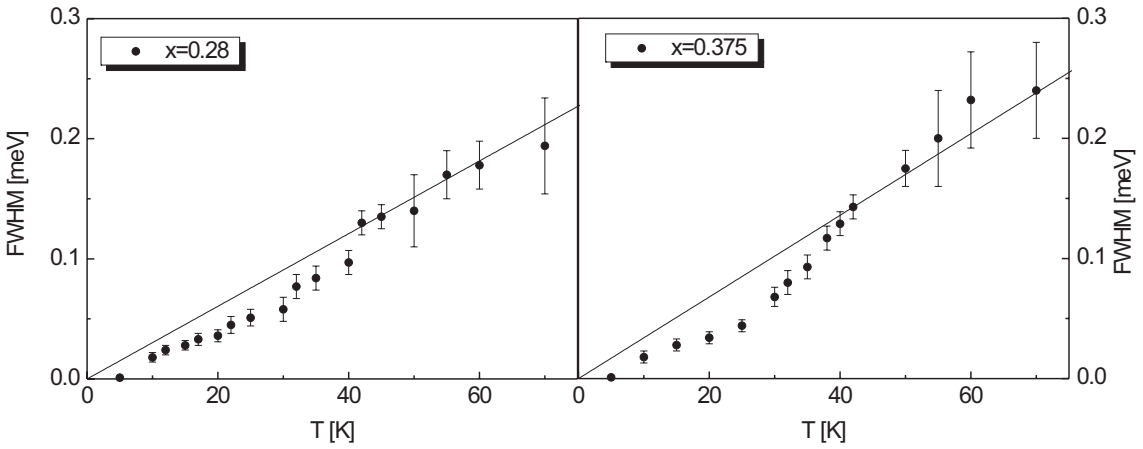

Figure 4.16: Relaxation data for the non-superconducting compounds $La_{1.96-x}Sr_xHo_{0.04}CuO_4$ with $x = 0.28$ close to the superconducting phase boundary (left panel) and x=0.375 (right panel).

4.7.3 Discussion of the oxygen isotope and pressure effect on T^*

The oxygen isotope substituted samples show the same behavior as their ^{16}O counterparts except that T^* is systematically higher. The isotope effect ΔT^* is most pronounced at the lowest doping level where the ratio $\Delta T^*/T^*(^{16}O)$ equals 26%, it decreases to 14% and 10% at x=0.15 and x=0.2, respectively and finally vanishes in the heavily overdoped regime. The results are summarized in Table 4.5, see also Refs. [267, 268].
Fig 4.15 illustrates the relaxation data taken for $La_{1.81}Sr_{0.15}Ho_{0.04}CuO_4$ at ambient pressure and at 0.8 as well as at 1.2 GPa. It is obvious to the eye that T^* decreases with pressure. The quantitative analysis yielded a pressure-induced shift of the pseudogap temperature in optimally doped LSCO of $\Delta T^* = (-5.2 \pm 2.8)$ K and $\Delta T^* = (-6.9 \pm 2.8)$ K at p=0.8 GPa and p=1.2 GPa, respectively. From these results we derive the pressure effect on T^* to be $\partial T^*/\partial p$=(-5.9±1.6) K/GPa. Our result is in reasonable agreement

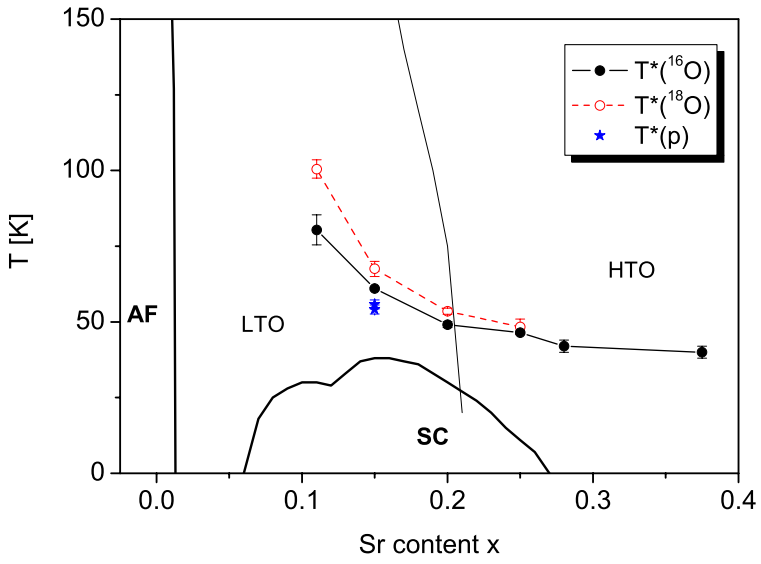

Figure 4.17: Values for T^* obtained by neutron crystal-field spectroscopy. The full black circles and the red open circles stand for the ^{16}O and ^{18}O compound, respectively. The blue stars denote the values obtained under pressure (0.8 GPa and 1.2 GPa).

with $dT^*/dp \approx$-10 K/GPa determined for slightly underdoped $YBa_2Cu_4O_8$ in NQR measurements [94]. We can definitely rule out an increase of T^* with pressure as has been reported for optimally doped $Hg_{0.82}Re_{0.12}Ba_2Ca_2Cu_3O_{8+\delta}$ from the analysis of resistivity measurements [96].
The existence of an oxygen isotope effect is believed to originate from a Q_2-type Jahn-Teller phonon mode in the CuO_2 layer, which is further supported by the absence a copper isotope effect in the optimally doped compound [90]. In a first approximation the phonon energy $h\nu$ of the active phonon mode is inversely proportional to the square root of the oxygen mass. Thus we find

$$\frac{1}{h\nu}\frac{\partial(h\nu)}{dM_O} = -0.057 \tag{4.29}$$

upon oxygen isotope substitution, whereas the application of pressure leads to

$$\frac{1}{h\nu}\frac{\partial(h\nu)}{\partial p} = -\gamma\kappa = +0.014 \tag{4.30}$$

with $\gamma \approx 2$ Grüneisen parameter and $\kappa = -6.8 \cdot 10^{-3}$ GPa^{-1} the volume compressibility [246].
The opposite effects of isotope substitution and pressure on the phonon energy $h\nu$ implies an opposite effect on T^* within models based on phonon-mediated mechanisms [228, 229, 230]: We start from a thermodynamic relation, which interrelates the change in T^* to the change in the phonon frequency $h\nu$:

$$\frac{\Delta T^*}{T^*} \equiv \beta\frac{\Delta h\nu}{h\nu}. \tag{4.31}$$

From oxygen isotope substitution ($\Delta T^* = (+10 \pm 3)$ K [89]) we deduce the scaling factor $\beta = -2.9 \pm 1.0$.
The application of pressure in terms of Eq. 4.31 reads

$$\frac{\partial(lnT^*)}{\partial p} \approx \beta \frac{\partial(lnh\nu)}{\partial p} = -\beta\gamma\kappa, \tag{4.32}$$

which yields a pressure effect of $\partial T^*/\partial p = (-2.5 \pm 0.9)$ K/GPa [271].

These semi-quantitative considerations explain the opposite effects of isotope substitution and pressure. However, lattice fluctuations alone cannot explain the measured pressure effect $\partial T^*/\partial p$, they account only for half of the experimentally observed decrease of T^*. We suggest that the second half of $\partial T^*/\partial p$ arises from the pressure dependence of antiferromagnetic fluctuations, because pressure modifies the structure, and therefore affects the superexchange between the copper ions. Unfortunately there are no experimental data or theoretical predictions available on the pressure dependence of the superexchange coupling J and the hopping integral t being the main ingredients of the tJ-model [16, 185], which is based on antiferromagnetic spin fluctuations.
The tendency for T^* being enhanced (decreased) upon isotope substitution (application of pressure) can be explained by a hybridization effect within Gor'kov's two-component model for the cuprates [272]. In this model T^* is assigned to the transition into a phase-separated state characterized by a local and an itinerant component. A Jahn-Teller polaron-like mechanism [239] induces a narrowing of the polaronic band V_p

$$\tilde{V}_p = V_p exp\left(-\frac{E_{JT}}{h\nu_p}\right). \tag{4.33}$$

Through the mixing with itinerant charge carriers, the local centers acquire an effective kinetic energy. Therefore hybridization effects tends to lower and even eliminate the first-order transition to phase separation. An increase in T^* as observed for isotope substitution, tentatively correlates with the decrease in hybridization.

Opposite behavior of T_c and T^*: It is worth noting that T_c and T^* show an opposite trend under pressure , but also upon isotope substitution: T_c decreases when ^{16}O is exchanged by ^{18}O, as is expected qualitatively from a BCS-behavior, whereas T^* is enhanced.
T_c and T^* both follow the tendency of the phonon frequency, but with opposite sign. Thus in Eq. 4.31 the scaling factor β have opposite signs:

$$\begin{aligned} T^* &: \quad \beta < 0, \\ T_c &: \quad \beta > 0 \end{aligned} \tag{4.34}$$

4.7.4 Results for the nature of the gap function

To our knowledge there are direct experimental results available neither on the nature of the gap function nor on the temperature evolution of the pseudogap in LSCO. Below we will outline some characteristics of the superconducting gap function based on our

relaxation data, and we will discuss the plausibility of the different models described in Section 4.3.2. These considerations, however, have to be considered with caution, since there are too many parameters and effects which influence the temperature dependence of the relaxation rate. Moreover, many parameters have a similar effect on the relaxation data, so that unambiguous conclusions cannot be made. We emphasize that our model calculations were motivated by the need to have a mathematical tool to describe the relaxation data rather than to obtain a detailed insight into the nature of the gap function. This is best exemplified by the model parameter Δ_0 whose value is always slightly below the empirical rule $\Delta_0 \approx 2k_BT$ established for LSCO [36].
Fig. 4.18 presents a summary of the relaxation data, where the data are plotted in reduced units $\Gamma(T)/\Gamma(T^*)$ as a function of T/T^*. It is eye-catching that the shape of the electronic excitation spectrum in the pseudogap region is dependent on doping: the smaller the doping the less gapped the relaxation data. The reasons for that experimental result can be manifold.

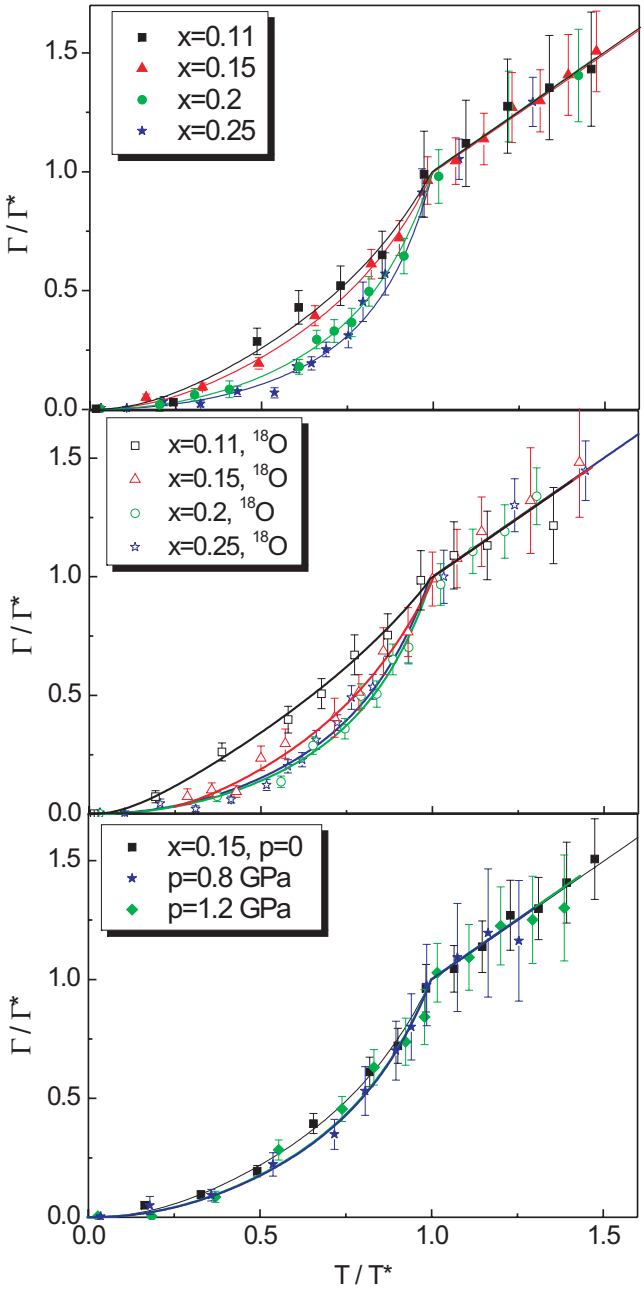

Figure 4.18: The relaxation data for Ho@LSCO observed in the present work are shown in reduced units Γ/Γ^* vs. T/T^* for different doping levels for the ^{16}O compound (upper panel), the ^{18}O compound (middle panel) and for the application of pressure (lower panel).

Table 4.6: Fitting parameters for $La_{1.96-x}Sr_xHo_{0.04}CuO_4$ using a non-superconducting volume fraction V and the inclusion of higher harmonics $1-B$ as explained in the text.

x	Δ_0 [K]	$1-\alpha$	$d\Gamma/dT$ [μeV/K]	B	V
0.11	1.60±0.2	0.25	4.7±0.2	0.85	0.75
0.15	1.40±0.2	0.15	5.9±0.2	0.95	0.9
0.20	1.55±0.1	0.10	6.2±0.1	1	1
0.25	1.5±0.1	0.0	3.8±0.2	1	1

There are three main characteristics in the doping dependence of the relaxation rates displayed in Fig. 4.18:

- The doping affects Γ in the whole temperature range $0 < T < T^*$. Such a behavior is inconsistent with a variation of the temperature exponent A of the gap function, see Fig. 4.4 (c). But it can be attributed either to changes in the gap amplitude Δ_0, an s-wave contribution α to the gap function, changes in the superconducting volume fraction V, or the contribution of higher harmonics B to the d-wave gap as illustrated in Figs. 4.4 (a), (b), (d), or (f), respectively.

- The relaxation rates become finite even at very low temperatures, thus we can rule out a pure s-wave gap for all doping levels, see Fig. 4.4 b.

- Since there is no clear indication of any anomalies around T_c in the relaxation rate (partly due to the lack of a sufficient number of data points), we do no longer consider the picture of gapless Fermi arcs (see Fig. 4.4 e) which, however, were used in the interpretation of the relaxation data taken for $HoBa_2Cu_4O_8$ [273].

The relaxation data in reduced units are also presented for the ^{18}O compounds (middle panel of Fig. 4.18) as well as for the results of the pressure experiments (lower panel of Fig. 4.18). For the case of the oxygen isotope substituted compounds we observe a supression of the relaxation rate with increasing doping, similar to the ^{16}O data within the experimental uncertainty. Both data sets show the characteristics stated above. The application of hydrostatic pressure does not affect the relaxation rate within the range of errors.

In our fitting procedure we consider the gap amplitude Δ_0 as the major fitting parameter, and we keep its temperature exponent fixed at $A = 4$. The remaining parameters we kept fixed at some reasonable values taken from other experiments as explained below.
In principle the growing of the linewidth as doping decreases can be interpreted by a small s-wave contribution to Δ_0 as has been found in Ref. [260]. Since a non-vanishing oxygen isotope effect on T^* is believed to implicate a phonon-contribution to the pseudogap formation, where the electron-phonon interaction is isotropic, the superconducting gap must contain an s-wave contribution $1-\alpha$. We therefore set up the following constraint
ΔT^*

$$\frac{\Delta T^*}{T^*} \approx \frac{\alpha}{1-\alpha} \tag{4.35}$$

It has been shown repeatedly that underdoped high-T_c compounds are inhomogeneous, i.e., superconducting and antiferromagnetic domains coexist as evidenced by an incomplete Meissner fraction of the superconducting state (see e.g. Refs. [274, 191]). As a result the onset of bulk superconductivity results from a percolation mechanism. We therefore introduce an incomplete superconducting volume fraction $V < 1$ for the underdoped compounds in our model calculations.
Finally we include higher harmonics into the gap function up to the optimum doping, i.e. for the underdoped region we use values $B < 1$ as observed for underdoped BSCCO [10, 263].
The parameters used for the fitting procedure of the relaxation data are summarized in Table 4.6. With these parameters we are able to reproduce the observed relaxation data in a satisfactory manner, see Fig. 4.4.

4.8 Conclusions

4.8.1 Crystal-field excitations

The general features of the crystal-field level scheme could be fairly well obtained by an extrapolation of the crystal-field parameters from $HoBa_2Cu_3O_7$: it predicts the first excited level to be at 0.25 meV, while the higher levels are supposed to lie above 10 meV, which is confirmed by the experiment [245].
However, the doping dependence of the crystal-field excitations cannot be explained by structural effects alone, it is necessary to take into account a charge transfer.
Furthermore we observed that the residual linewidth is dependent on doping, which reflects the increasing local distortion around the Ho^{3+} ion with raising doping. This observation nicely reveals that the crystal-field is a local probe.

4.8.2 The pseudogap in $La_{1.96-x}Sr_xHo_{0.04}CuO_4$

We applied neutron crystal-field spectroscopy systematically to $La_{1.96-x}Sr_xHo_{0.04}CuO_4$ ($0.11 \leq x \leq 0.25$) in order to study the effects of doping, oxygen isotope substitution and pressure application at the Ho^{3+} sites which are situated close to the superconducting copper-oxide planes. More specifically, we were able to determine directly the pseudogap temperature T^* from the temperature dependence of the linewidth of the lowest-lying crystal-field transition associated with the Ho^{3+} ions. We found clear evidence for the existence of the pseudogap in the whole doping range, even for the heavily overdoped compound (x=0.25) [267]. T^* gradually decreases with increasing doping, and we found $T^* > T_c$ in the whole doping range. The oxygen isotope substituted samples exhibit a similar behavior, however, the values of T^* are systematically higher. The isotope effect ΔT^* decreases with increasing doping and vanishes eventually for the heavily overdoped sample (x=0.25). The application of pressure to the optimally doped sample results in a

downward shift of T^*. A summary of our results is displayed in Fig. 4.17.
It is worth mentioning that the superconducting transition temperature T_c exhibits a behavior opposed to the one of the pseudogap temperature T^* upon oxygen isotope substitution as well as pressure application: the isotope effect on T_c is negative, whereas T_c increases with pressure. In both cases the effects are considerably smaller (at least a factor 2) than the ones for T^*.
We would like to point out that the observed reduction of the linewidth and therefore the suppressed interaction with the charge carrier is a purely dynamic effect because there is no structural phase transition in the low-temperature regime ($T \leq$100 K). Hence the sudden decrease of the relaxation rate at T^* clearly originates from the opening of the pseudogap.
Our relaxation data suggest that the superconducting gap has generally d-wave symmetry. For the interpretation of the relaxation data in the underdoped regime we had to include some doping dependent effects, namely the existence of a non-superconducting volume fraction as well as the inclusion of higher harmonics into the d-wave gap function. These two effects nicely support the percolative nature of the superconductivity as well as the growing importance of magnetic interaction below the optimum doping level.

The existence of the pseudogap in the heavily overdoped regime up to a Sr content of 37.5% supports the concept of preformed pairs [68]. It reveals that in the non-superconducting domain, pairs are indeed formed, however, they never achieve phase coherence to produce a superconducting state. The occurrence of a pseudogap without a low-temperature superconducting state has recently been observed in the bilayer manganite $La_{1.2}Sr_{1.8}Mn_2O_7$ [85]. The colossal magnetoresistivity is a phenomenon completely different from superconductivity, therefore the existence of a pseudogap is not necessarily related to a superconducting phase at low temperatures.
The opposite effect of oxygen isotope substitution and pressure on T^* can be qualitatively explained by theoretical models including phonon-mediated mechanisms of the pseudogap formation [228, 229, 230]. However, lattice fluctuation alone cannot reproduce the observed downward shift of T^* under the application of hydrostatic presssure, since pressure also modifies the spin degrees of freedom. We therefore conclude on the basis of our experimental results that a theoretical approach should contain both lattice as well as antiferromagnetic fluctuations as supported by recent calculations of oxygen isotope effects in high-T_c cuprates which started from the t-J scenario and included at the same time the coupling of the electronic degrees of freedom to a Jahn-Teller Q_2-type mode[275].

Chapter 5

Spin dynamics of the Mn^{2+} tetramer based α-$MnMoO_4$

α-$MnMoO_4$ is known to be a compound with tetranuclear clusters which orders antiferromagnetically below 10.7 K. Our goal has been to investigate the magnetic excitations of the cluster and to determine the intra- and intertetramer coupling constants. To do so, we performed inelastic neutron scattering experiments on a single-crystal after the preliminary measurements on a powder. The obtained dispersive behavior of the magnetic excitations has been analyzed within a cluster model based on RPA.
We also developed a toy model of a dimer chain and studied the dependence of the dispersion relations on the coupling parameters. This way we are able to state the differences between the dispersion relations obtained by linear spin-wave theory based on the individual spins and the ones deduced from a random phase approximation cluster model.

5.1 Structural properties

The structural properties of polycrystalline α-$MnMoO_4$ have already been determined by means of x-ray scattering by Abrahams [276].

5.1.1 Chemical structure

α-$MnMoO_4$ crystallizes in the monoclinic space group $C2/m$ with the following lattice constants and angle β between the a and the c axes:

$$a = 10.47 \text{ Å}, \qquad b = 9.52 \text{ Å}, \qquad c = 7.14 \text{ Å}$$
$$\beta = 106.6^\circ$$

The transformation T which maps a vector of the crystal system given in reduced lattice units to the corresponding vector in real space (Cartesian system) is given by

$$T := \begin{pmatrix} 10.47 & 0 & -2.004 \\ 0 & 9.52 & 0 \\ 0 & 0 & 6.853 \end{pmatrix}$$
$$\Rightarrow \mathbf{a} = T(1,0,0)^T = (10.47, 0, 0)^T$$

$$\begin{aligned} \mathbf{b} &= T(0,1,0)^T = (0, 9.52, 0)^T \\ \mathbf{c} &= T(0,0,1)^T = (-2.004, 0, 6.853)^T \end{aligned} \tag{5.1}$$

From now on we will denote any positions in the crystal system in reduced lattice units. The chemical unit cell is displayed in the left panel of Fig 5.1. The structure contains tetranuclear cluster composed of four edge-sharing MnO_6 octahedra, which are arranged in a way that the Mn_4O_{16} clusters have a $2/m(C_{2h})$ symmetry as displayed in the right panel of Fig. 5.1.
The individual ions of a cluster are located at the following positions:

$$\begin{aligned} \mathbf{R}_1 &= (0.5, 0.3185, 0.5) \\ \mathbf{R}_2 &= (0.5, 0.6815, 0.5) \\ \mathbf{R}_3 &= (0.297, 0.5, 0.141) \\ \mathbf{R}_4 &= (0.7028, 0.5, 0.859) \end{aligned}$$

A single cluster is shown in Fig. 5.2, all the manganese ions lie in a plane which is tilted by 60° as compared to the *bc*-plane.

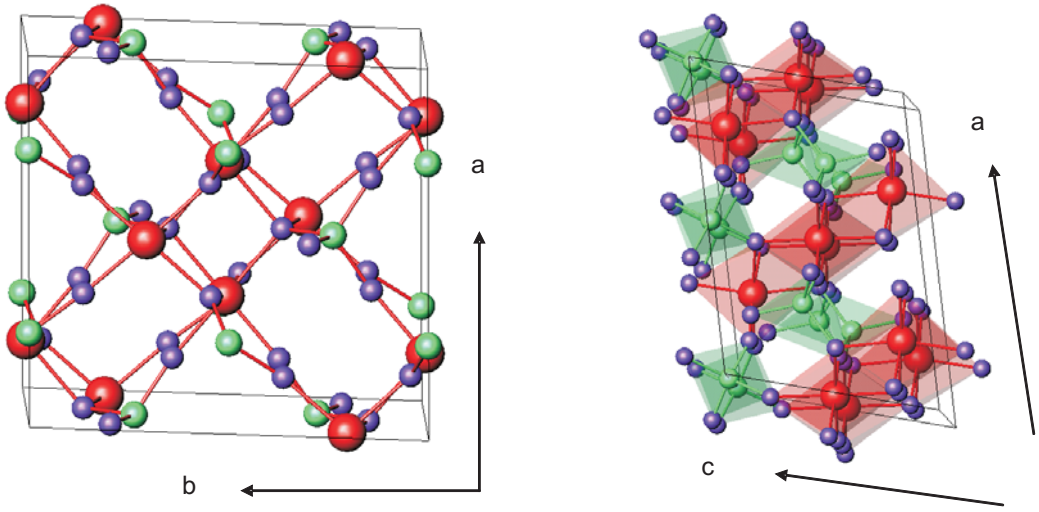

Figure 5.1: Structure of the α-$MnMoO_4$. Left panel: Chemical unit cell in the *ab* projection. Right panel: Mn_4 clusters are composed of four edge-sharing MnO_6 octahedra, the chosen projection is the *ac*-plane.

5.1.2 Magnetic structure

The manganese ions in the title compound are in the high-spin configuration

$$Mn^{2+} = [Ar]4s^2d^5.$$

Due to the ligand field of the surrounding charges, the degeneracy of the $5d$ orbitals is partly lifted which results in two sets, the e_g and the t_{2g} orbitals. It turns out that the extent to which these two sets of orbitals are split is small enough so that the Hund's rule

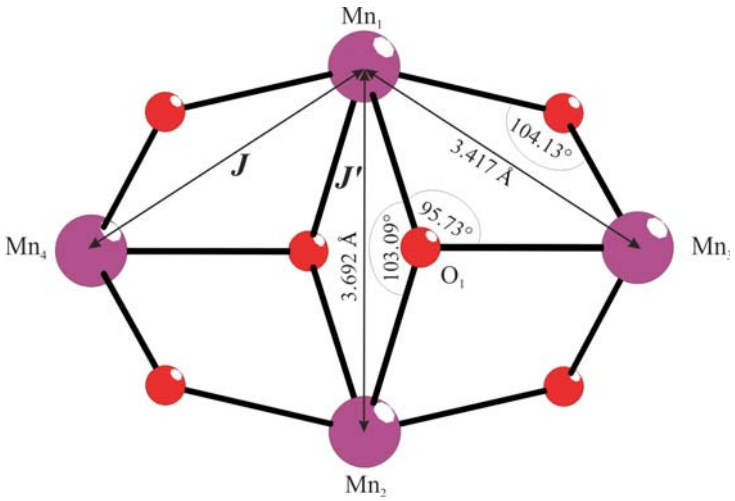

Figure 5.2: Structure of the Mn_4 cluster with relevant distances and angles indicated, the a-axis is perpendicular to the plane. J and J' are the exchange parameters along the edges and the short diagonal of the rhombus, respectively.

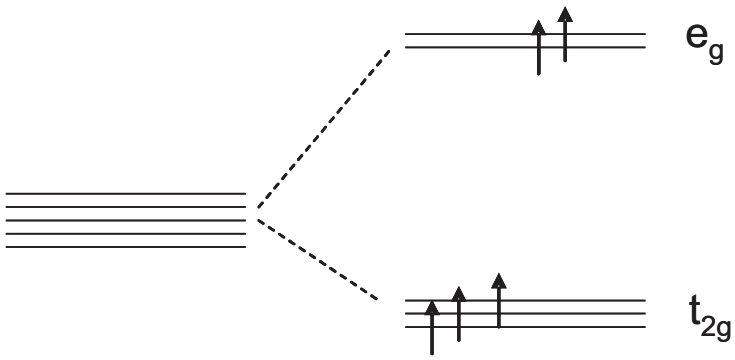

Figure 5.3: In α-$MnMoO_4$ the high-spin case is realized: the five electrons of the d-orbitals occupy both sets, t_{2g} and e_g.

is dominant. Therefore the electrons occupy the t_{2g} and the e_g set, which means that the high-spin case is realized, see Fig. 5.3. Therefore each Mn^{2+} ion carries a spin of 5/2.
α-$MnMoO_4$ undergoes a transition to a three-dimensional magnetic order at $T_N = 10.7$ K, which has been revealed by neutron diffraction experiments on a powder [109]. The order is characterized by a ferromagnetic alignment of the Mn^{2+} spin within the cluster, resulting in a cluster spin

$$S = \sum_{i=1}^{4} S_i = 4 \cdot 5/2 = 10$$

These high cluster spins are ordered antiferromagnetically below the Neél temperature T_N. As compared to the chemical unit cell, the magnetic unit cell is obtained by doubling the c-axis:

$$\mathbf{a}_m = \mathbf{a}, \qquad \mathbf{b}_m = \mathbf{b}, \qquad \mathbf{c}_m = 2\mathbf{c}$$

The cluster spins are located at the position of the center of mass of a cluster, indexed in the chemical unit cell:

$$\begin{aligned} \mathbf{R}_1 &= \left(\frac{1}{2}, \frac{1}{2}, 0\right) \quad \in \text{ sublattice A} \\ \mathbf{R}_2 &= \left(\frac{1}{2}, \frac{1}{2}, \frac{1}{2}\right) \quad \in \text{ sublattice B.} \end{aligned}$$

The parallel alignment of the four spins within each Mn_4O_{16} cluster is not obvious at first sight: the net value of the interaction J between two Mn^{2+} ions is composed of $5 \times 5 = 25$ orbital contributions, where some of them are ferro- and other antiferromagnetic. The balance can tip towards a ferromagnetic net J, when the bridging angles Φ at the ligand approach 90°. In accordance with this statement, ferromagnetic couplings have been reported for the dimer $Fe_2F_9^{3-}$ where $\Phi = 91.77°$, see Ref. [277] and also for the alkoxo-brideged dimer $[Fe_2(salmp)_2]$ ($\Phi = 97.06°$) (Ref. [278]). Note that Fe^{3+} and Mn^{2+} are isoelectronic. In Ref. [279] the angle dependence of the exchange interaction in the case of Fe^{3+} is discussed.
The weaker intercluster superexchange interaction is mediated through the molybdate groups MoO_4 as observed in other molybdates, see References [280, 281]. This coupling is of antiferromagnetic origin and it results in a 3D order where the neighboring clusters have opposite spin directions. The intercluster exchange pathway is of the order of 7 to 8 Å.
We will discuss the interaction partners in detail in Section 5.4.3.

5.1.3 Reciprocal space: the Brioullin zone

If we want to study the dispersive behavior of magnetic excitations i.e. the energy of magnetic excitations as a function of $\mathbf{Q}$, it is crucial and necessary to know the Brillouin zone.
We start with the computation of the reciprocal lattice vectors:

$$\begin{aligned} \mathbf{a}^* : &= 2\pi \frac{\mathbf{b} \times \mathbf{c}}{\mathbf{a} \cdot \mathbf{b} \times \mathbf{c}} = (0.6, 0, 0.175) \\ \mathbf{b}^* : &= 2\pi \frac{\mathbf{c} \times \mathbf{a}}{\mathbf{b} \cdot \mathbf{c} \times \mathbf{a}} = (0, 0.66, 0) \\ \mathbf{c}^* : &= 2\pi \frac{\mathbf{a} \times \mathbf{b}}{\mathbf{c} \cdot \mathbf{a} \times \mathbf{b}} = (0, 0, 0.917). \end{aligned} \tag{5.2}$$

Hence the reciprocal lattice is also monoclinic with an angle $\beta^* = 63.66°$ between the a^*- and c^*- axis. We are then able to write down the basis transformation matrix, which converts a vector of the reciprocal nuclear lattice in reduced lattice units to a vector of the reciprocal lattice given in Cartesian coordinates with units 1/Å:

$$U := \begin{pmatrix} 0.6 & 0 & 0 \\ 0 & 0.66 & 0 \\ 0.175 & 0 & 0.917 \end{pmatrix} \tag{5.3}$$

The occurrence of nuclear Bragg peaks is governed by

$$h + k = 2n + 1 \quad n \in \mathbb{N} \qquad \text{paucity} \tag{5.4}$$

which is typical for $C2/m$ symmetry.
The reflection conditions for magnetic Bragg peaks are

$$h + k = 2n + 1,\ n \in \mathbb{N}; \quad \text{and} \quad l = \frac{1}{2}(2m + 1),\ m \in \mathbb{N}. \tag{5.5}$$

Based on Eqs. 5.4 and 5.5 we performed a Monte-Carlo simulation, see Appendix D, in order to compute the Brillouin zone. The result projected to the a^*b^*, a^*c^* and b^*c^* planes is displayed in Fig. 5.4. In addition, the **Q**-scans performed in the experiments are also shown and labeled by Ai, Bi, C, Di and E, where $i = 1, 2$ corresponding to optical and acoustic type, respectively.

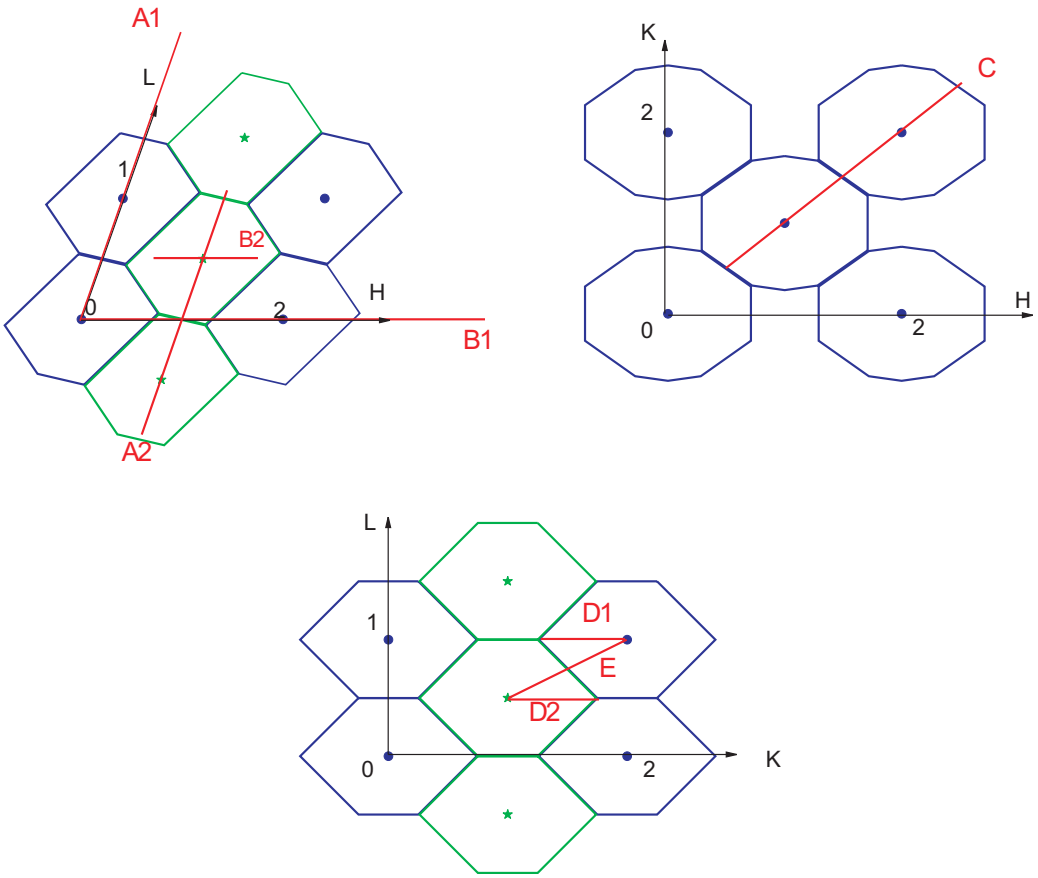

Figure 5.4: Projections of the reciprocal space to the a^*b^*-, a^*c^*- and b^*c^*-plane illustrating the first Brillouin zone. The blue circles denote nuclear Bragg peaks, the green stars stand for magnetic Bragg peaks. The corresponding zone is then called an optical zone if its center is a nuclear Bragg peak and an acoustic zone, if its center is a magnetic Bragg peak. Ai, Bi, C, Di and E refer to the **Q**-scans performed in the experiments, with $i = 1, 2$ corresponding to optical and acoustic type, respectively.

5.2 Magnetic interactions

The tetranuclear compound α-$MnMoO_4$ exhibits intracluster as well as intercluster interactions. Due to the large number of magnetic ions in the magnetic unit cell - 8 Mn^{2+} ions - and their rich interaction, a computation of the **q**-dependent energy eigenvalues of the system based on spin wave theory for the single Mn^{2+} spins is rather cumbersome. We therefore take advantage of the cluster formation to obtain a simpler description of the system. Thus we decompose the Hamiltonian of the total system into an *intracluster* and an *intercluster* Hamiltonian

$$\mathcal{H} = \mathcal{H}_{intra} + \mathcal{H}_{inter}. \tag{5.6}$$

The intracluster interaction of the tetramer can be described by

$$\begin{aligned} \mathcal{H}_{intra} &= -2J \cdot (\mathbf{S}_1 \cdot \mathbf{S}_3 + \mathbf{S}_1 \cdot \mathbf{S}_4 + \mathbf{S}_2 \cdot \mathbf{S}_3 + \mathbf{S}_2 \cdot \mathbf{S}_4) \\ &\quad -2J' \cdot \mathbf{S}_1 \cdot \mathbf{S}_2 - 2J''\mathbf{S}_3 \cdot \mathbf{S}_4 \end{aligned} \tag{5.7}$$

where J, J' and J'' denote the intracluster exchange parameters of the Mn^{2+} ions along the edge, across the short diagonal and across the long diagonal of the rhomb, respectively, as illustrated in Fig 5.2.
We will treat both parts separately, where $\mathcal{H}_{intra}$ will be solved exactly. The interaction between the clusters produces a wave vector dependence of the eigenenergies of the total system. In a first step following Ref. [282] $\mathcal{H}_{inter}$ will be treated within a mean-field approximation, which yields an average value for excitation energy as well as an average value for the intercluster coupling. A more detailed and sophisticated analysis in terms of random phase approximation serves to understand the dispersive behavior of the magnetic excitations and the various coupling parameters can then be deduced.

5.2.1 States of the cluster within mean-field approximation

The four Mn^{2+} ions building the cluster are characterized individually by their quantum numbers

$$\begin{aligned} (\mathbf{S}_i, M_i) \qquad \text{with} \qquad & \mathbf{S}_i^2|S_i, M_i\rangle = S_i(S_i+1)|S_i, M_i\rangle \\ & S_i^z|S_i, M_i\rangle = M_i|S_i, M_i\rangle, \quad S_i = 5/2. \end{aligned} \tag{5.8}$$

For every spin there are $(2S_i + 1) = 6$ states available, so in total there are 6^4 possible combination for the states of the cluster.
In order to characterize this tetranuclear cluster unambiguously, it is necessary to introduce three additional quantum numbers

$$\begin{aligned} \mathbf{S}_{12} &= \mathbf{S}_1 + \mathbf{S}_2, \qquad 0 \le S_{12} \le 2 \cdot S_i \quad i = 1, 2 \\ \mathbf{S}_{34} &= \mathbf{S}_3 + \mathbf{S}_4, \qquad 0 \le S_{34} \le 2 \cdot S_k \quad k = 3, 4 \\ \mathbf{S} &= \mathbf{S}_1 + \mathbf{S}_2 + \mathbf{S}_3 + \mathbf{S}_4, \qquad |S_{12} - S_{34}| \le S \le (S_{12} + S_{34}). \end{aligned} \tag{5.9}$$

The clusters are therefore defined by the wave function $|S_{12}, S_{34}, S\rangle$ with eigenvalues

$$\begin{aligned} \mathbf{S}_{12}^2|S_{12}, S_{34}, S\rangle &= S_{12} \cdot (S_{12}+1)|S_{12}, S_{34}, S\rangle \quad 0 \le S_{12} \le 2S_i \quad i = 1, 2 \\ \mathbf{S}_{34}^2|S_{12}, S_{34}, S\rangle &= S_{34} \cdot (S_{34}+1)|S_{12}, S_{34}, S\rangle \quad 0 \le S_{34} \le 2S_k \quad k = 1, 2 \\ \mathbf{S}^2|S_{12}, S_{34}, S\rangle &= S \cdot (S+1)|S_{12}, S_{34}, S\rangle \quad |S_{12} - S_{34}| \le S \le (S_{12} + S_{34}). \end{aligned}$$

The degeneracy of these cluster states is $(2S+1)$-fold and can be removed by the presence of a magnetic field.
Next we compute the eigenstates of a single tetramer cluster i.e. the eigenstates of $\mathcal{H}_{intra}$ in Eq. 5.7. Recalling that

$$\mathbf{S}_i\mathbf{S}_k = \frac{1}{2}(\mathbf{S}_i\mathbf{S}_k - \mathbf{S}_i - \mathbf{S}_k), \tag{5.10}$$

we find the eigenstates of intracluster Hamiltonian

$$\mathcal{H}_{intra}|S_{12}, S_{34}, S\rangle = E(S_{12}, S_{34}, S)|S_{12}, S_{34}, S\rangle \tag{5.11}$$

with the corresponding eigenenergies

$$\begin{aligned} E_{intra}(S_{12}, S_{34}, S) &= -J[S(S+1) - S_{12}(S_{12}+1) - S_{34}(S_{34}+1)] \\ &+ J'[S_{12}(S_{12}+1) - 2S_i(S_i+1)] \\ &- J''[S_{34}(S_{34}+1) - 2S_i(S_i+1)]. \end{aligned} \tag{5.12}$$

In the following we will neglect the interaction along the long diagonal J''.

Mean-field approach

Below T_N the clusters order antiferromagnetically, their interaction is described by an effective field $\mathbf{H}$ within the mean-field approach. Thus $\mathcal{H}_{inter}$ in Eq. 5.6 reads

$$\mathcal{H}_{inter} = -g\mu_B\mathbf{H}\cdot\sum_i \mathbf{S}_i = -g\mu_B\mathbf{H}\cdot\mathbf{S}. \tag{5.13}$$

Note that $\mathbf{H}$ could also include an external field.
The presence of the internal molecular field splits the cluster states $|S_{12}, S_{34}, S\rangle$ and lifts completely the $(2S+1)$-fold degeneracy of the tetramer states. Thus there is need for an additional quantum number M to distinguish the split states, so that the eigenvalues and eigenenergies of $\mathcal{H}_{inter}$ read

$$\begin{aligned} \mathcal{H}_{inter}|S_{12}, S_{34}, S, M\rangle &= E_{inter}(M)|S_{12}, S_{34}, S, M\rangle \\ E_{inter}(M) &= -g\mu_B HM \end{aligned} \tag{5.14}$$

where we assumed that $\mathbf{H}$ and $\mathbf{S}$ are parallel, so that we may write their scalar product $\mathbf{HS} = HS^z$. E_{inter} is added to E_{intra} in Eq. 5.12, which yields the eigenenergy of the total system

$$\begin{aligned} \mathcal{H}|S_{12}, S_{34}, S, M\rangle &= (\mathcal{H}_{intra} + \mathcal{H}_{inter})|S_{12}, S_{34}, S, M\rangle = E(S_{12}, S_{34}, S, M)|S_{12}, S_{34}, S, M\rangle \\ E(S_{12}, S_{34}, S, M) &= E_{intra}(S_{12}, S_{34}, S) + E_{inter}(M) \\ &= -J[S(S+1) - S_{12}(S_{12}+1) - S_{34}(S_{34}+1)] \\ &\quad +J'[S_{12}(S_{12}+1) - 2S_i(S_i+1)] \\ &\quad +g\mu_B HM \end{aligned} \tag{5.15}$$

where g is the gyromagnetic factor, μ_B denotes the Bohr magneton and $HM = \mathbf{H} \cdot \mathbf{S}$. We then find the lowest-lying cluster states with the following eigenenergies

$$\begin{aligned}
|\Gamma_0\rangle &= |5,5,10,10\rangle : \quad E_0(5,5,10,10) = -50J - 12.5J' - 10g\mu_B H_z \\
|\Gamma_1\rangle &= |5,5,10,9\rangle : \quad E_1(5,5,10,9) = -50J - 12.5J' - 9g\mu_B H_z \\
|\Gamma_2\rangle &= |4,5,9,9\rangle : \quad E_2(4,5,9,9) = -40J - 2.5J' - 9g\mu_B H_z \\
|\Gamma_3\rangle &= |5,4,9,9\rangle : \quad E_3(4,5,9,9) = -40J - 12.5J' - 9g\mu_B H_z \\
|\Gamma_4\rangle &= |5,5,9,9\rangle : \quad E_4(5,5,9,9) = -30J - 12.5J' - 9g\mu_B H_z. \qquad (5.16)
\end{aligned}$$

where we neglected J'', the interaction parameter over the long diagonal.
The ratio of J'/J determines the order of the states $|\Gamma_i\rangle$ as a function of energy. To simplify matters, we neglected the Zeeman splitting because it is only a constant when plotting E_i as a function of J'/J. And we consider only the states with $S = 10$ and $S = 9$. While the energies of the states Γ_i, $i = 0, 3, 4$ proceed in a parallel manner, E_2 crosses the energy of the other states depending on J'/J as illustrated in Fig. 5.5.

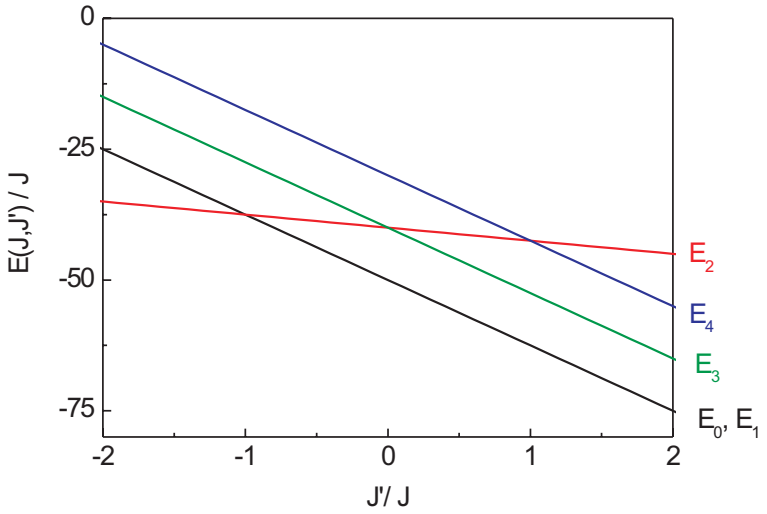

Figure 5.5: The energy of the cluster states $E(J.J')/J$ with $S = 10$ and $S = 9$ as a function of $J'/$.We set the quantum number M to be zero, so that E_0 and E_1 coincide.

At $J'/J = 0$ the states Γ_2 and Γ_3 are degenerate. For $J'/J < -1$, Γ_2 has the lowest energy of the states Γ_i, $i = 0..4$ under consideration. Fig. 5.5 is relevant to determine the ground state: Assuming that the interaction strength along the edges J is stronger than the one across the diagonal J', i.e. $|J| > |J'|$ gives the following two possible ground states:

- $J > 0$ (ferromagnetic) $\Rightarrow$ the state Γ_0 is the ground state, which means that the spins are ferromagnetically aligned.
- $J < 0$ (antiferromagnetic) $\Rightarrow$ the ground state is Γ_j which is either the state Γ_2 or a state with $S \leq 8$ which we have not included in this computation.

Obviously the second case doesn't make sense due to the experimentally observed antiferromagnetic order [109]. We conclude that Γ_0 is the ground state and that $J > 0$, which is in agreement with the magnetic structure obtained by neutron diffraction [109].
The allowed transitions from the ground state to an excited state are then derived from the dipole selection rules for tetramer excitations (see Appendix B.1 and Ref. [119]):

$$\begin{aligned} \Delta S &= 0, \pm 1; \qquad \Delta M = 0, \pm 1 \\ \Delta S_{12} &= 0, \pm 1 \quad \text{and } \Delta S_{34} = 0 \\ \Delta S_{12} &= 0 \quad \text{and } \Delta S_{34} = 0, \pm 1, \end{aligned} \tag{5.17}$$

which give rise to the subsequent ground state transitions:

$$\begin{aligned} |\Gamma_0\rangle = |S_{12} = 5, S_{34} = 5, S = 10, M = 10\rangle &\rightarrow |5, 5, 10, 9\rangle = |\Gamma_1\rangle \\ |\Gamma_0\rangle = |5, 5, 10, 10\rangle &\rightarrow |4, 5, 9, 9\rangle = |\Gamma_2\rangle \\ |\Gamma_0\rangle = |5, 5, 10, 10\rangle &\rightarrow |5, 4, 9, 9\rangle = |\Gamma_3\rangle \\ |\Gamma_0\rangle = |5, 5, 10, 10\rangle &\rightarrow |5, 5, 9, 9\rangle = |\Gamma_4\rangle. \end{aligned} \tag{5.18}$$

The eigenvalues and eigenstates of the system contain a constant term $g\mu_B HM$, the corresponding energy H can be determined from experimental data. H is related to the intercluster interaction by:

$$H = g\mu_B \lambda \langle S_i \rangle, \qquad \lambda = \frac{2}{g\mu_B} \sum_r z_r J_r \tag{5.19}$$

where λ is the molecular field parameter, z_r denotes the number of clusters in the r^{th} neighboring coordination shell. J_r is the corresponding intercluster exchange parameter, which is responsible for a dispersive behavior of the excitations.
The molecular field parameter λ allows to estimate the magnetic ordering temperature θ, see Refs. [283, 284]:

$$T_N = 0.77 \frac{2S(S+1)}{3k_B} \lambda. \tag{5.20}$$

5.2.2 Random phase approximation for clusters

Since there is an antiferromagnetic 3D order below T_N, we may consider the cluster spin $\mathbf{S} = \sum_{k=1}^{4} \mathbf{S}_k$ located at the center of mass of the cluster as a unit. And we will treat the interaction between the clusters within random phase approximation. We therefore end up with two interacting cluster spins per magnetic unit cell, see Section 5.1.2.

Dispersion relation

In order to solve the RPA equation deduced in Section 2.4.3., Eq. 2.54

$$\chi(\mathbf{q}, \omega) = \chi^0(\omega) \cdot \left[1 - \chi^0(\omega) J(\mathbf{q})\right]^{-1}, \tag{5.21}$$

we have to compute the single-ion susceptibility $\chi^0(\omega)$ for the sublattices A and B first:

$$\chi^0(\omega) = \begin{pmatrix} \tilde{\chi}^0_A(\omega) & 0 \\ 0 & \tilde{\chi}^0_B(\omega) \end{pmatrix} \tag{5.22}$$

where $\tilde{\chi}^0_A(\omega)$ and $\tilde{\chi}^0_B(\omega)$ are 3×3 matrices with entries $(\chi^0)^{\alpha\beta}_A(\omega)$ and $(\chi^0)^{\alpha\beta}_B(\omega)$. Hence the single-ion susceptibility tensor is a 6×6 matrix.
In the case of cluster transitions these components are

$$\begin{aligned} (\chi^0)^{\alpha\beta}_r(\omega) &= 2 \cdot \sum_{i=1}^{4} \frac{\langle \Gamma_i | S^\alpha | \Gamma_0 \rangle_r \langle \Gamma_0 | S^\beta | \Gamma_i \rangle_r}{E_i - E_0 - \hbar\omega} \quad r = A, B \\ |\Gamma_i\rangle &= |S^i_{12}, S^i_{34}, S^i, M^i\rangle, \end{aligned} \tag{5.23}$$

where α, β are Cartesian coordinates, i stands for the four possible transitions from the ground state with energy E_0 to excited tetramer states with energy E_i. We neglected the population factors and consider only ground state transitions $|\Gamma_0\rangle \rightarrow |\Gamma_i\rangle$, because we are interested exclusively in the low-temperature behavior.
A system of spins forming a cluster is generally described by a tensor operator formalism, where the components S^α_j of the spin operator $\mathbf{S}_j$ of the individual ions have to be replaced by irreducible tensor operators $\hat{T}^q_j$ as indicated already in Chapter 2:

$$\begin{aligned} S^x_j &= \frac{\sqrt{2}}{2}\left(\hat{T}^{+1}_j - \hat{T}^{-1}_j\right) \\ S^y_j &= \frac{\sqrt{2}}{2i}\left(-\hat{T}^{+1}_j - \hat{T}^{-1}_j\right) \\ S^z_j &= \hat{T}^0_j \end{aligned} \tag{5.24}$$

The transition matrix elements $\langle \Gamma_i | S^\alpha | \Gamma_0 \rangle$ in Eq. 5.23 then consist of 6-j and 3-j symbols and are given in Appendix B.1.
Also the expression for the single-ion tensor is derived in Appendix B.2. Here we give the results

$$\begin{aligned} (\chi^0)^{\alpha\alpha}_A &= (\chi^0)^{\alpha\alpha}_B \equiv f(\omega) \qquad \alpha = x, y \\ (\chi^0)^{\alpha\beta}_A &= -(\chi^0)^{\alpha\beta}_B = i \cdot f(\omega) \qquad \alpha \neq \beta = x, y \\ (\chi^0)^{\alpha\beta}_A &= (\chi^0)^{\alpha\beta}_B = 0 \qquad \alpha = z \text{ or } \beta = z \\ \Rightarrow \chi^0(\mathbf{q}) &= \begin{pmatrix} f(\omega) & i \cdot f(\omega) & 0 & & & \\ i \cdot f(\omega) & f(\omega) & 0 & 0 & & \\ 0 & 0 & 0 & & & \\ & & & f(\omega) & i \cdot f(\omega) & 0 \\ & 0 & & i \cdot f(\omega) & f(\omega) & 0 \\ & & & 0 & 0 & 0 \end{pmatrix} \end{aligned} \tag{5.25}$$

where

$$f(\omega) \equiv (0.79)^2 \left(\frac{1}{\Delta_1 - \hbar\omega} + \frac{1}{\Delta_4 - \hbar\omega}\right) + (1.12)^2 \left(\frac{1}{\Delta_2 - \hbar\omega} + \frac{1}{\Delta_3 - \hbar\omega}\right)$$

The deviation of $f(\omega)$ can also be found in Appendix B.2.
The exchange coupling tensor is constructed from the Fourier-transformed coupling constants

$$J(\mathbf{q}) = \begin{pmatrix} \tilde{J}_{AA}(\mathbf{q}) & \tilde{J}_{AB}(\mathbf{q}) \\ \tilde{J}_{BA}(\mathbf{q}) & \tilde{J}_{BB}(\mathbf{q}) \end{pmatrix} \tag{5.26}$$

Again the interaction tensor $J(\mathbf{q})$ is a 6×6 matrix with block matrices $\tilde{J}_{AA}(\mathbf{q})$, $\tilde{J}_{BB}(\mathbf{q})$ and $\tilde{J}_{AB}(\mathbf{q})$, $\tilde{J}_{BA}(\mathbf{q})$, which describe the intrasublattice and the intersublattice exchange coupling, respectively. In the case of fully symmetric exchange i.e. Heisenberg model, these matrices are diagonal e.g.

$$\tilde{J}(\mathbf{q})_{AA} = \begin{pmatrix} J_{AA}(\mathbf{q}) & 0 & 0 \\ 0 & J_{AA}(\mathbf{q}) & 0 \\ 0 & 0 & J_{AA}(\mathbf{q}) \end{pmatrix} \tag{5.27}$$

Furthermore the following relations hold

$$\begin{aligned} \tilde{J}(\mathbf{q})_{AA} &= \tilde{J}(\mathbf{q})_{BB} \\ \tilde{J}(\mathbf{q})_{BA} &= \tilde{J}(\mathbf{q})^{\dagger}_{AB} = \tilde{J}(\mathbf{q})_{AB} \end{aligned} \tag{5.28}$$

The last equals sign is valid because $J(\mathbf{q}) \in \mathbb{R}$, which will become clear when we treat the interaction parameters in concrete details, see Section 5.4.3.
The RPA equation reads then

$$\chi(\mathbf{q},\omega) = \begin{pmatrix} \tilde{\chi}^0_B(\omega) & 0 \\ 0 & \tilde{\chi}^0_A(\omega) \end{pmatrix} \cdot \begin{pmatrix} \mathbb{1} - \tilde{\chi}^0_A(\omega)\tilde{J}_{AA}(\mathbf{q}) & \tilde{\chi}^0_A(\omega)\tilde{J}_{AB}(\mathbf{q}) \\ \tilde{\chi}^0_B(\omega)\tilde{J}_{AB}(\mathbf{q})^{\dagger} & \mathbb{1} - \tilde{\chi}^0_B(\omega)\tilde{J}_{AA}(\mathbf{q}) \end{pmatrix}^{-1} \tag{5.29}$$

The four block matrices of the second matrix in Eq. 5.29 are diagonal because of the isotropic exchange coupling e.g.

$$\tilde{\chi}^0_A(\omega)\tilde{J}_{AA}(\mathbf{q}) = \begin{pmatrix} f(\omega)J_{AA}(\mathbf{q}) & 0 & 0 \\ 0 & f(\omega)J_{AA}(\mathbf{q}) & 0 \\ 0 & 0 & 0 \end{pmatrix} = \tilde{\chi}^0_B(\omega)\tilde{J}_{AA}(\mathbf{q}). \tag{5.30}$$

We therefore obtain

$$\begin{aligned} &\chi(\mathbf{q},\omega) = \\ &\frac{1}{D(\mathbf{q},\omega)} \begin{pmatrix} \mathbb{1} - f(\omega)\tilde{J}_{AA}(\mathbf{q}) & -f(\omega)\tilde{J}_{AB}(\mathbf{q}) \\ -f(\omega)\tilde{J}_{AB}(\mathbf{q})^* & \mathbb{1} - f(\omega)\tilde{J}_{AA}(\mathbf{q}) \end{pmatrix} \cdot \begin{pmatrix} f(\omega)\cdot\mathbb{1} & 0 \\ 0 & f(\omega)\cdot\mathbb{1} \end{pmatrix} \end{aligned} \tag{5.31}$$

where

$$\begin{aligned} D(\mathbf{q},\omega) &= \left(1 - f(\omega)J_{AA}(\mathbf{q})\right)^2 - \left(f(\omega)J_{AB}(\mathbf{q})\right)\left(f(\omega)J_{AB}(\mathbf{q})^*\right) \\ &= \left[1 - f(\omega)\left(J_{AA}(\mathbf{q}) + |J_{AB}(\mathbf{q})|\right)\right] \cdot \left[1 - f(\omega)\left(J_{AA}(\mathbf{q}) - |J_{AB}(\mathbf{q})|\right)\right]. \end{aligned} \tag{5.32}$$

According to Section 2.4.3, the poles of the wave-vector dependent susceptibility $\chi(\mathbf{q},\omega)$ determine the magnetic excitation energies. So the two different kinds of poles which are generated, will be referred to as the acoustic and optic branches of the dispersion relation. Hence we find the energies of the resulting excitation branches by inserting $f(\omega)$ as given in Appendix B.2

$$\begin{aligned} \hbar\omega(\mathbf{q})_i &= \left[\Delta_i^2 - 2M_i^2\Delta_i \cdot (J_{AA}(\mathbf{q}) \pm |J'_{AB}(\mathbf{q})|)\right]^{1/2} \quad i = 1..4 \\ M_i &= \langle\Gamma_i|\hat{T}|\Gamma_0\rangle \quad \text{and} \quad \Delta_i = E_i - E_0. \end{aligned} \tag{5.33}$$

The + and − sign corresponds to the acoustic and optical branch, respectively. From Eq. 5.33 we find that the stronger the coupling of the cluster spins, the more dispersive the excitation is. This is the same formula as used in Ref. [285] in order to describe the dispersion of a crystal-field transition.
In the case of weak dispersion i.e. weak coupling, the square root can be approximated by a Taylor expansion up to 1^{st} order:

$$\begin{aligned} \hbar\omega(\mathbf{q})_i &= \Delta_i - M_i^2 \cdot (J_{AA}(\mathbf{q}) + |J'_{AB}(\mathbf{q})|) \quad \text{acoustic} \\ \hbar\omega(\mathbf{q})_i &= \Delta_i - M_i^2 \cdot (J_{AA}(\mathbf{q}) - |J'_{AB}(\mathbf{q})|) \quad \text{optic.} \end{aligned} \tag{5.34}$$

It is worth noticing that in principle two spins per magnetic unit cell give rise to two excitation branches, where one of them is of acoustic and the other one of optical type. But the introduction of Δ_i and M_i^2 which are dependent on the specific cluster transition $|\Gamma_0\rangle \rightarrow |\Gamma_i$. Eq. 5.34 indeed yields $2 \times 4 = 8$ branches, which is consistent with 8 spins per magnetic unit cell.
Let us now consider the intensity of these branches as a function of the scattering vector $\mathbf{Q} = \mathbf{q} + \boldsymbol{\tau}$, where $\mathbf{q}$ belongs to the first Brillouin zone and $\boldsymbol{\tau}$ is a reciprocal lattice vector. If the two sublattices are separated by a vector $\boldsymbol{\rho}$, we find for the exchange coupling

$$\begin{aligned} J_{AA}(\mathbf{Q}) &= J_{AA}(\mathbf{q}) \\ J_{AB}(\mathbf{Q}) &= J_{AB}(\mathbf{q})e^{i\boldsymbol{\tau}\boldsymbol{\rho}} = \pm|J_{AB}(\mathbf{q})|e^{i\Phi} \\ \text{with} \qquad & \Phi = \boldsymbol{\rho}\cdot\boldsymbol{\tau} + arctan\left(\frac{\Im J_{AB}(\mathbf{q})}{\Re J_{AB}(\mathbf{q})}\right) \end{aligned} \tag{5.35}$$

Using the definition

$$\chi(\mathbf{Q},\omega) = \frac{1}{2}\sum_{\alpha\beta}\chi_{\alpha\beta}(\mathbf{Q},\omega) \tag{5.36}$$

and performing a partial fraction decomposition leads to

$$\begin{aligned} \chi(\mathbf{Q},\omega) &= \frac{1}{2}\left(1 + cos(\Phi)\right)\chi_{ac}(\mathbf{q},\omega) + \frac{1}{2}\left(1 - cos(\Phi)\right)\chi_{op}(\mathbf{q},\omega) \\ & \chi_{ac}(\mathbf{q},\omega) = \left[1 - \chi^0(\omega)(J_{AA}(\mathbf{q}) + |J_{AB}(\mathbf{q})|)\right]^{-1} \cdot \chi^0(\omega) \\ & \chi_{op}(\mathbf{q},\omega) = \left[1 - \chi^0(\omega)(J_{AA}(\mathbf{q}) - |J_{AB}(\mathbf{q})|)\right]^{-1} \cdot \chi^0(\omega) \end{aligned} \tag{5.37}$$

Since the Fourier transformed exchange coupling is real (see Section 5.4.3.), the acoustic and optical branches are detected in accordance to the change of the phase

$$\Phi = \boldsymbol{\rho}\boldsymbol{\tau} = \pm n\pi \quad n \in \mathbb{N}. \tag{5.38}$$

Thus the prefactors in the equation for the susceptibility (Eq. 5.37) vanish in turn.

Tensor model for exchange coupling

The exchange coupling parameters might be dependent on the cluster state and we adopt the exchange tensor formalism originally developed by Levy [286]:

$$J(\mathbf{q}) \equiv \tilde{J}(\mathbf{q}, |\Gamma_i\rangle, |\Gamma_j\rangle), \tag{5.39}$$

The tensor is symmetric because $\tilde{J}(\mathbf{q}, |\Gamma_i\rangle, |\Gamma_j\rangle) = \tilde{J}(\mathbf{q}, |\Gamma_j\rangle, |\Gamma_i\rangle)$ for all $i, j = 0..4$. Entries which symbolize excited transitions $\tilde{J}(\mathbf{q}, |\Gamma_i\rangle, |\Gamma_j\rangle)$ with $i, j \geq 1$ are of neither importance nor interest at low temperatures.
$\tilde{J}(\mathbf{q})$ symbolizes that the exchange parameters are dependent on the quantum numbers involved in the transition $|\Gamma_i\rangle \rightarrow |\Gamma_j\rangle$. In principle such a tensor formalism implies a dependence of the exchange parameter on the transition matrix elements. In the simplest approximation we may assume that the exchange parameters scale with the transition matrix elements M_{0i} of the four ground state cluster transitions:

$$\tilde{J}(\mathbf{q}, |\Gamma_0\rangle, |\Gamma_n\rangle) \cdot M_{0n}^2 = \tilde{J}(\mathbf{q}, |\Gamma_0\rangle, |\Gamma_m\rangle) \cdot M_{0m}^2 \quad m, n = 1, ..4. \tag{5.40}$$

5.3 Experimental results

We present the results obtained by inelastic neutron scattering experiments on a single crystal. We also give a summary of the inelastic neutron scattering measurements on polycrystalline α-$MnMoO_4$, which have been previously performed by Ochsenbein et al. [282]. The neutron diffraction measurements on a single-crystal are also discussed.

5.3.1 Diffraction on a single-crystal

We performed inelastic neutron experiments on the single-crystal diffractometer TriCS, where we were specifically searching for magnetic Bragg peaks. Among the symmetry-related magnetic Bragg peaks, $(-1, 0, 1/2)$ is by far the strongest one. A projection on the 2-dimensional detector of a typical omega scan of $(-1, 0, 1/2)$ is shown in Fig. 5.6.
Fig. 5.6 displays also the intensity of the magnetic Bragg peak as a function of temperature. The temperature where the intensity of $(-1, 0, 1/2)$ vanishes, is determined as the 3D-ordering temperature.

5.3.2 Inelastic neutron scattering experiments on polycrystalline α-$MnMoO_4$

The experiments on polycrystalline α-$MnMoO_4$ have been performed on FOCUS [282]. Fig. 5.7 shows the spectrum which gives evidence for four well-resolved excitations labeled by I, II, III and IV.
The linewidth of peak II corresponds roughly to the instrumental resolution, whereas the widths of the peaks I, III and IV result from intrinsic line broadening.
The intensities of the four transition exhibit very distinct dependencies on the modulus of the scattering vector $\mathbf{Q}$ as illustrated in Fig. 5.8.

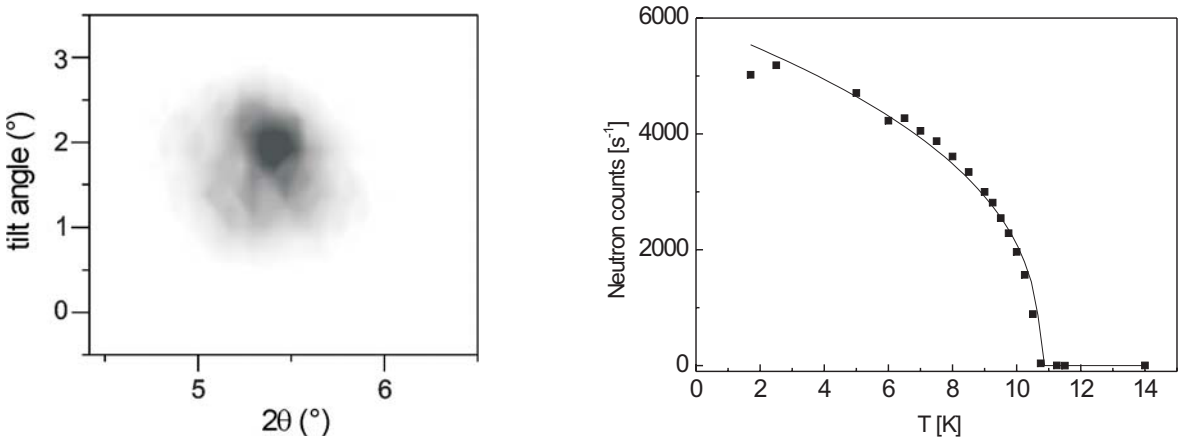

Figure 5.6: $(-1, 0, 1/2)$ magnetic Bragg peak in α-$MnMoO_4$ measured on TriCS: (a) Contour plot at 1.5 K. (b) Intensity as a function of temperature visualizing the transition to 3D-order below T_N.

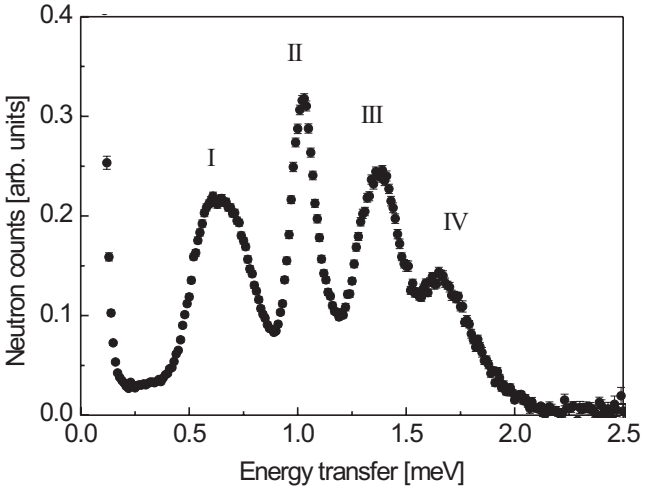

Figure 5.7: INS spectrum of polycrystalline α-$MnMoO_4$ as taken on FOCUS at 1.5 K and λ=4.75 Å [282]. The inelastic peaks labeled by I to IV correspond to the ground-state transitions to excited tetramer states.

5.3.3 Inelastic neutron scattering experiments on a single-crystal α-$MnMoO_4$

Energy scans

The inelastic single-crystal data have been performed on triple-axes spectrometers at 1.5 K. Fig. 5.9 shows typical energy spectra scattered from neutrons: in panel (a) the spectra at two different Bragg points are compared:

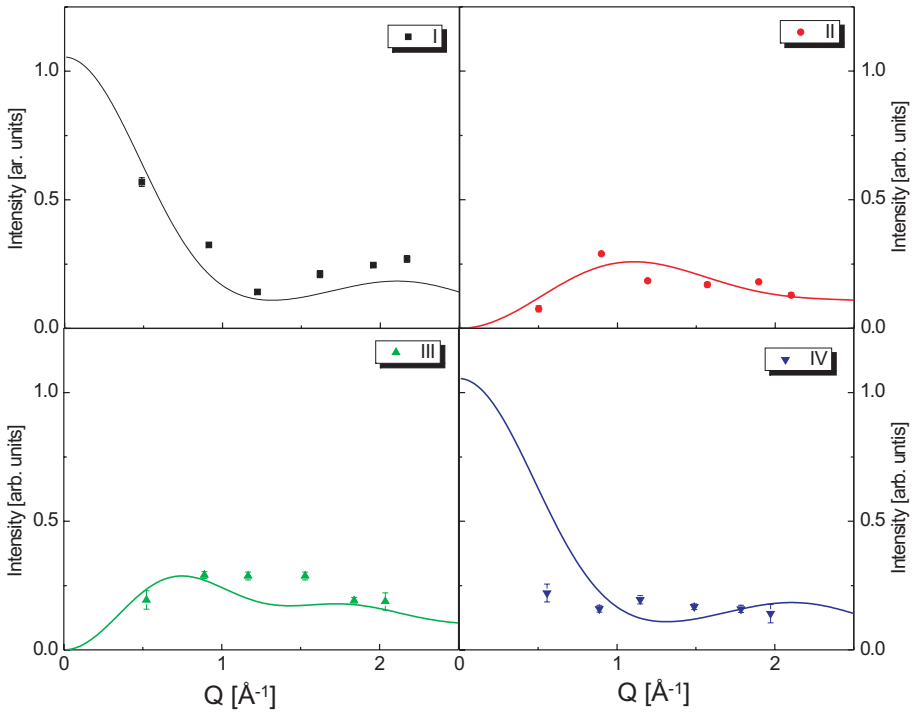

Figure 5.8: INS intensities for the transitions I-IV as a function of $|\mathbf{Q}| = Q$ [282]. The full symbols denote the experimental data, whereas the full lines correspond to the calculated intensities.

$$\mathbf{Q} = (-1, 0, 0.65) = \mathbf{q} + \boldsymbol{\tau} \Rightarrow \mathbf{q} = (0, 0, 0.15), \quad \boldsymbol{\tau} = (-1, 0, \frac{1}{2})$$

and

$$\mathbf{Q} = (-1, 0, 0.8) = \mathbf{q} + \boldsymbol{\tau} \Rightarrow \mathbf{q} = (0, 0, 0.3), \quad \boldsymbol{\tau} = (-1, 0, \frac{1}{2})$$

where $\boldsymbol{\tau}$ is a reciprocal lattice point. It is obvious that the peak position as well as the intensities vary with $\mathbf{q}$. In Panel (b) the data at two symmetry-related $\mathbf{Q}$-points are shown

$$\mathbf{Q} = (1, 0, 0) = \mathbf{q} + \boldsymbol{\tau} \Rightarrow \mathbf{q} = (1, 0, 0) \qquad \boldsymbol{\tau} = (1, 0, \frac{1}{2})$$

and

$$\mathbf{Q} = (3, 0, 0) = \mathbf{q} + \boldsymbol{\tau} \Rightarrow \mathbf{q} = (1, 0, 0) \qquad \boldsymbol{\tau} = (3, 0, \frac{1}{2})$$

Since these data belong to the same $\mathbf{q}$, the peak positions are expected to be identical, which is indeed the case. But the neutron scattering cross section is dependent on the form factor $F(Q)^2$ and the polarization factor (see Chapter 3), thus the intensities are different: At $\mathbf{Q} = (3, 0, 0)$ the lowest transition even vanishes.

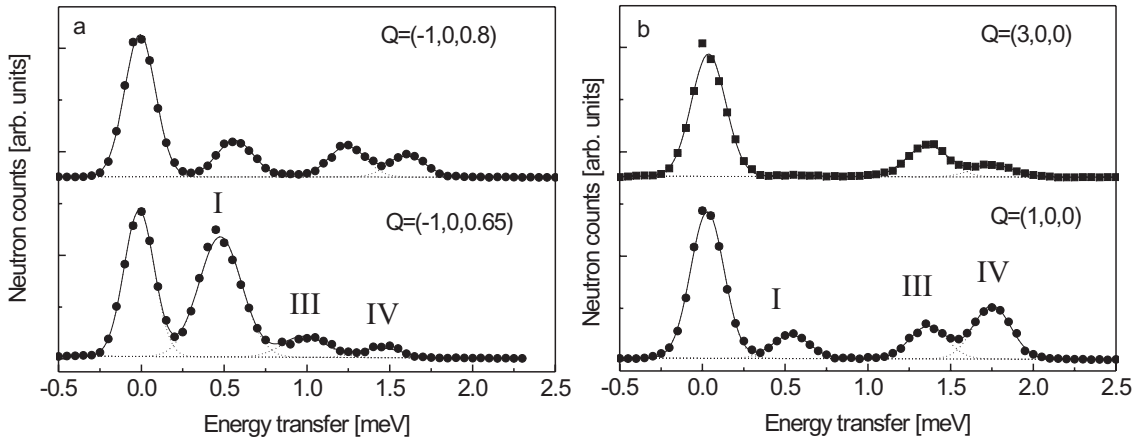

Figure 5.9: Energy spectra of scattered neutrons form α-$MnMoO_4$ as taken on RITA II. (a) The peak position of an excitation varies with Q. In (b) the two Q points are equivalent with respect to the first Brillouin zone, therefore the peak positions are identical, but the intensities are different. The solid line corresponds to a least-squares fitting procedure, the dotted lines illustrate the subdivions into the individual peaks as explained in the text.

The inelastic peaks were fitted by Gaussians with correlated linewidths.
The energy dispersions along different directions in reciprocal space have then been established based on the two subsequent criteria:

1. Symmetry:
   The excitation energies obtained from spectra at symmetry-related **Q**-points have to be equal.

2. Continuity:
   Within the same Brillouin zone, both the excitation energy and the corresponding intensity have to change continuously with varying **Q**. Additionally, the width of the excitations is expected to develop smoothly, any sudden increase is interpreted as an overlap of peaks corresponding to different modes.

Note that the intensity is released from the symmetry constraint, because the scattering cross section is dependent on the wave vector **Q**.
The correlation of the linewidths is essential in finding the correct energy positions of the modes whose peaks are overlapping, an example is shown in panel (a)-(c) of Fig. 5.10. But sometimes even an improved resolution is necessary in order to clarify this issue: For instance, we have measured the energy transfer at the symmetry-related **Q**-points $\mathbf{Q} = (0, 1.3, 1.5) \equiv (0, 0.3, 0)$ with k_f =1.54 Å^{-1} and $\mathbf{Q} = (0, 1.3, 0.5)$ with k_f=1.1 Å^{-1}, see panel (d) and (c) of Fig. 5.10, respectively. We observed that the first spectrum exhibits only one intense peak at 1.3 meV with a slight tail on the right side, while the second spectrum reveals at least the existence of two individual excitations. The

devolution of the dispersion, (criterium (2)) determines that there are not two, but three peaks overlapping.

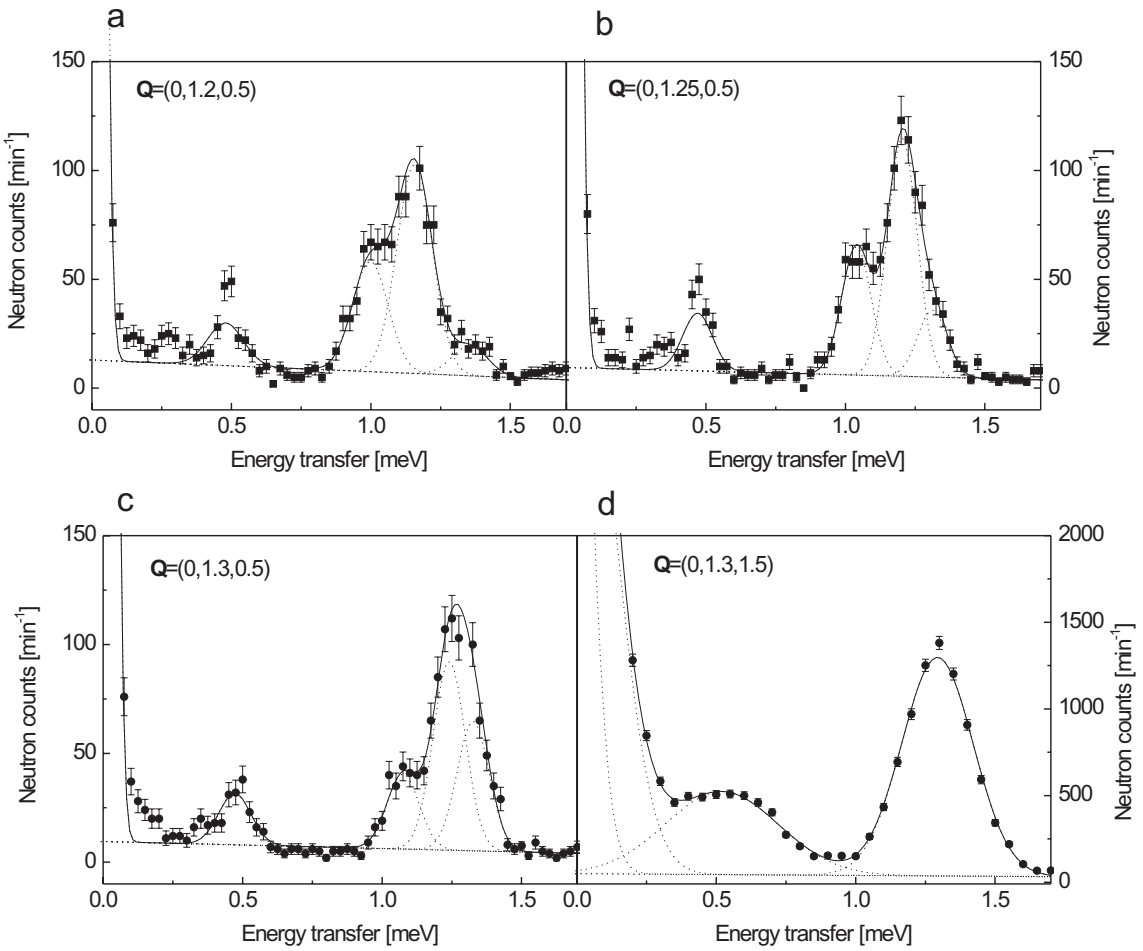

Figure 5.10: An overlap of three peaks: panel (a)-(c) display the continuous devolution of the energy dispersion from $\mathbf{Q} = (0, 1.2, 0.5)$ to $\mathbf{Q} = (0, 1.3, 0.5)$ taken for k_f=1.1 Å^{-1}. Applying the criteria how to establish a dispersion, reveals the overlap of three peaks around 1.3 meV. As a comparison the spectrum taken at the symmetry-related $\mathbf{Q} = (0, 1.3, 1.5)$ is shown, where the resolution (k_f=1.54 Å^{-1}) is insufficient. The solid lines correspond to a least-squares fitting procedure, while the dotted lines illustrate the subdivisions into the individual peaks.

Dispersive behavior of the magnetic excitations

We performed energy scans along various directions in reciprocal space, they reveal the **Q**-dependent energy dispersions. The scans are taken in the optical as well as in the acoustic zone, where the optical and acoustic branches occur. We have chosen the directions of the scans in reciprocal space through either a magnetic or nuclear Bragg point, i.e. we measured from the zone center to the zone boundary. Table 5.1 assembles the experiments and the type of the dispersion. Note that the type of scans parallel to $(h, 0, 0)$ (scan B1

Table 5.1: Energy scans along different directions in reciprocal space. The wave vector $\mathbf{Q}$ is decomposed into $\mathbf{q}$ belonging to the first Brillouin zone and $\boldsymbol{\tau}$ a reciprocal lattice vector: $\mathbf{Q} = \boldsymbol{\tau} + \mathbf{q}$. The type of the dispersion is given - either optical (op) or acoustical (ac) - it refers to the Brillouin zone whose Bragg peak $\boldsymbol{\tau}$ - being nuclear or magnetic - is crossed.

$\mathbf{q}$	$\mathbf{Q}$	scan	$\boldsymbol{\tau}$	type	width ΔE [meV]
$(h,0,0)$	$(H,0,0)$	B1	$(2n,0,0)$ $n=0..2$	op	0.45 - 0.5
	$(H,0,-1/2)$	B2	$(1,0,-1/2)$	ac	
$(h,h,0)$	$(H,H,0)$	C	$(0,0,n)$ $n=0,1,2,3$	op	0.5
$(0,0,l)$	$(0,0,L)$	A1	$(n,0,0)$ $n=0,1,2$	op	0.3
	$(-1,0,L)$	A2	$(-1,0,n/2)$ $n=-1,1$	ac	0.3
$(0,k,0)$	$(0,K,1)$	D1	$(0,2,0)$	op	0.5
	$(0,K,3/2)$	D2	$(1,0,0)$	ac	0.5
$(0,k,k/2)$	$(0,K,K/2)$	E	$(2,0,0)$	op	0.5
	$(0,K,K/2)$	E	$(1,0,0)$	ac	0.5

and B2) or $(0,k,0)$ (scan A1 and A2) as well as the scans along $(0,k,k/2)$ (scan E) changes from acoustic to optical and vice versa due to the shape of the Brillouin zone, see Fig. 5.4. In that case the term 'optical' and 'acoustic' refers to the Brillouin zone whose center $\boldsymbol{\tau}$ is crossed.

We outline that scans in reciprocal space for a particular direction have been performed in the acoustic as well as in the optical zone.

Energy scans have been carried out parallel to $(0,0,l)$ (scan A1 and A2) through two different zones in reciprocal space: Recalling Fig. 5.4 it is clear that the scan A1 reveals the optical modes, because the wave vector $\mathbf{Q} = (0,0,L)$ is always in a Brillouin zone whose center is a nuclear Bragg peak. On the other hand the scan A2 ($\mathbf{Q} = (-1,0,L)$) goes through a magnetic Bragg point and the modes are therefore acoustic. Fig. 5.11 illustrates the experimental results obtained from the energy scans along $\mathbf{q} = (0,0,l)$ in the acoustic zones (A2) on the left side and in the optical zones (A1) on the right side. It is obvious that the upper two branches are parallel and that they exhibit a minimum of the excitation energy at the zone center, whereas the dispersion increases to a maximum at the zone boundary.

In the case of the acoustic branches the contour plot in panel (a) of Fig. 5.11 nicely displays the progression of the dispersion of the lowest branch which softens near the magnetic Bragg point $\mathbf{Q} = (-1,0,\pm 1/2)$ and gains a lot of intensity at the strong magnetic reflection $\mathbf{Q} = (-1,0,1/2)$ at the same time. The resulting dispersions are plotted in panel (b) with their corresponding intensities in (c). The dotted lines denote the zone center and zone boundaries. On the right side the corresponding graphs (d)-(f)

for the scans along $\mathbf{Q} = (0, 0, L)$ are shown. The width of the dispersion is approximately 0.4 meV.

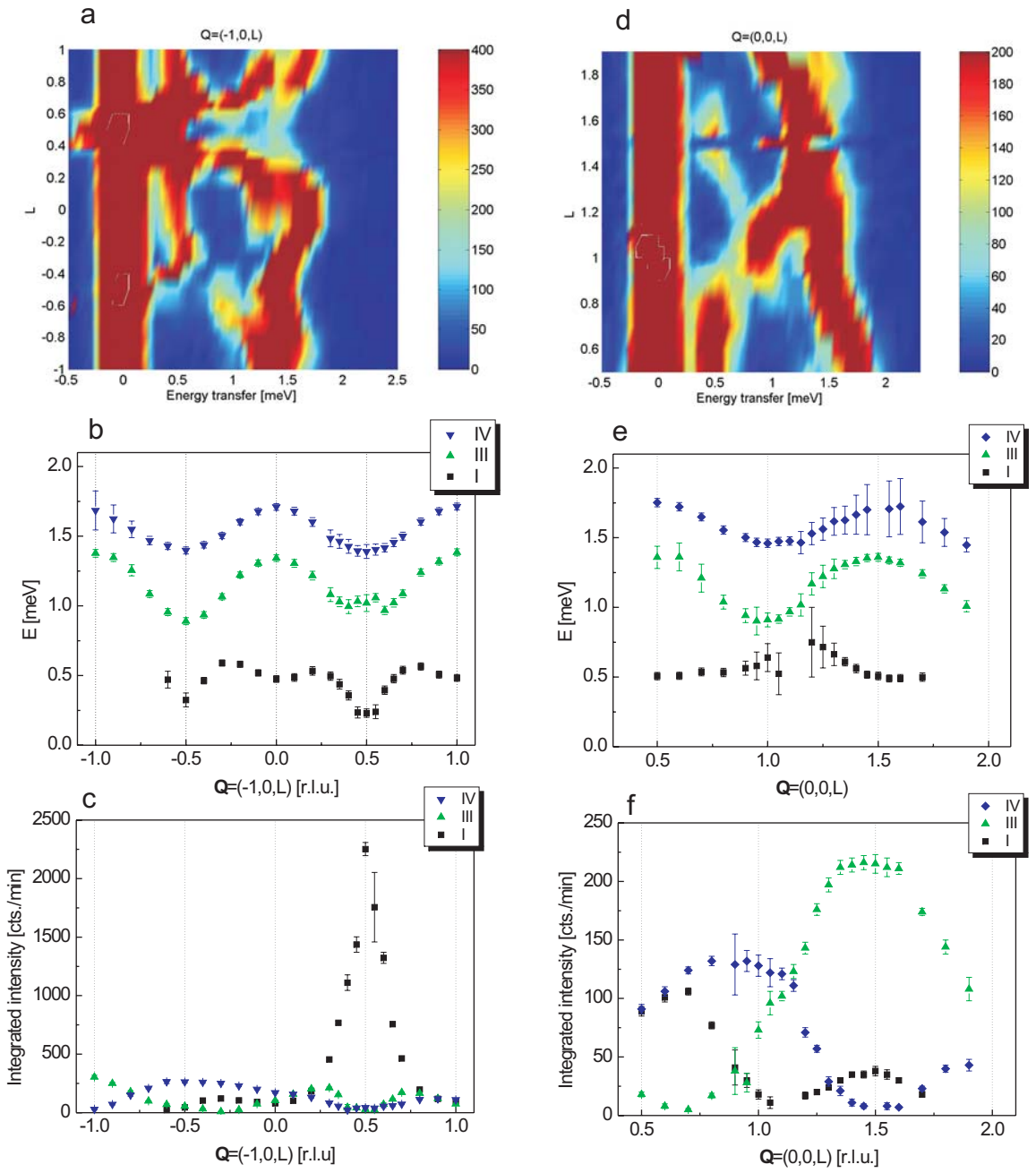

Figure 5.11: Experimental results for the dispersion along $\mathbf{Q} = (-1, 0, L)$ (a-c) and $\mathbf{Q} = (0, 0, L)$ (d-f). The contour plots in panel (a) and (d) summarize the energy scans taken at different $\mathbf{Q}$ values. (b) and (e) show the dispersion and (c) and (f) the corresponding intensity of the excitations, respectively. The zone center and the zone boundaries are indicated by dotted lines.

The dispersions and intensities along $\mathbf{q} = (h, 0, 0)$ are shown in Fig. 5.12. Panel (a) and (b) belong to the scan B2, i.e. to the wave vector $\mathbf{Q} = (H, 0, 1/2)$ crossing a magnetic

Bragg point, whereas (c) and (d) present the optical analogue along $\mathbf{Q} = (H, 0, 0)$ (scan B1). The width of the dispersion is 0.45-0.5 meV in the optical zone, thus the dispersion is slightly more pronounced than in the $(0, 0, l)$ direction. Note that we have not fully measured the acoustic zone along $(h, 0, 0)$.

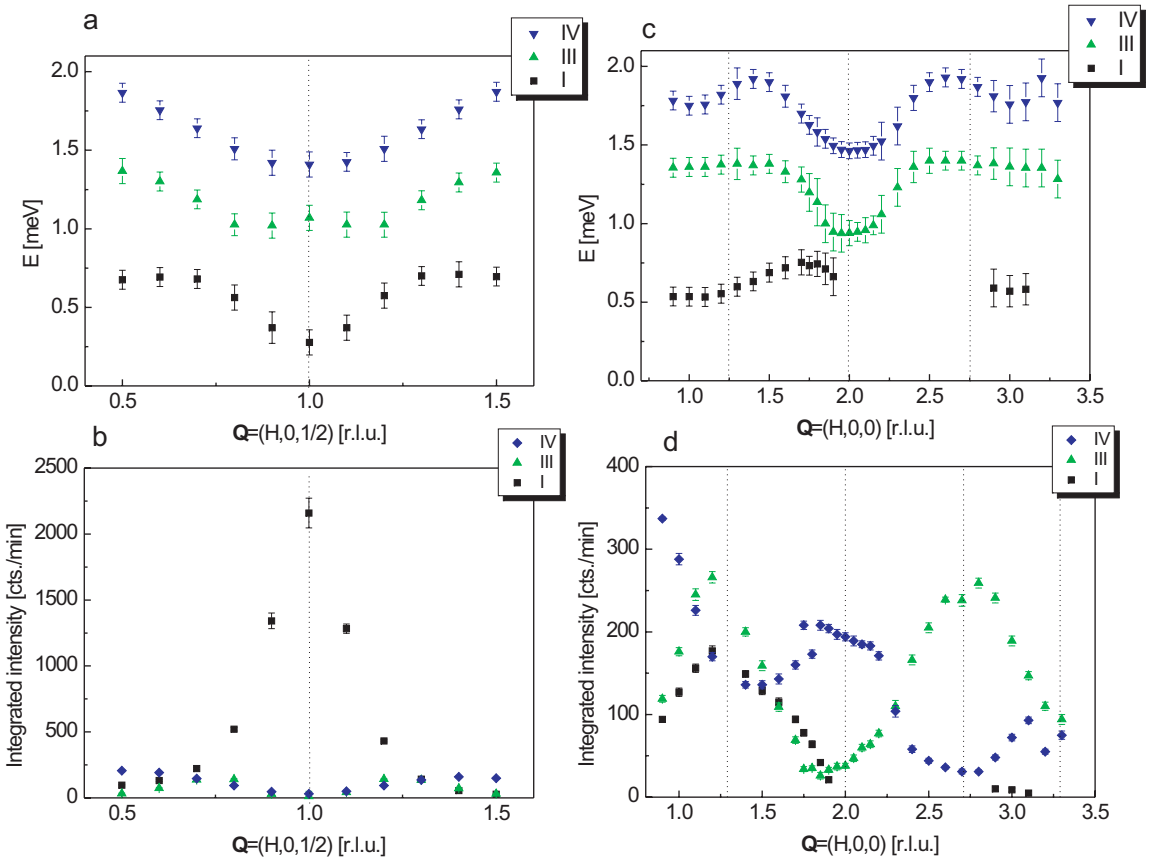

Figure 5.12: (a) Dispersion and (b) intensities along $\mathbf{Q} = (H, 0, 1/2)$ going through the magnetic Bragg point $(2, 0, 0)$. In (c) and (d) the dispersion and intensities along $\mathbf{Q} = (H, 0, 0)$, respectively, are shown. The dotted lines denote the zone center and zone boundaries.

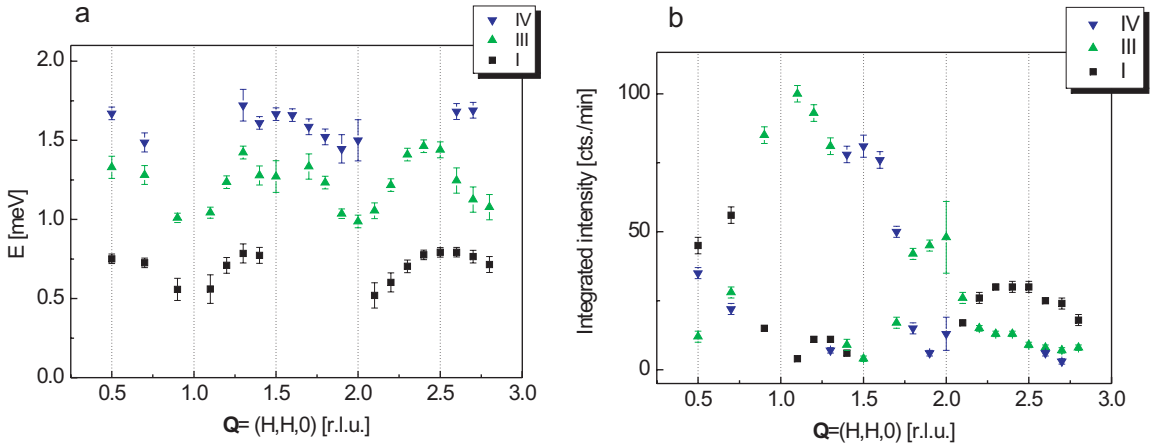

Figure 5.13: (a) Dispersion and (b) intensities along $\mathbf{Q} = (H, H, 0)$ where the branches are of optical type only.

Fig. 5.13 presents the dispersive behavior of the magnetic excitations in scan C along $\mathbf{Q} = (H, H, 0)$. The HK-plane is fully covered by optical Brillouin zones, therefore the excitations are optical.
The excitation energy of the lowest branch could be easily determined in the acoustic zone, scan A2 ($\mathbf{Q} = (-1, 0, L)$) and scan B2 ($\mathbf{Q} = (H, 0, 1/2)$) due to the well pronounced peaks. It seems that this branch behaves qualitatively different from the upper two: it still has a minimum at the zone center, but its maximum is between the zone boundary and the zone center. Hence it decreases to a local minimum at the zone boundary $\mathbf{Q} = (-1, 0, 0)$. Such a sign of a higher periodicity in $\mathbf{q}$ suggests that next next-nearest neighbor coupling may have to be included, this issue is addressed in Section 5.3.3.

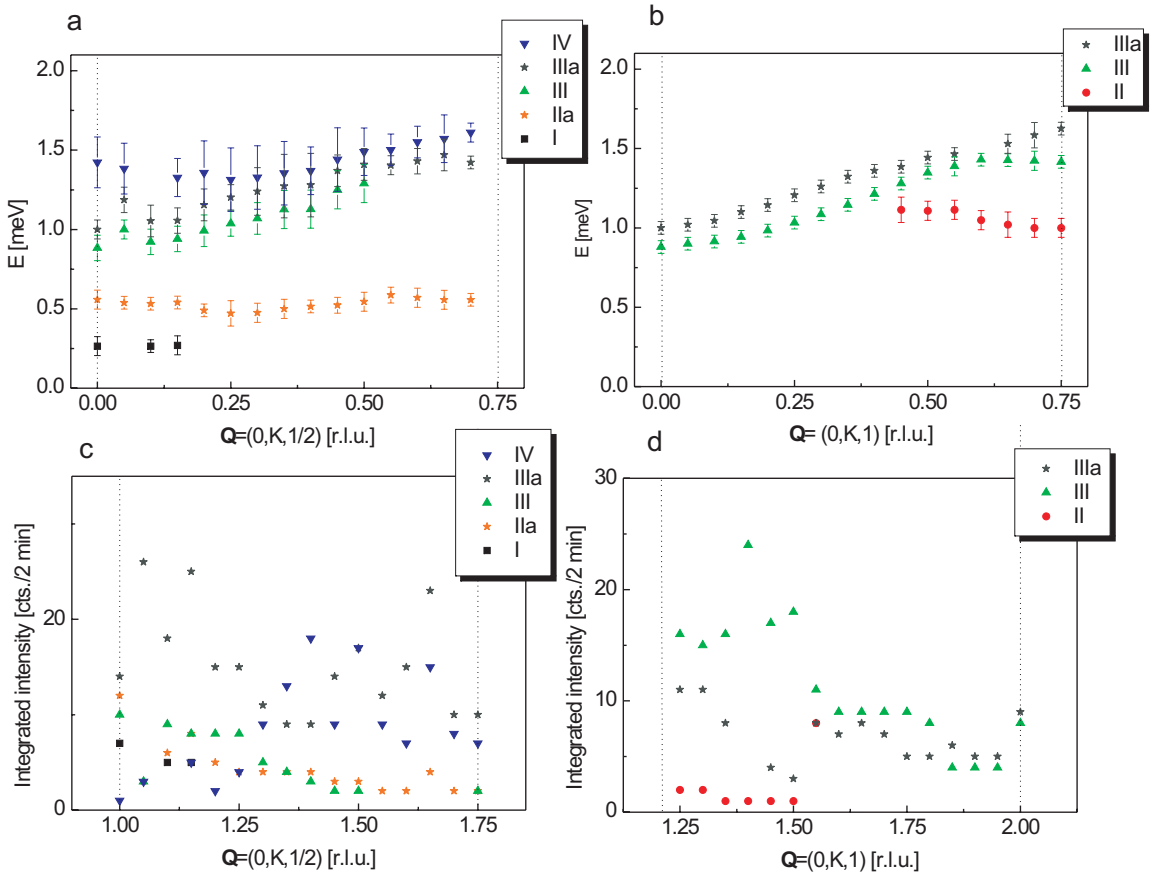

Figure 5.14: Panel (a) and (c) illustrate the dispersion and intensities along $\mathbf{Q} = (0, K, 1/2)$ where the acoustic zone center is crossed, hence the data belong to the acoustic branches. Similarly (b) and (d) display the dispersion and intensities along $\mathbf{Q} = (0, K, 1)$ and are therefore of optical nature.

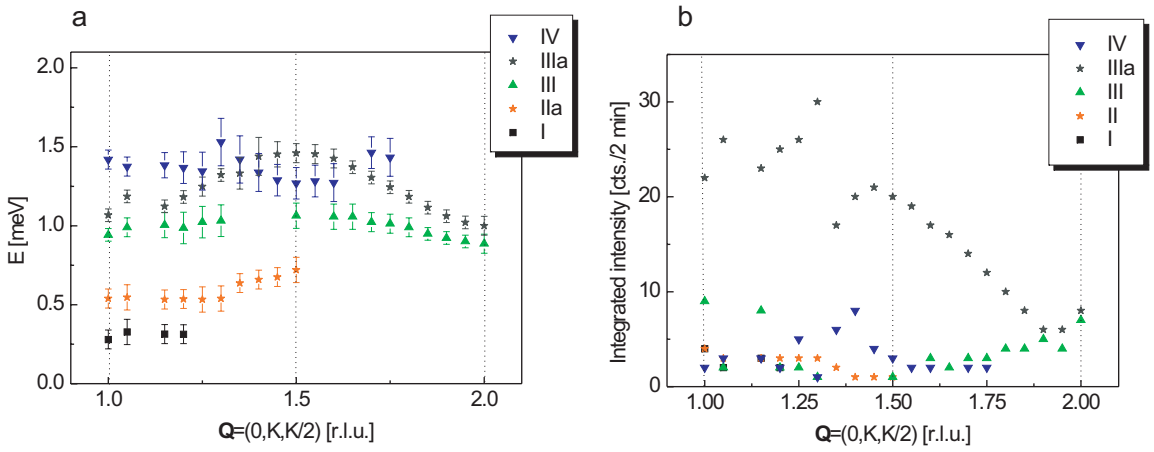

Figure 5.15: (a) Dispersion and (b) intensities along $\mathbf{Q} = (0, K, K/2)$. Up to $K = 1.5$ $\mathbf{Q}$ is in the acoustic zone, whereas for $1.5 \leq K \leq 2$ $\mathbf{Q}$ belongs to the optical zone.

The scans along $\mathbf{q} = (0, k, 0)$ have been performed at k_f=1.1 Å^{-1}, which yielded a much better resolution, see Table 3.2. The results are shown in Fig. 5.14 where we observed that two branches - labeled by III and IIIa - are very close and continue in a parallel way. It is worth mentioning that the width of the dispersion is around 0.5 meV for these branches, but the branches II (scan D2) is hardly dispersive. This observation is in agreement with the inelastic powder data, where the peak at 1.05 meV corresponding to transition II (see below) is much narrower than the other peaks. Also the branch IIa (scan D2) is almost flat. Furthermore we observe five branches along $\mathbf{Q} = (0, K, 1/2)$, whereas the scans along $\mathbf{Q} = (0, K, 1)$ as well as the directions described above (scan A1, A2, B1, B2 and C) revealed only three branches.
The dispersion along the diagonal direction $\mathbf{Q} = (0, K, K/2)$ is special in the sense that $\mathbf{Q}$ crosses the zone boundary between the acoustic and optical zone. As can be seen in Fig. 5.15 the transitions from acoustic to the optical branches are smooth, the dispersions do not jump.

Note that in the scans D1 and D2 as well as E, the intensity of the lowest mode is much smaller than the one of the other excitations. We observed this branch only near the magnetic Bragg point $\boldsymbol{\tau} = (0, 1, 0.5)$. The increased intensity near zero energy transfer in panel (a)-(c) of Fig. 5.10 is associated with an asymmetric shape of the elastic line, which remains unchanged in the whole scan and may originate from instrumental settings.

To summarize, we mention the most important observations:

- The observed excitations behave in a parallel manner in one particular direction. Exceptions are transition II, IIa and IV in the $(0, k, 0)$ and $(0, k, k/2)$ direction.
- The width of the dispersion is roughly 0.4 to 0.5 meV.
- The transition from the optical to the acoustic zone is smooth.

- The lowest excitation can be traced reliably only in scan A2 and B2, because its intensity is very low or even vanishing in the other scans.
- The acoustic branch of transition I exhibits a more pronounced dispersive behavior than its optical counterpart.
- Branch II and IIa as well as IIIa could be found only in scans involving the k-direction (scan D1, D2 and E).

As for the labeling and identifications of the excitations we refer to the following section.

5.4 Discussion

5.4.1 Magnetic structure

By analyzing the elastic scans at 15 K we confirmed the symmetry $C2/m$ already obtained from powder experiments [109]. In addition, the refinement of the lattice parameters yields values which are in excellent agreement with the results obtained from the diffraction experiments on polycrystalline α-$MnMoO_4$ [109].
The intensity of the $(-1, 0, 1/2)$ magnetic Bragg peak is proportional to the magnetization M, we therefore conclude that the phase transition into an anitferromagnetically ordered state occurs at 10.7±0.1 K in excellent agreement with the powder data [109]. We applied a fit to the data - as shown in Fig. 5.6 using the following power law near T_N:

$$M \sim |T - T_N|^{\beta}. \tag{5.41}$$

The critical exponent β turned out to be 0.388 ± 0.022 which is very close to the classical 3-D Heisenberg value of $\beta = 0.36$.
The observation of the magnetic Bragg peak $(-1, 0, 1/2)$ means a doubling of the unit cell along the c-axis as soon the temperature drops below T_N.
We found that the translational symmetry of the magnetic structure is described by a propagation vector $(1, 0, 1/2)$ in agreement with Ref. [287].

5.4.2 Powder experiments

Intracluster coupling

The measurements have been carried out at 1.5 K, therefore only the ground state is populated and we associate the four observed inelastic peaks with the four ground state transitions according to the selection rules in Eq. 5.17. The eigenenergies of the cluster system are given in Eq. 5.15 in terms of the two dominant exchange interaction J and J', along the edges of the tetramer and across the short diagonal of the Mn_4 rhombus, respectively.
From the parallel alignment of the spins within a cluster in the ordered phase, which has been determined by neutron diffraction, we conclude that J in Eq. 5.15 is dominant and positive, i.e. ferromagnetic, as has been pointed out already in Section 5.2.1. The interaction J' across the short diagonal can be either ferro- or antiferromagnetic which

Table 5.2: Exchange parameters determined from measurements on a polycrystalline powder of $MnMoO_4$.

interaction parameter	strength of interaction [meV]
J	0.051±0.004
J'	-0.019±0.003
J_{inter}	-4.5×10^{-3}

then in turn interchanges the states $|\Gamma_2\rangle$ and $|\Gamma_3\rangle$, see Fig 5.5.
However, the Mn_1-O_1-Mn_2 bridging angle of 130° favors a negative i.e. antiferromagnetic value of J'. Hence the four peaks I - IV in Fig. 5.7 are assigned to the following transitions [282] given Eq. 5.18 obeying the selection rules in Eq. 5.17:

$$\begin{aligned}
\text{Transition I: } |\Gamma_0\rangle &\rightarrow |\Gamma_1\rangle \qquad \Delta_1 = g\mu_B H_z = 0.66 \pm 0.17 \text{ meV} \\
\text{Transition II } : |\Gamma_0\rangle &\rightarrow |\Gamma_2\rangle \qquad \Delta_2 = 10J + 10J' + g\mu_B H_z = 1.05 \pm 0.08 \text{ meV} \\
\text{Transition III } : |\Gamma_0\rangle &\rightarrow |\Gamma_3\rangle \qquad \Delta_3 = 10J + g\mu_B H_z = 1.38 \pm 0.13 \text{ meV} \\
\text{Transition IV } : |\Gamma_0\rangle &\rightarrow |\Gamma_4\rangle \qquad \Delta_4 = 20J + g\mu_B H_z = 1.71 \pm 0.16 \text{ meV}
\end{aligned}$$

A least-squares fitting procedure yields $J = 0.051\pm0.004$ meV and $J' = -0.019 \pm 0.003$ meV for the intracluster coupling and for the energy associated with the molecular field we obtain $g\mu_B H = 0.72 \pm 0.04$ meV. The latter can be expressed in terms of intercluster exchange parameters according to Eq. 5.19: Taking each cluster as a unit, we then may write

$$g\mu_B H = 2\langle S\rangle z J_{inter}, \tag{5.42}$$

where the $\langle S\rangle = 10$ denotes the cluster spin, $z = 8$ is the number of nearest neighbors on the opposite sublattice. Hence the near-neighbor interaction parameter turns out to be $J_{inter} = -4.5 \times 10^{-3}$ meV [282]. J_{inter} being negative and about an order of magnitude smaller than the intracluster parameters J and J' is expected from the persistence of the cluster picture below T_N. These results are summarized in Table 5.2.
The molecular field parameter can be used to predict the 3D-ordering temperature using Eq. 5.20

$$\begin{aligned}
\theta &= \frac{S(S+1)}{3k_B} 8 J_{inter} \\
&\Rightarrow \theta = 11.9 \text{ K}
\end{aligned} \tag{5.43}$$

which is in reasonable agreement with the experimental T_N=10.7 K. This confirms the validity of the cluster picture, where each cluster is considered as one magnetic unit with a cluster spin $S = 10$ at a temperature of 1.5 K.
The intercluster coupling J_{inter} gives rise to a dispersive behavior of the magnetic excitations which will be addressed while discussing the single-crystal data.

Table 5.3: Experimental and calculated INS excitation energies and relative intensities. For the calculation of the intensities Eq. 5.44 were integrated over the same Q-range as the experimental data and scaled to 1 for transition I. The parameter values are given in Table 5.2.

transition	E_{obs} [meV]	E_{calc} [meV]	I_{obs}	I_{calc}
I	0.65±0.04	0.72	1.00±0.02	1.00
II	1.04±0.03	1.04	0.63±0.02	0.62
III	1.36±0.05	1.23	0.81±0.08	0.65
VI	1.68±0.10	1.74	0.61±0.10	0.69

We have also computed the Q-dependencies of the INS intensities. The formula for the cross section for magnetic excitations within a tetramer of rhombohedral symmetry is given in Eq. 3.18 in Chapter 3. The intensities σ_i for the individual transitions then read

$$\begin{aligned} \text{II:} \qquad & \Delta S_{12} = -1,\ \Delta S_{34} = 0,\ \Delta S = -1,\ \Delta M = -1 \\ \sigma_{II} \quad \propto \quad & F^2(Q) \left[1 - \frac{sin(QR_{12})}{QR_{12}}\right] |\langle \hat{T}_1 \rangle|^2 \end{aligned}$$

$$\begin{aligned} \text{III:} \qquad & \Delta S_{12} = 0,\ \Delta S_{34} = -1,\ \Delta S = -1,\ \Delta M = -1 \\ \sigma_{III} \quad \propto \quad & F^2(Q) \left[1 - \frac{sin(QR_{34})}{QR_{34}}\right] |\langle \hat{T}_3 \rangle|^2 \end{aligned}$$

$$\begin{aligned} \text{I \& IV:} \qquad & \Delta S_{12} = 0,\ \Delta S_{34} = 0,\ \Delta S = 0(-1),\ \Delta M = -1 \\ \sigma_{IV} \quad \propto \quad & F^2(Q) \left(\left[1 + \frac{sin(QR_{12})}{QR_{12}}\right] |\langle \hat{T}_1 \rangle|^2 \right. \\ & + \left[1 + \frac{sin(QR_{34})}{QR_{34}}\right] |\langle \hat{T}_3 \rangle|^2 \\ & \left. +4 \left[\frac{sin\left(\frac{Q}{2}\sqrt{R_{12}^2 + R_{34}^2}\right)}{\left(\frac{Q}{2}\sqrt{R_{12}^2 + R_{34}^2}\right)} \right] \langle \hat{T}_1 \rangle \langle \hat{T}_3 \rangle \right). \end{aligned} \tag{5.44}$$

We found that the calculated energies as well as INS intensities are in excellent agreement with the observed values, see Table 5.3. The Q-dependencies of the four transitions is shown in Fig. 5.8.
These arguments strongly supports the cluster formation in α-$MnMoO_4$.

We would like to emphasize that the ferromagnetic nature of the dominant interaction parameter J along the edges of the rhombus is extraordinary: In most insulating Mn^{2+} and high spin Fe^{3+} compounds, nearest neighbor superexchange is antiferromagnetic. We ascribe the ferromagnetic coupling in the Mn_4 clusters to the particular bonding situation

at the oxygen atom labeled O_1 in Fig. 5.1. We note a particularly small angle of 95.7° at O_1 for the pathway corresponding to J. And this is the dominant ferromagnetic interaction within the cluster.
The net value of interaction J between two Mn^{2+} ions is composed of $5 \times 5 = 25$ orbital contributions, where some of them are ferro- and other antiferromagnetic. The balance can tip towards a ferromagnetic net J, when the bridging angles Φ at the ligand approach 90°.

5.4.3 Intercluster coupling

First the observed excitations have to be identified with the cluster transitions. The powder measurements collect the excitation energies over a large Q-range, where the $\mathbf{q}$-values at the zone boundary mainly contribute to the cross section: In order to understand that, let us consider the density of states $D(E)$:

$$D(E)dE = \frac{V}{(2\pi)^3}\left(\int_{E(\mathbf{q})=const.} \frac{d\mathbf{f}}{|grad_{\mathbf{q}}E(\mathbf{q})|}\right)dE. \tag{5.45}$$

The main contribution to $D(E)$ is provided by those $\mathbf{q}$-points in reciprocal space where $|grad_{\mathbf{q}}E(\mathbf{q})|$ vanishes (van Hove singularity). The dispersions are flat at the zone center and at the zone boundary, but at the zone center the volume element is small, thus the $\mathbf{q}$-points at the zone boundary provide the largest part of the density of states. Hence the excitations observed in the powder experiment E_i^p are mainly determined by the energies obtained by the single-crystal experiments at the zone boundary E_i^{sc}:

$$E_i^{sc}(\mathbf{q} = \text{zone boundary}) \approx E_i^p.$$

Another tool to find out which mode belongs to which transition is the intensity of the peaks: the neutron scattering cross section is proportional to the product of structure factor, form factor and transition matrix elements, i.e. selection rules: if these terms vanishes along a direction for a specific mode, the occurrence of the corresponding mode is prohibited.

Structure factor

The geometry of a cluster goes into the neutron scattering cross section through the structure factor $S(\mathbf{Q})$ as written in Eq. 3.20. For a tetranuclear cluster, the structure factor has been given in Chapter 3, see Eqs. 3.20 and 3.21.
Inserting the states of the cluster elaborated in Eq. 5.16 and their transition matrix elements given in Table B.1 in Appendix B, we find that the intensities of the four transitions are proportional to the following expressions:

$$\begin{aligned}
\text{I \& IV:}\quad \sigma_{I,IV} &\propto (-0.79)^2\,[1 + cos(\mathbf{Q}\cdot\mathbf{R}_{12}) + 1 + cos(\mathbf{Q}\cdot\mathbf{R}_{34}) \\
&\quad +4\cdot cos(\mathbf{Q}\cdot\mathbf{R}_{13}))] \\
\text{II:}\quad \sigma_{II} &\propto (1.12)^2\,[1 - cos(\mathbf{Q}\cdot\mathbf{R}_{12})] \\
\text{III:}\quad \sigma_{III} &\propto (1.12)^2\,[1 - cos(\mathbf{Q}\cdot\mathbf{R}_{34})]
\end{aligned} \tag{5.46}$$

Note that in principle also effects due to interference of eigenfunctions have to be taken into account [131]. But the above consideration is sufficient to determine a total vanishing of a transition along a specific direction in reciprocal space.
Hence we conclude that transition II and III vanish for certain directions:

$$\begin{aligned} \text{II:} \quad & S(\mathbf{Q}) = 0 \quad \text{for } \mathbf{Q} = (H,0,0),(0,0,L) \\ \text{III:} \quad & S(\mathbf{Q}) = 0 \quad \text{for } \mathbf{Q} = (0,K,0) \end{aligned} \tag{5.47}$$

Indeed the energy scans B1 and B2 ($\mathbf{q} = (h,0,0)$) as well as the scans A1and A2 ($(0,0,l)$) revealed only three inelastic peaks, which could be identified as transition I, III and IV. As for the direction parallel to $\mathbf{q} = (0,k,0)$, we have chosen the scans D1 and D2 in order to obtain the k-dependent dispersion. The reason is that the scans along $\mathbf{Q} = (0,K,0)$ have been taken with an experimental setup ($E_f = 4.9$ meV) where the resolution turned out to be insufficient to identify the peaks. In addition the intensity in this Brillouin zone was too weak. Note that in the scans D1 and D2 all transitions are allowed.
In the other $\mathbf{Q}$-directions, no transition is prohibited regarding the structure factor.

Identification of the branches

According to the previous paragraph, transition II is not allowed along $\mathbf{Q} = (0,0,L)$ (scan A1). At the zone boundary there are three peaks at energies 0.48meV, 1.38meV and 1.71 meV, see panel (b) of Fig. 5.11, which can be identified unambiguously with transition I, III and IV observed in the powder experiment [282] according to Table 5.3. The acoustic counterparts can easily be found in scan A2, see panel (a) of Fig. 5.11. The same considerations hold for the $\mathbf{q} = (h,0,0)$ (scan B1 and B2). In scan C, the identification of the exitations can be obtained by symmetry reasons: at the zone center the energies have to be equal to the ones at the zone center of scan A1.

The situation becomes more complicated in the $\mathbf{q} = (0,k,0)$ and $\mathbf{q} = (0,k,k/2)$ direction. The same considerations as described above are applied in order to identify transition I, III and IV. However, in all these scans we observe an excitation, labeled by IIIa, close to transition III. Moreover, an unidentified transition IIa occurs in scan D1 and E. These excitations cannot be explained within the frame of the RPA cluster model. We refer to its limits in the last paragraph of this section.

Interaction parameters

Before we are capable to explain the dispersive behavior of the magnetic excitations shown in Section 5.5.3., we have to determine a set of reasonable cluster-cluster interaction parameters. As a first approximation we restrict the possible interaction partners to the clusters within the nearest-neighbor coordination shell.
Considering the direct distance from the center of mass of the center tetramer to its neighbors yields eight nearest neighbors. But in reality, the interaction occurs through the pathway Mn-O-Mo-O-Mn. Hence we take into account all neighbors which are connected to the center tetramer through an exchange pathway of type Mn-O-Mo-O-Mn.

Table 5.4: Coupling between different sublattices and between ions belonging to the same sublattice.

J_i coupling parameter spin alignment	interaction vector $\vec{\rho_i}$	exchange pathway angles [°]	length of exchange pathway [Å]
J_5 ↑↓	±(1/2,1/2,0) ±(-1/2,1/2,0)	Mn2-O3-Mo1-O4-Mn1 159, 107, 159	7.815
J_7 ↑↓	±(0,0,1)	Mn2-O3-Mo1-O3-Mn2 159, 113, 159	7.709
J_6 ↑↑	±(0,1,0)	Mn1-O5-Mo2-O5-Mn1 167, 111, 167	7.684
J_8 ↑↑	±(1/2,1/2,1) ±(-1/2,1/2,1) ±(1/2,-1/2,1) ±(1/2,1/2,-1)	Mn2-O4-Mo1-O3-Mn2 123, 107, 159	7.872
J_9 ↑↑	±(1,0,0)	Mn2-O3-Mo1-O3-Mn2 159, 113, 159	7.829
J_{10} ↑↑	±(1,0,1) ±(-1,0,1)	Mn2-O4-Mo1-O4 -Mn2 124, 117, 124	8.037

Therefore we have to deal with 22 interaction partners in total.
The different coupling parameters J_i are summarized in Table 5.4, two of them are antiferromagnetic, whereas four parameters describe the interaction between cluster spins of the same sublattice.
Note that we observed a dip in the dispersion of transition I in the acoustic zone, scan A2, which may originate from a next-nearest-neighbor interaction. But such an interaction would be active over a distance of 14.3 Å, which is much larger than the other exchange pathways. In addition, the acoustic branch of transition I is the only excitation which shows such a behavior. We therefore neglect any kind of next-nearest-neighbor interaction.

Application of the cluster model

As presented in Section 5.4.2., the analysis of the powder data yielded a mean-field value for the intercluster interaction, see Eq. 5.42 and Table 5.2. However, the individual interaction parameters associated with the dispersive behavior of the magnetic excitations, can only be obtained by single-crystal experiments. To do so we apply the RPA cluster model developed in Section 5.3.3. to α-$MnMoO_4$.
Since we have worked out the interaction parameters in the previous paragraph, we are now ready to give an explicit expression for the Fourier transformed coupling constant: All couplings are symmetric i.e. for every interaction partner at site $\mathbf{R}_i$ there is another one located at $-\mathbf{R}_i$ (see Table 5.4), thus the Fourier transformed coupling constants $J_{AA}(\mathbf{q})$ and $J_{AB}(\mathbf{q})$ are real:

$$\begin{aligned} J_{ss'}(\mathbf{q}) &= \frac{1}{N}\sum_{i\neq j} J_{ij} e^{-i\mathbf{q}\cdot(\mathbf{R}_i-\mathbf{R}_j)} = \sum_{i\neq j} J_{ij} e^{-i\mathbf{q}\cdot(\mathbf{R}_{ij})} \\ &= 2\sum_{i\neq j} J_{ij} cos(\mathbf{q}\cdot\mathbf{R}_{ij}) \in \mathbb{R} \qquad s,s' \in A,B. \end{aligned} \tag{5.48}$$

Taking $\mathbf{q}=(h,k,l)$, $\mathbf{r}=(r_x,r_y,r_z)$ and recalling that $\mathbf{q}\cdot\mathbf{r} = 2\pi(h\cdot r_x + k\cdot r_y + l\cdot r_z)$ the explicit expressions for $J_{AA}(\mathbf{q})$ and $J_{AB}(\mathbf{q})$ read according to Table 5.4

$$\begin{aligned} J_{AB}(\mathbf{q}) &= 2J_5\left[cos(\pi(h+k)) + cos(\pi(-h+k))\right] + 2J_7 cos(2\pi l) \\ J_{AA}(\mathbf{q}) &= 2J_6 cos(2\pi k) + 2J_9 cos(2\pi h) \\ &\quad +2J_8\left[cos(\pi(h+k+2l)) + cos(\pi(-h+k+2l))\right. \\ &\quad \left. +cos(\pi(h-k+2l)) + cos(\pi(h+k-2l))\right] \end{aligned} \tag{5.49}$$

In order not to complicate matters, we omit the interaction parameter J_{10} and therewith reduce the set of fitting parameters. Note that the parameters J_7 and J_9 are a projection of J_{10} onto the ab-plane and the bc-plane, respectively. We insert $J_{AB}(\mathbf{q})$ and $J_{AA}(\mathbf{q})$ as well as the matrix elements M_{0j} given in Table B.1 of Appendix B.1 into the dispersion formula in Eq. 5.34. Furthermore we assume that the coupling parameters depend on the particular transition, more precisely on the matrix element, see Eq. 5.40. Thus the concrete expression for the eight dispersion relations turns out to be

$$\begin{aligned} \hbar\omega(\mathbf{q})_{1,4} &= \Delta_1 - (0.79)^2\cdot(2J_6 cos(2\pi k) + 2J_8 cos(\boldsymbol{\rho}_i\cdot\mathbf{q}) + 2J_9 cos(2\pi h) \\ &\quad \pm|2J_5\left[cos(\pi(h+k)) + cos(\pi(-h+k))\right] + 2J_7 cos(2\pi l)|) \\ \hbar\omega(\mathbf{q})_{2,3} &= \Delta_1 - (0.79)^2\cdot(2J_6 cos(2\pi k) + 2J_8 cos(\boldsymbol{\rho}_i\cdot\mathbf{q}) + 2J_9 cos(2\pi h) \\ &\quad \pm|2J_5\left[cos(\pi(h+k)) + cos(\pi(-h+k))\right] + 2J_7 cos(2\pi l)|) \end{aligned} \tag{5.50}$$

In the case of J_8 we have used the abbreviation $\boldsymbol{\rho}_i$ given in Table 5.4 and $\mathbf{q}=(h,k,l)$. Note that the coupling parameters J_i are different for different transitions, so that in fact

$$J_i \equiv J_i(|\Gamma_0\rangle,\Gamma_n\rangle), \quad n=1..4,\ i=5..9$$

according to the tensor model developed in Section 5.2.3.
We apply the simplest approximation of the tensor model in Eq. 5.40 to the coupling parameters of branches I-IV:

$$\begin{aligned} J_i^{0n}\cdot M_{0n}^2 &= J_i^{0m}\cdot M_{0m}^2 \quad n,m=1..4, \quad i=5..9 \\ &\Rightarrow \begin{cases} J_i^{02} = J_i^{03} & i=5..9 \\ J_i^{01} = J_i^{04} & i=5..9 \end{cases} \end{aligned} \tag{5.51}$$

To summarize we implemented the following constraints in a least-squares fitting procedure:

- One branch is simultaneously fitted in all directions.

Table 5.5: The values of the coupling parameters resulting from a least-squares fitting procedure based on the RPA cluster model. The coupling parameters are renormalized to M_{02}, see Eq. 5.51.

Δ_I [meV]	0.65±0.02
Δ_{II} [meV]	1.07±0.02
Δ_{III} [meV]	1.27±0.02
Δ_{IV} [meV]	1.75±0.02
Δ_{IIa} [meV]	0.75±0.02
Δ_{IIIa} [meV]	1.4±0.02
J_6 [μeV]	20±0.5
J_8 [μeV]	19±0.5
J_9 [μeV]	49±0.8
J_5 [μeV]	-10±0.5
J_7 [μeV]	-10±0.5

- The coupling parameters of branches I -IV are related through their matrix elements M_{0n}.

The results of the fitting procedure are displayed in Figs. 5.16 and 5.17, where the data are presented in the reduced Brillouin zone i.e. as a function of $\mathbf{q}$ instead of $\mathbf{Q}$ like in Figs. 5.11- 5.15. The plots (a) and (b) on the left side show the acoustic branches and on the right side the plots (c)-(e) correspond to the optical branches. Note that along $\mathbf{q} = (h, 0, 0)$ we restricted the fit to the $\mathbf{q}$-points belonging to the same Brillouin zone. The constraint in Eq. 5.51 leads to a reasonable fit, see Figs. 5.16 and 5.17.
From these fits we deduce the values of the coupling parameters, the results are assembled in Table 5.5. Note that the values of Δ_I, Δ_{II}, Δ_{III} and Δ_{IV} are in excellent agreement with the peak positions from the powder experiment.
Apart from the unexplained excitations IIa and IIIa, the experimental data are in good agreement with the fit. We therefore draw the conclusion that the title compound can be partly understood as a cluster system.

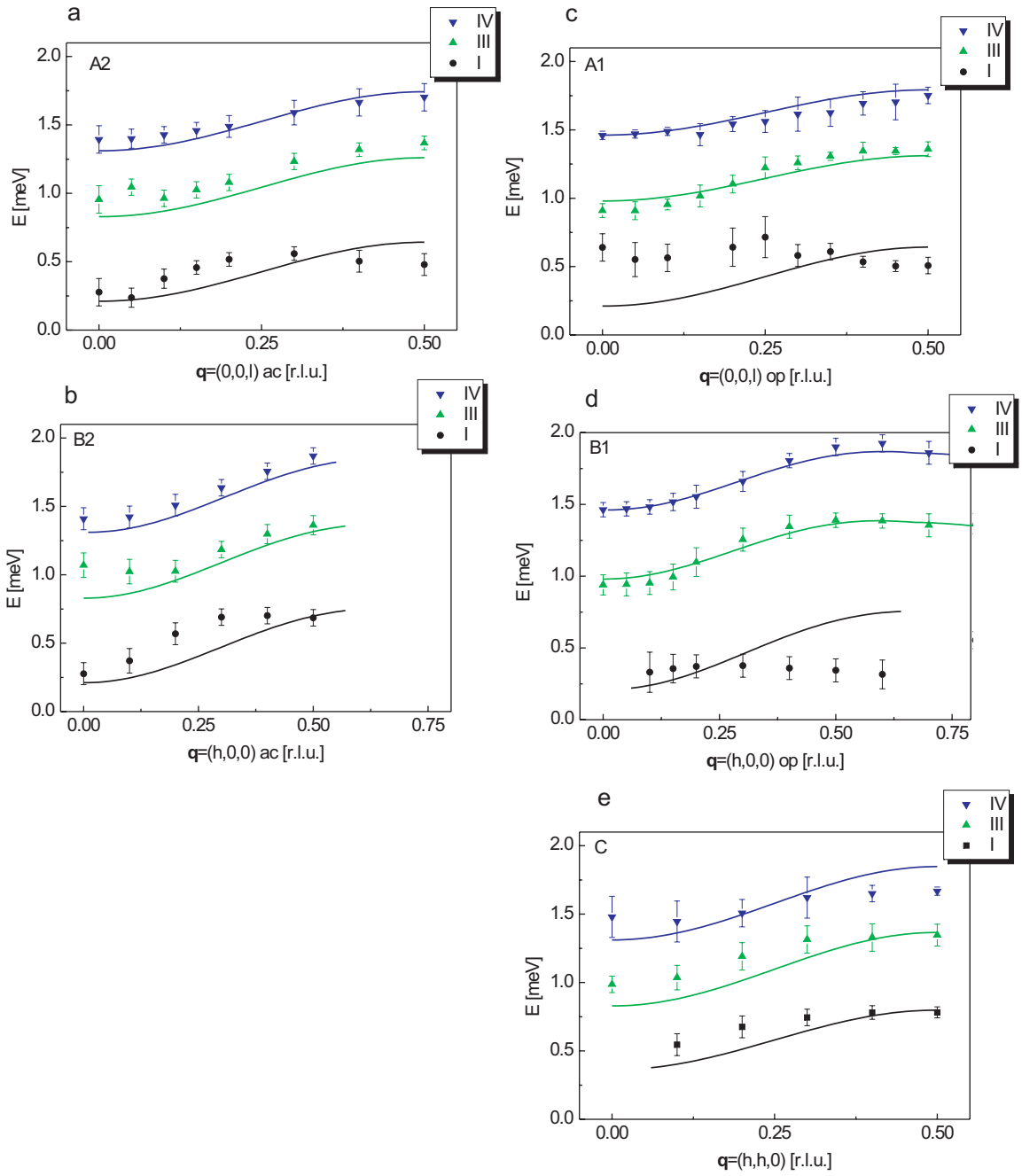

Figure 5.16: Energy dispersion in the reduced Brillouin zones in the a^*b^*-plane. Panel (a) and (b) show the energy dispersions in the $(0, 0, l)$ direction (ac=acoustic and op=optical), panel (c)-(e) display the fit of the experimental data in the a^*b^* plane. The solid lines are the results of a least-squares fitting procedure based on a RPA cluster model as explained in the text.

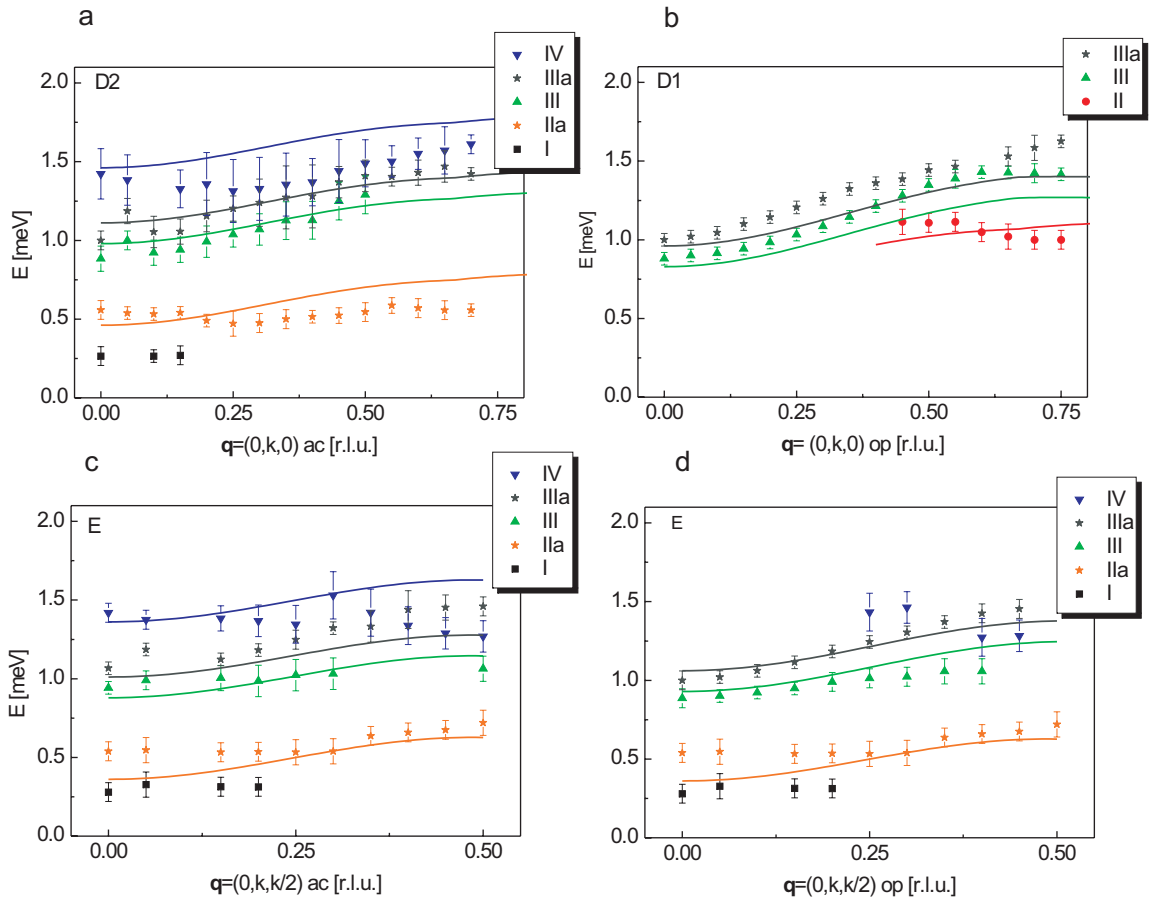

Figure 5.17: Energy dispersion in the reduced Brillouin zones in the b^*c^*-plane. Panel (a) and (b) show the energy dispersions along $(0, k, 0)$ in the acoustic (ac) and optical (op) zone, panel (c) and (d) display the acoustic (ac) and optical (op) energy dispersion in the b^*c^*-plane. The solid lines are the results of a least-squares fitting procedure based on a RPA cluster model as explained in the text.

Limits of the cluster model

The powder data are in excellent agreement with the cluster model and so are parts of the single-crystal data. However, some of the single-crystal experiments cannot be explained by the RPA cluster model, in particular the occurrence of transition IIa and IIIa, which reveals the limitations of the cluster picture. The powder data give no indication of the existence of an additional excitation at approximately 0.75 meV, whereas the excitation IIIa might be contained in the broad peak of the powder spectrum, see Fig. 5.9.
Another point is that at first sight it is surprising to find five branches along $\mathbf{Q} = (0, K, 1/2)$, because the cluster model predicts eight ground state transitions, four in the acoustic zone and four in the optical zone.
Possible explanations are:

- transition from an excited state to a higher excited state:
  However, at 1.5 K even the first excited state being at approximately $\hbar\omega \approx 0.3$ meV, is only weakly populated:

$$\frac{1}{e^{\hbar\omega/k_BT} - 1} \approx 0.01 \quad \text{Bose-Einstein population factor.} \tag{5.52}$$

  But anyway, the lowest mode vanishes rapidly along $(0, K, 1/2)$ with increasing K. Hence the interpretation of one of these peaks as a transition from the first excited state to a higher-lying state fails.

- phonons:
  It is possible that the excitations IIa or IIIa arise from a phonon. In order to verify this hypothesis it is necessary to study the temperature dependence of the transitions in question.

- Van Vleck interaction between magnons and magnetic excitations:
  The so-called van Vleck interaction describes the coupling of a magnon with an exciton associated with a transition between higher-lying magnetic states, which has been pointed out in Refs. [288, 289]. The transitions III and IIIa along $\mathbf{q} = (0, k, 0)$ show parallel dispersion branches, separated by approximately 0.2 meV. This energy difference corresponds more or less to the energy of transition I. Hence one may conclude that the additional peak in the neutron spectra originate from a resonance between the first ground state transition (transition I) and a transition between higher-lying levels of comparable energy. Similar considerations also apply to the excitation IIa: The energy difference between transition IIa and IV amounts to 1.0 meV, which corresponds to branch II.

Within a spin-wave model it is not surprising to find five branches along $\mathbf{Q} = (0, K, 1/2)$, and three excitations along ($\mathbf{Q} = (0, K, 1)$, because the total number of excitations along one particular direction is supposed to be eight corresponding to eight spins in the magnetic unit cell whereas the cluster model predicts eight ground state transitions, four in the acoustic zone and four in the optical zone.
Moreover, the RPA cluster model cannot explain why the dispersive behavior of transition I is more pronounced in the acoustic zone than in the optical zone.

5.5 Toy model: dimer chain

This section is dedicated to a toy model of dimer clusters whose dispersion relations will be computed within linear spin-wave theory. The idea is to study the influence of interaction (intra- and interdimer) and anisotropy parameters on the energy dispersion within a model as simple as possible.
How does a strong dimerization affect the dispersion? How does the anisotropy come into play? Furthermore we will also apply the cluster model introduced in Section 5.3 and compare these results with the ones obtained from linear spin-wave theory.
Finally we intend to derive qualitative features for the 3D crystal α-$MnMoO_4$.

5.5.1 Presentation of the model and dispersion relations

The toy model is sketched in Fig. 5.18. The chemical unit cell contains one atom, whereas four spins build up the magnetic unit cell, they are equally separated by a distance a. These four spins are arranged in dimers: the spins aligned ferromagnetically form a cluster with an intradimer interaction of strength J. The interaction between the clusters is of antiferromagnetic nature, where J' sets the scale of interaction between the neighboring spins of two different dimers. Hence the situation is qualitatively similar to the magnetic structure of α-$MnMoO_4$, except that here we consider dimers instead of tetramers and we restrict the discussion to a one-dimensional system.

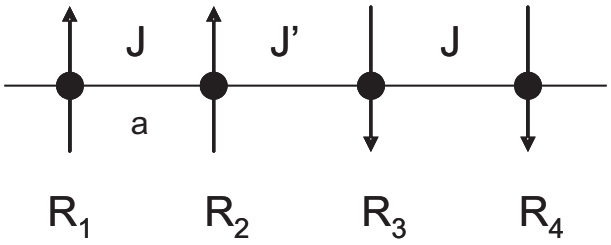

Figure 5.18: 1D-toy model: the magnetic unit cell contains four spins where two of them form a dimer. Within a dimer, the spins are ferromagnetically aligned described by J, whereas J_1 is the antiferromagnetic interdimer coupling.

The Hamiltonian describing the system of Fig. 5.18 including an anisotropic exchange D reads

$$\begin{aligned}
\mathcal{H} &= J\sum_i \left[\mathbf{S}^A_{i,1}\mathbf{S}^A_{i,2} + \mathbf{S}^B_{i,3}\mathbf{S}^B_{i,4}\right] \\
&\quad + J'\sum_i \left[\mathbf{S}^A_{i,2}\mathbf{S}^B_{i,3} + \mathbf{S}^A_{i,1}\mathbf{S}^B_{i-1,4} + \mathbf{S}^A_{i+1,1}\mathbf{S}^B_{i,4}\right] \\
&\quad + D\sum_i \left[(\mathbf{S}^A_{i,1})^2 + (\mathbf{S}^A_{i,2})^2 + (\mathbf{S}^B_{i,3})^2 + (\mathbf{S}^B_{i,4})^2\right] \\
&= J\sum_i \left[\mathbf{S}^A_{i,1}\mathbf{S}^A_{i,2} + \mathbf{S}^B_{i,3}\mathbf{S}^B_{i,4}\right] \\
&\quad + J'\sum_i \left[\mathbf{S}^A_{i,2}\mathbf{S}^B_{i,3} + \mathbf{S}^A_{i,1}\mathbf{S}^B_{i-1,4} + \mathbf{S}^A_{i+1,1}\mathbf{S}^B_{i,4}\right] \\
&\quad + 2D\sum_i \left[(\mathbf{S}^A_{i,1})^2 + (\mathbf{S}^B_{i,3})^2\right]
\end{aligned} \tag{5.53}$$

We intend to compute the eigenvalues of this system. To do so, we apply linear spin-wave theory as introduced in Chapter 2. Hence the first step is to perform the linear Holstein-Primakoff transformation for the sublattices A and B:

$$\begin{aligned}
S^{A+}_j &= \sqrt{2S}a_j \qquad j=1,2 & S^{B+}_j &= \sqrt{2S}b^\dagger_j \quad j=3,4 \\
S^{A-}_j &= \sqrt{2S}a^\dagger_j & S^{B-}_j &= \sqrt{2S}b_j \\
S^{Az}_j &= S - a^\dagger_j a_j & S^{Bz}_j &= -(S - b^\dagger_j b_j)
\end{aligned} \tag{5.54}$$

Next we introduce the Fourier transform for the 2 sublattices

$$\begin{aligned}
a_n &= \frac{1}{\sqrt{N}}\sum_q e^{iqR_n}a_{q,n} \quad n=1,2 & b_n &= \frac{1}{\sqrt{N}}\sum_q e^{-iqR_n}b_{q,n} \quad n=3,4 \\
a^\dagger_n &= \frac{1}{\sqrt{N}}\sum_q e^{-iqR_n}a^\dagger_{q,n} & b^\dagger_n &= \frac{1}{\sqrt{N}}\sum_q e^{iqR_n}b^\dagger_{q,n}
\end{aligned} \tag{5.55}$$

where $a^\dagger_q$ and a_q, $b^\dagger_q$ and b_q create or annihilate a magnon on the sublattice A and B, respectively. Applying these transformations yields the Hamiltonian of the dimer system expressed in terms of creation and annihilation operators:

$$\begin{aligned}
\mathcal{H} &= JS\sum_q \Big[e^{-iqa}a_{q,1}a^\dagger_{q,2} + e^{iqa}a^\dagger_{q,1}a_{q,2} + NS - a^\dagger_{q,1}a_{q,1} - a^\dagger_{q,2}a_{q,2} \\
&\quad + e^{-iqa}b_{q,3}b^\dagger_{q,4} + e^{iqa}b^\dagger_{q,3}b_{q,4} + NS - b^\dagger_{q,3}b_{q,3} - b^\dagger_{q,4}b_{q,4}\Big] + 2JNS^2 \\
&\quad + J'S\sum_q \Big[e^{-iqa}a_{q,2}b^\dagger_{q,3} + e^{iqa}a^\dagger_{q,2}b_{q,3} - NS + a^\dagger_{q,2}a_{q,2} + b^\dagger_{q,3}b_{q,3} \\
&\quad + e^{-iqa}a_{q,1}b^\dagger_{q,4} + e^{iqa}a^\dagger_{q,1}b_{q,4} - NS + a^\dagger_{q,1}a_{q,1} + b^\dagger_{q,4}b_{q,4} \\
&\quad + e^{-iqa}a_{q,1}b^\dagger_{q,4} + e^{iqa}a^\dagger_{q,1}b_{q,4} - NS + a^\dagger_{q,1}a_{q,1} + b^\dagger_{q,4}b_{q,4}\Big] - 4J'NS^2 \\
&\quad + DS\sum_q \Big[4SN - a^\dagger_{q,1}a_{q,1} - a^\dagger_{q,2}a_{q,2} - b^\dagger_{q,3}b_{q,3} - b^\dagger_{q,4}b_{q,4}\Big] + 4DNS^2
\end{aligned} \tag{5.56}$$

We then symmetrize the Hamiltonian using the commutator relations

$$\begin{aligned}[a_{q,n}, a^\dagger_{q',m}] &= [b_{q,n}, b^\dagger_{q',m}] = \delta_{q,q'}\delta_{n,m} \\ & [a_{q,n}, b_{q',m}] = [a^\dagger_{q,n}, b^\dagger_{q',m}] = 0. \end{aligned} \tag{5.57}$$

We may write the Hamiltonian of Eq. 5.56 as

$$\mathcal{H} = \mathcal{H}_0 + \mathcal{H}_q \tag{5.58}$$

where constant terms are collected in $\mathcal{H}_0$ and the q-dependency goes into $\mathcal{H}_q$.
We now intend to compute the eigenenergies of $\mathcal{H}$ i.e.

$$\mathcal{H}|q\rangle = (E_0 + \epsilon_q)|q\rangle \tag{5.59}$$

where the constant contribution to eigenenergy arising from $\mathcal{H}_0$ is

$$E_0 = 2JNS^2 - 4J'NS^2 + 4DNS^2. \tag{5.60}$$

The Hamiltonian $\mathcal{H}_q$ is a quadratic form in terms of the vectors α_j and α_j^T, where

$$\alpha^T_{q,j} = \left[a_{q,1}, a^\dagger_{q,1}, a_{q,2}, a^\dagger_{q,2}, b_{q,3}, b^\dagger_{q,3}, b_{q,4}, b^\dagger_{q,4}\right]^T. \tag{5.61}$$

Therefore $\mathcal{H}_q$ can be expressed as follows:

$$\begin{aligned}\mathcal{H}_q &= \sum_{ij} \alpha_i M_q \alpha^\dagger_j \\ M_q &= \begin{pmatrix} A_q & B_q \\ B_q^\dagger & A_q^T \end{pmatrix} \end{aligned} \tag{5.62}$$

with block matrices

$$A_q = \begin{pmatrix} 0 & 0 & \frac{1}{2}Je^{-iqa} & 0 \\ 0 & 0 & 0 & \frac{1}{2}Je^{iqa} \\ \frac{1}{2}Je^{iqa} & 0 & 0 & 0 \\ 0 & \frac{1}{2}Je^{-iqa} & 0 & 0 \end{pmatrix} - \mathbb{1} \cdot \frac{1}{2}(J - J' + D)$$

and

$$B_q = \begin{pmatrix} 0 & 0 & 0 & J'e^{iqa} \\ 0 & 0 & J'e^{-iqa} & 0 \\ 0 & \frac{1}{2}J'e^{-iqa} & 0 & 0 \\ \frac{1}{2}J'e^{iqa} & 0 & 0 & \end{pmatrix} \tag{5.63}$$

It is straightforward to perform a consistency check by showing that the Hamiltonian is self-adjoint i.e. that the energy eigenvalues are real:

$$\begin{aligned} M_q^\dagger &= \begin{pmatrix} A_q^\dagger & (B_q^\dagger)^\dagger \\ B_q^\dagger & (A_q^T)^\dagger \end{pmatrix} = \begin{pmatrix} A_q & B_q \\ B_q^\dagger & A_q^T \end{pmatrix} = M \\ &\Rightarrow \ \mathcal{H}_q \text{ self-adjoint} \\ &\Rightarrow \ \epsilon_q \in \mathbb{R}. \end{aligned} \tag{5.64}$$

The diagonalization of M yields the energy eigenvalues, which we will write down in a complex notation with a vanishing imaginary part

$$\epsilon_q = \frac{1}{\xi_q^2}\left[\frac{1}{2}\xi_q^2(-J+J'-D) \pm\frac{1}{4}\sqrt{\xi_q^4(4J^2+10J'^2)+2\sqrt{8J^2J'^2+\xi_q^8(20J^2J'^2+9J'^4)+8\xi^{16}J^2J'^2}}\right],$$

with $\xi_q = e^{\pi i q a}$.

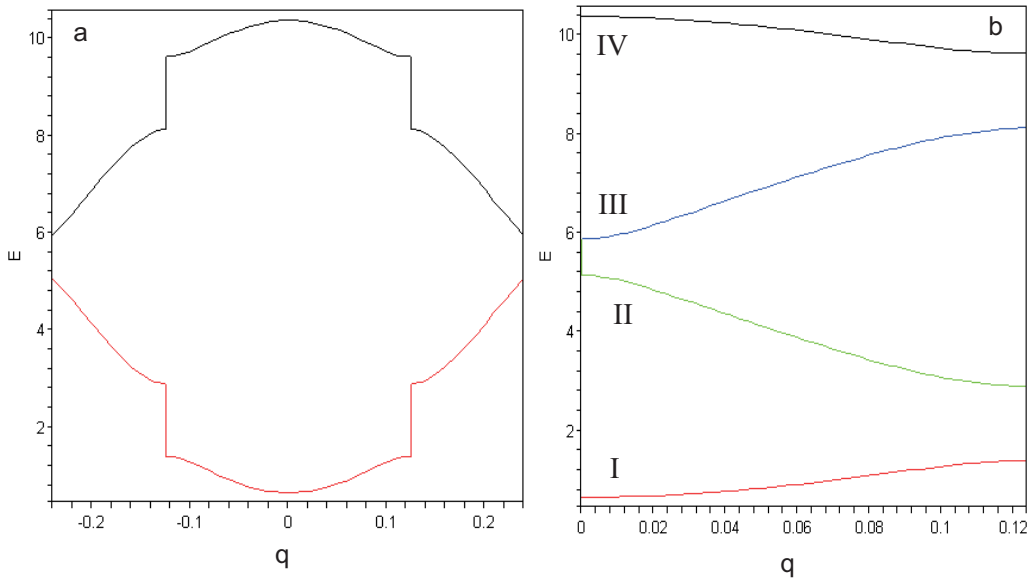

Figure 5.19: Energy dispersion for the 1D toy model. Panel (a) shows the dispersion in half of the Brillouin zone. (b) illustrates the dispersion after the *umklapp process* in the reduced Brillouin zone.

Even though Eq. 5.65 gives only two different terms for the dispersion, we still get four branches by the so-called *umklapp process*: Since there are four spins in the magnetic unit cell, the whole information about the dispersion is already contained in a fourth of the first Brillouin zone as illustrated in Fig. 5.19. Note that in Fig. 5.19 q is taken in units of $2\pi/a$.

5.5.2 Discussion

Next we will discuss how a change in the interaction parameters J, J' and D will affect the dispersion relation.

Anisotropy D

The variation of D simply shifts the whole dispersion without affecting its shape, it creates a gap for the lowest branch. The larger $|D|$, the larger the gap as illustrated in Fig. 5.20.

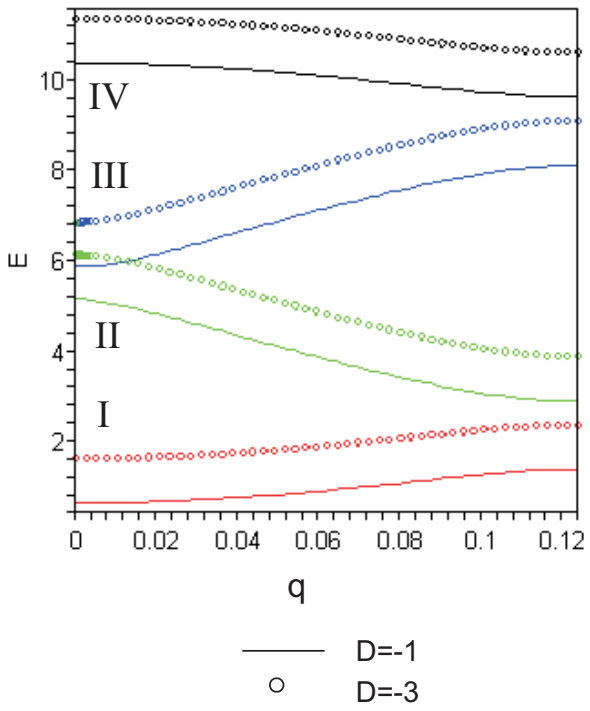

Figure 5.20: Influence of the anisotropy parameter D. The solid line is obtained with $D = -1$, whereas the points refer to the dispersion with the same J and J', but $D = -3$.

Ratio J/J'

A variation of J' with fixed J and D modifies the shape of the dispersion. The results for different values of $|J/J'|$ are plotted in Fig. 5.20 where we kept $J = -5$ and $D = -1$ fixed. It is obvious that not only the width of the dispersion of the individual branches is affected, but also the splitting between the branches II and III as well as the overall splitting and the gap of the lowest excitation.

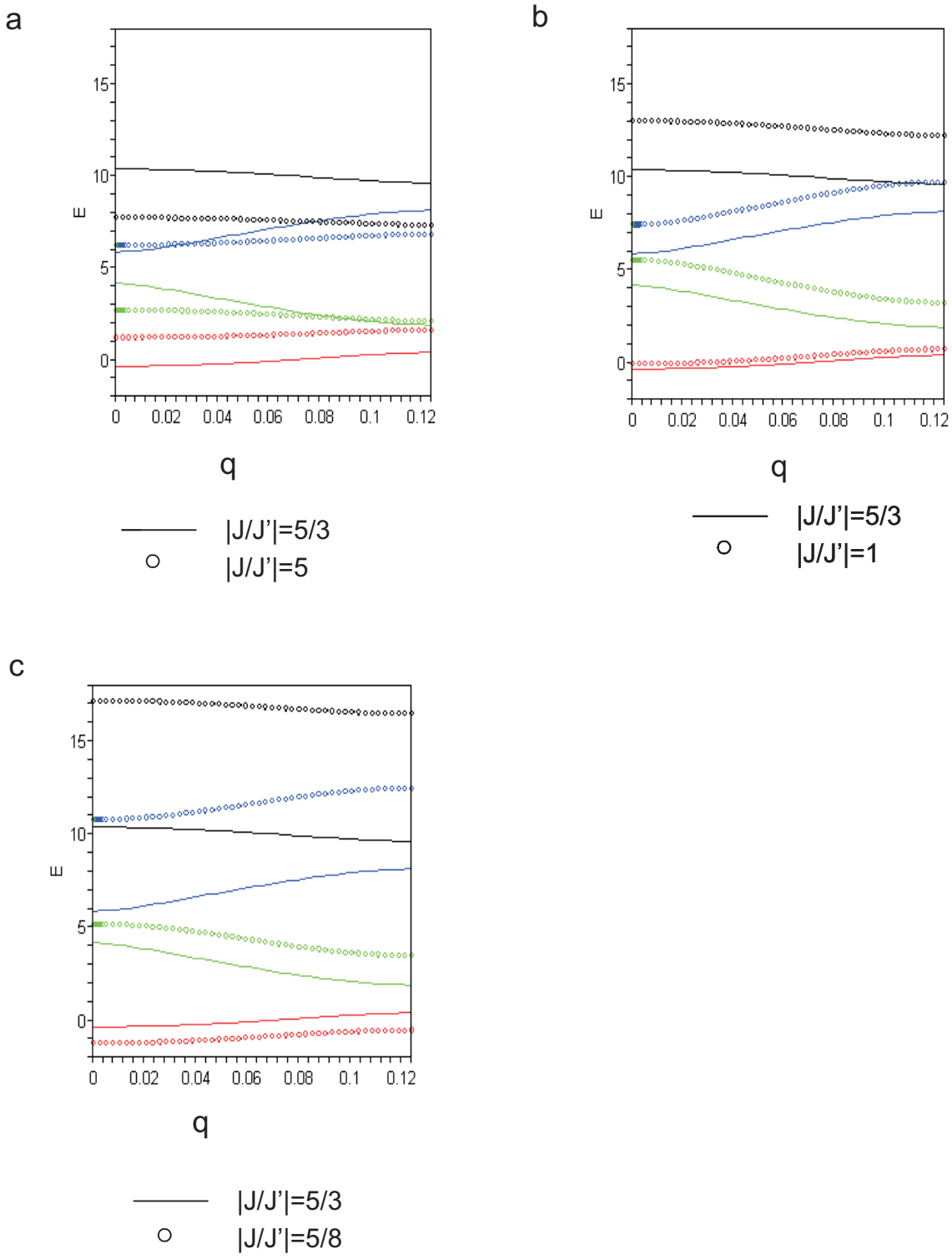

Figure 5.21: Influence of the ratio of the intradimer and interdimer coupling parameter $|J/J'|$. The solid line always corresponds to $|J/J'| = 5/3$. Panel (a) shows the comparison with a strong dimerization i.e. weak interdimer coupling, in (b) J and J' are of equal strength and in (c) the dimerization occurs between the singlets.

In order to characterize and to compare the branches corresponding to different values of J' we introduce

$$\begin{aligned}
\delta_i(J') &:= \frac{|\epsilon_i(J', q=0) - \epsilon_i(J', q=0.125)|}{|\epsilon_4(J', q=0)|} \quad i = 1..4 \\
\kappa_{23}(J') &:= \frac{|\epsilon_3(J', q=0) - \epsilon_2(J', 0)|}{|\epsilon_3(J', q=0.125) - \epsilon_2(J', q=0.125)|} \\
\kappa_{14}(J') &:= \frac{|\epsilon_4(J, q=0.125) - \epsilon_1(J', q=0.125)|}{|\epsilon_4(J', q=0) - \epsilon_1(J', q=0)|}
\end{aligned} \tag{5.65}$$

where we suppressed the parameters $J = -5$ and $D = -1$ which $\epsilon_i(J, J', q)$ also depends on.
$\delta_i(J')$ and $\kappa_{ij}(J')$ are a measure for the degree of dispersion dependent on the ratio of J/J': when the branches are most dispersive, $\delta_i(J')$ has a maximum, whereas $\kappa_{ij}(J')$ is minimal. Fig. 5.22 displays the values of $\delta_i(J')$ and $\kappa_{ij}(J')$ as a function of J'.
In panel (a) it is obvious that a decrease of J' flattens the dispersion i.e. the parameter δ_i is lower for $J/J' = 5$ than for $J/J' = 5/3$. On the other hand the splitting between the branches II and III is enhanced with smaller J/J', i.e. κ is growing. Hence the branches are well separated and only slightly dispersive. In the extreme case of zero interdimer coupling, the branches would show no dispersion as expected for non-interacting, i.e. isolated clusters.
If the coupling strength of the J and J' is equal, there is no dimerization anymore. The dispersive behavior is then still prominent.
With a raising value of J', the ratio $|J/J'|$ decreases and so does the width of dispersion. In this case the pairing occurs between spin up and spin down, whose ground state is a singlet. Even though the dimers have then a different character, the dispersion does not significantly change.

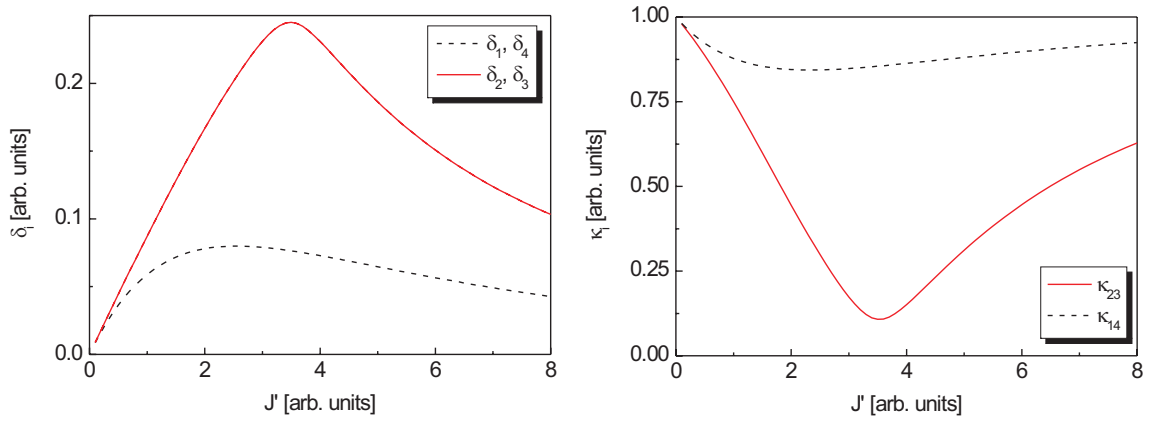

Figure 5.22: $\delta_i(J')$ and $\kappa_{ij}(J')$ as a function of J'.

The value for J/J' where the excitations are most dispersive can be found by considering the functions $\delta_i(J')$, $\kappa_{23}(J')$ and $\kappa_{14}(J')$ as a function of J'. The numerical calculation

revealed that the maximum of $\delta_i(J')$ and the minimum of $\kappa_{ij}(J')$ are sharper than for the acoustic branches and always higher and lower, respectively, which means that the optical modes are more dispersive at a given value of J'. Surprisingly these extremals do not occur at the same value of J':

$$\begin{aligned} \delta_i(J') &\stackrel{!}{=} max \quad \text{and} \quad \kappa_{14}(J') \stackrel{!}{=} max \qquad i = 1,4 \Rightarrow J' = 2.6 \\ \delta_i(J') &\stackrel{!}{=} max \quad \text{and} \quad \kappa_{23}(J') \stackrel{!}{=} max \qquad i = 2,3 \Rightarrow J' = 3.5 \end{aligned} \tag{5.66}$$

This fact emphasizes the non-monotonic behavior of the excitations within linear spin-wave theory.

5.5.3 Comparison with the cluster model

Now let us apply the cluster model based on RPA in order to compute the dispersion of the toy model and compare these results to the dispersions obtained by linear spin-wave theory in the previous section.

Dispersion within the RPA cluster model

We assume the intradimer interaction to be much stronger than the interdimer one, so that we are left with two cluster spins $\tilde{\mathbf{S}}_i$ per magnetic unit cell, separated by a distance $2a$. Since we assume only nearest neighbor interaction, J_{AA} vanishes and the Hamiltonian reduces to

$$\mathcal{H}_{Cluster} = -J_{AB} \sum_{i \neq j} \tilde{\mathbf{S}}_i \tilde{\mathbf{S}}_j \tag{5.67}$$

For the dispersion based on the cluster model we find according to Eq. 5.34

$$\begin{aligned} \tilde{\epsilon}(q) &= \Delta_i - M_i^2 \left(J_{AA}(q) \pm |J_{AB}(q)| \right) \quad i = 1,2 \\ &= \Delta_i \mp M_i^2 |J_{AB}(q)| \\ &= \Delta_i \mp M_i^2 |J_{AB} cos(4\pi q a)|, \end{aligned} \tag{5.68}$$

with energies Δ_i and matrix elements M_i. Note that the interaction between clusters of the same sublattice are assumed to be negligible, i.e. $J_{AA} \equiv 0$ where the energies Δ_i and the matrix elements M_i remain to be determined.
To do so we consider a mean-field approach for the dimer system just as in Section 5.3.2:

$$\mathcal{H}_{mf} = -2J \tilde{\mathbf{S}}_1 \tilde{\mathbf{S}}_2 + g\mu_B \mathbf{H}\mathbf{S} \tag{5.69}$$

where J denotes the intradimer interaction. $\mathbf{H}$ is the internal molecular field generated by the intercluster interaction, it is related to J_{AB} trough

$$g\mu_B H = 4\langle S \rangle J_{AB} \tag{5.70}$$

like in Eq. 5.42.
The state of a binuclear cluster is described by the wave function including the quantum

numbers S_1 and S_2 of the individual spins $\tilde{\mathbf{S}}_1$ and $\tilde{\mathbf{S}}_2$ as well as the quantum number S and M of the total spin $\mathbf{S} = \tilde{\mathbf{S}}_1 + \tilde{\mathbf{S}}_2$:

$$|\Gamma\rangle = |S_1, S_2, S, M\rangle. \tag{5.71}$$

We assume $S_1 = S_2 = 1/2$. The eigenvalues of Eq. 5.69 then read

$$\begin{aligned} E(S) &= -J\left[S(S+1) - 2S_1(S_1+1)\right] - g\mu_B H M, \\ &\qquad 0 \le S \le 2S_1, \quad -S \le M \le S \\ &\Rightarrow \begin{cases} \Delta_1 = g\mu_B H \\ \Delta_2 = J + g\mu_B H. \end{cases} \end{aligned} \tag{5.72}$$

From this expression it becomes clear that the stronger the intradimer interaction is, the more the two energy levels are separated. In the ground state the spins of the dimer are ferromagnetically aligned as shown in Fig. 5.18, therefore the ground state is a triplet state. Since the transition to excited states have to fulfill the selection rules $\Delta S = 0, \pm 1$ and $\Delta M = 0, \pm 1$, the excited states have triplet and a singlet character:

$$\begin{aligned} &\text{ground state:} && |\uparrow\uparrow\rangle : \quad |\frac{1}{2}, \frac{1}{2}, 1, 1\rangle \\ &\text{excited state:} && \frac{1}{\sqrt{2}}\left(|\uparrow\downarrow\rangle + |\uparrow\downarrow\rangle\right) : \quad |\frac{1}{2}, \frac{1}{2}, 1, 0\rangle \\ & && \frac{1}{\sqrt{2}}\left(|\uparrow\downarrow\rangle - |\uparrow\downarrow\rangle\right) : \quad |\frac{1}{2}, \frac{1}{2}, 0, 0\rangle. \end{aligned} \tag{5.73}$$

The nonvanishing transition matrix elements are computed in Appendix C, they turn out to be

$$\begin{aligned} \langle\frac{1}{2}, \frac{1}{2}, 0, 0|\hat{T}_j^1|\frac{1}{2}, \frac{1}{2}, 1, 1\rangle &= 0.499 \quad j = 1, 2 \\ \langle\frac{1}{2}, \frac{1}{2}, 1, 0|\hat{T}_j^1|\frac{1}{2}, \frac{1}{2}, 1, 1\rangle &= -0.499 \quad j = 1, 2 \\ \Rightarrow M_i^2 = |\langle\Gamma_i|S|\Gamma_0\rangle|^2 &= \frac{1}{2}\sum_{j=1}^{2} |\langle\Gamma_i|\hat{T}_j^1|\Gamma_0\rangle|^2 = (0.499)^2. \end{aligned} \tag{5.74}$$

The resulting dispersive branches are displayed in Fig. 5.23, where we assumed the intradimer coupling to be $J = -5$ yielding Δ_1 and Δ_2: The branches II and IV, which decrease with increasing q, are the optical branches corresponding to the + sign in Eq. 5.68, they can also be obtained by an *umklapp process* of the branches 1 and 3. Panel (a) illustrates the results for strongly interacting dimers ($J_{AB} = 3$) which is equivalent to the molecular field energy $g\mu_B H$, in (b) we assumed a weak coupling between the cluster spins ($J_{AB} = 0.7$).

Differences between the linear spin wave and RPA cluster model

The main difference is that in the cluster model the branches I, II and III, IV touch at the zone boundary pair wise, whereas these branches are always separated in the spin-wave

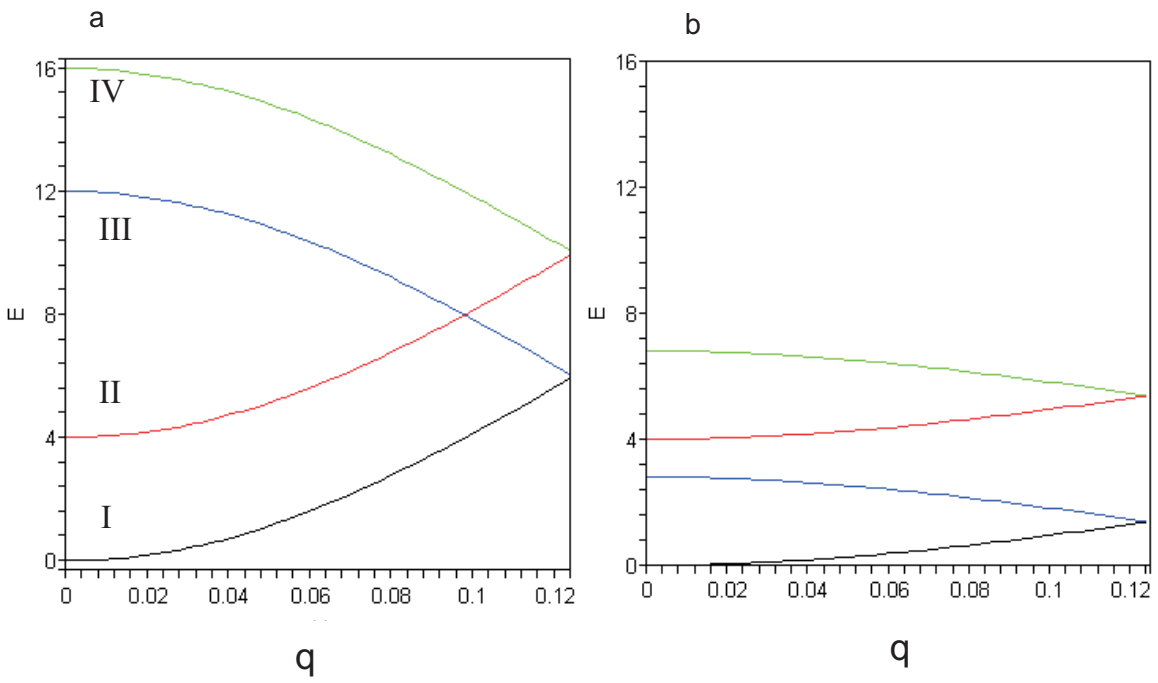

Figure 5.23: Dispersions of the four branches based on the RPA model for cluster excitations. In (a) the clusters are strongly interacting ($J_{AB} = 3$), in (b) we assumed a weak intercluster coupling ($J_{AB} = 0.7$).

model. Moreover, depending on the intracluster splitting and intercluster interaction, the branches may cross in the cluster model, which never occurs in the spin wave calculation. Within the cluster model the lowest excitation is a gapless mode, but the spin wave approach yields a variation in $\epsilon_1(q = 0)$ which can be even increased by the inclusion of D.

The comparison of these two types of dispersion shows that in the case of the RPA model, the branches are all equally dispersive, which means that the parameters δ_i and κ_{ij} are identical for all the modes. But the spin wave modes are all less dispersive and their parameters δ_i and κ_{ij} differ, e.g. the energy difference between the zone boundary and the zone center are different for the different modes, see Table. 5.6. In addition, in the spin-wave model the dispersive behavior is not the same for all the branches, the optical branches exhibit a less pronounced dispersion than their acoustic counterparts.

With a decreasing interdimer interaction, the difference between the spin wave and the RPA model is less pronounced: in panel (a) of Fig. 5.21 and in Fig. 5.23 branches II and III are separated at the zone boundary, the branches do not cross. Furthermore the different shape of the acoustic and optical modes obtained within linear spin-wave theory is no longer ostentatious.

Hence we conclude, that for weakly interacting clusters, the RPA cluster model captures the relevant dynamics of the magnetic system and in this case there is no need to perform intricate computations to diagonalize the spin wave Hamiltonian.

Table 5.6: Comparison of the dispersive behavior of the branches obtained by linear spin-wave theory and RPA. In both cases the exchange coupling parameters were set to be: $J = -5$, $J' = 3$ and $D = -1$.

branch	spin wave approach $\lvert\epsilon_i(q=0) - \epsilon_i(q=0.125)\rvert$ [arb. units]	RPA $\tilde{\epsilon}_i(q=0) - \tilde{\epsilon}_i(q=0.125)$ [arb. units]
I	0.7	5.9
II	2.2	5.9
III	2.2	5.9
IV	0.7	5.9

5.5.4 Conclusions for the real α-$MnMoO_4$ system

The experimental data reveal that the lowest mode is gapped. Such a gap indicates the existence of an anisotropy term such as the last term in Eq. 5.53 In the toy model we obtained the optical modes by using the *umklapp process*. Such a procedure is only applicable if the **Q**-direction under investigation crosses alternating a nuclear and magnetic Bragg point. The only direction to be considered out of all the acquired data, is therefore $\mathbf{Q} = (0, K, K/2)$. The data are depicted in the reduced Brillouin zone in Fig. 5.24: the open symbols corresponding to the optical branches are almost identical to the full symbols which denote the acoustic modes.
Thus the acoustic and optical modes are almost degenerate due to the significant ferromagnetic interaction among the clusters.
As compared to the RPA cluster model, the optical branches exhibit a less pronounced dispersion than their acoustic counterparts within the spin-wave model. This feature is observed in the experiment for the lowest mode in the scans A1, A2 and B1, B2.
The fact that the cluster model above cannot explain all experimental dispersion data, is an indication that the individual spins are strongly interacting. Therefore a spin wave approach detached from the cluster model would be appropriate, but such a calculation would be rather cumbersome due to eight spins per magnetic unit cell, and moreover including ten coupling parameters makes the fitting procedure very difficult. It would then be necessary to perform band structure calculations in order to determine the dominant interactions.

5.6 Conclusions

We have studied the tetramer-based Mn^{2+} compound α-$MnMoO_4$ by elastic and inelastic neutron scattering. The magnetic structure has already been revealed by powder neutron diffraction [109], it is characterized by a ferromagnetic alignment of the four spins within the cluster and an antiferromagnetic order of the cluster spins on the two sublattices. Our elastic neutron scattering experiments on a single crystal nicely confirm the structural properties obtained by Attfield [109].
For the first time we investigated the dynamic properties of α-$MnMoO_4$ single-crystal, i.e.

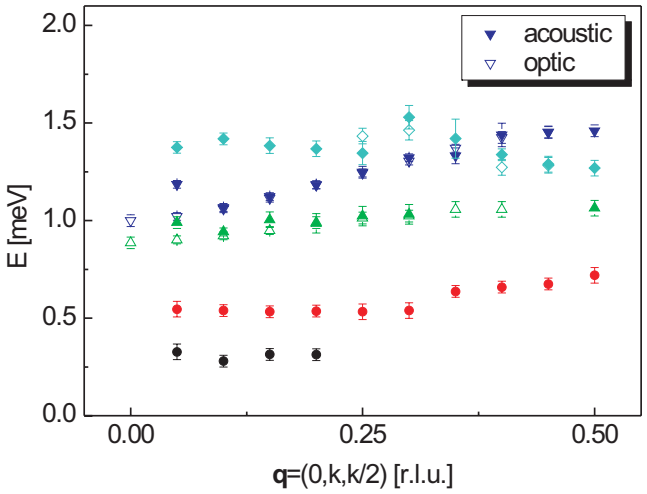

Figure 5.24: Dispersion data along $\mathbf{Q} = (0, Q, Q/2)$ in the reduced Brillouin zone, where the optical data have been projected by the *umklapp process*. The full and open symbols correspond to the acoustic and optical modes, respectively.

we studied the magnetic excitations.
Our main results are:

- INS experiments on a powder:
  The INS spectrum at 1.5 K revealed clearly four inelastic peaks. Within the frame of a mean-field cluster model, these excitations can be associated with transitions from the ground state to excited states of the cluster. Model calculations yield the intracluster interaction parameter as well as a molecular field which accounts for the weaker intercluster interaction. Also the observed intensities are in excellent agreement with the calculated intensities based on the mean-field cluster model.
  $\Rightarrow$ The magnetic properties of α-$MnMoO_4$ in the 3D antiferromagnetic order are extremely well described by considering an assembly of weakly interacting Mn_4 clusters.

- INS experiments on a single crystal:
  The data taken on triple-axis spectrometers unambiguously revealed the dispersive behavior of the magnetic excitations which have been assigned to cluster transitions in the powder experiments. These magnetic excitations have been analyzed in terms of a random phase approximation model based on cluster spins in order to derive the relevant coupling parameters and thereby to understand quantitatively the interplay and competition between the intra- and inter-tetramer interactions. Our analysis goes considerably beyond the preliminary powder investigation in the sense that the single-crystal data open the possibility to deduce the direction-dependent interaction parameters for the cluster-cluster interaction.
  However, we also noticed that the simple cluster model is not able to describe all dispersions along all the measured directions. This indicates the limits of the cluster model, because it shows that the individual spins are strongly interacting.

- Toy model:
  From model calculation for a one-dimensional dimer chain, we conclude that the q-dependence of the modes has a distinguished behavior. The dispersive behavior of the optical modes is less pronounced than the one of the acoustic modes. In addition, if the dimers are strongly interacting, the dispersion obtained within linear spin-wave theory for the individual spins differs clearly from the RPA cluster dispersions.
  $\Rightarrow$ The dispersive behavior of the magnetic excitations can be well described in terms of a cluster model based on random phase approximation up to a certain degree. The deviation from the cluster model in certain directions implies the breakdown of the cluster picture, which means that the intercluster coupling is comparable to the intracluster interaction and that the Mn^{2+} spins have to be treated as individual spins.

Chapter 6

Conclusions and Outlook

This thesis has been devoted to the study of

- a dilute magnetic system: Ho@LSCO, which is subject to crystal-field effects associated with the holmium ion.
- a classical magnetic cluster system α-$MnMoO_4$ with a dispersive behavior of the magnetic excitations associated with the cluster states resulting from intercluster interactions.

Both systems belong to the class of strongly correlated electron systems and both are examples of a Mott insulator - $La_{1.96-x}Sr_xHo_{0.04}CuO_4$ at least for x=0. We applied neutron diffraction and susceptibility measurements in order to characterize the samples regarding the structure as well as the superconducting transition and the magnetic ordering temperature, respectively. Inelastic neutron scattering experiments unraveled the dynamical behavior.

6.1 LSCO-type high-temperature superconductors

In $La_{1.96-x}Sr_xHo_{0.04}CuO_4$ it has been taken advantage that the crystal-field associated with the rare-earth ion Ho acts as a local probe of its environment: The crystal-field levels interact with the charge carriers in the CuO_2 which results in a finite lifetime of the crystal-field states. Hence a suppression of the density of states of the charge carriers at the Fermi level, which originates from the opening of the pseudogap, is directly monitored by a sudden decrease of the relaxation rate of the crystal-field states.
In the normal state the interaction of the $4f$ electrons of the Ho^{3+} ion with the holes induced by doping with Sr is the provides the dominant relaxation channel. Consequently the relaxation rate is a linear function of temperature according to the well known Korringa law. However, in the pseudogap state the relaxation is exponentially decreased due to the opening of the electronic gap - the pseudogap. Thus the deviation of the relaxation rate from the Korringa behavior is assigned to the pseudogap temperature T^* as obtained from neutron crystal-field spectroscopic measurements.
We would like to point out that the observed reduction of the linewidth and therefore the suppressed interaction with the charge carrier is a purely dynamic effect because there

is no structural phase transition in the low-temperature regime ($T \leq$100 K). Hence the sudden decrease of the relaxation rate at T^* clearly originates from the opening of the pseudogap.

In these experiments we used the rare-earth ion Ho^{3+} only as a tool which offers us the possibility to have insights in the relaxation rate of the crystal-field states which in turn reveals the opening of the pseudogap. We studied systematically the doping (x=0.11, 0.15, 0.2, 0.25), oxygen isotope (78% ^{18}O vs. ^{16}O) and pressure ($p = 0.8, 1.2$ GPa) dependence of T^*.

6.1.1 Ho@LSCO: Results and conclusions

Our results can be summarized as follows:

- The pseudogap persists far into the overdoped regime ($x = 0.25$):
  T^* gradually decreases with increasing doping, and we found $T^* > T_c$ in the whole doping range.

- Oxygen isotope substitution leads to an enhancement of T^* in the whole doping range and ΔT^* gets smaller as doping increases.

- The application of pressure to the optimally doped sample results in a downward shift of T^*.

The relaxation data do not exhibit any anomalous behavior around T_c, i.e., there is no evidence that the magnitude of the superconducting gap goes to zero at T_c. This supports the idea that the superconducting gap emerges smoothly from the normal state pseudogap [68]. Our relaxation data suggest that the superconducting gap has generally d-wave symmetry. For the interpretation of the relaxation data in the underdoped regime we had to include some doping dependent effects, namely the existence of a non-superconducting volume fraction as well as the inclusion of higher harmonics into the d-wave gap function. These two effects nicely support the percolative nature of the superconductivity as well as the growing importance of magnetic interaction below the optimum doping level.
The existence of the pseudogap in the heavily overdoped regime suggests that its origin may be considered as a precursor to superconductivity by the formation of preformed pairs at T^* [68].
The opposite effect of oxygen isotope substitution and pressure on T^* can be qualitatively explained by theoretical models including phonon-mediated mechanisms of the pseudogap formation [228, 229, 230]. However, lattice fluctuations alone cannot reproduce the observed downward shift of T^* under pressure application, since pressure also modifies the spin degrees of freedom. We therefore conclude on the basis of our experimental results that a theoretical approach should contain both lattice as well as antiferromagnetic fluctuations, e.g. [275].

6.1.2 Outlook

We have already investigated the pseudogap issue in Ho@LSCO in great detail by means of neutron crystal-field spectroscopy. However, since there is no consensus yet about the origin of the pseudogap or about the pairing mechanism leading to superconductivity in the cuprates, there is still a lot of room for experimental as well as theoretical work.

For instance the intrinsic relation between superconductivity and static magnetic order is still an open question. The glass phase of LSCO has been studied in detail by different groups and different experimental methods [20, 21, 19]. The results suggest that superconductivity and static order are at least compatible.
I think at this point there is need for a systematic neutron scattering and/or μSR study of oxygen isotope exchanged samples. It would be highly interesting to continue the work initiated by Shengalaya et al. [231] who observed an isotope effect on the spin glass temperature T_g in Mn-doped LSCO samples in the non-superconducting regime. Moreover, it is not clear so far why the doping of Mn induces such a huge isotope effect, which is another important issue to concentrate on.

The investigation of such issues may reveal if lattice effects influence also magnetic features through a slight structural distortion of the oxygen octahedral around the Cu ion, which modifies the exchange integral of the Cu spins or whether phonons affect only the superconducting properties. An isotope effect on T_g may give information about the relation of lattice fluctuations and antiferromagnetic order in the cuprates. This way we could contribute to the understanding if isotope effects produce only a shift of the phase diagram or if phonons are directly involved in the pairing mechanism.

6.2 Spin dynamics in tetramer-based cluster system α-$MnMoO_4$

In the past inelastic neutron scattering has been proven to be one of the most powerful techniques to study the interplay of intra- and intercluster interaction. It is unique in allowing the direct spectroscopic determination of exchange and anisotropy splittings in zero field.
Previous neutron powder diffraction measurements [109] have shown that α-$MnMoO_4$ contains the tetranuclear Mn_4 clusters. The compound undergoes a 3D antiferromagnetic order below $T_N = 10.7$ K, while the four spins within a Mn_4 cluster are aligned ferromagnetically. From susceptibility measurements it has been found that the intercluster interactions persist in the paramagnetic phase up to temperatures wee above T_N.

We have been investigating the magnetic interactions in this compound, which is characterized by a complicated interplay of inter- and intracluster interaction.

6.2.1 α-$MnMoO_4$: Results and conclusions

We obtained the following results:

- Neutron diffraction on a single crystal:
  A transition into a 3D antiferromagnetically ordered state occurs below T_N=10.7 K. The associated change in symmetry is a doubling of the unit cell along the c-axis as has been deduced from the powder data [109].

- INS on polycrystalline α-$MnMoO_4$ at $T = 1.5$ K:
  Four prominent peaks between 0.5 and 2.0 meV - corresponding to the eigenvalues of the system - are assigned to magnetic excitations of the $(Mn^{2+})_4$ cluster. An analysis within a mean-field approach yielded the intracluster exchange parameters. The intercluster interactions are accounted for by a molecular field. α-$MnMoO_4$ proved to be very well described as a system of weakly interacting clusters.

- INS on a single-crystal:
  The magnetic excitations of the cluster exhibit a considerable dispersive behavior in all directions indicating that the compound is a 3D system. The dispersions have been analyzed within RPA cluster model, which allows to deduce the direction-dependent intercluster interactions.
  The lowest mode is gapped, which implies magnetic anisotropy.

$\Rightarrow$ These experimental findings demonstrate that cluster magnetic phenomena can be observed not only in molecular materials but also in continuous lattices which happen to display an ordered clustering of the magnetic ions.

However, it turned out that a RPA cluster model, where the clusters are considered to be a unit, cannot explain all dispersions, which means that the cluster model encounters its limits. In order to draw some qualitative conclusions we developed a toy model of a 1D dimer chain, where the dimers are formed by the parallel alignment of two spins. We calculated the dispersion relations and investigated how the energy of these modes depends on the various coupling parameters.
Our main results are

- The q-dependence of the modes has a distinguished, non-monotonic behavior.

- Only if the dimers are weakly interacting, the dispersion obtained within linear spin-wave theory for the individual spins are well approximated by the RPA cluster model.

6.2.2 Outlook

In order to establish an accurate exchange coupling scheme, more theoretical as well as experimental work is essential.
On the theoretical side it would be necessary to treat the $(Mn^{2+})_4$ not as a unit, but as four individual spins. Since the resulting spin wave calculation is going to incorporate

significantly more coupling parameters, there is need for band structure calculations to assess the dominant coupling parameters. However, due to the complexity of the system, this is certainly not an easy task and it is doubtful how accurate the corresponding predictions will be.
Moreover, it remains to be clarified why the intensity of the lowest transition is low or even vanishing in most of the reciprocal space studied so far.
Concerning experimental investigations additional INS experiments on a triple-axis spectrometer have to be performed with a higher resolution: The experiments performed on TASP with $k_f = 1.1$ Å^{-1} revealed that two excitations continue in a parallel manner, separated only by ~ 0.2 meV along $\mathbf{q} = (0, k, 0)$. Thus it is necessary to verify if one of the observed inelastic peaks of the measurements taken with a worse actually comprises two excitations.
The occurrence of two unidentified excitations in the single-crystal experiment may originate from a van Vleck interaction, but further clarifications are needed, in particular temperature dependent measurements remain to be performed in order to decide if the branches are of magnetic or phononic nature.
Finally magnetic susceptibility measurements should shed light on possible magnetic anisotropies as implied by the spin gap of the lowest mode.

Bibliography

[1] T.M. Rice, J. Phys. Chem. Solids **63**, 1319 (2002).

[2] H. Kamerlingh-Onnes, Reports u. Comm. 4. Intern. Kältekongress, London 1924, 175.

[3] J. Bardeen, L.N. Cooper, and J.R. Schrieffer, Phys. Rev. **106**, 162 (1957).

[4] J.G. Bednorz and K.A. Müller, Z. Phys. B Condensed Matter **64**, 189 (1986).

[5] A. Fujimori, E. Takayama-Muromachi, Y. Uchida, and B. Okai, Phys. Rev. B **35**, 8814 (1987).

[6] J.M. Tranquada, S.M. Heald, A.R. Moodenbaugh, and M. Suenaga, Phys. Rev. B **35**, 7187 (1987).

[7] A. Schilling, C. Michel, G. van Tendeloo, M. Hervieu, and B. Raveau, Physcia C **216**, 6 (1993).

[8] Z.X. Shen, D.S. Dessau, B.O. Wells, D.M. King, W.E. Spicer, A.J. Arko, D. Marshall, L.W. Lombardo, A. Kapitulnik, P. Dickinson, S. Doniach, J. DiCarlo, T. Loseserm and C.H. Park , Phys. Rev. Lett. **70**, 1553 (1993).

[9] H. Ding, M.R. Norman, J.C. Campuzano, M. Randeria, A.F. Bellman, T. Yokoya, T. Takahashi, T. Mochiku, K. Kadowski, Phys. Rev. B **54**, R9678 (1996).

[10] J. Mesot, M.R. Norman, H. Ding, M. Randeria, J.C. Campuzano, A. Paramekanti, H.M. Fretwell, A. Kaminski, T. Takeuchi, T. Yokoya, T. Sato, T. Takahashi, T. Mochiku, and K. Kadowaki, Phys. Rev. Lett. **83**, 840 (1999).

[11] J.R. Kirtley, C.C. Tsuei, J.Z. Sun, C.C. Chi, Lock See Yu-Jahnes, A. Gupta, M. Rupp, M.B. Ketchen, Nature **373**, 225 (1995).

[12] D. Driscoll, V. Dombrovski, and B. Zhang, IEE Power Engineering Review, **12** (2000).

[13] W.V. Hassenzahl, IEEE Power Engineering Review, **4** (2000).

[14] G. Shirane, Y. Endoh, R.J. Birgeneau, M.A. Kastner, Y. Hidaki, M. Oda, M. Suzuki, and T. Murakami, Phys. Rev. Lett. **59**, 1613 (1987).

[15] Y. Endoh, K. Yamada, R.J. Birgeneau, D.R. Gabbe, H.P. Jenssen, M.A. Kastner, C.J. Peters, P.J. Picone, T.R. Thurston, J.M. Tranquada, G. Shirane, Y. Hidaka, M. Oda, Y. Enomoto, M.Suzuki, ang T. Murakami, Phys. Rev. B **37**, 7443 (1988).

[16] P.W. Anderson, Science **235**, 1196 (1987).

[17] R.J. Birgeneau, D.R. Gabbe, H.P. Jenssen, M.A. Kastner, P.J. Picone, T.R. Thurston, G. Shirane, Y. Endoh, M. Sato, K. Yamada, Y. Hidaka, M. Oda, Y. Enomomot, M. Suzuki, and T. Murakami, Phys. Rev. B **38**, 6614 (1988).

[18] B. Keimer, N. Belk, R.J. Birgeneau, A. Cassanho, C.Y. Chen, M. Greven, M.A. Kastner, A. Aharony, Y. Endoh, R.W. Erwin, and G. Shirane, Phys. Rev. B **46**, 14034 (1992).

[19] F.C. Chou, F. Borsa, J.H. Cho, D.C. Johnston, A. Lascialfari, D.R. Torgeson, Phys. Rev. Lett. **71**, 2323 (1993).

[20] M. Matsuda, M.Fujita, K. Yamada, R.J. Birgeneau, M.A. Kastner, H. Hiraka, Y. Endoh, S. Wakimoto, G. Shirane, Phys. Rev. B **62**, 9148 (2000).

[21] Ch. Niedermayer Ch. Bernhard, T. Blasius, A. Golnik, A. Moodenbaugh, adn J.I. Budnick, Phys. Rev. Lett. **80**, 3843 (1998).

[22] M.-H. Julien, cond-mat/0211178 (2002).

[23] P.G. Radaelli, D.G. Hinks, A.W. Mitchell, B.A. Hunter, J.L. Wagner, B. Dabrowski, K.G. Vandervoort, H.K. Viswanathan, and J.D. Jorgensen, Phys. Rev. B **49**, 4163 (1996).

[24] R. Kleiner and P. Müller, Phys. Rev. B **49**, 1327 (1994).

[25] Proceedings of the workshop on *Phase separation in cuprate superconductors* Erice, Italy May 1992, edited by K.A. Müller and G.Benedek.

[26] V. Hizhnyakov, E. Sigmund, M. Schneider, Phys. Rev. B **44**, 795 (1991).

[27] R.K. Kremer, E. Sigmund, V. Hizhnyakov, F. Hentsch, A. Simon, K.A. Müller, M. Mehring, Z. Phys. B Cond. Matter **86**, 319 (1992).

[28] T.R. Thurston, R.J. Birgeneau, M.A. Kastner, N.W. Preyer, G. Shirane, Y. Fuji, K. Yamada, Y. Endoh, K. Kakurai, M. Matsuda, Y. Hidaki, Phys. Rev. B **40**, 4585 (1989).

[29] T.E. Mason, G.Aeppli, and H.A. Mook, Phys. Rev. Lett. **68**, 1414 (1992).

[30] G. Aeppli, T.E. Mason, S.M. Hayden, H.A. Mook, J. Kulda, Science **278**, 1432 (1997).

[31] Ph. Bourges, in *The gap symmetry and fluctuations in high-temperature superconductors*, edited by J. Bok, G. Deutscher, D. Pavuna, and S.A. Wolf (Plenum Press, 1988) (cond-mat/9901333).

[32] J. Rossat-Mignod, L.P. Regneault, C. Vettier, P. Bourges, P. Burlet, J. Bossy, J.Y. Henry and G. Lapertot, Physica C **185-189**, 86 (1991).

[33] H.F. Fong, P. Bourges, Y. Sidis, L.P. Regnault, A. Ivanov, G.D. Gu, N. Koshizuka, B. Keimer, Nature **398**, 588 (1999).

[34] J.W.Loram, J.L. Luo, J.R. Cooper, W.Y. Liang, and J.L. Tallon, Physcia C **341-348**, 831 (2000).

[35] J.W. Loram, K.A. Mirza, J.R. Cooper, and W.Y. Liang, Phys. Rev. Lett. **71**, 1740 (1993).

[36] M. Ido, M. Momono and M. Oda , J. Low Temp. Phys., **117**, 329 (1999).

[37] H. Takagi, T. Ido, S. Ishibashi, M. Uto, and S. Uchida, Phys. Rev. B **40**, 2254 (1989).

[38] H.Y. Hwang, B. Batlogg, H. Takagi, H.L. Kao, J. Kwo, R. J. Cava, J.J. Krajeewski, and W. F. Peck, Jr., Phys. Rev. Lett. **72**, 2636 (1994).

[39] H. Takagi, B. Batlogg, H.L. Kao, J.Kwo, R.J. Cava, J.J. Krajewski, and W.F. Peck, Jr., Phys. Rev. Lett. **69**, 2975 (1992).

[40] W.W. Warren, Jr., R.E. Walstedt, G.F. Brennert, R.J. Cava, R. Tycko, R.F. Bell, and G.Dabbagh, Phys. Rev. Lett. **62**, 1193 (1989).

[41] M. Takigawa, A.P. Reyes, P.C. Hammel, J.D. Thompson, R.H. Heffner,Z. Fisk and C. Ott, Phys. Rev. B**43**, 247 (1991).

[42] H. Alloul, A. Mahajan, H. Casalta and O. Klein, Phys. Rev. Lett. **70**, 1171 (1993).

[43] G.V.M. Williams, J.L. Tallon, J.W. Quilty, H.J. Trodahl, and N.E. Flower, Phys. Rev. Lett. **80**, 377 (1998).

[44] A. Rigamonti, F. Borsa, and P. Carretta, Rep. Prog. Phys. **61**, 1367 (1998).

[45] D.S. Marshall, D.S. Dessou, A.G. Loeser, C.H. Park, A.Y. Matsuura, J.N. Eckstein, I. Bozovic, P. Fournier, A. Kapitulnik, W.E. Spicer, and Z.X. Shen, Phys. Rev. Lett. **76**, 4841 (1996).

[46] H. Ding et al., T. Yokoya, J.C. Campuzano, T. Takahashi, M. Randeria, M.R. Norman, T. Mochiku, K. Kadowski, Nature **382**, 51 (1996).

[47] J.M. Harris, Phys. Rev. B, **54**, 15665 (1996).

[48] J.C. Campuzano, M.R. Norman, and M. Randeria, cond-mat/0209476 (2002).

[49] F. Slakey, M.V. Klein, J.P. Rice, and D. Ginsberg, Phys. Rev. B **42**, 2643 (1990).

[50] See, e.g., T. Timusk and B. Statt, Rep. Progr. Phys. **62**, 61 (1999).

[51] V.M. Krasnov, A. Yurgens, D. Winkler, P. Delsing, and T. Claeson, cond-mat/002172 (2000).

[52] H. Kugler, O. Fischer, C. Renner, S. Ono, and Y. Ando, Phys. Rev. Lett. **86**, 4911.

[53] J.L. Tallon, J.W. Loram, G.V.M. Williams, J.R. Cooper, I.R. Fisher, J.D. Johnson, M. P. Staines, C. Bernhad, Phys. Stat. Sol. (b) **215**, 531 (1999).

[54] A. Furrer, Struct. Bond **114**, 171 (2005).

[55] B. Fauque, Y. Slidis, V. Hinkov, S. Pailhes, C.T. Lin, X. Chaud, and P. Bourges, cond-mat/0509210 (2005).

[56] C.M. Varma, Phys. Rev. B **55**, 14554 (1997).

[57] C.M. Varma, Phys. Rev. Lett. **83**, 3538 (1999).

[58] M.E. Simon and C.M. Varma, Phys. Rev. Lett. **89**, 247003 (2002). .

[59] S.-W. Cheong, G. Aeppli, T.E. Mason, H. Mook, S.M. Hayden, P.C. Canfield, Z. Fisk, K.N. Clausen, and J.L. Martinez, Phys. Rev. Lett. **67**, 1791 (1991).

[60] Bourges, Y. Sidis, H.-F. Fong, L.P. Regnault, J. Bossy, A. Ivanov, B. Keimer, Science **288**, 1234 (2000).

[61] C.M. Varma, P.B. Littlewood, S. Schmitt-Rink, E. Abrahams, and A.E. Ruckenstein, Phys. Rev. Lett. **63**, 1996 (1989).

[62] S. L. Lee, P. Zimmermann, H. Keller, M. Warden, I.M. Savić, R. Schauwecker, D. Zech, R. Cubitt, E.M. Forgan, P.H. Kes, T.W. Li, A.A. Menovsky, and Z. Tarnawski, **71**, 3862 (1993).

[63] R. Gilardi, Dissertation ETH Zürich, LNS-216 (2004).

[64] E.M. Forgan, D. McK. Fault, H.A. Mook, P.A. Timmins, H. Keller, S. Sutton, J.S. Abell, Nature **343**, 735 (1990).

[65] R. Gilardi, J. Mesot, A. Drew, U. Divakar, S.L. Lee, E. M. Forgan, O. Zaharko, K. Conder, V.K. Aswal, C.D. Dewhurst, R. Cubitt, N. Momono, M. Oda, Phys. Rev. Lett. **88**, 217003 (2002).

[66] R. Gilardi, . Mesot, A.J. Drew, U. Divakar, S.L. Lee, N.H. Andersen, J. Kohlbrecher, N. Momono, M. Oda, Physica C **408-410**, 491 (2004).

[67] R. Cubitt, E,M. Forgan, G. Yang, S.L. Lee, D. McK. Paul, H.A. Mook, M. Yethiraj, P.H. Kes, T.W. Li, A.A. Menovsky, Z. Tarnawski, K. Mortensen, Nature **365**, 407 (1993).

[68] V.J. Emery and S.A. Kivelson, Nature **374**, 434 (1995).

[69] N.E. Bickers, D. J. Scalapino, and R.T. Scalettar, Intl. J. Modern Physics B **1**, 687 (1987).

[70] G. Kotliar, Phys. Rev. B **37**, 3664 (1988).

[71] G. Kotliar, and J. Liu, Phys. Rev. B **38**, 5142 (1988).

[72] F.C. Zhang, C. Gros, T.M. Rice, and H. Shiba, Supercond. Sci. Technol. **1**, 36 (1988).

[73] M. Randeria, N. Trivedi, A. Moreo, and R. T. Scalettar, Phys. Rev. Lett. **69**, 2001 (1992).

[74] A.Junod, A. Erb, and C. Renner, Physica C **317**, 333 (1999).

[75] J.D. Axe, A.H. Moudden, D. Hohlwein, D.E. Cox, K.M. Mohanty, A.R. Moodenbaugh, and Y. Xu, Phys. Rev. Lett. **62**, 2751 (1989).

[76] H. Kimura, K. Hirota, H. Matsushita, K. Yamada, Y. Endoh, S.-H. Lee, Ch. F. Majkrzak, R. Erwin, G. Shirane, M. Greven, Y. S. Lee, M.A. Kastner, R. J. Birgeneau, Phys. Rev. B **59**, 6517 (1999).

[77] T. Suzuki, T. Goto, K. Chiba, T. Shinoda, T. Fukase, H. Kimura, K. Yamada, M. Ohashi, Y. Yamaguchi, Phys. Rev. B **57**, R3229 (1998).

[78] M. Fujita, K. Yamada, H. Hiraka, P.M. Gehring, S.H. Lee, S. Wakimoto and G. Shirane, Phys. Rev. B **65**, 064505 (2002).

[79] N. Nagosa, J. Phys.: Condens. Matter **10**, 11386 (1998).

[80] C. Castellani, C. Di Castro, and M. Grilli, Z. Phys. **103**, 137 (1997).

[81] A.J. Millis, H. Monien, and D. Pines, Phys. Rev. B **42**, 167 (1990). .

[82] S. Sachdev and J. Ye, Phys. Rev. Lett. **69**, 2411 (1992).

[83] M. Vojita, Y. Zhang, and S. Sachdev, Phys. Rev. Lett. **85**, 4940 (2000).

[84] C. Castellani, C. Di Castro, and M. Grilli, Phys. Rev. Lett. **75**, 4650 (1995).

[85] N. Manella, W. L. Yang, X.J. Zhou, H. Zheng, J.F. Mitchell, J. Zaanen, T.P. Devereaux, N. Nagaosa, Z. Hussain, and Z.-X. Shen, Nature **438**, 474 (2005).

[86] H. Keller, Struct Bond (2005) **114**; 143-169, Springer Verlag Berlin Heidelberg 2005.

[87] A. Lanzara, G.-M. Zhao, M.L. Saini, A. Bianconi, K. Conder, H. Keller and K.A. Müller, J. Phys.: Condens. Matter **11**, L541 (1999).

[88] A. Shengelaya, H. Keller, K.A. Müller, B.I. Kochelaev, K. Conder, Phys. Rev. B **63**, 144513 (2001).

[89] D. Rubio Temprano, J. Mesot, S. Janssen, K. Conder, A. Furrer, H. Mutka, and K.A. Müller, Phys. Rev. Lett. **84**, 1990 (2000).

[90] D. Rubio Temprano, K. Conder, A. Furrer, H. Mutka, V. Trounov, and K.A. Müller,Phys. Rev. B **66**, 184506 (2002).

[91] D. Rubio Temprano, J. Mesot, S. Janssen, K. Conder, A. Furrer, A. Sokolov, V. Trounov, S.M. Kazakov, J. Karpinski, and K.A. Müller, Eur. Phys. J. B **19**, 5 (2001).

[92] D. Rubio Temprano, Dissertation ETH Zürich, Nr.14501 (2002).

[93] S. Paihles, P. Bourges, Y. Slidis, C. Bernhard, B. Keimer, C.T. Lin, J.T. Tallon, cond-mat/0503208 (2005).

[94] T. Machi, M. Kosuge, N. Koshizuka, and H. Yamada, in *Advances in Superconductivity IX*, edited by S. Nakayima and M. Murakami (Springer, Berlin, 1996), pp. 111-114.

[95] L.J. Shen, C.C. Lam, V. Anand, S.H. Li, Physica C **341-348**, 929 (2000).

[96] E.V.L. de Mello, M.T.D. Orlando, J.L. González, E.S. Caixeiro, and E. Baggio-Saitovich, Phys. Rev. B **66**, 092504 (2002).

[97] W. Heisenberg, Z. Physik **38**, 411 (1926).

[98] P.A.M. Dirac, Proc. Roy. Soc. A**112**, 661 (1926).

[99] J.H. Van Vleck, *The theory of electric and magnetic susceptibility*, University Press, Oxford (1932).

[100] Yu-Jun Zhao, W.T. Geng, A.J. Freeman, and B. Delley, Phys. Rev. B **65**, 113202 (2002).

[101] Ch. Rüegg, N. Cavadini, A. Furrer, H.U. Güdel, K. Krämer, H. Mutka, A. Wildes, K. Habicht and P. Vorderwisch, Nature **423**, 62 (2003).

[102] N.V. Prokof'ev, P.C.E. Stamp, J. Low. Temp. Phys. **104**, 143 (1996).

[103] St. Wessel, M. Indergand, A. Läuchli, U. Ledermann, and M. Sigrist, Phys. Rev. B **67**, 184517 (2003).

[104] R. Sessoli, H.Lian Tsai, A.R. Schake, S. Wang, J.B. Vincent, K. Folting, D.Gatteschi, G. Christou, D.N. Hendrickson, J. Am. Chem. Soc. **115**, 1804 (1993).

[105] A. Furrer and H.U. Güdel, J. Magn. Magn. Mat. **14**, 256 (1979).

[106] W. Wernsdorfer, S. Bhaduri, R. Tiro, D.N. Hendrickson, and G. Christou, Phys. Rev. Lett. **89**, 197201 (2002).

[107] B. Barbara, Nature **421**, 32 (2003).

[108] W. Wernsdorfer, N. Aliaga-Alcalde, D.N. Hendrickson, and G. Christou, Nature **416**, 406 (2002). .

[109] J.P.Attfield, J. Phys.: Condens. Matter **2**,6999 (1990).

[110] M. Jamet, W. Werndsdorfer, C. Thirion, D. Mailly, V. Dupuis, P. Mélinon, A. Perez, Phys. Rev. Lett. **86**, 4676 (2002). .

[111] B. Barbara, E.M. Chudnovsky, Phys. Lett. A **145**, 205 (1990).

[112] E. Dagotta, T.M. Rice, Science **271**, 618 (1996).

[113] Q.F. Zhong, S. Sorella, Europhys. Lett. **21**, 629 (1993).

[114] J.S. Griffith, vol. 10 (Springer, Berlin), p. 87 (1972).

[115] J.S. Smart in *Magnetism, Vol. III*, ed. by G.T. Rado and H. Suhl (Academic Press, New York), p. 63 (1963).

[116] H.U. Güdel, U. Hauser, and A. Furrer, Inorg. Chem. **18**, 2730 (1979).

[117] A. Furrer and H.U. Güdel, J. Phys. C **10**, L191 (1977).

[118] A. Furrer and H.U. Güdel, Phys. Rev. Lett. **39**, 657 (1977).

[119] A. Furrer, LNS-report AF-SSP-107 (1988).

[120] P. Fulde, in *Handbook on the physics and chemistry of rare earths*, edited by A. Gschneider and L. Eyring (North Holland, Amsterdam) (1978).

[121] B. Leuenberger, A. Steble, H.U. Güdel, A. Furrer, R. Feile, J.K. Klemm, Phys. Rev. B **30**, 6300 (1984).

[122] P.W. Anderson, Phys. Rev. **86**, 694 (1952).

[123] A. Zheludev, G.Shirane, Y. Sasago, M. Hase, K, Uchinokura, Phys. Rev. B **53**, 11642 (1996).

[124] I. Affleck, J. Phys.: Condens. Matter **1**, 3074 (1989).

[125] M. Hase, I. Terasaki, and K. Uchinokura, Phys. Rev. Lett. **70**, 3651 (1993). .

[126] H. Kageyama, M. Nishi, N. Aso, K. Onizuka, T. Yosihama, K. Nukui, K. Kodama, K. Kakurai, and Y. Ueda, Phys. Rev. Lett. **84**, 5876 (2000). .

[127] P. Schiffer and A.P. Ramirez, Comments Condens. Matter Phys. **18**, 21 (1996).

[128] A.P. Ramirez, B. Hessen, and M. Winkelmann, Phys. Rev. Lett. **84**, 2957 (2000).

[129] F. Mila, Euro. J. Phys. **21**, 499 (2000).

[130] W. Brenig and A. Honecker, Phys. Rev. B **65**, 140407 (2002).

[131] N. Cavadini, G. Heigold, W. Henggeler, A. Furrer, H.-U. Güdel, K. Krämer, and H. Mutka, Phys. Rev. B **63**, 172414 (2001).

[132] T.M. Rice, Science **298**, 760 (2002).

[133] T. Nikuni, M. Oshikawa, A.Oosawa, and H. Tanaka, Phys. Rev. Lett. **84**, 5868 (2000).

[134] M. Matsumoto, B. Normand, T. M. Rice, and M. Sigrist, Phys. Rev. Lett. **89**, 077203 (2002).

[135] N. Cavadini, Ch. Rüegg, A. Furrer, H.-U. Güdel, K. Krämer, H. Mutka, and P. Vorderwisch, Phys. Rev. B **65**, 132415 (2002).

[136] Ch. Rüegg, N. Cavadini, A. Furrer, K. Krämer, H.-U. Güdel, P. Vorderwisch, H. Mutka, Appl Phys. A **74**, S840 (2002).

[137] M. Matsumoto, B. Normand, T.M. Rice, and M. Sigrist, Phys. Rev. B **69**, 054423 (2004).

[138] B. Normand, M. Matsumoto, O. Nohadani, S. Wessel, S. Haas, T.M. Rice and M. Sigrist, J. Phys." Condens. Matter **16**, S867 (2004).

[139] M. Johnsson, K.W. Törnross, F. Mila, and P. Millet, Chem. Matter **12**, 2853 (2000).

[140] O. Zaharko, A. Daoud-Aladine, S. Streule, and J. Mesot, Phys. Rev. Lett. **93**, 217206 (2004).

[141] P. Lemmens, K.Y. Choi, E.E. Kaul, Ch. Geiberl, K. Becker W. Brenig, R. Valenti, C. Gros, M. Johnsson, P. Millet, and F. Mila, Phys. Rev. Lett, **87**, 227201 (2001).

[142] M. Prester, A. Smontara, I. Živković, A. Bilusšić, D. Drobac, H. Berger, and F. Bussy, Phys. Rev. B **69**, 180401 (2004).

[143] C. Gros, P. Lemmens, M. Voita, R. Valenti, K.-Y. Choi, H. Kageyama, Z. Hiroi, N.V. Mushnikov, T. Goto, M. Johnsson, P. Millet, Phys. Rev. B **67**, 174405 (2003).

[144] R.I. Bewley, S.J. Levett, C. Ritter, Phys. Rev. B **71**, 224430 (2005).

[145] W. Brenig, Phys. Rev. B **67**, 064402 (2003).

[146] L. Thomas, F. Lionti, R. Ballou, D. Gatteschi, R. Sessioli, and B. Barbara, Nature **383**, 145 (1996).

[147] J.R. Friedman, M.P. Sarachik, J. Tejada, and R. Ziolo, Phys. Rev. Lett. **76**, 3830 (1996).

[148] R. Sessoli, D. Gatteschi, A. Caneschi, and M.A. Novak, Nature **365**, 141 (1993).

[149] W. Wernsdorfer, R. Sessioli, Science **284**, 133 (1999).

[150] W. Wernsdorfer, Adv. Chem. Phys. **118**, 99 (2001).

[151] J.R. Friedmann, M.P. Sarachik, J. Tejada, and R. Ziolo, Phys. Rev. Lett. **76**, 3830 (1996).

[152] S.M.J. Aubin, M.W. Wemple, D.M. Adams, H.-L. Tsai, G. Christou, D.N. Hendrickson, J. Am. Chem. Soc. **118**, 7746 (1996).

[153] S.M. Aubin, N.R. Dilley, M.W. Wemple, M.B. Maple, G. Christou, D.N. Hendrickson, J. Am. Chem. Soc. **120**, 839 (1998).

[154] S.M. Aubin, N.R. Dilley, L. Pardi, J. Krzystek, M.W. Wemple, L.-C. Brunnel, M.B. Maple, G. Christou, D.N. Hendrickson, J. Am. Chem. Soc. **120**, 4991 (1998).

[155] C. Sangregorio, T. Ohm, C. Paulsen, R. Sessioli, D. Gatteschi, Phys. Rev. Lett. **78**, 4645 (1997).

[156] W. Wernsdorfer, T. Ohm, C. Sangregorio, R. Sessioli, D. Mailly, C. Paulsen, Phys. Rev. Lett. **82**, 3903 (1999).

[157] L.K. Thompson, O. Waldmann, Z. Xu, in *Magnetism: Molecules to Materials IV*, edited by J.S. Miller, M. Drillon, Wiley/VCH, p.173 (2002).

[158] M. Ruben, J. Rojo, F.J. Romero-Slguero, L.H. Uppadine, J.-M. Lehn, Angew. Chem. Int. Ed. **43**, 3644 (2004).

[159] L.K. Thompson, Coordin. Chem. Rev. **233-234**, 193 (2002).

[160] L.K. Thompson, C.J. Matthews, L. Zhao, Z. Xu, D.O. Miller, C. Wilson, M.A. Leech, J.A. K. Howard, S.L. Heath, A.G. Whittaker, R.E.P. Winpenny, J. Solid. State. Chem. **159**, 308 (2001).

[161] Z. Xu, L.K. Thompson, C.J. Matthews, D.O. Miller, A.E. Goeta, J.A.K. Howard, Inorg. Chem. **40**, 2446 (2001).

[162] R.W. Saalfrank, I. Bernt, E. Uller, F. Hample, Angew. Chem. Int. Ed. **36**, 2482 (1997).

[163] Y. Shapira, V. Bindilattii, J. Appl. Phys. **92**, 4155 (2002).

[164] O. Waldmann, J. Hassmann, P. Müller, D. Volkner, U.S. Schubert, J.-M. Lehn, Phys. Rev. B **58**, 3277 (1998).

[165] K.L. Taft, S.J. Lippard, J. Am. Chem. Soc. **112**, 9629 (1990).

[166] K.L. Taft, C.D. Delfs, G.C. Papaefthymiou, S. Foner, D. Gatteschi, S.J. Lippard, J. Am. Chem. Soc. **116**, 823 (1994). .

[167] I.M. Atkinson, C. Benelli, M. Murrie, S. Parsons, R.E.P. Winpenny, Cehm. Commun., 285 (1999).

[168] A.L. Dearden, S. Parson, R.E.P. Winpenny, Angew. Chem. Int. Ed. **40**, 151 (1997).

[169] J. van Slageren, R. Sessioli, D. Gatteschi, A.A. Smith, M. Helliwell, R.E.P. Winpenny, A. Cornia, A.L. Barra, A.G.M. Jansen, E. Rentscher, G.A. Timico, Chem. Eur. J. **8**, 277 (2002).

[170] J. Schnack, M. Luban, Phys. Rev. B **63**, 014418 (2001).

[171] A. Cornia, A.G.M. Jansen, M. Affronte, Phys. Rev. B **60**, 12177 (1999).

[172] O. Waldmann, J. Schülein, R. Koch, P. Müller, I. Bernt, R.W. Saalfrank, H.P. Andres, H.U. Güdel, P. Allenspach, Inorg. Chem. **38**, 5879 (1999).

[173] O. Waldmann, R. Koch, S. Schromm, J. Schülein, P. Müller, I. Bernt, I. Bernt, R.W. Saalfrank, Inorg. Chem. **40**, 2986 (2001).

[174] P.W. Anderson, Benjamin/Cummings Publishing Co., Menlo Park, p.44 (1984).

[175] O. Waldmann, Phys. Rev. B **65**, 024424 (2001).

[176] F. Meier, V. Cerletti, O. Gywat, D. Loss, and D.D. Awschalom, Phys. Rev. B **69**, 195315 (2004).

[177] M. Ouyang and D.D. Awschalom, Physics World **17**, 21 (2004). .

[178] M. Ouyang and D.D. Awschalom, Science **301**, 1074 (2003).

[179] R. D. Somma, quant-ph/0512209 (2005).

[180] M. Breuer, B. Büchner, R. Müller, M. Cramm, O. Maldonado, A. Freimuth, B. Roden, R. Borowski, B. Heyner, and D. Wohleben, Physica C **208**, 217 (1993).

[181] K. Conder, Mater. Sci. Eng. R**32**, 41 (2001).

[182] N.F. Mott, Proc. Phys. Soc. A **62**, 416 (1949).

[183] Jahn and Teller, Proc. Roy. Soc. **A 161**, 220 (1937).

[184] E. Dagotta, Rev. Mod. Phys. **66**, 763 (1994).

[185] P.W. Anderson, P.A. Lee, M. Randeria, T.M. Rice, N. Trivedi and F.C. Zhang, J. Phys.: Condens. Matter **16**, R755 (2004).

[186] P.A. Frigeri, C. Honerkamp, and T.M. Rice, Euro. Phys. J. B **28**, 61, (2002).

[187] R.C. Zhang and T.M. Rice, Phys. Rev. B **37**, 3759 (1988).

[188] V.J. Emery, s. A. Kivelson, and H.-Q. Lin, Phys. Rev. Lett. **64**, 475 (1990). .

[189] J.M. Tranquada, B.J. Sternlieb, J.D. Axe, Y. Nakamura and S. Uchida, Nature **375**, 561 (1995).

[190] K.M. Lang, V. Madhavan, J.E. Hoffman, E.W. Hudson, H. Eisaki, S. Uchida, and J.C. Davis, Nature **415**, 412 (2002).

[191] L. Gor'kov and V. Kresin, J. Supercond. **13**, 239 (2000).

[192] M.T. Hutchings, in *Solid State Physics*, ed. by F. Seitz and D. Turnbull (Academic, New York, 1964), Vol. 16, p. 227.

[193] R.M. Sternheimer, Phys. Rev. **146**, 140 (1966).

[194] R.M. Sternheimer, M. Blume, and R.F. Peierls, Phys. Rev.**173**, 376 (1968).

[195] C.A. Morrison, *Angular Momentum Theory Applied to Interactions in Solids*, Berlin: Springer, p. 111 (1988).

[196] J. Mesot, P. Allenspach, U. Staub, and A. Furrer, Phys. Rev. B **47**, 6027 (1993).

[197] A. Furrer, P. Brüsch and P. Unternährer, Phys. Rev. B **38**, 4616 (1988).

[198] D. J. Newman and G. E. Stedman, J. Chem. Phys. **51**, 3013 (1969).

[199] K.W. Becker, P.Fulde, J. Keller, Z. Physik b **28**, 9 (1977). .

[200] P. Fulde, M. Loewenhaupt, Adv. Phys. **43**, 589 (1986).

[201] C. Kittel, *Quantum Theory of Solids*, John Wiley & Sons, Inc.

[202] U. Fano and G. Racah, *Irreducible Tensorial Sets*, Academic Press New York (1959).

[203] E.P. Wigner, *Group Theory abd its Application to the Quantum Mechanics of Atomic Spectra*, Academic Press New York (1959).

[204] P. Fischer, G. Frey, M. Koch, M. Könnecke, V. Pomjakushin, J. Schefer, R. Thut, N. Schlumpf, R. Bürge, U. Greuter, S. Bondt, E. Berruyer, Physica B **276-278**, 146 (2000).

[205] J. Schefer, M. Könnecke, A. Murasik, A. Czopnik, Th. Strässle, P. Keller, N. Schlumpf, Physica B **276-278**, 168 (2000).

[206] J. Mesot, S. Janssen, L. Holitzner, R. Hempelmann, J. Neutr. Res. **3**, 293 (1996).

[207] S. Janssen, J. Mesot, L.Holitzner, A. Furrer, R. Hempelmann, Physica B **234-236**, 1174 (1997).

[208] http://www.ill.fr/YellowBook/IN4/.

[209] A.D. Taylor, R.C. Ward, W.G. Williams, Y. Endoh, N. Watanabe, Proc ICANS-IX (ed. F. Atchison, W. Fischer) p.535 (1987).

[210] A.D. Taylor, M. Arari, S.M. Bennington, Z.A. Bowden, R. Osborn, K. Andersen, W.G. Stirling, T. Nakane, K. Yamada, D. Welz, Proc. 11^{th} ICANS Meeting, KEK, Tsukuba, 22-26 October (1990).

[211] S.N. Klausen, K. Lefmann, D.E. McMorrow, F. Altdorfer, S. Janssen, M. Lüthy, Appl. Phys. A **74** [Suppl.], S1508 (2002).

[212] K. Lefmann, D.F. McMorrow, H.M. Rønnow, K. Nielson, K.N. Clausem, B. Lake, G. Aeppli, Physica B **283**, 343 (2000).

[213] P. Böni and P. Keller, PSI Proceedings 96-02 35-42 (1996).

[214] W.B. Pearson and I.M. Templeton, 1094 (1958).

[215] A. Eiling and J.S. Schilling, J. Phys. F: Metal Phys. **11**, 623 (1981).

[216] E. Maxwell, Phys. Rev. **78**, 477 (1950).

[217] W. Buckel and R. Kleiner, *Supraleitung, Grundlagen und Anwendungen*, WILEY-VCH Verlag GmbH & Co. KGaA (2004).

[218] A.S. Alexandrov, N.F. Mott, Int. J. Mod. Phys. **8**, 2075 (1994). .

[219] W.L. McMillan, Phys. Rev. **167**, 331 (1968). .

[220] C. Buzea and T. Yamashita, Supercond. Sci. Technol. **14**, R115 (2001).

[221] G.M. Zhao, K. Conder, H. Keller, K.A. Müller, J. Phys.: Condens. Matter **10**, 9055 (1998).

[222] G.M. Zhao, H. Keller, K. Conder, J. Phys.: Condens. Matter **13**, R569 (2001).

[223] J.P. Franck, J. Jung, A.K. Mohamed, Phys. Rev. B **44**, 5318 (1991).

[224] W.E. Pickett, R.E. Cohen, H. Krakauer, Phys. Rev. Lett. **67**, 228 (1991).

[225] R. Khasanov, A. Shengelaya, E. Morenzoni, M. Angst, K. Conder, I.M. Savić, D. Lampakis, E. Liarokapi, A. Tatsi, H. Keller, Phys. Rev. B **68**, 220506 (2003).

[226] D. Zech, H. Keller, K. Conder, E. Kaldis, E. Liarokapis, N. Poulakis, K.A. Müller, Nature **317**, 681 (1994).

[227] P.M. Singer, W. Hunt, A.F. Cederström, and T. Imai, Phys. Rev. B **60**, 15345 (1999).

[228] S. Andergassen, S. Caprara, C. Di Castro, and M. Grilli, Phys. Rev. Lett. **87**, 056401 (2001).

[229] A. Bussmann-Holder, J. Supercond. **13**, 773 (2000).

[230] L.P. Gor'kov, J. Supercond. **13**, 765 (2000).

[231] A. Shengelaya, Guo-meng Zhao, C.M. Aegerter, K. Conder, I.M. Savić, and H. Keller, Phys. Rev. Lett. **83**, 5142 (1999).

[232] J.S. Schilling, cond-mat/0110267 (2001).

[233] M.C. Murayama, Y. Iye, T. Enomoto, N. Môri, Y. Yamada, T. Matsumoto, Y. Kubo, Y. Shimakwa, and T. Manako,urayama, Physica C **183**, 277 (1991).

[234] A. Bussmann-Holder and H. Keller, cond-mat/0409738 (2004).

[235] K.H. Höck, H. Nickisch, H. Thomas, Helv. Phys. Acta **56**, 237 (1983).

[236] A. Lanzara, P.V. Bogdanov, X.J. Zhou, S.A. Keller, D.I. Feng, E.D. Lu, T. Yoshida, H. Eisaki, A. Fujimori, K. Kishio, J.I. Shimoyama, T. Noda, S. Uchida, Z. Hussain, Z.-X. Shen, Nature **412**, 510 (2001).

[237] Y. Petrov, T. Egami, R.J. McQueency, M. Yethiraj, H.A. Mook, F. Dogan, cond-mat-0003414 (2000).

[238] A. Bianconi, N.L. Saini, A. Lanzara, M. Missori, T. Rossetti, H. Oyanagi, H. Yamaguchi, K. Oka, T. Ito, Phys. Rev. Lett. **76**, 3412 (1996).

[239] L. Gor'kov and A.V. Sokol, JETP Letters **46**, 420 (1987).

[240] G.M. Zhao, M.B. Hunt, H. Keller and K.A. Müller, Nature **385**, 236 (1997).

[241] G.M. Zhao, K. Conder, H. Keller and K.A. Müller, J. Phys.: Condens. Matter **10**, 9055 (1998).

[242] B.I. Kochelaev, J. Sichelschmidt, B. Elschner, W. Lemor, and A. Loidl, Phys. Rev. Lett. **79**, 4274 (1997).

[243] J. Mesot and A. Furrer, J. Supercond. **10**, 623 (1997).

[244] Fischer, K. Kakurai, M. Steiner, K.N. Clausen, B. Lebech, F. Hulliger, H.R. Ott, P. Brüsch, P. Unternährer, Physica C **152**, 145 (1988).

[245] A. Podlesnyak, P.S. Häfliger, K. Conder, and A. Furrer, J. Phys.: Condens. Matter **17**, S801 (2005).

[246] H. Takahashi, H. Shaked, B.A. Hunter, P.G. Radaelli, R.L. Hittermann, Hinks, and J. D. Jorgensen et al., Phys. Rev. B **50**, 3221 (1994).

[247] A.T. Boothroyd, A. Mukherjee, A.P. Murani, Phys. Rev. Lett. **77**, 1600 (1996).

[248] J. Korringa, Physica (Utrecht) **16**, 601 (1950).

[249] V.L. Aksenov and V.V. Kabanov, Phys. Rev. B**49**, 3524 (1994).

[250] R. Osborn and E.A. Goremychkin, Physica C **185-189**, 1179 (1991).

[251] Z. Kovacevic and N.M. Plakida, Physica C **228**, 15 (1994).

[252] J. Rossat-Mignod, L.P. Regenault, C. Vettier, P. Bourges, P. Burlet, J. Bossy, J.Y. Henry and G. Lapertot, Phys. C **185-189**, 86 (1991).

[253] U. Staub, M. Gutmann, F. Fauth and W. Kagunya, J. Phys.: Condens. Matter **11**, L59 (1999).

[254] S.W. Lovesy and U. Staub, Phys. Rev. B **61**, 9130 (2000).

[255] R. Orbach, Proc. R. Soc. London, Ser. A **264**, 458 (1966).

[256] W.M. Yen and P.M. Selzer, in *Laser Spectroscopy of Solids*, edited by W.M. Chen and P.M. Selzer (Springer-Verlag, Berlin 1981), pp. 141-188. .

[257] A.T. Boothroyd, Phys. Rev. B **64**, 066501 (2001).

[258] J. Mesot, P. Allenspach, U. Staub, A.Furrer, H. Mutka, R. Osborn and A. Taylor, Phys. Rev. B **47**, 6027 (1993).

[259] J. Mesot, G. Böttiger, H. Mutka, and A. Furrer, Europhys. Lett. **44**, 498 (1998).

[260] H.J.H. Smilde, A.A. Golubov, Ariando, G. Rijndrs, J. M. Dekkers, S. Harkema, D.H.A. Blank, H. Rogalla, and H. Hilgerkamp, Phys. Rev. Lett. **95**, 257001 (2005).

[261] J. Mesot and A. Furrer, *Neutron Scattering in Layered Copper-Oxide Superconductors* ed A. Furrer (Dordrecht: Kluwer) 335 (1998).

[262] M.R. Norman, H. Ding, M. Randeria, J.C. Campuzano, T. Yokoya, T. Takeuchi, T. Takahashi, T. Mochiku, K. Kadowski, P. Guptasarma, D.G. Hinks, Nature **392**, 157 (1998).

[263] A.Schnyder, A.Bill, C. Mudry, R. Gilardi, H.M. Rønnow, J. Mesot, Phys. Rev. B **70**, 214511 (2004).

[264] G.Xiao, M.Z. Cieplak, J.Q. Xiao and C.L. Chien, Phys. Rev. B **42**, 8752 (1990).

[265] T.P. Devereaux and D. Belitz, cond-mat/9502094 (1994).

[266] A. Ino, T. Mizokawa, K. Kobayashi, A. Fujimori, T. Sasagawa, T. Kimura, K. Kishio, K. Tamasaku, H.Eisaki, and S. Uchida, Phys. Rev. Lett. **81**, 2124 (1998).

[267] P. S. Häfliger et al., A. Podlesnyak, K. Conder, E. Pomjakushina, and A. Furrer, Europhys. Lett. **67**, 1018 (2004).

[268] A. Furrer, K. Conder, P.S. Häfliger, A. Podlesnyak, Physica C **408-410**, 773 (2004).

[269] N. Momono, T. Matsuzaki, M. Oda, and M. Ido, J. Phys. Soc. Jpn. **71**, 2832 (2002).

[270] J.L. Tallon and J.W. Loram, Physica C **349**, 53 (2001).

[271] P.S. Häfliger, A. Podlesnyak, K. Conder, and A. Furrer, Europhys. Lett. **73**, 260 (2006).

[272] L.P. Gor'kov, J. Supercond.: Incorporating Novel Magnetism **13**,765 (2000).

[273] A. Furrer, D. Rubio Temprano, J. Mesot, K. Conder and K.A. Müller, J. Supercond. **15**, 361 (2002).

[274] P.G. Radaelli, C.U. Serge, D.G. Hinks and J.D. Jorgensen, Phys. Rev. B **45**, 4923 (1992).

[275] A. Bussmann-Holder and H. Keller, cond-mat/0409738 (2004).

[276] S.C. Abrahams, J.M. Reddy, J. Chem. Phys. **43**, 2533 (1965).

[277] R. Schenker, H. Weihe, and H.U. Güdel, Inorg. Chem. **40**, 4319 (2001).

[278] B.S. Snyder, G. S. Patterson, A.J. Abrahamson, and R.H. Holm, J. Am. Chem. Soc. **111**, 5214 (1989).

[279] F. Le Gall, D. Gatteschi, Inorg. Chem. Acta **262**, 123 (1997).

[280] P.D. Battle, A.K. Cheetham, G.L. Long, and G. Longworth, Inorg. Chem. **21**, 4223 (1982).

[281] P.D. Battle, A.K. Cheetham, W.T.A. Harrison, N.J. Pollard, and J. Faber, J. Solid State Chem. **58**, 221 (1985).

[282] St. T. Ochsenbein, G. Chaboussant, A. Sieber, H.-U. Güdel, St. Janssen, A. Furrer and J.P. Attfield, Phys. Rev. B **68**, 092410 (2003).

[283] L.J. Jongh and A. R. Miedema, Adv. Phys. **23**, 1 (1974).

[284] N.W. Ashcroft and N. D. Mermin, *Solid State Physics* (Harcourt Brace College Publishers, New York, 1976).

[285] W. Henggeler,T. Chattopadhyay, B. Roessli, D.J. Zhigunov, S.N. Barilo, A. Furrer, Z. Phys. B **99**, 465 (1996).

[286] P.M. Levy, Phys. Rev. **177**, 509 (1969).

[287] G. Lautenschläger et al., Zeitschrift f. Kristallographie **209**, 936 (1994).

[288] I. Peschel, M. Klenin, and P. Fulde, J. Phys. C: Solid State Phys., **5**, L194 (1972).

[289] H.-G. Purwins, J.G. Houmann, and P. Bak, Phys. Rev. Lett. **31**, 1585 (1973).

[290] J. Jensen, A.R. Macintosh *Rare earth magnetism, Structres and Excitations*, Clarendon Press - Oxford (1991).

Appendix A

Spin systems

A.1 Mean-field treatment

Expressing the spin operator as

$$\mathbf{S}_i = (\mathbf{S}_i - \langle \mathbf{S} \rangle) + \langle \mathbf{S} \rangle, \tag{A.1}$$

yields the following expression for the product $\mathbf{S}_i \mathbf{S}_j$

$$\mathbf{S}_i \mathbf{S}_j = \mathbf{S}_i \langle \mathbf{S} \rangle + \mathbf{S}_j \langle \mathbf{S} \rangle - \langle \mathbf{S} \rangle^2 + (\mathbf{S}_i - \langle \mathbf{S} \rangle)(\mathbf{S}_j - \langle \mathbf{S} \rangle). \tag{A.2}$$

and Eq. 2.26 follows.

A.2 RPA

A.2.1 Response function

The purpose of linear response theory is to give an expression for $\langle \delta B(t) \rangle$ as in Eq. 2.40. To do so, it is necessary to compute expectation values which are dependent on the density operator $\rho(t)$, see Eq. 2.32.
Just as the Hamiltonian, also the density operator has to be decomposed into to ρ_0 of the thermal-equilibrium state and ρ_1 of the perturbation:

$$\rho(t) = \rho_0 + \rho_1(t) \tag{A.3}$$

We then go over to the interaction picture

$$\begin{aligned} \rho_I(t) &:= e^{i\mathcal{H}_0 t/\hbar} \rho(t) e^{-i\mathcal{H}_0 t/\hbar} \qquad 1^{st} \text{ step} \\ \frac{d}{dt}\rho_I(t) &= -\frac{i}{\hbar} e^{i\mathcal{H}_0 t/\hbar} [\mathcal{H}_1, \rho(t)] e^{-i\mathcal{H}_0 t/\hbar}. \end{aligned} \tag{A.4}$$

Recalling that $\mathcal{H}_1 = Af(t)$ is linear in $f(t)$ we continue with

$$\begin{aligned} \rho(t) &\rightarrow \rho_0 \qquad 2^{nd} \text{ step} \\ \Rightarrow \frac{d}{dt}\rho_I(t) &\sim \frac{i}{\hbar}[A_0(t), \rho_0] f(t), \end{aligned} \tag{A.5}$$

where we defined $A_0(t) = e^{i\mathcal{H}_0 t/\hbar} A e^{-i\mathcal{H}_0 t/\hbar}$. Thus Eq. 2.40 follows.

Example: ferromagnetic Heisenberg chain

We intend to derive the energy dispersion within the RPA for a ferromagnetic Heisenberg chain where the spins are equally separated by a distance δ. To do so, we first have to compute the single-ion susceptibility. We will point out only the important steps, details can be found elsewhere, e.g.in Ref. [290] We consider the mean-field Hamiltonian introduced in Section 2.4.1.:

$$\begin{aligned} \mathcal{H}_{mf} &= \sum_i \mathcal{H}_i^{mf} \\ \mathcal{H}_i &= -S_i^z J(0)\langle S\rangle + \frac{1}{2}J(0)\langle S\rangle^2. \end{aligned} \tag{A.6}$$

The single-ion eigenstates of $\mathcal{H}_i^{mf}$ are

$$\begin{aligned} \mathcal{H}_i^{mf}|SM\rangle &= E_M|S^z\rangle = E_M|M\rangle \qquad \text{with } M = -S, -S+1, ..., S \\ E_M &= -MJ(0)\langle S^z\rangle = -M\Delta, \qquad \Delta = J(0)\langle S^z\rangle \end{aligned} \tag{A.7}$$

where we discarded the constant energy contribution. The interaction is determined by

$$\begin{aligned} J(q) &= J\sum_\delta e^{iq\cdot\delta} = \frac{1}{2}J\left(e^{iq\cdot\delta} + e^{-iq\cdot\delta}\right) \\ &= cos(q\cdot\delta) \end{aligned} \tag{A.8}$$

We are now able to give a concrete expression for the single-ion susceptibility using Eq. 2.46. Considering that only terms with $\alpha = M+1$ and $\alpha' = M$ contribute to the sum, it is straight forward to show that

$$\begin{aligned} \chi^0_{+-}(\omega) &= \frac{2\langle S^z\rangle_0}{\Delta - \hbar\omega} = \chi_{-+}(-\omega) \\ \chi_{++}(\omega) &= \chi_{--}(\omega) = 0 \end{aligned} \tag{A.9}$$

We now build physical observable with the help of the relations

$$S^x = \frac{1}{2}(s^+ + S^-) \qquad S^y = \frac{1}{2i}(S^+ - S^-) \tag{A.10}$$

which lead to the following quadratic terms

$$\begin{aligned} S^xS^x &= \frac{1}{4}(S^+S^+ + S^+S^- + S^-S^+ + S^-S^-) \\ S^xS^y &= \frac{1}{4i}(S^+S^+ - S^+S^- + S^-S^+ - S^-S^-) \\ S^yS^x &= \frac{1}{4i}(S^+S^+ + S^+S^- - S^-S^+ - S^-S^-) \\ S^yS^y &= -\frac{1}{4}(S^+S^+ - S^+S^- - S^-S^+ + S^-S^-) \end{aligned} \tag{A.11}$$

This way we construct the complex single-ion susceptibility tensor $\chi^0_{\alpha\beta}(\omega)$:

$$\begin{aligned} \chi^0_{xx}(\omega) = \chi^0_{yy}(\omega) &= \frac{1}{4}\left(\chi^0_{+-}(\omega) + \chi^0_{-+}(\omega)\right) = \frac{\Delta\langle S^z\rangle}{\Delta^2 - (\hbar\omega)^2} \\ \chi^0_{xy}(\omega) = -\chi^0_{yx}(\omega) &= -\frac{1}{4i}\left(\chi^0_{+-}(\omega) - \chi^0_{-+}(\omega)\right) = \frac{i\hbar\omega\langle S^z\rangle}{\Delta^2 - (\hbar\omega)^2} \end{aligned} \tag{A.12}$$

No dynamic contribution from the z direction occurs, reflecting the alignment of the system under the influence of the mean field. It often comprises an elastic contribution. Now we insert

$$\begin{aligned} \chi^0(\omega) &= \begin{pmatrix} \chi^0_{xx}(\omega) & \chi^0_{xy}(\omega) \\ \chi^0_{yx}(\omega) & \chi^0_{yy}(\omega) \end{pmatrix} \\ J(q) &= \begin{pmatrix} J(q) & 0 \\ 0 & J(q) \end{pmatrix} \end{aligned} \tag{A.13}$$

into the RPA equation 2.53, which leads to the following solution

$$\begin{aligned} \chi_{xx}(q,\omega) &= \frac{E(q)\langle S^z\rangle}{E(q)^2 - (\hbar\omega)^2} \\ E(q) &= \Delta - \langle S^z\rangle J(q) = \langle S^z\rangle[J(0) - J(q)] \end{aligned} \tag{A.14}$$

where $E(q)$ corresponds to the well known dispersion relation. In the long-wavelength limit ($|q \cdot a \ll 1$) the dispersion may be approximated by

$$E(q) = 2\langle S^z\rangle J(1 - (q \cdot a)^2) \tag{A.15}$$

Note that the susceptibility given in Eq. A.14 can be interpreted as

$$\chi_{xx}(q,\omega) = \frac{1}{2}\langle S^z\rangle \lim_{\epsilon\to 0}\left(\frac{1}{E(q) - \hbar\omega - i\hbar\epsilon} + \frac{1}{E(q) - \hbar\omega + i\hbar\epsilon}\right) \tag{A.16}$$

A.3 Linear spin-wave theory

The product $\mathbf{S}_i\mathbf{S}_j$ can be written in terms of spin operators S^+ and S^-:

$$\begin{aligned} \mathbf{S}_i\mathbf{S}_j &= S_i^x S_j^x + S_i^y S_j^y + S_i^z S_j^z \\ &= S_i^+ S_j^- + S_i^- S_j^+ + 2S_i^z S_j^z \end{aligned} \tag{A.17}$$

where we made use of

$$\begin{aligned} S^+ &= S^x + iS^y, \qquad S^+|M>= \sqrt{(S-M)(S+M+1)}|M+1> \\ S^- &= S^x - iS^y \qquad S^-|M>= \sqrt{(S+M)(S+M+1)}|M-1>. \end{aligned} \tag{A.18}$$

The components S_j^x, S_j^y and S_j^z involved in the Hamiltonian 2.55 are not independent, but are connected by $\mathbf{S}_j^2 = S(S+1)$. It is therefore more convenient to work with operators which are independent. Such operators - the boson creation and annihilation operators $a_j^\dagger$, a_j - are defined by the so-called *Holstein-Primakoff transformation*:

$$\begin{aligned} S_j^+ &= \sqrt{2S}\left(1 - \frac{a_j^\dagger a_j}{2S}\right)^{1/2} a_j \qquad \text{Holstein-Primakoff} \\ S_j^- &= \sqrt{2S}a_j^\dagger\left(1 - \frac{a_j^\dagger a_j}{2S}\right)^{1/2} \end{aligned} \tag{A.19}$$

with

$$[a_j, a_l^\dagger] = \delta_{jl} \tag{A.20}$$

From Eq. A.19 the transformation for S_j^z can be obtained

$$S_j^z = S - a_j^\dagger a_j \tag{A.21}$$

From Eq. A.21 the meaning of $a_j^\dagger$ and a_j becomes clear: $\sum_j a_j^\dagger a_j$ is the number operator of reduced spins or in the case of spin 1/2 it denotes the number of reversed spins.
The resulting Hamiltonian is non linear and approximations have to be made to compute the dispersion relation.
In *linear spin-wave theory* the Holstein-Primakoff transformation given in Eq. A.19 is linearized under the assumption that the fractional spin reduction is small

$$\begin{aligned} \frac{\langle a_j^\dagger a_j \rangle}{S} &\ll 1 \\ \Rightarrow S_j^+ &= \sqrt{2S} a_j \qquad \text{Linear Holstein-Primakoff} \\ S_j^- &= \sqrt{2S} a_j^\dagger. \end{aligned} \tag{A.22}$$

Here we used a Taylor approximation to expand the square root and kept terms only up to zeroth order. The transformation for S_j^z still holds. Next we introduce the Fourier-transformed operators

$$\begin{aligned} a_k &= \frac{1}{\sqrt{N}} \sum_j e^{ikR_j} a_j \\ a_k^\dagger &= \frac{1}{\sqrt{N}} \sum_j e^{-ikR_j} a_j^\dagger \end{aligned} \tag{A.23}$$

with commutation relations:

$$[a_k, a_{k'}^\dagger] = \delta_{kk'} \qquad [a_k, a_{k'}] = [a_k^\dagger, a_{k'}^\dagger] = 0. \tag{A.24}$$

$a_k^\dagger$ (a_k) denotes the creation (annihilation) of a magnon. Thus within the frame of *linear* spin-wave theory an excitation is described as a linear superposition of states in which a single spin is changed from its ground-state position. Using Eq. A.22 we may express the Hamiltonian 2.55 in terms of spin wave variables and after some algebra we find:

$$\begin{aligned} \mathcal{H} &= -JNzS^2 + \mathcal{H}_0 \\ \mathcal{H}_0 &= \sum_k 2JzS(1 - \gamma_k) a_k^\dagger a_k \end{aligned} \tag{A.25}$$

where

$$\gamma_k = \frac{1}{z} \sum_\delta e^{ik\cdot\delta} = \frac{1}{2} \left(e^{ik\cdot\delta} + e^{-ik\cdot\delta} \right) = cos(k \cdot \delta) \tag{A.26}$$

assuming $z = 2$ nearest neighbor in the case of a ferromagnetic Heisenberg chain. Note that the exchange contribution to the magnon frequency is of the form of the de Broglie dispersion for a free particle of mass m^*, namely

$$\omega_k = \frac{1}{2m^*}k^2; \qquad 2JS\delta^2 = \frac{1}{2m^*} \tag{A.27}$$

For conventional ferromagnets ($T_c \sim 300$ K), m^* is approximately 10 times larger than the electronic mass [201].

Antiferromagnetic magnons

We then have to introduce separate annihilation and creation operators for the sublattice A and B:

$$\begin{aligned} S^+_{Aj} &= \sqrt{2S}a_j & \qquad S^+_{Bj} &= \sqrt{2S}b^\dagger_j \\ S^-_{Aj} &= \sqrt{2S}a^\dagger_j & \qquad S^-_{Bj} &= \sqrt{2S}b_j \\ S^z_{Aj} &= S - a^\dagger_j a_j & \qquad S^z_{Bj} &= -S + b^\dagger_j b_j \end{aligned} \tag{A.28}$$

Introducing the spin wave variables

$$\begin{aligned} a_k &= \frac{1}{\sqrt{N}}\sum_j e^{ikR_j}a_j & \qquad b_k &= \frac{1}{\sqrt{N}}\sum_j e^{-ikR_j}b_j \\ a^\dagger_k &= \frac{1}{\sqrt{N}}\sum_j e^{-ikR_j}a^\dagger_j & \qquad b^\dagger_k &= \frac{1}{\sqrt{N}}\sum_j e^{ikR_j}b^\dagger_j \end{aligned} \tag{A.29}$$

with

$$[a_k, a^\dagger_{k'}] = \delta_{kk'} = [b_k, b^\dagger_{k'}]$$

$$[a_k, a_{k'}] = [a^\dagger_k, a^\dagger_{k'}] = [b_k, b_{k'}] = [b^\dagger_k, b^\dagger_{k'}]$$

$$[a_k, b_{k'}] = 0 \tag{A.30}$$

yields the Hamiltonian in magnon variables

$$\begin{aligned} \mathcal{H} &= 2NzJS^2 + \mathcal{H}_0 \\ \mathcal{H}_0 &= 2JzS\sum_k \Big[\gamma_k(a^\dagger_k c^\dagger_k + a_k b_k) + (a^\dagger_k a_k + b^\dagger_k b_k)\Big]. \end{aligned} \tag{A.31}$$

γ_k is defined as in Eq. 2.59.
The above Hamiltonian is a linear form in the vectors $[a_k, a^\dagger_k, b_k, b^\dagger_k]$ and $[a^\dagger_k, a_k, b^\dagger_k, b_k]^T$, but it is not diagonal. The transformation to a new basis is obtained by the so-called Bogoliubov transformation to operators $\alpha^\dagger$, α and $\beta^\dagger$, β.

Appendix B

Tetrameric clusters in α-$MnMoO_4$

B.1 Transition matrix elements

Here we will give the values for the matrix elements of the cluster transitions introduced in Section 5.3.3. To do so we follow the formulas given in Refs. [105, 119].
The M-dependence of the matrix elements for the transition $|S_{12}, S_{34}, S, M\rangle \rightarrow S'_{12}, S'_{34}, S', M'\rangle$ is split by the Wigner-Eckart theorem

$$\begin{aligned}\langle S'_{12}, S'_{34}, S', M'||\hat{T}^q_j||S_{12}, S_{34}, S, M\rangle &= (-1)^{S-M}\begin{pmatrix} S & 1 & S' \\ -M & q & M' \end{pmatrix} \\ &\cdot \langle S'_{12}, S'_{34}, S'||\hat{T}_j||S_{12}, S_{34}, S\rangle. \end{aligned} \tag{B.1}$$

The reduced matrix elements $\langle S'_{12}, S'_{34}, S'||\hat{T}_j||S_{12}, S_{34}, S\rangle$ are given by:

$$\begin{aligned}&\langle S'_{12}, S'_{34}, S'||\hat{T}_1||S_{12}, S_{34}, S\rangle = \\ &\quad \delta(S_{34}, S'_{34}) \times (-1)^{S_1+S_2+S_{12}+S'_{12}+S_{34}+S'} \\ &\quad \sqrt{(2S+1)(2S'+1)(2S_{12}+1)(2S'_{12}+1)} \\ &\quad \begin{bmatrix} S & S' & 1 \\ S'_{12} & S_{12} & S_{34} \end{bmatrix} \cdot \begin{pmatrix} S_{12} & S'_{12} & 1 \\ S'_1 & S_1 & S_2 \end{pmatrix} \cdot \langle S_1||\hat{T}_1||S'_1\rangle \\ &\quad \langle S'_{12}, S'_{34}, S'||\hat{T}_2||S_{12}, S_{34}, S\rangle = (-1)^{S_{12}-S'_{12}}\langle S'_{12}, S'_{34}, S'||\hat{T}_1||S_{12}, S_{34}, S\rangle \end{aligned}$$

and

$$\begin{aligned}&\langle S'_{12}, S'_{34}, S'||\hat{T}_3||S_{12}, S_{34}, S\rangle = \\ &\quad \delta(S_{12}, S'_{12}) \times (-1)^{S_3+S_4+S_{12}+2S'_{34}+S'} \\ &\quad \sqrt{(2S+1)(2S'+1)(2S_{34}+1)(2S'_{34}+1)} \\ &\quad \begin{bmatrix} S & S'1 & \\ S'_{34} & S_{34} & S_{12} \end{bmatrix} \cdot \begin{pmatrix} S_{34} & S'_{34} & 1 \\ S'_3 & S_3 & S_4 \end{pmatrix} \cdot \langle S_3||\hat{T}_3||S'_3\rangle \\ &\quad \langle S'_{12}, S'_{34}, S'||\hat{T}_4||S_{12}, S_{34}, S\rangle = (-1)^{S_{34}-S'_{34}}\langle S'_{12}, S'_{34}, S'||\hat{T}_3||S_{12}, S_{34}, S\rangle. \end{aligned}$$

From the symmetry properties of the 3-j and 6-j symbols as well as from the δ-functions we recover the dipole selection rules for the transitions of a tetramer system

$$\Delta S = 0, \pm 1; \qquad \Delta M = 0, \pm 1$$

Table B.1: Values for matrix elements of transitions from the ground state to excited tetramer states.

$\|5,5,10,10\rangle \rightarrow$	$\langle \hat{T}_j^q \rangle$
$\|5,5,10,9\rangle$	$\langle \hat{T}_1^1 \rangle = -0.79 = \langle \hat{T}_3^1 \rangle$
$\|4,5,9,9\rangle$	$\langle \hat{T}_1^1 \rangle = 1.12$
$\|5,4,9,9\rangle$	$\langle \hat{T}_1^1 \rangle = 1.12$
$\|5,5,9,9\rangle$	$\langle \hat{T}_1^1 \rangle = -0.79 = \langle \hat{T}_3^1 \rangle$
$\|5,5,10,-10\rangle \rightarrow$	$\langle \hat{T}_j^q \rangle$
$5,5,10,-9\rangle$	$\langle \hat{T}_1^{-1} \rangle = -0.79 = \langle \hat{T}_3^{-1} \rangle$
$\|4,5,9,-9\rangle$	$\langle \hat{T}_1^{-1} \rangle = 1.12$
$\|5,4,9,-9\rangle$	$\langle \hat{T}_1^{-1} \rangle = 1.12$
$\|5,5,9,-9\rangle$	$\langle \hat{T}_1^{-1} \rangle = -0.79 = \langle \hat{T}_3^{-1} \rangle$

$$\begin{aligned} &\text{for the operators } \hat{T}_1, \hat{T}_2: && \Delta S_{12} = 0, \pm 1; \quad \Delta S_{34} = 0; \\ &\text{for the operators } \hat{T}_3, \hat{T}_4: && \Delta S_{12} = 0; \quad \Delta S_{34} = 0, \pm 1; \end{aligned} \tag{B.2}$$

It is then straight forward to compute the values of these matrix elements, which we call shortly $\langle \hat{T}_j^q \rangle$ see Table B.1.

B.2 Single-ion susceptibility tensor

In order to get the expressions for the components of the single-ion tensor, we have to compute the matrix elements $\langle \Gamma_i | S^\alpha | \Gamma_0 \rangle_r$:

$$\begin{aligned} \langle \Gamma_i | S^x | \Gamma_0 \rangle_r &= \frac{\sqrt{2}}{2} \langle \Gamma_i | (\hat{T}^{+1} - \hat{T}^{-1}) | \Gamma_0 \rangle_r \\ \langle \Gamma_i | S^y | \Gamma_0 \rangle_r &= \frac{\sqrt{2}}{2i} \langle \Gamma_i | (-\hat{T}^{+1} - \hat{T}^{-1}) | \Gamma_0 \rangle_r \end{aligned} \tag{B.3}$$

Here we introduced $\hat{T}^{\pm 1}$ with the following property

$$|\langle \Gamma_i || \hat{T}^{\pm 1} || \Gamma_0 \rangle|^2 = \frac{1}{n} \sum_{j=1}^{n} |\langle \Gamma_i || \hat{T}_j^{\pm 1} || \Gamma_0 \rangle|^2 \tag{B.4}$$

where n denotes the number of non-vanishing matrix elements $\langle \Gamma_i || \hat{T}_j^{\pm 1} || \Gamma_0 \rangle$.
Note that for the transitions with spin up e.g. $|5,5,10,10\rangle \rightarrow |5,5,10,9\rangle$, only the matrix element with $\hat{T}^{+1}$ contributes because the 3-j symbol makes the matrix element with $\hat{T}^{-1}$ vanish and vice versa.
We therefore find

$$
\begin{aligned}
(\chi^0)^{xx}_A(\omega) &= 2\sum_{i=1}^{4} \frac{|\langle\Gamma_i||\frac{\sqrt{2}}{2}\hat{T}^1||\Gamma_0\rangle|^2}{E_i - E_0 - \hbar\omega} \\
&= \sum_{i=1}^{4} \frac{\frac{1}{n}\sum_{j=1}^{n}|\langle\Gamma_i||\hat{T}^1_j||\Gamma_0\rangle}{\Delta_i - \hbar\omega} \\
&= (0.79)^2\left(\frac{1}{\Delta_1 - \hbar\omega} + \frac{1}{\Delta_4 - \hbar\omega}\right) + (1.12)^2\left(\frac{1}{\Delta_2 - \hbar\omega} + \frac{1}{\Delta_3 - \hbar\omega}\right) \\
&\equiv f(\omega) \qquad \text{(B.5)}
\end{aligned}
$$

Appendix C

Toy model

C.1 Binuclear cluster

According to Ref. [119] the transition matrix elements for $|\Gamma_0\rangle \rightarrow |\Gamma_i\rangle$, $i = 1, 2$ are given by

$$\begin{aligned}\langle S_1', S_2' S'.M'\rangle|\hat{T}_j^q|S_1, S_2, S, M\rangle &= (-1)^{S-M} \\ &\quad \begin{pmatrix} S & 1 & S' \\ -M & q & M' \end{pmatrix} \langle S_1', S_2', S'||\hat{T}_j||S_1, S_2, S\rangle \\ &\quad j = 1, 2, \end{aligned} \tag{C.1}$$

where

$$\begin{aligned}\langle S_1', S_2', S'||\hat{T}_1||S_1, S_2, S\rangle &= \delta(S_2, S_2') \times (-1)^{S_1+S_2+S'+1} \\ &\sqrt{(2S+1)(2S'+1)} \begin{bmatrix} S & S' & 1 \\ S_1' & S_1 & S_2 \end{bmatrix} \times \langle S_1'||\hat{T}_1||S_1\rangle \end{aligned} \tag{C.2}$$

$$\langle S_1'||\hat{T}_j||S_j\rangle = \delta(S_1, S_1')\sqrt{S_1(S_1+1)(2S_1+1)} \tag{C.3}$$

There is a smilar expression for $\langle S_1', S_2', S'||\hat{T}_2||S_1, S_2, S\rangle$, which can be found in Ref. [105].

Appendix D

Numerics

Here we present the basic principles of a program which we have developed in order to compute the Brillouin zone of α-$MnMoO_4$.
The first Brillouin zone is defined as all points in reciprocal space whose distance to the origin $(0, 0, 0)$ is smaller than the distance to any other reciprocal lattice point **nlp** (nuclear lattice point) or **mlp** (magnetic lattice point), in other words:

$$|\mathbf{pp}| < |\mathbf{nlp} - \mathbf{pp}| \quad \text{and} \quad |\mathbf{pp}| < |\mathbf{mlp} - \mathbf{pp}| \tag{D.1}$$

We have implemented this criteria into a Monte-Carlo simulation using Matlab:

(1)	create the coordinate system of the reciprocal space
	basis vectors in units of $Å^{-1}$: **v1**, **v2**, **v3**
(2)	create the nuclear Bragg points $\mathbf{nlp} = h_n \cdot \mathbf{v1} + k_n \cdot \mathbf{v2} + l_n \cdot \mathbf{v3}$
	create the magnetic Bragg point $\mathbf{mlp} = h_m \cdot \mathbf{v1} + k_m \cdot \mathbf{v2} + l_m \cdot \mathbf{v3}$
(3)	generate a random array of points
	generate random vectors in reciprocal space **pp**
(4)	criteria for Brillioun zone, Eq. D.1
(5)	draw point **pp** which fullfill criteria (5)

Acknowledgements

I had the chance to accomplish this Ph.D. research work at the Laboratory for Neutron Scattering ETH Zurich & PSI Villigen within three years. The two projects have been financially supported by the Swiss National Science Foundation as well as the MaNEP National Center of Competence in Research (NCCR).
I would like to thank Prof. Dr. A. Furrer for involving me in these hot topics. I gratefully acknowledge his confidence in my scientific skills and his advice concerning the data acquisition and the interpretation. A special thanks for supervising my work also goes to Prof. Dr. M. Sigrist from the Institute of Theoretical Physics at ETH Zurich. I appreciated the fruitful discussions and his wise suggestions, especially concerning the α-$MnMoO_4$ project.
I also acknowledge the great teamwork with Prof. Dr. H.-U. Güdel and St. Ochsenbein from the Department of Chemistry and Biochemistry at the University of Berne. Together with St. Ochsenbein, the fellow Ph.D. student, I performed the experiments on TASP, RITA II and TriCS. His efficent and goal-oriented style contributed significantly to the successful results. Without Dr. B. Trusch and Dr. J. Hulliger growing the single crystal α-$MnMoO_4$, this fascinating work would not have been possible.
I express my gratefulness to Dr. A. Podlesnyak who collaborated in the LSCO-project as the local contact during the FOCUS experiments. In addition he was involved in the interpretation of the experimental data. I gained lots of experiences from his experimental know-how. I would like to thank Dr. K. Conder and Dr. E. Pomjakushina for producing all the LSCO samples. Our ideas were realized by a successful collaboration.
I had the chance to talk to Prof. K.A. Müller who discovered the phenomenon of high-temperature superconductivity. I appreciated our discussions about his interpretations of my data.
The excellent collaboration with local contacts Dr. B. Roessli, Dr. O. Zharako and Dr. Ch. Niedermayer is highly appreciated.
I greatly acknowledge the help of the sometimes very long discussions with Dr. Ch. Niedermayer, Prof. Dr. M. Kenzelmann, Dr. H. Rønnow's, Dr. L. Keller, Dr. M. Zolliker, Dr. F. Juranyi as well as with the leader of the diffraction group, Dr. J. Schefer and the Condensed Matter Theory Group at PSI, Dr. A. Bill, A. Schnyder, Dr. Ch. Mudry and Dr. B. Delley. Special thanks goes to the technical support from W. Latscha, St. Fischer, Ch. Kägi and Th. Mühlebach.
At the top of my thank you list, I include my office mates M. Schneider, Dr. R. Gilardi and J. Chang for their support and for being able to help me work in an efficient atmosphere.
Last but not least, I would like to thank my parents Hanny and Toni and my brother Marc for their loving support.

Curriculum Vitae

Personal Data

First Name	Petra S.
Last Name	Häfliger
Date of Birth	14.05. 1976
Place of Birth	Luzern, Switzerland
Nationality	Swiss

Education

05/2002-01/2006	Ph.D. thesis in experimental condensed matter research at the Laboratory for Neutron Scattering ETH Zurich & PSI Villigen
04/2002	awarded *Dipl. Phys. ETHZ*
10/2001-03/2002	Diploma thesis in experimental condensed matter research *Electronic properties of an electron gas in an $Al_xGa_{1-x}As$- parabolic quantum well* at the University of California Santa Barbara, USA Supervisor: Prof. Dr. D. Awschalom (UCSB) & Prof. Dr. K. Ensslin (ETHZ)
02/2001-04/2001	Internship in experimental condensed matter research at the Tokyo Institute of Technology, Japan *Preparation and characterization of II-V diluted magnetic semiconductors GaInMnAs on InP substrate* Supervisor: Prof. Dr. H. Munekata (Titech) & Prof. Dr. K. Ensslin (ETHZ)

1996-2001	Studies in physics at ETH Zurich
10/2001	Schlussdiplom in experimental physics
10/1999	2. Vordiplom in physics
10/1998	2. Vordiplom in mathematics
05/1996	Matura Type B

Languages

German:	mother tongue
English:	fluently, diploma thesis in Santa Barabara (USA)
French:	very good
Italien:	basic knowledge
Japanese:	basic knowledge

Extracurricular Activities

08/2004 - 10/2005	Collaboration in public relations PSI
10/2003 - 10/2005	Counselor for students, departement of physics, ETHZ
1996 - 2002	Foundation of the sports club "Einrad-Renn Club Luzern" (unicycling) organization of events
1995 -2000	FIS-ski slalom referee

Private Interests

1986 -2002	Unicycle racing 3*rd* rank world championship in Beijing, China Swiss champion (400 m, 800 m, obstacle course)

Publications

submitted to Phys. Rev. B
P.S. Häfliger, A. Podlesnyak, K. Conder, E. Pomjakushina, and A. Furrer
The pseudogap in LSCO-type high-temperature superconductors as seen by neutron crystal-field spectroscopy

in preparation
P.S. Häfliger, St. Ochsenbein, B. Trusch, J. Hulliger, S. Gvasaliya, Ch. Niedermayer, O. Zaharko, A. Furrer and H.U. Güdel
Magnetic excitations in α-$MnMoO_4$

05/2006
C.R.H. Bahl, K. Lefmann, A.B. Abrahamsen, H.M. Rønnow, F. Saxild, T.B.S. Jensen, L. Udbt, N.H. Anderson, N.B. Christensen, H.S. Jakobsen, T. Larson, P.S. Häfliger, S. Streule, Ch. Niedermayer
Inelastic neutron scattering experiments with the monochromatic imaging mode of the RITA-II spectrometer
Nucl. Instr. Meth. B, **246**, 452 (2006).

01/2006
P.S. Häfliger, A. Podlesnyak, K. Conder, E. Pomjakushina, and A. Furrer
Pressure Effect on the Pseudogap in the optimally doped high-temperature superconductor $La_{1.81}Sr_{0.15}Ho_{0.04}CuO_4$
Europhys. Lett. **73**, 260 (2006).

03/2005
A. Podlesnyak, P.S. Häfliger, K. Conder, and A. Furrer
Neutron spectroscopic study of the pseudogap formation in $La_{1.81}Sr_{0.15}Ho_{0.04}CuO_4$
J. Phys.: Condens. Matter **17**, S801 (2005)

07/2004
P.S. Häfliger, A. Podlesnyak, K. Conder, E. Pomjakushina, and A. Furrer
Observation of the pseudogap in the heavily overdoped high-temperature superconductor $La_{1.71}Sr_{0.25}Ho_{0.04}CuO_4$
Europhys. Lett. **67**, 1018 (2004)

03/2004 A. Furrer, K. Conder, P.S. Häfliger, A. Podlesnyak
Isotope, pressure and doping effects on the pseudogap in LSCO-type compounds studied by neutron spectroscopy
Physica C **408-410**, 773 (2004)